UNIVERSITÀ
DEGLI STUDI
FIRENZE

DOTTORATO DI RICERCA IN
FISICA E ASTRONOMIA

CICLO XXXVI

Outflowing active galactic nuclei and where to find them

Settore Scientifico Disciplinare
FIS/05

Dottoranda
Giulia Tozzi
Giulia Tozzi

Supervisori
Dott. Giovanni Cresci

Prof. Alessandro Marconi
Alessandro Marconi

Coordinatore
Prof. Giovanni Modugno
Giovanni Modugno

Anni 2020/2023

Ai fantastici 3 di Arcetri,
Giovanni, Alessandro e Filippo

Declaration

The work presented in this PhD thesis was undertaken between 1 November 2020 and 30 October 2023 under the supervision of Dr. Giovanni Cresci and Prof. Alessandro Marconi, in the Department of Physics and Astronomy of the Università degli Studi di Firenze (UNIFI), in collaboration with INAF - Osservatorio Astrofisico di Arcetri.

Portions of this work have appeared (or are to appear) in the following papers:

- Chapter 2: **G. Tozzi**, R. Maiolino, G. Cresci, J. M. Piotrowska, F. Belfiore, M. Curti, F. Mannucci, and A. Marconi, 2023, MNRAS, 521, 1264, *Unveiling hidden active nuclei in MaNGA star-forming galaxies with HeIIλ4686 line emission.*

- Chapter 3: **G. Tozzi**, E. Lusso, L. Casetti, M. Romoli, G. Andreuzzi, I. Montoya Arroyave, E. Nardini, G. Cresci, R. Middei, S. Bertolini, P. Calabretto, V. Cammelli, F. Cuadra, M. Dalla Ragione, C. Marconcini, A. Miceli, I. Mini, M. Palazzini, G. Rotellini, A. Saccardi, L. Samà, M. Sangalli, L. Serafini, and F. Spaccino, 2022, A&A, 667, L12, *The optically elusive, changing-look active nucleus in NGC 4156.*

- Chapter 4: **G. Tozzi**, G. Cresci, A. Marconi, F. Mannucci et al., in prep., *Comparing MUSE and KMOS panoramic IFU spectroscopy of NGC 6240.*

- Chapter 5: **G. Tozzi**, G. Cresci, A. Marasco, E. Nardini, A. Marconi, F. Mannucci, G. Chartas, F. Rizzo, A. Amiri, M. Brusa, A. Comastri, M. Dadina, G. Lanzuisi, V. Mainieri, M. Mingozzi, M. Perna, G. Venturi, C. Vignali, 2021, A&A, 648, A99, *Connecting X-ray nuclear winds with galaxy-scale ionised outflows in two* $z \sim 1.5$ *lensed quasars.*

- Chapter 6: **G. Tozzi**, G. Cresci, M. Perna, V. Mainieri, F. Mannucci, A. Marconi, et al., 2023, to be submitted, *SUPER VIII. Fast & Furious: type-2 active nuclei host faster ionised winds than type-1 at* $z \sim 2$.

The work described in Chapter 2 was carried out also under the supervision of Prof. Roberto Maiolino at the Kavli Institute for Cosmology, University of Cambridge (UK). Chapter 3 is based on data acquired at the Telescopio Nazionale Galileo (TNG) by UNIFI students, within an introductory course on observational astronomy led by Profs. Elisabeta Lusso, Lapo Casetti and Marco Romoli.

In addition to the work presented in this thesis, I have collaborated to the following publications:

- A. Marasco, G. Cresci E. Nardini, F. Mannucci, A. Marconi, P. Tozzi, G. Tozzi, A. Amiri, G. Venturi, E. Piconcelli, G. Lanzuisi, F. Tombesi, M. Mingozzi, M. Perna, S. Carniani, M. Brusa, S. di Serego Alighieri, 2020, A&A, 644, A15, *Galaxy-scale ionised winds driven by ultra-fast outflows in two nearby quasars.*

- F. Mannucci, F. Belfiore, M. Curti, G. Cresci, R. Maiolino, A. Marasco, A. Marconi, M. Mingozzi, G. Tozzi, A. Amiri, 2021, MNRAS, 508, 1582, *The diffuse ionized gas (DIG) in star-forming galaxies: the influence of aperture effects on local H* II *regions.*

- F. Mannucci, E. Pancino, F. Belfiore, C. Cicone, A. Ciurlo, G. Cresci, E. Lusso, A. Marasco, A. Marconi, E. Nardini, E. Pinna, P. Severgnini, P. Saracco, G. Tozzi, S. Shen, 2022, Nature Astronomy, 6, 1185, *Unveiling the population of dual and lensed active galactic nuclei at sub-arcsec separations.*

- A. Ciurlo, F. Mannucci, S. Yeh, A. Amiri, S. Carniani, C. Cicone, G. Cresci, E. Lusso, A. Marasco, C. Marconcini, A. Marconi, E. Nardini, E. Pancino, P. Rosati, K. Rubinur, P. Severgnini, M. Scialpi, G. Tozzi, G. Venturi, C. Vignali, M. Volonteri, 2022, A&A Astronomy, 671, L4, *New multiple AGN systems with subarcsec separation: Confirmation of candidates selected via the novel GMP technique.*

- G. Cresci, G. Tozzi, M. Perna, M. Brusa, C. Marconcini, A. Marconi, S. Carniani, M. Brienza, M. Giroletti, F. Belfiore, M. Ginolfi, F. Mannucci, L. Ulivi, J. Scholtz, G. Venturi, S. Arribas, H. Übler, F. D'Eugenio, M. Mingozzi, B. Balmaverde, A. Capetti, E. Parlanti, T. Zana, 2023, A&A, 672, A128, *Bubbles and outflows: The novel JWST/NIRSpec view of the* $z = 1.59$ *obscured quasar XID2028.*

- D. Kakkad, V. Mainieri, G. Vietri, I. Lamperti, S. Carniani, G. Cresci, C. Harrison, A. Marconi, M. Bischetti, C. Cicone, C. Circosta, B. Husemann, A. Man, F. Mannucci, H. Netzer, P. Padovani, M. Perna, A. Puglisi, J. Scholtz, G. Tozzi, C. Vignali, L. Zappacosta, 2023, MNRAS, 520, 5783, *SUPER VII. Morphology and kinematics of H*α *emission in AGN host galaxies at cosmic noon with SINFONI.*

- C. Marconcini, A. Marconi, G. Cresci, G. Venturi, L. Ulivi, F. Mannucci, F. Belfiore, G. Tozzi, M. Ginolfi, A. Marasco, S. Carniani, A. Amiri, E. Di Teodoro, M. Scialpi, N. Tomicic, M. Mingozzi, M. Brazzini, B. Moreschini, 2023, A&A, 677, A58, *MOKA*^{3D}*: An* *innovative approach to 3D gas kinematic modelling. I. Application to AGN ionised outflows.*

- M. V. Zanchettin, C. Feruglio, M. Massardi, A. Lapi, M. Bischetti, S. Cantalupo, F. Fiore, A. Bongiorno, A. Malizia, A. Marinucci, M. Molina, E. Piconcelli, F. Tombesi, A. Travascio, G. Tozzi, R. Tripodi, 2023, A&A, eprint arXiv:2308.04108, *NGC 2992: The interplay between the multiphase disk, wind and radio bubbles.*

- F. Mannucci, M. Scialpi, A. Ciurlo, S. Yeh, C. Marconcini, G. Tozzi, G. Cresci, A. Marconi, A. Amiri, F. Belfiore, S. Carniani, C. Cicone, E. Nardini, E. Pancino, K. Rubinur, P. Severgnini, L. Ulivi, G. Venturi, C. Vignali, M. Volonteri, E. Pinna, F. Rossi, A. Puglisi, G. Agapito, C. Plantet, E. Ghose, L. Carbonaro, M. Xompero, P. Grani, S. Esposito, J. Power, J. C. Guerra Ramon, M. Lefebvre, A. Cavallaro, R. Davies, A. Riccardi, M. Macintosh, W. Taylor, M. Dolci, A. Baruffolo, H. Feuchtgruber, K. Kravchenko, C. Rau, E. Sturm, E. Wiezorrek, Y. Dallilar, M. Kenworthy, A&A, in press, eprint arXiv:2305.07396, *GMP-selected dual and lensed AGNs: selection function and classification based on near-IR colors and resolved spectra from VLT/ERIS, KECK/OSIRIS, and LBT/LUCI.*

Giulia Tozzi
December 2023

Acknowledgements

Questa tesi di dottorato è frutto anche delle esperienze che ho vissuto e delle fantastiche persone che ho incontrato in questi anni. Il grazie più grande va a Giovanni Cresci, per avermi seguita con costante dedizione, entusiasmo e stima fin da quando non sapevo cosa fosse un cubo di dati. Insieme a lui, ringrazio anche Alessandro Marconi e Filippo Mannucci, per avermi insegnato non solo i segreti più nascosti dei nuclei galattici attivi, ma anche ad amare la ricerca e a divertirmi nel farla.

Un grande grazie va poi ad altre due persone che sono state fondamentali nel mio percorso. Ad Antonino Marasco, per avermi insegnato a fittare le mie prime Gaussiane, a non arrendermi mai di fronte agli errori di python e alla fine… ad averla (quasi) sempre vinta. Grazie anche per i preziosi consigli, che continua a dispensare a distanza di anni. Un grazie sincero poi a Roberto Maiolino per avermi dato la fanstatica opportunità di lavorare con lui a Cambridge, e fatto ritrovare l'entusiamo per questo lavoro dopo la prima ondata di Covid-19. È stato come tornare a respirare.

Ringrazio anche gli studenti, i postdoc e ricercatori che ho conosciuto in questi anni ad Arcetri, con i quali ho condiviso gioie e dolori del dottorato. Un grazie speciale va a Elena Bertola e Martina Scialpi, per l'instancabile supporto, le risate (a volte isteriche) e tutto ciò che abbiamo condiviso. Spero di continuare a scovare insieme a voi nuovi UFOs e dual AGN!

Un grazie di cuore va infine alla mia famiglia, che mi ha sostenuto e incoraggiato in ogni momento di questo percorso, sempre con amore e entusiasmo (a volte anche con un po' di pazienza). Alla mia dolce mamma, per tutto quello che mi ha insegnato e i constanti stimoli che non mi ha mai fatto mancare fin da bambina. A mio babbo, per l'affetto, la stima e la curiosità che ha sempre mostrato per l'Universo ed i miei studi. Grazie a mia sorella Rebecca, riferimento fondamentale nella mia vita, a cui auguro di vivere un percorso di dottorato appassionante tanto quanto lo è stato il mio. Infine, un grazie di cuore a Federico, per essermi sempre vicino e volermi bene così come sono, con la testa sempre un po' tra le stelle.

Table of contents

List of acronyms **xv**

Abstract **xvii**

1 Active Galactic Nuclei **1**

1.1 AGN structure and multi-wavelength emission 2

1.1.1 The nuclear engine: accreting BHs 2

1.1.2 The complex AGN zoo 3

1.1.2.1 AGN Unified Model 5

1.1.2.2 Evolutionary models of active galaxies 6

1.1.2.3 The restless nature of AGN: variability and changing-look events 7

1.1.3 The complete AGN census: a multi-wavelength search 10

1.2 The role of AGN in galaxy evolution 13

1.2.1 The need for AGN feedback 14

1.2.2 The radiative mode: AGN-driven outflows 18

1.2.2.1 Acceleration mechanisms of AGN winds 19

1.2.2.2 Negative or positive feedback? 21

1.2.3 Multi-phase and multi-scale AGN outflows 22

1.2.3.1 Highly ionised outflows 24

1.2.3.2 Ionised outflows 26

1.2.3.3 Molecular and atomic neutral outflows 27

1.3 Investigating AGN with Integral Field Spectroscopy 29

1.3.1 Basics of IFU observations 29

1.3.2 Ground-based IFU facilities used in this thesis 31

1.3.3 Spectral fitting of IFU data cubes 32

1.4 Goals and strategy of this thesis 35

2 Unveiling hidden AGN in MaNGA star-forming galaxies with He IIλ4686 37
2.1 Sample selection and classification 39
2.1.1 MaNGA data 39
2.1.2 Spatially resolved emission line diagrams 39
2.1.2.1 BPT and He II diagnostic diagrams 40
2.1.2.2 Comparing the two diagnostic diagrams 42
2.1.3 Selecting AGN host galaxies in MaNGA 42
2.1.3.1 Excluding cases of dubious He II line emission 43
2.1.3.2 Need for re-modelling some MaNGA data cubes 43
2.1.3.3 Search for type-1 AGN and He II due to WR stars 46
2.1.3.4 Final refined AGN sample 47
2.1.4 Verifying the AGN-like nature of He II line emission 51
2.2 Properties of the AGN host galaxies 52
2.3 Discussion 55
2.3.1 Estimating the number of undetected He II-only AGN 55
2.3.2 Implications for the AGN census and quenching scenarios 57
2.4 Conclusions 60

3 The optically elusive, changing-look active nucleus in NGC 4156 63
3.1 TNG/DOLORES observations of NGC 4156 65
3.1.1 Data reduction 66
3.2 Spectral analysis 67
3.2.1 Modelling of broad-line emission 71
3.2.2 Modelling of narrow-line emission 72
3.3 Results 73
3.3.1 Single-epoch estimates of AGN properties 74
3.3.2 Constant (ambiguous) narrow-line emission in NGC 4156 75
3.4 Discussion and conclusions 76

4 Comparing MUSE and KMOS panoramic IFU spectroscopy of NGC 6240 79
4.1 NGC 6240: a local merger hosting a double AGN 81
4.2 KMOS and MUSE observations of NGC 6240 82
4.2.1 Near-IR *H*- and *K*-band KMOS small mosaic 82
4.2.2 Optical MUSE Wide Field Mode observations 84
4.3 Data analysis 85
4.3.1 MUSE WFM data cube 85
4.3.2 KMOS *H*- and *K*-band data 89

4.4 Preliminary results 91
    4.4.1 Gas morphology and kinematics 93
        4.4.1.1 Optical emitting gas 93
        4.4.1.2 Near-IR emitting gas 97
    4.4.2 Ionised gas properties 102
    4.4.3 Near-IR emission-line diagnostics 105
        4.4.3.1 The [Fe II]/Brγ – H_2(1-0)S(1)/Brγ diagram 106
        4.4.3.2 The H_2(1-0)S(2)/H_2(1-0)S(0) – H_2(2-1)S(1)/H_2(1-0)S(1) diagram 109
4.5 Conclusions and future steps 110

5 Connecting X-ray UFOs with galaxy-scale ionised winds in two z~1.5 lensed AGN 115
5.1 Description of the quasars in this work 116
    5.1.1 Selection of targets 116
        5.1.1.1 HS 0810+2554 117
        5.1.1.2 SDSS J1353+1138 118
    5.1.2 SINFONI observations and data reduction 119
    5.1.3 Lens models for the two quasars 120
5.2 Data analysis 121
    5.2.1 Spectral fitting 121
        5.2.1.1 Phases I-II. Modelling full data cubes 122
        5.2.1.2 Phase III. Modelling narrow emission lines in subtracted data cubes 122
    5.2.2 Modelling a ‘double’ BLR in SDSS J1353+1138 125
    5.2.3 Testing the spatially resolved emission of the ionised outflows 128
5.3 Results 131
    5.3.1 Distribution and kinematics of the ionised gas 131
    5.3.2 Correcting outflow properties for lens effects 136
        5.3.2.1 Approximated reconstruction of the unlensed outflow in HS 0810+2554 136
        5.3.2.2 Inferring unlensed size and flux of ionised outflows 139
    5.3.3 Outflow energetics 140
5.4 Discussion 144
    5.4.1 Connection with nuclear X-ray UFOs 144
    5.4.2 Comparison with other AGN hosting UFOs 148
5.5 Conclusions 150

6 Fast & Furious: type-2 AGN host faster ionised winds than type-1 at z~2 in SUPER 153
6.1 The SUPER survey 154
6.1.1 The type-2 AGN subsample 155
6.1.2 Observations and data reduction 155
6.2 Data analysis 158
6.2.1 Spectral fitting 159
6.2.2 Integrated *H* and *K*-band spectra 160
6.3 Results 161
6.3.1 Ionised gas kinematics: evidence of spatially resolved outflows 161
6.3.2 Ionised outflow properties and energetics 169
6.3.2.1 Directly measured outflow properties: velocity, radius and luminosity 169
6.3.2.2 Ionised outflow mass rate 171
6.3.3 Comparison with SUPER type-1 AGN 172
6.3.3.1 Faster outflows in type-2 AGN at the low-luminosity end of SUPER 173
6.3.3.2 Outflow mass rate as a function of bolometric luminosity . . 176
6.3.4 Can ionised outflows escape galaxy gravitational potential? 178
6.4 Discussion 179
6.5 Conclusion 183

Conclusions and perspectives 184

Bibliography 189

List of acronyms

AGN	Active Galactic Nuclei
AO	Adaptive Optics
BAL	Broad Absorption Line
BD	Balmer Decrement
BH	Black Hole
BLR	Broad-Line Region
BPT	Baldwin, Phillips & Terlevich
CL	Changing-Look
DM	Dark Matter
EW	Equivalent Width
FWHM	Full Width at Half Maximum
FoV	Field of View
GV	Green Valley
IFU	Integral Field Unit
IFS	Integral Field Spectroscopy
IR	InfraRed
ISM	InterStellar Medium
KS	Kolmogorov-Smirnov
LINER	Low-Ionisation Nuclear Emission-line Region
MS	Main Sequence
NAL	Narrow Absorption Line
NLR	Narrow-Line Region
PSF	Point Spread Function
SED	Spectral Energy Distribution
SF	Star Formation
SFR	Star Formation Rate
SIE	Singular Isothermal Ellipsoid

SIS	Singular Isothermal Sphere
S/N	Signal-to-Noise
SSP	Single Stellar Population
UFO	UltraFast Outflow
ULIRG	Ultra-Luminous Infrared Galaxy
UV	UltraViolet
WFS	WaveFront Sensor
WR	Wolf-Rayet

Abstract

Active Galactic Nuclei (AGN) represent a key stage of galaxies' life cycle, powered by accretion of matter onto a central supermassive black hole (BH) ($M_{\rm BH} \sim 10^6 - 10^{10}$ M$_\odot$). Featured by high luminosity and strong variability, AGN present the unique property of leaving imprints over the entire electromagnetic spectrum (from radio to γ-rays). As a consequence, AGN find application in many research areas, from extragalactic astronomy to cosmology.

In the last three decades, AGN have increasingly become protagonists of galaxy evolution studies, because of the profound effects an accreting BH can have on its host galaxy - the so-called AGN feedback. Nowadays, theoretical and numerical works invoke AGN feedback to reconcile observational results with model predictions, and to explain the observed co-evolution of BHs with their host galaxies (e.g. Kormendy and Ho 2013). In particular, AGN feedback is considered to be responsible for the quenching of star formation (SF) in massive galaxies, through multi-phase outflows launched from close to the accretion disk and extending up to galaxy scales, which may either expel or heat (via energy injection) the host gas reservoir, eventually halting the formation of new stars. Although AGN-driven outflows have been extensively observed from low to high redshift, placing observational constraints on model predictions is challenging, with several questions still unanswered. For instance, *what is the real impact of outflows on their host? How are outflows accelerated and propagated from nuclear to galaxy scales? What are their physical properties and how do different gas phases relate to each other?*

Besides addressing these questions on AGN outflows, this PhD thesis investigates standard and novel optical diagnostic methods to get a complete and unbiased census of AGN from low to high redshift, necessary to properly compare observational results with theoretical predictions; and also faces AGN variability taking the form of dramatic optical type transitions - the so-called changing-look AGN - which challenge the standard AGN unified picture (e.g. Urry and Padovani 1995). To address most of these topics, this thesis widely employs Integral Field Unit (IFU) observations obtained with several ground-based facilities, which allow us to detect AGN-driven outflows and faint local signatures of AGN activity by spatially tracing gas emission and its kinematics.

In the first science chapter (Chapter 2) we use the optical He II diagnostic (Shirazi and Brinchmann, 2012) to select AGN galaxies in the local IFU MaNGA survey (Bundy et al., 2015). Compared to standard optical diagnostics (i.e. BPT diagrams; Baldwin et al. 1981), He II line emission proves its higher efficiency at unveiling hidden AGN in highly star-forming galaxies, with important applications at high redshift (e.g. Nakajima and Maiolino 2022). The second science chapter (Chapter 3) instead faces the variable nature of AGN, reporting on the recent discovery of optical changing-look (CL) events in the local AGN galaxy NGC 4156, demonstrating how such unexpected type transitions can make visible even more elusive AGN. In spite of the increasing number of newly discovered CL AGN (Ricci and Trakhtenbrot, 2022), the mechanism at their origin is still uncertain. Important insights into CL events in NGC 4156 might come from our ongoing joint X-ray and optical monitoring with *Swift* and the Asiago telescope, respectively.

The remaining science chapters focus on the main topic addressed by this PhD research: the study of AGN outflows using spatially resolved IFU observations, from the local Universe with the intriguing case of the galaxy merger NGC 6240, to more distant objects at $z \sim 2$ - the golden epoch of AGN feedback (e.g. Madau and Dickinson 2014). For NGC 6240 (Chapter 3), we combine optical MUSE and near-IR KMOS observations to get an unprecedented panoramic view of ionised and warm molecular phases in this galaxy, aiming at studying corresponding outflow components as well as gas ionisation and excitation properties via optical (Baldwin et al., 1981, Veilleux and Osterbrock, 1987) and near-IR emission-line diagnostics (e.g. Mouri 1994, Riffel et al. 2013). Moving to $z \sim 2$, we focus on the ionised phase of AGN outflows traced via rest-frame optical [O III]λ5007 in near-IR SINFONI observations (Chapters 5 and 6). In Chapter 5, we shed light on the acceleration mechanism of large-scale outflows in two gravitationally lensed quasars, by studying their link with co-hosted nuclear X-ray winds in the framework of ‘wind feedback’ models (e.g. King and Pounds 2015). Finally, Chapter 6 completes this series of works on AGN outflows by presenting results on a sample of X-ray bright but optically obscured AGN from the SUPER survey (Circosta et al., 2018). By comparing outflow and host galaxy properties, this work provides observational evidence of a more efficient wind acceleration in obscured type-2 objects, thus supporting the ‘blow-out’ evolutionary scenario (e.g. Hopkins et al. 2006, Menci et al. 2008), where AGN transition through different obscuring states.

New advanced IFU spectrographs, NIRSpec on *JWST* and ground-based AO-assisted facilities like ERIS at the VLT, are opening a new window at high spatial and spectral resolution on the $z > 2$ Universe. This will allow us to take the next step to fully understand feedback mechanisms and AGN evolution at the Cosmic Noon.

Chapter 1

Active Galactic Nuclei

Virtually all massive galaxies are nowadays known to host in their centre a supermassive black hole (BH) of mass $M_{\rm BH} \sim 10^6 - 10^{10}$ $\rm M_\odot$, including our own Milky Way (Ghez et al., 1998, Genzel et al., 2003, Gillessen et al., 2009). During their life, BHs occasionally experience episodes of intense matter accretion from the surrounding medium, which give rise to a so-called Active Galactic Nucleus (AGN). From an observational perspective, AGN are the most powerful, non-explosive sources in the Universe, presenting a wide range of interesting properties. These include: (1) very high luminosities (up to a bolometric luminosity $L_{\rm bol} \sim 10^{48}$ erg s^{-1}), which make them detectable up to very high redshifts (currently $z = 10.6$ is the highest redshift; Maiolino et al. 2023a); (2) a strong variability (e.g. Ulrich et al. 1997); (3) unique observational signatures over the whole electromagnetic spectrum, from radio to γ-rays (see Padovani et al. 2017 for a review).

Besides being fascinating sources to study, in the last three decades, AGN have played a major role in extragalactic astronomy research. Theoretical works and numerical simulations now show the profound effects that AGN potentially have on their host galaxy up to large scales. This so-called AGN feedback is moreover invoked as a crucial ingredient to reconcile theoretical predictions on galaxy evolution with observational results, and as main responsible for the observed growth in symbiosis of supermassive BHs with their host (e.g. Kormendy and Ho 2013 for a review). On the other hand, high-quality observations have provided increasing evidence for AGN feedback in galaxies, such as AGN-driven outflows and radio jets which are routinely detected from low to high redshift.

However, placing observational constraints on AGN feedback must face observational limits and deal with AGN samples biased against more obscured and/or weaker AGN, especially at high redshift. Moreover, AGN variability may challenge any proper comparison of observational results with theoretical predictions, thus complicating the global picture even more. As a consequence, the role of AGN in galaxies' evolution is an open field of research, with many questions remaining unanswered.

This PhD thesis uses a great variety of integral field unit (IFU) observations to investigate AGN-driven outflows in both local and distant ($z \sim 2$) AGN galaxies, as well as standard and novel methods to identify AGN galaxies aiming at obtaining complete and unbiased AGN samples. In doing so, this work also addresses AGN variability, not only in terms of related issues affecting observational measurements, but also as an intriguing property which can make *unexpectedly* visible even more elusive AGN.

This first chapter provides a general introduction to the main scientific topics examined in this thesis, as well as the basics of IFU spectroscopy; whereas more specific introductory material can be found at the beginning of individual science chapters.

1.1 AGN structure and multi-wavelength emission

To assist with the understanding of the topics investigated within this thesis, it is useful to introduce important physical parameters describing the growth of the inner BH (Sect. 1.1.1), as well as to provide an overview on the complex AGN 'zoo' (Sect. 1.1.2), showing how different models can account for it. All this will finally highlight the importance of a multi-wavelength and multi-epoch search for AGN to get a full picture of their complex physics (Sect. 1.1.3).

1.1.1 The nuclear engine: accreting BHs

According to the AGN standard physical model (Fig. 1.1), the powering engine of AGN is a central BH which is accreting matter from the surrounding medium. As the BH is being fed, the gravitational energy lost by in-falling material is converted into radiative energy. If a BH is growing at an effective mass rate $\dot{M}_{\rm BH}$, the accretion luminosity is given by:

$$L_{\rm acc} = \frac{\eta}{1-\eta}\dot{M}_{\rm BH}c^2, \tag{1.1}$$

where c is the speed of light, and η the mass-to-energy conversion efficiency, defined with respect to the large-scale mass inflow, with the dividing factor $(1-\eta)$ accounting for radiative losses (e.g. Shankar et al. 2013, Harrison et al. 2018). Typically, η is assumed to $\approx$0.1 (e.g. Soltan 1982), but its value depends on the BH spin and can vary within an expected range of $\eta = 0.05 - 0.42$ (e.g. Kerr 1963, Thorne 1974).

However, supermassive BHs cannot grow *indefinitely* as fast as they want. There is a theoretical maximum value of $L_{\rm acc}$, above which the radiation pressure sweeps away the in-falling gas, thus stopping accretion. This upper limit is called 'Eddington luminosity' ($L_{\rm Edd}$) and can be computed by assuming the inward gravitational force to be equal to the outward radiative force of $L_{\rm acc}$:

$$L_{\rm Edd} = \frac{4\pi G M_{\rm BH} m_{\rm p} c}{\sigma_{\rm T}} \approx 1.3 \times 10^{38} \left(\frac{M_{\rm BH}}{\rm M_\odot}\right) \text{erg s}^{-1}, \tag{1.2}$$

where G is the gravitational constant, m_p the proton mass, and σ_T the Thomson cross-section for electron scattering. To compare accretion rates over a wide range of BH masses, it is useful to consider the 'Eddington luminosity' ($\lambda_{\rm Edd}$), defined as the ratio of the observed accretion luminosity to the Eddington luminosity (i.e. $\lambda_{\rm Edd} = L_{\rm acc}/L_{\rm Edd}$). Large values of $\lambda_{\rm Edd}$ (i.e. $\lambda_{\rm Edd} \gtrsim 0.1$) usually identify systems accreting at a 'high' accretion rate. However, the Eddington parameter is not an insuperable limit: supermassive BHs can indeed undergo episodic phases of super-Eddington accretion ($\lambda_{\rm Edd} \gtrsim 1$; see Sect. 1.2.2).

1.1.2 The complex AGN zoo

As discussed in this section, AGN are being discovered at all wavelengths and found exhibiting a large variety of different spectral properties, including a variable behaviour. We here revise the main empirical classifications based on AGN emission in different spectral bands (see Padovani et al. 2017 for a review), namely, X-ray, optical and radio bands.

Starting from high energies, essentially all AGN are selected in the X-rays, but they may differ in X-ray absorption features, due to a different amount of intervening (absorbing) material. Usually, X-ray 'obscured' sources are those with high hydrogen column densities (i.e. $N_{\rm H} > 10^{22}$ cm^{-2}), as opposed to X-ray 'unobscured' counterparts (i.e. $N_{\rm H} < 10^{22}$ cm^{-2}). In most cases, such X-ray unobscured and obscured classes correspond to the optical AGN classification into type-1 and type-2 objects, depending on the presence or absence, respectively, of broad optical permitted emission lines (see Sect. 1.1.2). Moving to longer radio wavelengths, AGN appear extremely diverse, with radio luminosities differing by several orders of magnitude from 'radio-loud' compared to 'radio-quiet' AGN (e.g. Kellermann et al. 1989, Elvis et al. 1994), and different morphologies of radio emission. Historically, radio-loud AGN have ratios of radio (5 GHz) to optical (B-band) flux $F_{\rm 5GHz}/F_{\rm B} \gtrsim 10$ (Kellermann et al., 1989). However, 'radio-loud' has increasingly become a term to refer to AGN particularly luminous at radio wavelengths (e.g. with radio luminosities at 1.4 GHz $L_{\rm 1.4GHz} \gtrsim 10^{24}$ W Hz^{-1}; e.g. Best et al. 2005, Tadhunter 2016). Radio-loudness is also often associated with non-thermal synchrotron emission produced

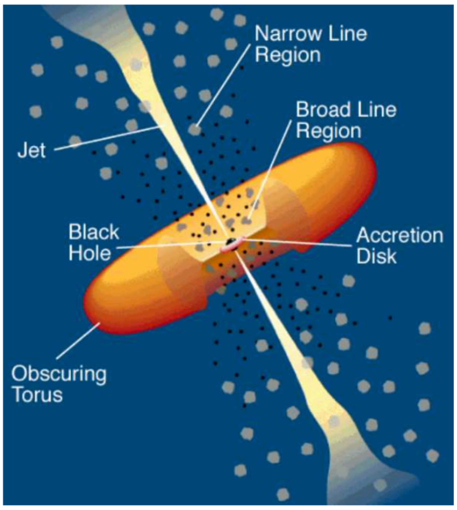

Fig. 1.1 *Schematic representation (adapted from Urry and Padovani 1995) of the AGN Unified Model, the currently most accepted model of AGN structure. A central BH surrounded by an accretion disk is enclosed by a geometrically and optically thick dusty torus. Above and below the accretion disk is a hot corona, while two distinct emission-line regions extend perpendicularly to the disk: a broad-line region (BLR) on nuclear scale (~pc), under the gravitational influence of the BH; a narrow-line region (NLR), which extends on galaxy scales (~1–10 kpc). Collimated radio jets may be also launched close to the accretion disk. 'AGN Unification' implies that, depending on the torus inclination to the line of sight, emission from inner AGN regions will be obscured, hence not observable. In contrast, emission originating on larger scales (e.g. NLR, torus, jets) is less affected by orientation effects.*

by collimated relativistic jets, which are launched close to the accretion disk. In contrast, radio-quiet AGN are usually dominated by thermal emission originating from compact sources, whose nature is more uncertain, with a wide range of possible mechanisms (e.g. Padovani et al. 2017; see Sect. 1.1.2.1).

The rest of this section aims at providing a basic description of the currently most accepted AGN model - the AGN Unified Model (e.g. Antonucci 1993; Sect. 1.1.2.1), which reconnects distinct AGN classes to a single 'unified' picture of AGN (Fig. 1.1). We will also discuss strengths and limits of this simplified model, showing how observational evidence sometimes favours alternative scenarios. Considering the topics addressed by this thesis, we will focus on galaxy evolutionary models to explain the observed dichotomy between obscured (type-2) AGN and unobscured (type-1) AGN at high redshift (Sect. 1.1.2.2), and on a possible combination of variable accretion and obscuration to explain recently discovered changing-look AGN (Sect. 1.1.2.3).

1.1.2.1 AGN Unified Model

In the standard AGN model (e.g. Antonucci 1993, Urry and Padovani 1995, Netzer 2015; Fig. 1.1), the central growing BH is surrounded by an optically thick accretion disk (e.g. Shakura and Sunyaev 1973), emitting a continuum thermal spectrum at a typical black-body temperature of $\approx 2\times10^5$ K, which peaks in the ultraviolet (UV), at $\lambda \approx 10-400$ nm for a typical AGN (i.e. with $M_{\rm BH} \approx 10^8$ $\rm M_\odot$ and $\lambda_{\rm Edd} \approx 0.1$). AGN are expected to emit mostly in the UV but, unfortunately, UV emission can be hardly detected from the ground due to atmospheric absorption. Around the accretion disk, an optically thin corona is thought to originate the X-ray power-law spectrum via inverse Compton scattering of UV photons produced by the accretion disk. Moreover, X-ray photons can be reflected by the dusty torus (see below) and/or by the accretion disk, thus resulting in an additional 'reflection' component in X-ray spectra (e.g. George and Fabian 1991).

UV photons from the accretion disk are also thought to excite dense (i.e. electron densities $n_{\rm e} \gtrsim 10^8$ cm^{-3}; Osterbrock and Ferland 2006), high-velocity gas clouds, which are gravitationally bounded to the BH located on typical scales of a few light-days to light-months (e.g. Peterson et al. 2004). This region is called broad-line region (BLR), since its emission consists of extremely broad permitted emission lines (typical full width at half maximum FWHM > 2000 km s^{-1}; GRAVITY Collaboration et al. 2018, 2020), due to high-velocity motion of gas near accreting supermassive BHs. Such a broad-line emission is exclusively observed in type-1 AGN (as mentioned at the beginning of Sect. 1.1.2), and not in type-2 systems. Forbidden emission lines do not originate from AGN BLR because of too high densities ($n_{\rm e} > 10^8$ cm^{-3}; Osterbrock and Ferland 2006), but can be emitted by low-density gas ($n_{\rm e} \lesssim 10^6$ cm^{-3}) extending on larger scales ($\approx 10^2 - 10^4$ pc), beyond the inner BLR. This region is referred to as narrow-line region (NLR) as opposed to BLR, since resulting emission lines have narrower line widths (i.e. $200 \lesssim$ FWHM $\lesssim 2000$ km s^{-1}).

According to the unified model, a geometrically and optically dusty region surrounds the central AGN region just described, whose inner radius is set by the dust sublimation temperature. In the standard picture, this region has a torus shape, but its real geometry is still uncertain and now widely accepted to be clumpy (e.g. Hönig et al. 2006, Nenkova et al. 2008, Tanimoto et al. 2019). Here, the dust absorbs UV photons from the accretion disk and, then, re-emits thermal radiation in the infrared (IR; $\lambda \approx 1-100$ μm; e.g. Polletta et al. 2000). An additional mid-IR contribution might be also of non-thermal origin, as observed in a large fraction of radio-loud AGN (e.g. Dicken et al. 2008).

Finally, AGN radio emission is traditionally associated with strong relativistic jets, launched close to the accretion disk. However, as discussed at the beginning of Sect. 1.1.2, radio emission might be produced also by other several mechanisms, acting on different scales: compact radio jets, supernovae, free-free emission from photoionised gas, and innermost accretion disk coronal activity (e.g. Polletta et al. 2000, Laor and Behar 2008, Panessa et al. 2019).

The main idea of AGN unification models is that the large empirical diversity of AGN is only partially related to intrinsic differences between AGN, but primarily due to secondary effects. In the standard unification scheme (e.g. Antonucci 1993, Urry and Padovani 1995; Fig. 1.1), distinct AGN classes are the result of a different inclination of the torus to the line of sight. In the case of nearly edge-on inclinations, the dusty torus shields emission from the inner AGN region (i.e. BLR, X-ray corona and accretion disk), thus leading to optical type-2 and X-ray obscured AGN classes. On the contrary, inner AGN emission remains visible in type-1 and X-ray unobscured AGN, which are assumed to be nearly face-one systems in this picture. Optical intermediate types can then result from a combination of viewing angles and a clumpy distribution of the obscuring material with different optical depths (Goodrich, 1989). A similar unification can be applied to radio-loud and radio-quiet AGN as well (e.g. Antonucci 2012), with extended jet-like radio structures preferentially observed for high inclination angles.

In spite of the success of the standard model in explaining a wide range of AGN observed properties, observations provide increasing evidence for phenomena which do not fit into this unified picture, thus leading to consider alternative models (see Sects. 1.1.2.2, 1.1.2.3).

1.1.2.2 Evolutionary models of active galaxies

According to an alternative, competing paradigm, AGN classes exhibiting a different level of obscuration might reflect a distinct life stage in galaxies' evolution (Fig. 1.2), at least at higher redshift ($z > 1$). Evolutionary models (e.g. Hopkins et al. 2006, Menci et al. 2008) indeed predict AGN galaxies to experience a first phase featured by rapid BH growth and intense star formation (SF), during which the central AGN is enshrouded in a dusty and dense environment. All this sets the optimal conditions for the short-lived (a few tens of Myr) 'blow-out' phase (Hopkins et al., 2008), during which powerful AGN-driven outflows clear out the obscuring material and make the AGN visible and definitely unobscured.

Such an evolutionary scenario was proposed to explain the observed dichotomy between red and blue quasars[1] (e.g. Klindt et al. 2019, Perrotta et al. 2019, Fawcett et al. 2023; Fig. 1.2), with the former representing the brief transitional phase during which strong winds blow out the obscuring dust, and ultimately reveal an unobscured blue quasar.

---

[1] The term 'quasar' originally stands for 'Quasi-Stellar Radio Source', but now is commonly used to refer to very luminous AGN (i.e. bolometric luminosities of $L_{\rm bol} \gtrsim 10^{45}$ erg s^{-1}), irrespective of their radio properties.

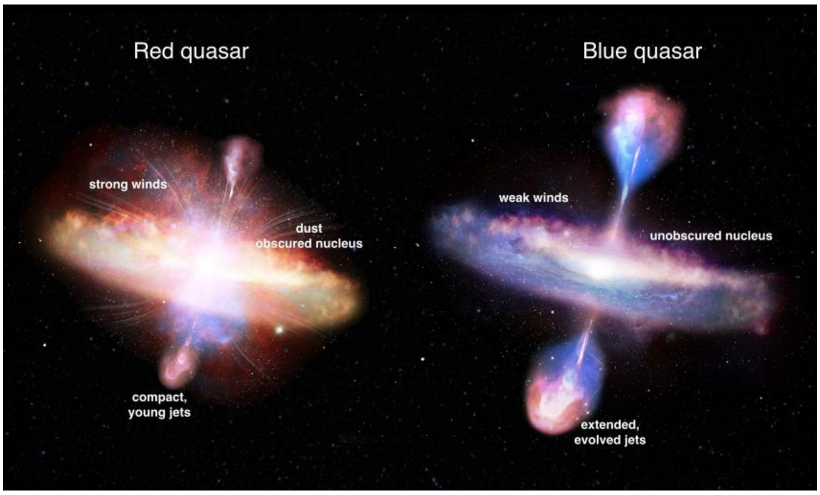

Fig. 1.2 *Red (left) and blue quasars (right), as distinct phases in galaxy evolution. Red quasars are the short-lived (a few tens of Myr) phase, featured by intense star formation (SF) and BH growth, where the AGN is enshrouded in gas and dust. This so-called 'blow-out' phase triggers the launch of strong outflows and powerful jets, which sweep away the obscuring gas and dust, and ultimately reveal an unobscured blue quasar. Artist's impression by S. Munro (visit https://ras.ac.uk/media/286), licensed under CC BY 4.0.*

Whereas orientation effects might drive the observed AGN classification at low redshift, as suggested by several studies on large AGN samples (e.g. Vaona et al. 2012, Mullaney et al. 2013, Bae and Woo 2014, Shen et al. 2016, Rakshit and Woo 2018, Rojas et al. 2020), they might play a minor role in more distant objects, especially at crucial epochs for galaxy formation and evolution (i.e. $z \sim 2$; see Sect. 1.2), where other complex mechanisms are likely involved. For this reason, X-ray bright but optically obscured (type-2) AGN at $z = 1-3$ have been deeply investigated as optimal candidates to be experiencing the blow-out phase (e.g. Brusa et al. 2010, 2016, Cresci et al. 2015a, Perna et al. 2015a,b), hence presenting the best conditions to catch AGN feedback and outflows in action.

1.1.2.3 The restless nature of AGN: variability and changing-look events

Despite not being primarily addressed by this thesis, the strong variability of AGN is an *unavoidable* property to deal with in almost all AGN studies. It was one of the first recognised properties of AGN (Matthews and Sandage, 1963, Smith and Hoffleit, 1963b,a), and now AGN are known to show flux variations across the entire electromagnetic spectrum (e.g. Vanden Berk et al. 2004, Uttley et al. 2005), with typical timescales ranging from minutes to years (Ulrich et al., 1997).

The minimum variability timescale measured in a certain band gives an estimate of the linear size of the source emitting at those specific wavelengths (e.g. Terrell 1967). The most rapid (~minutes, hours) and largest-amplitude flux variations are observed at

X-ray energies, and they are believed to originate in the innermost accretion flow (hot corona and inner accretion disk), as well as to drive part of the variability from the outer accretion disk, observed at longer wavelengths (UV and optical). Substantial contributions to variability observed in radio and γ-ray bands may also come from jet activity (e.g. Max-Moerbeck et al. 2014), via shock formation or injection of new particles (Marscher and Gear, 1985, Böttcher and Dermer, 2010).

AGN variability can be also indirectly probed on longer timescales by studying extended emission line regions, which are affected by lagged effects of past events. In this way, it is possible to trace the history of AGN emission over timescales of $10^4 - 10^6$ years, the typical light travel time from the nucleus to the gas within the emitting-line regions (e.g. Dadina et al. 2010, Keel et al. 2012, Gagne et al. 2014, Davies et al. 2015). As shown later in this thesis, the comparison of phenomena related with AGN activity, but occurring on different spatial scales (i.e. nuclear versus galactic scales) can shed light on AGN accretion history, possibly revealing differences between the past and present activities.

While this ‘ordinary’ variability is usually erratic and stochastic, with a typical amplitude of optical continuum variations of tens per cent (Vanden Berk et al., 2004), in recent years an increasing number of AGN have been discovered to experience much more dramatic and coherent changes in their spectral properties, over timescales of a few years or even several months. The events are usually referred to as changing-look (CL) AGN (see Ricci and Trakhtenbrot 2022 for a review) because of their varying appearance, observed in both X-ray and optical/UV bands with a possible different origin. In the following, we introduce the two main classes of CL events (Fig. 1.3), which feature different observational signatures and are thought to have a distinct physical origin. However, as shown within this thesis itself, a clear distinction between these two categories can be done only in case of intense multi-wavelength monitoring campaigns, otherwise being usually hard to distinguish between them.

Changing-obscuration AGN. Repeated X-ray observations of nearby AGN carried out with *XMM-Newton*, *NuSTAR*, *RXTE*, *Swift* and *Suzaku* have discovered a growing number of CL AGN due to a variable obscuration by neutral intervening gas, as a result of changes in the hydrogen column density (N_{H}) along the line of sight. These objects are usually known as changing-obscuration (CO) AGN (Mereghetti et al., 2021), and appear as X-ray transitions from a (high) unobscured state to a (low) heavily obscured, Compton-thick state (Fig. 1.3, left panel), as N_{H} increases and the re-processed X-ray radiation becomes dominant over the primary suppressed X-ray corona continuum. Such a N_{H} variability is often consequence of the clumpy obscuring material (associated with either

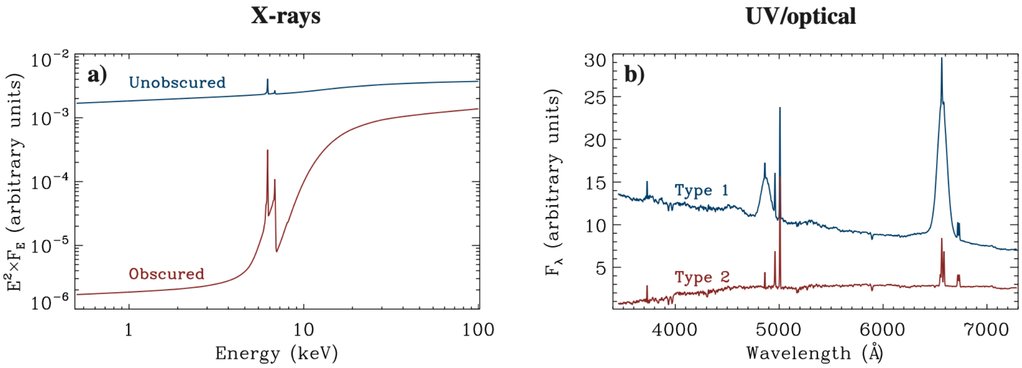

Fig. 1.3 *Typical spectral variations of X-ray and optical changing-look (CL) AGN. Left. In the X-ray, CL events usually consist of variations from an unobscured state (blue line) to a heavily obscured, Compton-thick state (red line). Right. In the optical band, CL AGN are generally identified as type transitions, from a type-1 (blue line) to a type-2 (red line) AGN as the blue continuum and the broad BLR line components disappear. Figure adapted from Ricci and Trakhtenbrot (2022).*

the BLR or the dusty torus; Risaliti et al. 2002), which may generate eclipses of the central X-ray source over timescales of a few hours[2]. Other possible explanations are: a variable ionised absorbing gas along the line of sight (e.g. Kaastra et al. 2014, Beuchert et al. 2015, Mehdipour et al. 2017, Kara et al. 2021), associated with outflows detected in X-ray/UV regimes (King and Pounds 2015; see Sect. 1.2.3.1); or an enhancement in the ionisation state of the obscuring gas produced by an increased AGN luminosity, which leads to an apparent variation of $N_{\rm H}$ (e.g. Yaqoob et al. 1989). In most extreme cases, CO AGN may be even associated with a switch off/on of the AGN (e.g. Guainazzi et al. 1998, Gilli et al. 2000).

Changing-state AGN. In the optical, CL AGN often show strong flux variations, with optical blue continuum and BLR broad-line emission appearing (disappearing) in previously known type-2 (type-1) AGN (e.g. Gregory et al. 1991, Tran et al. 1992, Storchi-Bergmann et al. 1993, Aretxaga et al. 1999, Eracleous and Halpern 2001; Fig. 1.3; Fig. 1.3, right panel). These CL events - known as changing-state (CS) AGN (Graham et al., 2020) - occur over timescales of a few years (e.g. Lawrence et al. 2016, Rumbaugh et al. 2018, Trakhtenbrot et al. 2019, Shen 2021), and are typically driven by rapid changes in the intrinsic AGN luminosity (e.g. Guolo et al. 2021). In particular, increased luminosities might be consequence of AGN feeding processes, which not only boost the BH accretion rate, but also gather gas to form new stars (see Storchi-Bergmann and Schnorr-Müller 2019 for a review on BH feeding), thus explaining why young to intermediate-age stars are

---

[2] Among main identified cases of eclipses, there are NGC 1365 (Iyomoto et al., 1997, Risaliti et al., 2000, 2005, 2007, 2009), NGC 4388 (Elvis et al., 2004), and NGC 4151 (Puccetti et al., 2007).

often observed in association with luminous AGN (e.g. Riffel et al. 2023). A few CS AGN have been also observed to undergo a full cycle, transitioning twice over a few decades[3]. Therefore, it was proposed that intrinsic BLR emission evolves along the optical classification sequence (i.e. from type-2 to type-1, passing through intermediate types) as AGN luminosity increases (Elitzur et al., 2014). In the X-rays, most CS AGN present flux variations correlated with the optical ones (e.g. Krumpe et al. 2017, Parker et al. 2019, Jana et al. 2021), with X-ray flux varying up to factors of a few tens. CS AGN are generally independent from CO AGN (LaMassa et al., 2015, Ricci et al., 2020), as supported by longer timescales ($\gtrsim$ 10 years) and unobscured spectral appearance (e.g. LaMassa et al. 2015, Husemann et al. 2016, MacLeod et al. 2016, Sheng et al. 2017, Yang et al. 2018, Ricci et al. 2020).

1.1.3 The complete AGN census: a multi-wavelength search

As shown previously throughout this section, AGN emit over the entire electromagnetic spectrum and exhibit a variety of spectral features in their both continuum and line emission. As a consequence, several techniques have been developed to identify galaxies hosting AGN, depending on the observing waveband and with their own advantages and disadvantages, such as a selection bias towards/against objects with specific properties. In the following, we describe the most common techniques adopted to select AGN galaxies in X-ray, optical/UV, IR, and radio bands. Whereas this thesis makes direct use of optical and IR diagnostics, and more indirectly of X-ray AGN selection, it does not deal with radio observations. However, being a characteristic spectral band for AGN emission and properties, it is worth mentioning it since radio observations contribute to drawing a complete picture of the global AGN population, supporting the need for multi-wavelength surveys to fully understand AGN phenomenology and physics.

X-ray. AGN have been known to be strong X-ray emitters for several decades (Elvis et al., 1978), and X-ray surveys have soon become a successful method to search for AGN galaxies. At X-ray 2–10 keV luminosities of $L_{2-10\ \mathrm{keV}} \gtrsim 10^{42}$ erg s^{-1}, AGN are dominant over all other possible contributions to the observed X-ray emission (e.g. hot gas, X-ray binaries and SF); however, at all luminosities, different spectral slopes and X-ray–to–optical flux ratios usually allow to distinguish among X-ray sources of different nature (e.g. Steffen et al. 2006, Lehmer et al. 2010). Compared to optical and UV energies, X-ray photons are

---

[3] Full transitions were observed, for instance, in Mrk 1018 (Cohen et al., 1986, McElroy et al., 2016), NGC 1566 (Alloin et al., 1986, Oknyansky et al., 2019), NGC 4151 (Penston and Perez, 1984, Shapovalova et al., 2010), Mrk 590 (Denney et al., 2014), and NGC 3516 (Ilić et al., 2020).

much less affected by obscuration effects and, therefore, they can unveil AGN even in dusty obscured environments, except for the most heavily obscured sources (with column densities $N_H \gtrsim 10^{24}$ cm^{-2}; e.g. Daddi et al. 2007, Kocevski et al. 2015).

Optical/UV. In the optical/UV, AGN and non-active galaxies appear remarkably different. Historically, colour diagnostics were the first widely used method to identify AGN in photometric surveys (Schmidt and Green, 1983, Boyle et al., 1990), but work well only with the more luminous AGN, where the stellar contamination is negligible. On other hand, optical spectroscopy has allowed to identify thousands of AGN at low redshifts (e.g. the Sloan Digital Sky Survey; SDSS; York et al. 2000), via optical emission lines: either through the detection of extremely luminous or broad (i.e. FWHM$\gtrsim$2000 km s^{-1}) profiles, which are not typical of non-active, star-forming galaxies; or using emission-line ratios. Whereas type-1 AGN are the easiest systems to identify thanks to the well visible broad-line emission typical of AGN BLR, narrow emission-line flux ratios and diagnostic diagrams represent a widely used method to identify luminous type-2 AGN using optical spectra (Kewley et al., 2001, 2006, Kauffmann et al., 2003). Among these, a commonly used optical diagnostic is the Baldwin, Phillips & Terlevich (BPT) diagram (Baldwin et al., 1981), which combines [O III]/Hβ and [N II]/Hα narrow-line[4] ratios to distinguish between AGN and SF as the main ionisation source. Alternative versions of BPT diagrams have been also developed, employing either [S II]/Hα or [O I]/Hα (Veilleux and Osterbrock, 1987) instead of [N II]/Hα, to further separate between these two ionisation mechanisms, and also to identify possible low-ionisation nuclear emission-fine regions (LINERs), whose ionisation is mainly due to shocks. More recently, UV diagnostics have been developed as a valuable alternative to distinguish between AGN and SF activity at high redshift (e.g. Feltre et al. 2016, Nakajima et al. 2018, Nakajima and Maiolino 2022, Mingozzi et al. 2023). Also, high-ionisation UV/optical emission lines (e.g. C IVλ1549, [Ne V]$\lambda\lambda$3346,3426, [Fe X]λ6374, or [Fe XI]λ7892) require a harder ionising continuum, which can hardly be produced by stars and, therefore, is likely to imply AGN activity (e.g. Mignoli et al. 2013, 2019, Feltre et al. 2016).

Although BPT diagrams have been leading the optical search for AGN at low redshift, there are important limitations to this method, related to its efficiency in unveiling AGN residing in star-forming galaxies. This becomes fundamental at high redshift, where galaxies form stars at a higher rate and more complex mechanisms may take place. As a consequence, developing novel emission-line diagnostics alternative to BPTs is necessary to make a complete census of AGN, with important implications on the role of AGN in

---

[4] The broad-line emission due to AGN BLR is excluded from these line ratios.

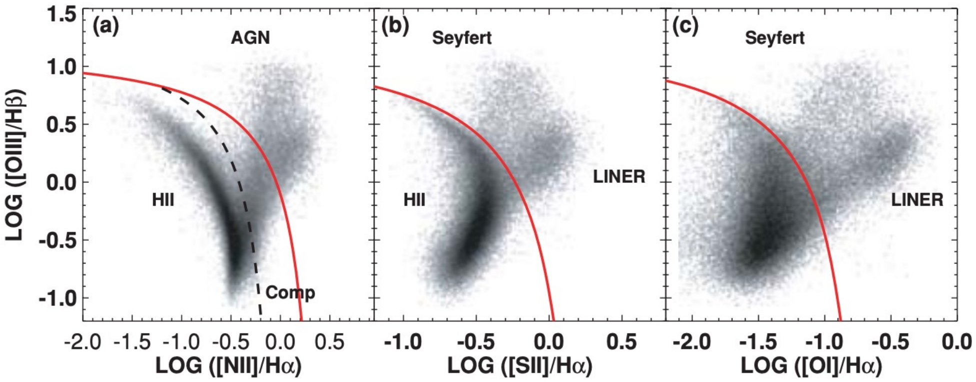

Fig. 1.4 *Three main versions of BPT diagrams obtained for SDSS galaxies. From left,* [O III]/Hβ *ratio is shown as a function of* [N II]/Hα, [S II]/Hα *and* [O I]/Hα*, respectively. Overall these diagrams distinguish among different ionisation mechanisms, namely: AGN (or Seyfert), SF (i.e.* H II *regions where stars form), shocks (i.e. low-ionisation nuclear emission-line region; LINER), or a 'composite' ionisation due to a possible mix of AGN and SF. Figure from Kewley et al. (2006).*

driving galaxy evolution (see Sect. 1.2). This topic will be the subject of Chapter 2, and optical diagnostics are used also in Chapters 3 and 4.

IR. AGN can also be identified in the IR band, thanks to bright IR emission from warm dust heated by AGN radiation field (described in Sect 1.1). There are several IR methods to identify AGN: mid-IR and near-IR colour diagnostics, extensively applied to IR photometric surveys (e.g. Stern et al. 2005, 2012, Donley et al. 2008, 2012); mid-IR spectroscopy revealing characteristic continuum emission as well as high-excitation emission lines (e.g. Weedman et al. 2005, Goulding and Alexander 2009); IR emission-line ratio diagnostics (e.g. Ramos Almeida et al. 2009, Riffel et al. 2013, 2020, Colina et al. 2015, Fernández-Ontiveros et al. 2016, 2017, Feltre et al. 2023). In particular, near-IR emission-line diagnostics allow to distinguish among different gas excitation mechanisms, and to identify the presence of shocks (Mouri, 1994, Larkin et al., 1998, Riffel et al., 2013, Colina et al., 2015). Near-IR diagnostics will be used in Chapter 4 to study the excitation properties of warm molecular and ionised gas in NGC 6240, a local gas-rich galaxy merger, hosting a double AGN. The main advantage of using mid-IR emission is that it should be visible for all viewing angles according to AGN unified models (Sect. 1.1.2.1; Fig. 1.1), therefore it can be used to trace more dust-obscured AGN, which are missed by even the deepest X-ray surveys. IR emission might have significant contributions from stars, especially in galaxies undergoing intense SF. In such cases, the most suitable technique to disentangle SF and AGN IR emission is a multi-component fitting to the spectral energy distribution

(SED) using photometric data from distinct bands at mid-IR and far-IR wavelengths (e.g. Mullaney et al. 2011).

Radio. Radio emission from AGN can be due to several physical mechanisms (Sect. 1.1.2.1). Indeed for decades, radio surveys have been used to build up AGN samples (e.g. Laing et al. 1983, Becker et al. 1995, Condon et al. 1998, Bock et al. 1999), resulting particularly useful in the search for low-accretion, radio-loud AGN, typically exhibiting extended radio jets, which can be hardly selected with other methods (e.g. Heckman and Best 2014). Instead, radio emission in the radio-quiet AGN population can have a more ambiguous origin and be easily due (at least in part) to SF processes. However, by comparing radio observations with results from SED fitting, some galaxies are found to show a 'radio excess' with respect to radio emission expected from SF (e.g. Del Moro et al. 2013), likely pointing to the presence of an AGN.

1.2 The role of AGN in galaxy evolution

As mentioned at the beginning of this chapter, AGN are widely accepted to play a key role in shaping galaxy evolution, as a consequence of the enormous amount of energy released by an accreting supermassive BH. The process by which this occurs is known as AGN feedback and it can be demonstrated by means of simple energetic considerations (see e.g. Fabian 2012). Given the velocity dispersion $\sigma_{\rm sph}$ and the mass $M_{\rm sph}$ of the galaxy spheroid, its binding energy can be estimated via the virial theorem as $E_{\rm sph} \approx M_{\rm sph}\sigma^2_{\rm sph}$. The energy produced by an active BH of mass $M_{\rm BH}$ can be instead approximated to $\sim 0.1 M_{\rm BH}c^2$, assuming a typical radiative efficiency of 10% (Soltan, 1982). From the observed correlation between $M_{\rm BH}$ and $M_{\rm sph}$ (i.e. $M_{\rm BH} \sim 10^{-3} M_{\rm sph}$, ; see Sect. 1.2.1), it follows $E_{\rm BH}/E_{\rm sph} \sim 10^{-4}(c/\sigma_{\rm sph})^2$. Then, considering typical values of $\sigma_{sph} < 400$ km s^{-1}, we get $E_{\rm BH}/E_{\rm sph} \gtrsim 50$, which means that the BH energy output exceeds the binding energy of the galaxy spheroid of a large factor. Therefore, if even a small fraction of $E_{\rm BH}$ is transferred to the surrounding medium, this will profoundly affect the host galaxy.

The major role played by AGN feedback in galaxy evolution is supported by observational evidence (described in Sect. 1.2.1), which has led to include it in both theoretical and numerical studies (e.g. Haehnelt and Kauffmann 2000, Di Matteo et al. 2005, Springel et al. 2005, Bower et al. 2006, Croton et al. 2006, Hopkins et al. 2006, Ciotti et al. 2010), as a crucial ingredient to reconcile model predictions with observations.

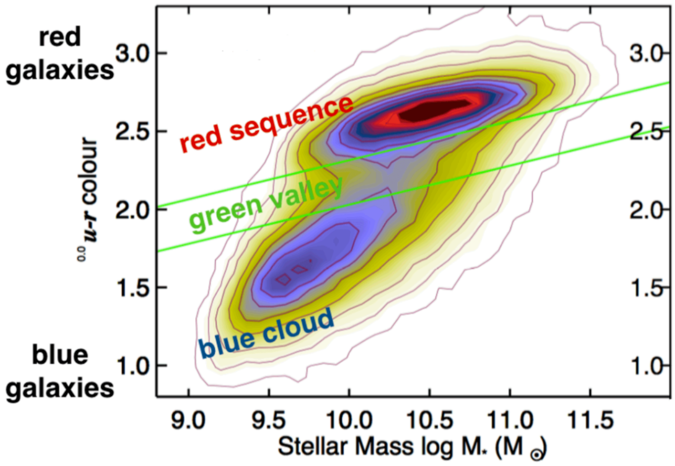

Fig. 1.5 *Colour-mass diagram from Schawinski et al. (2014), for a local sample of about 47700 galaxies. Galaxies lie in two main regions of the plane: the 'blue cloud', a diffuse blue region occupied by star-forming galaxies, and the 'red sequence', a narrow band region where are found quiescent galaxies. For at least more massive galaxies, AGN feedback is thought to be the main driver of galaxies' evolution from star-forming to quiescent systems, passing through the intermediate 'green valley' region.*

1.2.1 The need for AGN feedback

Optical surveys (Strateva et al., 2001, Baldry et al., 2004, 2006) have revealed a bimodal distribution of galaxies in colour-mass diagrams (e.g. Schawinski et al. 2014; see Fig. 1.5), pointing that galaxies follow an evolutionary track across the plane, as SF is progressively quenched. They are thought to evolve from the so-called 'blue cloud', occupied by star-forming systems, passing through the intermediate 'green valley' region, to finally reach the 'red sequence', where galaxies no longer form stars. As shown in this section, observational evidence suggests AGN feedback as main driver of such an observed evolution for (at least) more massive galaxies. In fact, it is included in theoretical, semi-analytic and numerical works (e.g. Haehnelt and Kauffmann 2000, Kauffmann and Haehnelt 2000, Granato et al. 2004, Di Matteo et al. 2005, Springel et al. 2005, Bower et al. 2006, Croton et al. 2006, Hopkins et al. 2006, 2018, Ciotti et al. 2010, Scannapieco et al. 2012, Vogelsberger et al. 2014, Schaye et al. 2015, Sijacki et al. 2015) as a key mechanism to explain several observed properties of galaxies, which models otherwise can hardly account for.

A first observational evidence supporting the need for AGN feedback is the discrepancy between the observed stellar mass function of galaxies (i.e. the number density of galaxies with a certain stellar mass) and that predicted by ΛCDM models of galaxy evolution (e.g. see Kormendy and Ho 2013 for a review). As shown in Fig. 1.6, at both low and high masses models predict a larger number of galaxies than those actually observed. The accordance

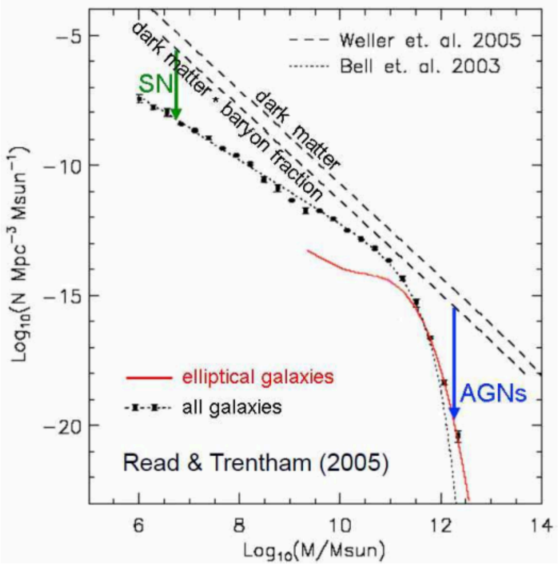

Fig. 1.6 *Galaxy (baryonic) mass function from Read and Trentham (2005), inferred for all galaxies (black points) and elliptical galaxies only (red line), fitted with a Schechter (1976) function (Bell et al. 2003; dotted line) and compared with: the mass spectrum of cold dark matter (DM) resulting from numerical simulations (Weller et al., 2005); and with the same DM mass function but multiplied by the universal baryon fraction of 0.163 (Hinshaw et al., 2013). Green and blue arrows indicate stellar (SN) and AGN feedback, the missing crucial ingredients to include in theoretical and numerical studies to reproduce the observed galaxy mass function at low and high masses, respectively. Figure from Kormendy and Ho (2013).*

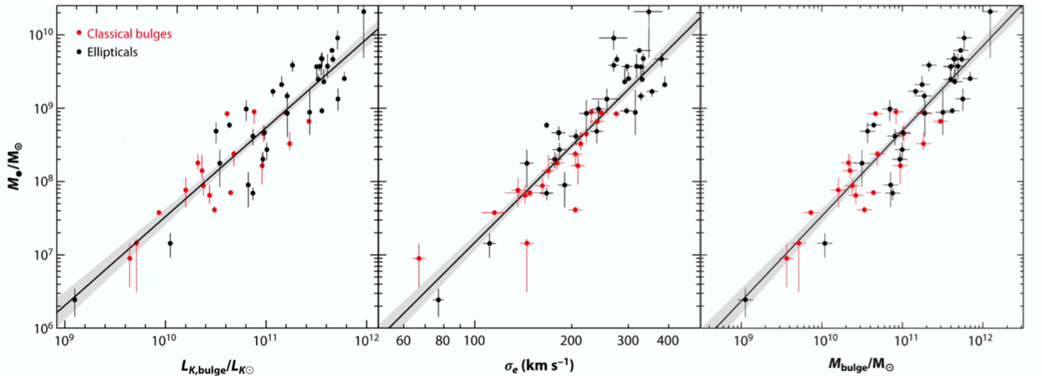

Fig. 1.7 *Observed scaling relations between BH masses and host galaxy spheroid properties, namely: K-band luminosity (left), stellar velocity dispersion (middle), and mass (right). Red and black points indicate measurements for classical spheroids and elliptical galaxies, respectively, whereas the black line is the best-fit to the data, with 1*σ *uncertainties (grey shading). Figure from Kormendy and Ho (2013).*

of theoretical predictions with observations at low masses is recovered by including in models stellar feedback due to supernovae (Dekel and Silk, 1986), acting through winds able to heat and sweep the gas out of the galaxy, thus preventing gas from collapsing to form new stars. Compared to AGN feedback, stellar feedback involves smaller energies and masses. In fact, it is believed to be effective in low-mass galaxies and becomes inefficient at higher masses up to $M \sim 3 \times 10^{10}$ M$_\odot$, where we observe the minimum discrepancy between the observed mass function and the ΛCDM prediction. Above this critical mass, the observed galaxy mass function steeply decreases and departs again from the predicted trend. At the high-mass end (i.e. $M > 10^{11}\ _\odot$) - the mass regime investigated within this thesis - extremely energetic processes are expected to take place and efficiently quench SF, thus explaining the lack of observed high-mass galaxies. Suck kind of powerful mechanism has been widely identified in AGN feedback, acting in the form of outflows and jets, which suppress SF in the host galaxy via either ejecting or heating the gas available to form stars.

Another strong piece of evidence of the key role played by AGN feedback in galaxy evolution comes from the discovery of scaling relations between BH masses and properties of their host galaxy spheroids[5]. Over the years, such relations have been deeply investigated and constrained by employing larger and larger samples of galaxies and better-quality observations. In particular, BH masses are observed to correlate with the following prop-

---

[5] Here, the term ‘spheroid’ indicates both the spheroidal component in disk galaxies and the entire galaxy itself in case of elliptical galaxies.

erties of the host spheroid: the luminosity ($M_{\rm BH} \sim L_{\rm sph}^{1.1}$)[6], the mass ($M_{\rm BH} \sim 10^{-3} M_{\rm sph}$)[7], and the stellar velocity dispersion ($M_{\rm BH} \sim \sigma_{\rm sph}^{4-5}$)[8]. Nowadays these BH-galaxy correlations are firmly established over several orders of magnitude in mass, luminosity and velocity dispersion. They also represent strong observational proof that supermassive BHs and their host galaxies do not evolve separately, but they mutually influence each other and co-evolve hand in hand. The mechanism responsible for the observed BH-galaxy co-evolution cannot be due to BH gravitational effects, since its sphere of influence is too small compared to the size of the host spheroid (i.e. by about a factor $\sim 5 \times 10^{-3}$). On the other hand, AGN feedback processes are the best candidates to establish a strict link between nuclear activity and host galaxy properties. In particular, these scaling relations naturally arise from simple models of AGN feedback (e.g. King and Pounds 2015), as the resulting effect of AGN-driven outflows (see Sect. 1.2.2.1).

Also, the observed cosmic histories of BH accretion and SF support the parallel evolution of BHs with their host galaxies. As shown in Fig. 1.8 (from Aird et al. 2015), BH growth and SF histories exhibit very similar trends over cosmic time[9], both reaching the peak of their activity around $z \sim 2$ (e.g. Madau et al. 1996, Lilly et al. 1999, Madau and Dickinson 2014). This cosmic epoch is usually known as 'Cosmic Noon', and more generally is used to indicate the range of redshift $z \sim 1-3$, where the bulk of both SF and BH accretion occurred (e.g. Ueda et al. 2003, Marconi et al. 2004, Shankar et al. 2009, Aird et al. 2010, 2015). All this strongly points to AGN feedback as the key self-regulating mechanism responsible for the coupling of two processes, hence for their observed symbiotic evolution. Being the epoch exhibiting simultaneously the most intense SF and BH growth, the Cosmic Noon is considered the *golden* epoch of AGN feedback, where more effective and powerful mechanisms are expected to take place.

---

[6] E.g. Kormendy 1993, Magorrian et al. 1998, Ho 1999, Merritt and Ferrarese 2001, Laor 2001, Kormendy and Gebhardt 2001, McLure and Dunlop 2002, Marconi and Hunt 2003, Ferrarese and Ford 2005, Graham 2007, Gültekin et al. 2009, Sani et al. 2011, Kormendy and Bender 2011, Vika et al. 2012, Graham and Scott 2013, McConnell and Ma 2013.

[7] E.g. Merritt and Ferrarese 2001, Kormendy and Gebhardt 2001, McLure and Dunlop 2002, Marconi and Hunt 2003, Häring and Rix 2004, Kormendy and Bender 2009.

[8] E.g. Ferrarese and Merritt 2000, Gebhardt et al. 2000, Merritt and Ferrarese 2001, Kormendy and Gebhardt 2001, Tremaine et al. 2002, Marconi and Hunt 2003, Ferrarese and Ford 2005, Graham 2007, 2008, Gültekin et al. 2009, Greene et al. 2010, Graham et al. 2011, Sani et al. 2011, Kormendy and Bender 2011, Graham and Scott 2013, McConnell and Ma 2013, Kormendy and Ho 2013.

[9] In Fig. 1.8, BH accretion history has been multiplied by a factor ~1500 to match the SF history, which is consistent with the $\sim 10^{-3}$ factor of the $M_{\rm BH} - M_{\rm sph}$ scaling relation.

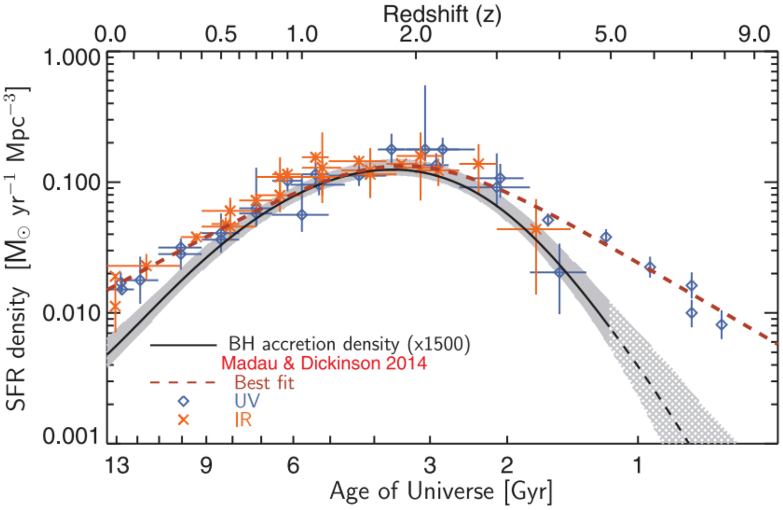

Fig. 1.8 *Total star formation rate (SFR) and BH accretion densities over cosmic time. The dashed red line shows the best fit to the SF history from Madau and Dickinson (2014), considering measurements based on rest-frame UV (blue diamonds) and IR (orange crosses) observations. The black line represents the BH accretion history estimated by Aird et al. (2015), re-scaled by a factor of 1500 and shown with a 99% confidence interval (grey shading). Both histories reach the peak of their activity at* $z \sim 2$, *that is the so-called 'Cosmic Noon' epoch. Figure from Aird et al. (2015).*

1.2.2 The radiative mode: AGN-driven outflows

Schematically, AGN feedback is split in two possible main modes (Alexander and Hickox 2012, Heckman and Best 2014; Fig. 1.9), depending on the form it takes. These are:

- **Radiative mode** (also known as quasar or superwind mode), where the AGN radiative output drives wide-angle, sub-relativistic outflows, potentially able to eject the gas out of the galaxy.
- **Kinetic mode** (often referred also as radio or maintenance mode), acting as relativistic, highly-collimated jets, launched from the inner accretion flow and typically detected in the radio band, which keep the gas in the galactic halo hot, thus preventing re-accretion on the galaxy and formation of new stars.

These two main forms of AGN feedback can be considered as typical of two distinct life stages of AGN, though they can also co-exist in some galaxies (e.g. Venturi et al. 2021). The radiative mode is expected to take place during bright, short-lived phases, featured by high accretion rates close to (or even above) the Eddington limit. On the other hand, kinetic feedback usually acts on longer timescales, in a later stage when the AGN is accreting at low rates.

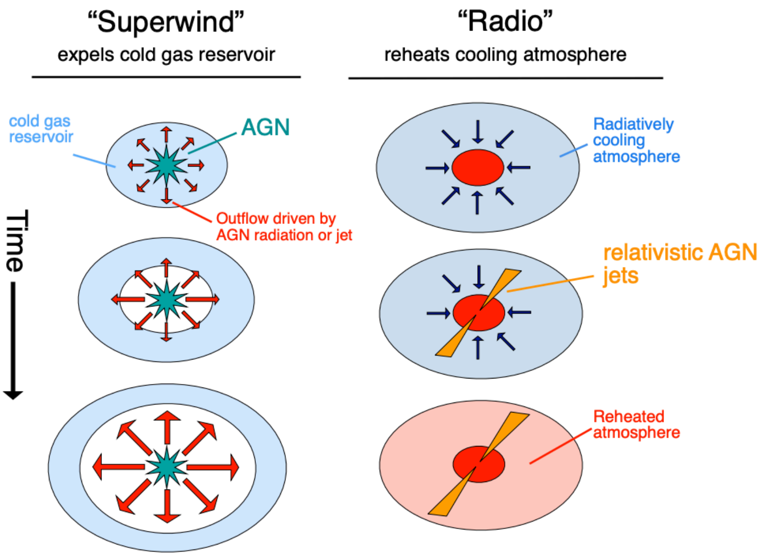

Fig. 1.9 *Schematic diagrams illustrating the two main modes of AGN feedback: radiative (or superwind) mode, acting as wide-angle outflows capable of expelling gas out of the galaxy; and kinetic (or radio) feedback, which takes the form of collimated, relativistic jets, typically observed in low-accretion rate AGN. Figure from Alexander and Hickox (2012).*

This thesis focuses on the study of AGN-driven outflows typically associated with radiative-mode feedback (Fig. 1.9), aiming at investigating their properties as well as their potential impact on the host. Proposed for the first time by Silk and Rees (1998) as main feedback channel of highly luminous AGN, radiative outflows are now routinely observed from low (e.g. Feruglio et al. 2010, 2013, Rupke and Veilleux 2011, Cicone et al. 2012, 2014, Müller-Sánchez et al. 2018, Venturi et al. 2018, Marasco et al. 2020, Vittoria Zanchettin et al. 2023) to high redshift (e.g. Maiolino et al. 2012, Cano-Díaz et al. 2012, Förster Schreiber et al. 2014, Carniani et al. 2015, Cresci et al. 2015a, 2023, Perna et al. 2015a, Brusa et al. 2016, 2018). However, whereas AGN-driven outflows are investigated in detail in low-redshift AGN, higher-redshift studies are usually biased to more luminous sources, with most of the search focusing on around the Cosmic Noon (i.e. $z \sim 1-3$; see Sect. 1.2.1 and Fig. 1.8), where AGN feedback and outflows are expected to be more powerful and effective (see Sect. 1.2.1).

1.2.2.1 Acceleration mechanisms of AGN winds

To understand how significant the impact of large-scale AGN outflows may be on their host galaxy, it is important to investigate first how they are accelerated and propagated across the galaxy up to kpc scales, where feedback is expected to take place. Models predict two main mechanisms of wind propagation, namely: 1) the so-called ‘wind’ feedback, which may act under two distinct regimes (i.e. momentum-driven or energy-driven outflows); and 2) radiation pressure-driven outflows, directly accelerated by AGN radiation pressure on dust grains. In the following, we provide details on these wind acceleration modes.

Momentum-driven and energy-driven outflows. According to wind feedback models (e.g. King 2010, King and Pounds 2015), mildly relativistic winds ($\sim 0.01 - 0.1c$), accelerated on nuclear scales by AGN radiation pressure, are the powering engine of massive outflows observed on galaxy scales. These inner winds are indeed expected to impact the galactic interstellar medium (ISM) and generate a shock, which consequently accelerates the swept-up gas of the host galaxy. Then, depending on the cooling efficiency in the shocked gas shell via mostly Inverse Compton, large-scale outflows may propagate according to two main modes. If radiative cooling in the shocked gas shell is effective[10], most of the pre-shock kinetic energy gets lost and, therefore, the galactic ISM receives only the inner wind momentum via its ram pressure. Feedback effects associated with this ‘momentum-driven’ regime are expected to have a low impact on the host (King and Pounds, 2015), since the masses and energies typically involved are quite small. On the other hand, if cooling is negligible, the accelerated ISM receives all the kinetic energy of the inner wind and expands adiabatically in an energy-driven scenario. In this picture, massive outflows are expected to be powered on galaxy scales, able to effectively sweep up a significant amount of gas out of the host galaxy.

According to a widely accepted picture, the observed BH-galaxy scaling relations are the result of AGN feedback acting through two subsequent phases (e.g. Fabian 2012, Zubovas and King 2012, King and Pounds 2015): a first momentum-driven phase, poorly affecting the surrounding gas, during which the BH keeps growing, while the outflow is confined within ~1 kpc from the central BH; then, a second energy-driven phase after the BH reached the $M_{\rm BH} - \sigma_{\rm sph}$ relation, during which the outflow can propagate beyond 1-kpc scales. However, as it will be shown in this thesis, distinguishing between these two mechanisms clearly may be a hard task, with observations suggesting that other complex processes might be at play, as well as a possible poor coupling of the energy released by the BH with the galactic ISM.

Radiation pressure-driven outflows. Another viable channel to accelerate large-scale outflows is direct AGN radiation pressure on ISM dust grains (e.g. Fabian 1999, Ishibashi and Fabian 2012, 2015, Thompson et al. 2015, Ishibashi and Fabian 2018, Ishibashi

---

[10] To be effective, radiative cooling must occur on a timescale shorter the flow time.

et al. 2021). As mentioned in Sect. 1.1.2.1, a considerable fraction of AGN emission is in the form of UV radiation, which may be efficiently absorbed by dust, if present. As a consequence, dust grains get partially ionised and are pushed away, dragging the gas with them. Compared to Thomson scattering, dust absorption has a cross-section which is about 1000 times larger than σ_T (Fabian et al., 2008), thus resulting in a far smaller critical luminosity $L'_{\rm Edd}$ (i.e. $L'_{\rm Edd} \sim 10^{-3} L_{\rm Edd}$; see Eq. 1.2). This implies that an AGN emitting at $L_{\rm Edd}$ (i.e. Eddington limit for ionised gas) corresponds to an object ~1000 times more massive, with an effective Eddington limit $L'_{\rm Edd}$ for dusty gas (e.g. Fabian 2012). This 1000 factor of difference is equal to the observed ratio between BH and galaxy bulge masses (i.e. $M_{\rm BH} \sim 10^{-3} M_{\rm sph}$; see Sect. 1.2.1), suggesting this mechanism might directly affect the galaxy spheroid and determine the observed $M_{\rm BH} - M_{\rm sph}$ relation. According to models, direct radiation pressure on dust can drive outflows on kpc scales (e.g. Ishibashi and Fabian 2012, 2015). Whereas for low IR optical depths (i.e. in single scattering limit) radiation pressure on dust can naturally explain outflow energetics compatible with a momentum-driven regime (i.e. in single scattering limit), it usually requires stronger assumptions (e.g. IR radiation trapping, AGN luminosity evolution; Ishibashi and Fabian 2018, Ishibashi et al. 2021) to account for more energetic outflows, such as those consistent with energy-driven predictions. Dust might play a major role in driving large-scale outflows in obscured AGN (e.g. Perrotta et al. 2019).

1.2.2.2 Negative or positive feedback?

As already discussed in previous sections, AGN-driven outflows are mostly expected to have a ‘negative’ impact on galactic SF, by reducing or even suppressing the formation of new stars. These may happen by: either ejecting the gas out of the host galaxy, thus reducing the host gas reservoir available for SF; or injecting energy into the galactic ISM (similarly to jets), which prevents gas from cooling and forming new stars. To date, one of the strongest observational evidence of negative feedback in action comes from a few AGN at z~2 (Cano-Díaz et al., 2012, Carniani et al., 2015, 2016, Cresci et al., 2015a). In these sources indeed, high-velocity [O III] emission associated with ionised outflows has been found to be spatially anti-correlated with narrow Hα line emission, tracing SF within the host galaxy. However, these outflows seem to affect the gas reservoir only along their path, with no significant impact on the overall galaxy SF, which remains globally high, with star formation rates (SFRs) of about ~100 $M_\odot yr^{-1}$. Moreover, the claimed outflow-SF anti-correlation has been recently questioned by Scholtz et al. (2020), as a possible result of dust effects shielding faint narrow Hα emission in more extincted regions of the galaxy. One of the candidate quasars to exhibit negative feedback in action (i.e. XID2028; Cresci et al.

2015a) has been recently observed with the near-IR IFU NIRSpec on *JWST*. Unfortunately, not even such new high-quality data have definitely confirmed (or disproved) the outflow-SF anti-correlation (Cresci et al., 2023, Veilleux et al., 2023), showing how still challenging this research topic is. Therefore, the search for conclusive observational proof of ongoing negative feedback is still open.

In addition to their traditional negative "flavour", AGN-driven outflows may have a positive effect on SF. Recent models indeed predict that the over-compression of molecular gas in the ISM due to outflow outward thrust may trigger SF (e.g. Silk and Norman 2009, Nayakshin and Zubovas 2012, Silk 2013, Zubovas et al. 2013a, Zubovas and Bourne 2017, Cresci and Maiolino 2018). Some observational evidence of positive feedback by AGN outflows was found at both low (Cresci et al., 2015b, Shin et al., 2019, Perna et al., 2020) and high redshift (Cresci et al., 2015a, Carniani et al., 2016). Interestingly, hints at possible ongoing positive feedback were found also in objects already showing signatures of negative feedback (e.g. Cresci et al. 2015a, Perna et al. 2020). This overall points to the picture where a single expanding outflow may have simultaneously both negative and positive effects: whereas SF is quenched in the outflow region, it is boosted in the over-compressed ISM region located at the outflow edges.

Recent models also predict that SF may be activated within galactic outflows themselves, as a consequence of compression, cooling and fragmentation of the outflowing gas (e.g. Ishibashi and Fabian 2012, 2014, Ishibashi et al. 2013, Zubovas et al. 2013b, Zubovas and King 2014). Observations point to outflows as a potentially ideal environment to host SF, being composed of a significant component of molecular outflowing gas (e.g. Cicone et al. 2014, Fiore et al. 2017, Fluetsch et al. 2019; see Sect. 1.2.3), which may be as dense ($n \sim 10^6$ cm^{-3}) and clumpy as typical star-forming molecular clouds (e.g. Aalto et al. 2015, Pereira-Santaella et al. 2016). Observational signatures of SF taking place within AGN-driven outflows were found in local AGN by Maiolino et al. (2017) and Gallagher et al. (2019), both studies employing spatially-resolved data.

1.2.3 Multi-phase and multi-scale AGN outflows

As described in Sect. 1.2.2, AGN feedback models predict the launch of fast radiative outflows from the AGN nuclear (~subpc-pc) region, which can extend up to galactic (~1–10 kpc) scales via different acceleration mechanisms (Sect. 1.2.2.1). Whereas radio jets have been observed for years up to high redshift (i.e. $z \sim 2-7$; e.g. McGreer et al. 2006, Stern et al. 2007, Nesvadba et al. 2008, 2011, Fu and Stockton 2009, Willott et al. 2010, Belladitta et al. 2020, Bañados et al. 2021), radiative outflows have been more elusive to detect over the years, since they require an accurate study of local gas kinematics. Only in

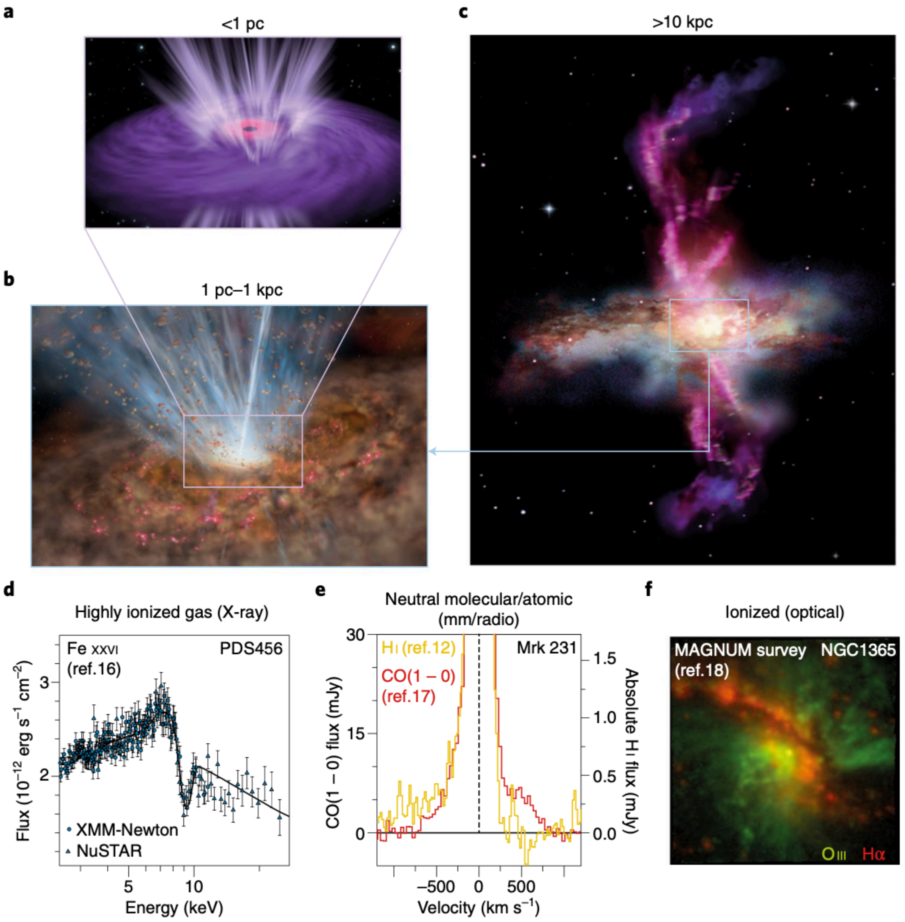

Fig. 1.10 *Artistic view and observational evidence of multi-phase AGN outflows, accelerated by the central engine (<1 pc;* ***a****), and then propagating through the surrounding ISM (1–1000 pc;* ***b****), out to galaxy edge (>10 kpc;* ***c****). Lower panels show AGN outflows detected in different gas phases in three well studied nearby AGN: the highly ionised, X-ray ultrafast outflow in PDS 456 (Nardini et al. 2015;* ***d****); the neutral outflow in both atomic and molecular phases, observed in Mrk 231 (Cicone et al. 2012, Morganti et al. 2016;* ***e****); the ionised outflow in NGC 1356, extending over kpc-scales (Venturi et al. 2018;* ***f****). Image from Cicone et al. (2018).*

more recent years spatially resolved spectroscopic studies, enabled by advanced optical, IR and mm facilities, have provided conclusive evidence of their existence. AGN-driven outflows are now routinely observed both locally (e.g. Feruglio et al. 2010, Rupke and Veilleux 2011, Cicone et al. 2014, Crenshaw et al. 2015, Nardini et al. 2015, Venturi et al. 2018, Revalski et al. 2021, Zanchettin et al. 2021; see also references in Sect. 1.2.2) and in more distant AGN (e.g. Harrison et al. 2012, Cano-Díaz et al. 2012, Carniani et al. 2015, Brusa et al. 2018, Chartas et al. 2021, Cresci et al. 2023; see also references in Sect. 1.2.2). Thanks to the Atacama Large Millimeter/submillimeter Array (ALMA) and the *James Webb Space Telescope (JWST)*, the hunt for AGN outflows has now been pushed to very high redshift, with detections at $z > 3$ (e.g. Carniani et al. 2023, Marshall et al. 2023, Perna et al. 2023, Übler et al. 2023).

However, in spite of their ubiquitous presence, we still miss crucial observational constraints on their real impact on the host galaxy, as well as on how the energy released by an accreting BH on nuclear scales couples to the galactic ISM, and consequently drives powerful galaxy-scale outflows. Understanding how efficient such coupling is allows us to assess the role of AGN outflows in galaxies' evolution, and requires an accurate comparison of observational results with theoretical predictions. Yet, such a comparison might be not particularly straightforward (Harrison et al., 2018), since observations usually trace a specific gas phase, depending on the adopted waveband; whereas models and simulations usually consider the whole outflowing material (i.e. composed of multiple gas phases).

Therefore, multi-wavelength observations are required to map all gas phases of AGN-driven outflows (e.g. Fiore et al. 2017, Cicone et al. 2018), each typical of certain spatial scales, hence representative of a particular stage in outflow propagation across the host galaxy (Fig. 1.10). In the following, we outline the main observational properties of AGN outflows detected in distinct gas phases, from subpc to kpc scales.

1.2.3.1 Highly ionised outflows

Observational signature of disk accretion winds, as predicted by models (see Sect. 1.2.2.1), have been found in AGN X-ray spectra, showing blueshifted absorption lines (Fig. 1.10, panel **d**) produced by outflowing gas intervening along the line of sight. The most extreme winds are the so-called 'ultrafast outflows' (UFOs; e.g. Cappi et al. 2009, Reeves et al. 2009, Nardini et al. 2015, Chartas et al. 2016, 2021), which feature mildly relativistic velocities ($\sim 0.1c$), large column densities ($N_{\rm H} \sim 10^{22} - 10^{24}$ cm^{-2}) and high ionisation parameters ($\log\xi \sim 3 - 6$ erg s^{-1} cm), being indeed typically traced by highly ionised metals (e.g. Fe, C, N, O). Originating on subpc scales close to the BH (e.g. Crenshaw et al. 2003, Tombesi et al. 2012), UFOs are observed in about 40% of nearby AGN (Tombesi et al., 2010, 2011, Gofford et al., 2013), with typical mass outflow rates of ~0.01-1 $M_\odot$ yr^{-1} and kinetic powers of $\log\dot{E}_K \sim 42-45$ erg s^{-1} (Tombesi et al., 2012). Such a kinetic power is higher than the minimum required by simulations for AGN winds to be effective in quenching SF, that is about 0.5-5% of AGN luminosity (e.g. Di Matteo et al. 2005, Hopkins and Elvis 2010).

UFOs are optimal candidates as primary driver of galaxy-scale ($\sim 1-10$ kpc) outflows, propagating according to momentum-driven or energy-driven regimes (see Sect. 1.2.2.1). Among the AGN currently known to host both UFOs and large-scale outflows, some of them resulted to be consistent with a momentum-driven propagation (e.g. Marasco et al. 2020, Zanchettin et al. 2021), other with an energy-driven regime (e.g. Tombesi et al. 2015, Feruglio et al. 2015). To date, there are however only few AGN with detection of both UFOs and galaxy-scale outflows, with the latter usually traced in only one (i.e. either molecular or ionised) and large uncertainties which prevent from an accurate distinction between the two proposed regimes. Moreover, UFO detection is mostly limited to the low-redshift Universe (e.g. Nardini et al. 2015, Matzeu et al. 2023, Mehdipour et al. 2023), due to the faintness of their X-ray signatures. As a consequence, a clear observational proof of the connection between UFOs and large-scale feedback is still lacking and the topic under debate.

In addition to X-ray UFOs, a different kind of disk accretion winds are detected via broad, blueshifted UV absorption features of highly ionised metals (e.g. C IV, N V), in the so-called 'broad absorption line' (BAL) quasars (typical FWHM>2000 km s^{-1}; e.g. Weymann et al. 1991, Ganguly et al. 2007, Chartas et al. 2009a). These absorption features indicate wind velocities up to ~30,000 km s^{-1}. UV winds are detected also in 'narrow line absorption' (NAL, FWHM<500 km s^{-1}; e.g. Chartas et al. 2009a), indicating velocities comparable with those measured in BAL quasars.

In literature, there are very few examples of NAL quasars with X-ray UFOs detected (e.g. HS 1700+6416, Lanzuisi et al. 2012; HS 0810+2554, Chartas et al. 2014, 2016). This might be consequence of the fact that UV and X-ray absorption lines originate from different outflow regions, with X-ray absorption produced closer to the continuum source than UV counterparts, which indeed exhibit a lower ionisation. Figure 1.11 (from Chartas et al. 2014) displays a schematic representation of a plausible geometry of the inner AGN region, showing how X-ray and UV absorption features can be both detected or not, depending on the inclination to the line of sight. For small inclinations angles of the obscuring, outflowing gas to the accretion disk, X-ray emission (long-dashed lines) from the hot corona does not intercept the shielding material (grey shaded regions), as opposed to UV disk emission (short-dashed lines), which hence produces UV NAL absorption.

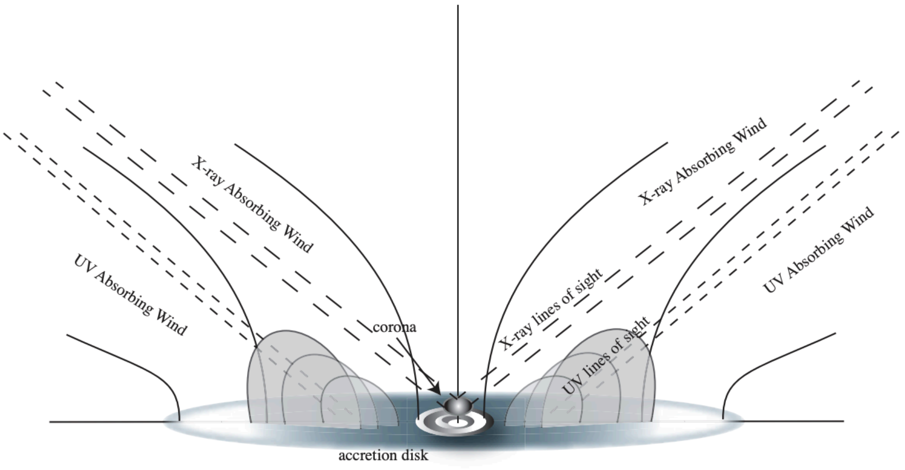

Fig. 1.11 *Schematic structure of a plausible geometry for the accretion disk, illustrating how nuclear winds can produce X-ray and/or UV absorptions. For small inclinations to the accretion disk, the shielding, outflowing gas (grey shaded regions) intercepts only UV emission from the accretion disk (short-dashed lines), but not X-ray emission from the hot corona (long-dashed lines). Image from Chartas et al. (2014).*

1.2.3.2 Ionised outflows

Galaxy-scale ionised outflows in AGN are usually detected through prominent asymmetric wings in optical emission-line profiles. Detected wings are found to be preferentially blueshifted, indicating approaching material along the line of sight. Such an observed feature is commonly interpreted as a combination of system geometry and dust obscuration. Considering a bi-conical outflow, the approaching side of the outflow lies above the galaxy disk, as opposed to the receding (redshifted) component, which is found preferentially below the disk and, therefore, is likely to be more affected by dust extinction. The most commonly adopted tracer of AGN ionised outflows is [O III]λ5007 (hereafter [O III]): being a forbidden transition, it can be produced only by regions with a gas density low enough (i.e. $n_e < 10^6$ cm^{-3}) to allow the collisionally-excited upper level to undergo radiative de-excitation. Therefore, it cannot originate from high-density gas of AGN BLR, thus resulting in an optimal tracer of ionised gas emission extended on AGN NLR scales (i.e. 1–10 kpc).

[O III] has been extensively employed to trace ionised outflows in large AGN samples (e.g. Weedman 1970, Heckman et al. 1984, Veilleux 1991, Boroson 2005, Komossa et al. 2008, Zhang et al. 2011, Bae and Woo 2014, Zakamska and Greene 2014, Balmaverde et al. 2016, Perna et al. 2017b), revealing that ionised outflows are a widespread phenomenon in AGN, with velocities up to few ~1000 km s^{-1}. In particular, such [O III]-based studies, mainly based on data from the Sloan Digital Sky Survey (SDSS), have pointed out the greater incidence of ionised outflows at increasing AGN luminosities and/or Eddington ratios (e.g. Mullaney et al. 2013, Bae and Woo 2014, Zakamska and Greene 2014, Balmaverde et al. 2016, Woo et al. 2016, Harrison et al. 2016, Perna et al. 2017b). Moreover, X-ray bright but optically obscured AGN have resulted to be optimal candidates to host ionised outflows (e.g. Cresci et al. 2015a, Perna et al. 2015a,b, Circosta et al. 2018), suggesting that an obscured and dusty environment may favour the launch of outflows via radiation pressure on dust (e.g King and Pounds 2015, Costa et al. 2018; see Sect. 1.2.2.1), as predicted by galaxy evolutionary models (e.g. Hopkins et al. 2008; see Sect. 1.1.2.2 and Fig. 1.2).

Longslit and integral field spectroscopic observations have unveiled outflows extended on ~1-10 kpc scales, with mass outflow rates from ~1 $M_\odot$ yr^{-1} to a few hundreds $M_\odot$ yr^{-1}. Low-redshift studies have enabled a detailed study of their properties (e.g. Crenshaw et al. 2015, Venturi et al. 2018, Mingozzi et al. 2019, Marconcini et al. 2023), whereas the search for ionised outflows at high redshift have been mostly focused on powerful and luminous sources around $z \sim 2$ (e.g. Cano-Díaz et al. 2012, Förster Schreiber et al. 2014, Carniani et al. 2015, Cresci et al. 2015a, 2023, Perna et al. 2015a,b, Harrison et al. 2016, Circosta et al. 2018, Veilleux et al. 2023; see Sect. 1.2.1). In addition to [O III], tracing medium-ionisation gas, broad wings in other optical emission lines (such as Hα and [N II]; e.g. Rupke and Veilleux 2013, Arribas et al. 2014, Marasco et al. 2020) or in UV/optical absorption lines (e.g. Shapley et al. 2003, Rupke and Veilleux 2011, Talia et al. 2012, Bordoloi et al. 2014) can also be used to map lower-ionisation gas carried by outflows.

As mentioned in Sect. 1.2.2.2, [O III]-traced ionised outflows have provided one of the strongest evidence so far of negative feedback in action in a few AGN at z~2 (Cano-Díaz et al., 2012, Carniani et al., 2015, 2016, Cresci et al., 2015a).

1.2.3.3 Molecular and atomic neutral outflows

Massive outflows are found on galaxy scales in molecular gas phase, featuring velocities from few 100 km s^{-1} to ~1000 km s^{-1} and substantial mass outflow rates of H_2 (from a few 100 $M_\odot$ yr^{-1} to above 1000 $M_\odot$ yr^{-1}). Molecular outflows are typically detected via faint broad features in sub-mm CO emission lines (e.g. Feruglio et al. 2010, 2013, Dasyra and Combes 2012, Cicone et al. 2014, Morganti et al. 2015, Dasyra et al. 2016, Brusa et al. 2018, Chartas et al. 2020, Vittoria Zanchettin et al. 2023; Fig. 1.10, panel **e**), in [C II]158μm emission line in the far-IR (e.g. Maiolino et al. 2012, Cicone et al. 2015), in near-IR and mid-IR H_2 emission lines (e.g. Dasyra and Combes 2011, Davies et al. 2014, Emonts et al. 2017, Fischer et al. 2017, Gnilka et al. 2020, Riffel et al. 2020), in emission lines from more complex molecules (e.g. HCN, HCO+, HNC), which trace high-density molecular gas with

$n > 10^4$ cm^{-3} (e.g. Aalto et al. 2012, 2015); and from characteristic P-Cygni profiles[11] of OH lines in far-IR spectra (e.g. Fischer et al. 2010, Sturm et al. 2011, Veilleux et al. 2013, Spoon et al. 2013). Compared to cold molecular gas ($T < 100$ K) detected via submm-mm CO line emission, IR H_2 roto-vibrational transitions trace a warmer phase of molecular gas with typical temperatures of $T \sim 100 - 1000$ K.

In AGN with a bolometric luminosity $< 10^{46}$ erg s^{-1}, the molecular phase represents the dominant contribution to the total outflowing gas, with masses larger by about two orders of magnitude than those typical of ionised outflows (Carniani et al., 2015, Fiore et al., 2017, Fluetsch et al., 2019). At higher luminosities (i.e. $> 10^{46}$ erg s^{-1}), such a discrepancy is not so clear, with distinct works coming to different conclusions (Carniani et al., 2015, Fiore et al., 2017).

Cicone et al. (2014) found molecular outflows to have momentum rates (i.e. $\dot{p}_{\rm out} = \dot{M}_{\rm out} v_{\rm out}$) larger by about a factor of 20 than the momentum transmitted to AGN photons (i.e. $\dot{p}_{\rm out} \sim 20 L_{\rm AGN}/c$, where $L_{\rm AGN}$ is the AGN luminosity due to accretion given by Eq. 1.1), which is consistent with the predictions of energy-driven winds (e.g. Zubovas and King 2012, Faucher-Giguère and Quataert 2012, King and Pounds 2015; see Sect. 1.2.2.1). However, by comparing nuclear UFOs and molecular large-scale outflows, only a few objects were found to be compatible with an energy-driven propagation (Tombesi et al., 2015, Chartas et al., 2016, Feruglio et al., 2015, 2017, Chartas et al., 2020), whereas most of them exhibit sub-energy-driven regimes. This might indicate either that other acceleration mechanisms are at play, or still an energy-driven scenario but with a poor coupling between the nuclear wind and the galactic ISM (Fluetsch et al., 2019).

Outflows are also detected in the neutral atomic phase through blueshifted wings in the optical Na I D absorption line doublet (Rupke et al., 2005, Rupke and Veilleux, 2011, 2015, Perna et al., 2017b, 2020, 2021, Cresci et al., 2023), in the 21-cm H I absorption line in the radio band (e.g. Morganti et al. 2005a,b, 2016, Schulz et al. 2018), or in UV hydrogen Lyα and Lyβ absorption lines (e.g. Shapley et al. 2003, Talia et al. 2012). Besides tracing molecular gas, broad wings in the far-IR [C II] emission line trace also the neutral atomic phase of outflows (e.g. Maiolino et al. 2012, Janssen et al. 2016, Bischetti et al. 2019).

Neutral atomic outflows are observed only in a small fraction (i.e. ~1%) of nearby AGN, and preferentially reside in ultra-luminous infrared galaxies (ULIRGs), typically featured by both intense SF and AGN activity (e.g. Rupke et al. 2005, Villar Martín et al. 2014, Cazzoli et al. 2016, Sarzi et al. 2016, Perna et al. 2017b). This may indicate that neutral atomic outflows are mostly SF-driven rather than AGN-driven (e.g. Bae and Woo 2018, Concas

---

[11] P-Cygni line profiles consist of a blueshifted absorption feature due to approaching material, and a redshifted emission tracing receding gas.

et al. 2019), or that they require obscured environments rich of cold gas to funnel into the outflow (Perna et al., 2017b). However, there is still large uncertainty on the nature of this form of outflows and their driving mechanisms.

1.3 Investigating AGN with Integral Field Spectroscopy

Except for data presented in Chapter 3, this thesis is based on data obtained via Integral Field Spectroscopy (IFS), an observational technique which delivers 2D spatially resolved spectra. These observations are optimally suited to study gas spatial distribution and kinematics in detail across the galaxy up to kpc scales. In Chapter 2, spatially resolved data from a large optical IFS survey are employed to unveil faint signatures of AGN activity; in Chapters 4, 5 and 6, optical and near-IR IFS of local and $z \sim 2$ AGN galaxies are used to trace AGN-driven outflows and to investigate their properties. Therefore, this section aims at providing basics of IFS, by briefly describing how it works (Sect. 1.3.1), and presenting the ground-based instruments used in this thesis (Sect. 1.3.2), showing also how ground-based IFS can compete with analogue space observations thanks to adaptive optics (AO).

1.3.1 Basics of IFU observations

IFS is an advanced observational technique which provides 3D information of the astronomical object being targeted. Data obtained with integral field spectrographs consist of data cubes, with two spatial dimensions (i.e. [x, y] or [RA, DEC]), and a third wavelength dimension (i.e. λ) containing spectral information. By combining information stored in these data cubes, it is possible both to obtain images of the target in distinct spectral channels, and to extract spectra from every spatial pixel [x, y], with plenty of applications to different types of analysis. IFS data are indeed employed in a wide range of common extragalactic studies, including: (1) measuring gas and stellar dynamics; (2) searching for and characterising gas outflows and/or inflows; (3) mapping the spatial distribution of ongoing SF across galaxies; (4) spatially resolving stellar populations.

Integral field spectrographs work in optical or IR bands, and consist of two main components: an integral field unit (IFU), which samples the light from the 2D spatial plane into distinct spatial components; and a spectrograph to disperse the light. IFUs may sample the light through lenslets, fibres or image slicers. These three different techniques are briefly described below and illustrated in Fig. 1.12.

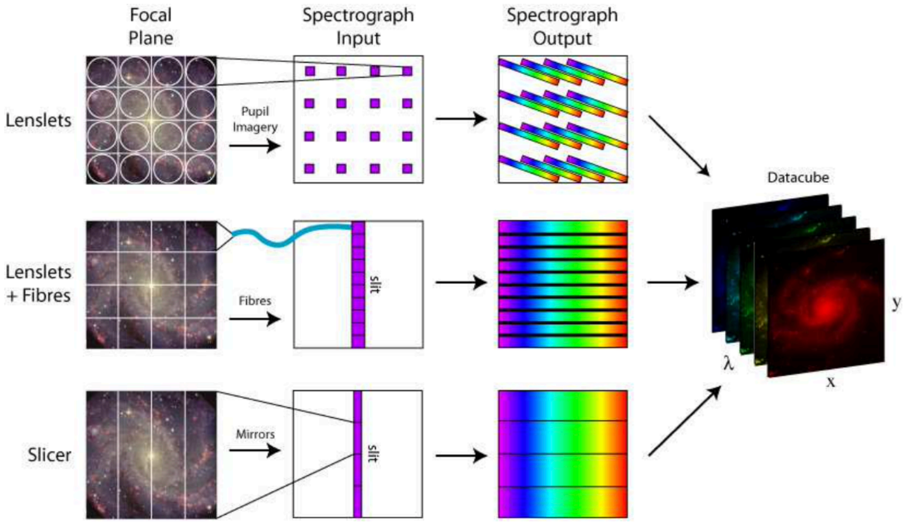

Fig. 1.12 *Schematic description of main IFU techniques to obtain spatially resolved IFS data. IFU can split the 2D spatial plane into a contiguous array by means of a lenslet array (top row), optical fibres (middle row), or an image slicer (bottom row). The formatted light is then sent to a spectrograph to be dispersed. The data reduction process then reformats the spectrograph output into a data cube. Image Credit: M. Westmoquette; adapted from Allington-Smith and Content (1998).*

- *Lenslet arrays* are microlens arrays and can be used to split the image into multiple light points, which are then dispersed by the spectrograph. The dispersed light is angled to avoid overlap between distinct spectra.

- *Optical fibres* can be behind a lenslet array or grouped in a bundle to sample to sample the image directly. The light from the fibers is the reformatted into a ‘pseudoslit’, and finally directed to the spectrograph.

- An *image slicer* uses a segmented mirror to split the image into thin horizontal sections (‘slices’), which are separately sent in slightly different directions. A second segmented mirror reformats the slices so that they are laid out end to end to form a ‘pseudoslit’, which is then passed to the spectrograph.

After being sampled via one of the above methods, the light is collimated and dispersed by the spectrograph and finally recorded by the detector. The final output of this process is a 2D image consisting of multiple stripes of adjacent spectra, corresponding to different positions in the original image (see Fig. 1.12). Each single spectrum is then reformatted into the final 3D data cube during the data reduction process.

1.3.2 Ground-based IFU facilities used in this thesis

The IFS observations used in this thesis were all obtained with four different ground-based optical/near-IR spectrographs. Note that before *JWST*, equipped of both a near-IR (NIRSpec) and a mid-IR (MIRI) IFU spectrograph, IFS could be done only from the ground. Chapter 2 is based on data from (1) the IFU survey Mapping Nearby Galaxies at Apache Point Observatory (MaNGA; Bundy et al. 2015), using IFU fibre arrays. The other IFS observations presented were instead carried out with spectrographs on the Very Large Telescope (VLT), at the ESO Paranal Observatory (Chile). These are: (2) the Multi-Unit Spectroscopic Explorer (MUSE; Bacon et al. 2010); (3) the K-band Multi Object Spectrograph (KMOS; Sharples et al. 2013); and (4) the (decommissioned) Spectrograph for INtegral Field Observations in the Near Infrared (SINFONI; Eisenhauer et al. 2003). All these spectrographs use IFU image slicers. In the following, we provide a brief overview of the IFU spectrograph used for MaNGA, as well as of the three VLT instruments.

1. **MaNGA** is one of the three core programs in the fourth Sloan Digital Sky Survey (SDSS), which acquired IFS of 10,000 nearby galaxies, thanks to 17 simultaneous IFUs composed of tightly-packed arrays of optical fibers. The observed wavelength range is 3600–10000 Å, with a spectral resolution $R \sim 2000$. The spatial scale is $0.5''$. MaNGA data are used in Chapter 2.

2. **MUSE** is an optical spectrograph composed of 24 identical IFUs, which together sample in Wide Field Mode (WFM) a contiguous $1' \times 1'$ field of view (FoV), with a $0.2''$ pixel scale. The nominal wavelength range covered by MUSE is 4800–9300 Å, with a mean spectral resolution $R \sim 3000$. Alternative to the WFM, MUSE offers a Narrow Field Mode covering a $7.4'' \times 7.4''$ FoV with a $0.025''$ pixel scale. MUSE is also equipped with an AO module. WFM MUSE data (with no AO) are presented in Chapter 4.

3. **KMOS** is a near-IR spectrograph equipped with 24 configurable arms, which can be used either separately to perform IFS of 24 distinct targets simultaneously, or together to map contiguous areas in a 8-point or 16-point dither pattern (mosaic mode). Each IFU has a $2.8'' \times 2.8''$ FoV, with a pixel scale of $0.2''$. Five spectral gratings are available (*IZ*, *YJ*, *H*, *K* and *HK*), covering a total wavelength range of 0.8–2.5 μm. In Chapter 4, we use KMOS mosaic observations in *H* and *K* bands.

4. **SINFONI** is a decommissioned near-IR (1.1–2.45 μm) spectrograph, employing an IFU image slicer. The spectrograph had four different gratings (*J*, *H*, *K*, *HK*). There were three different pixel scales available: $0.25''$, $0.1''$ and $0.025''$ corresponding

to a FoV of $8'' \times 8''$, $3'' \times 3''$ and $0.8'' \times 0.8''$, respectively. In Chapter 5, we use J-band observations in seeing-limited mode and a $0.25''$ pixel scale, whereas H- and K-band data with AO and a $0.1''$ pixel scale in Chapter 6.

Despite being extremely cheaper compared to space missions, ground-based observations are strongly affected by atmospheric turbulence, which inevitably worsens their quality. Temporal and spatial variations in the refractive index induce fluctuations of the wavefront phase, warping the originally flat wavefronts emitted by the source, which can result in blurry images of the astronomical target. Adaptive Optics (AO) allows us to overcome these effects of turbulence and to exploit the full capabilities of ground-based telescopes by restoring their diffraction limit. The basic principle of AO is to compensate for the turbulence-induced wavefront distortions, and to flatten the distorted wavefronts (e.g. Beckers 1993). As a first step, the AO system measures wavefront aberrations through a wavefront sensor (WFS). The signal from the WFS is then analysed by a real-time computer, which calculates an appropriate correction to send to a deformable mirror. Consequently, the deformable mirror properly changes so as to produce flat reflected wavefronts. To accurately follow the temporal evolution of turbulence-induced distortions, this feedback loop - regulating the overall functioning of an AO system - typically works at 1 kHz.

1.3.3 Spectral fitting of IFU data cubes

All data presented in this thesis are analysed using the fitting code presented in Marasco et al. (2020) and Tozzi et al. (2021), I contributed to developing and implementing during my Master's and PhD studies at UNIFI and INAF-OAA. This code was originally designed to analyse optical MUSE data of local AGN (Venturi et al., 2018, Mingozzi et al., 2019, Marasco et al., 2020), but over the years we have implemented it to also handle IFU data obtained with other instruments, introducing adjustments and new functionalities depending on the specific necessities of the data examined. In Chapter 2, we modify the code to analyse optical IFU data from the MaNGA survey, while in Chapter 3 we propose a simplified version of the fitting code suitable for the spectral analysis of single integrated optical spectra. An advanced, customised version is employed in Chapter 4 to analyse complex and detailed pieces of information contained in MUSE observations of a local galaxy merger, hosting a double AGN. In Chapters 4–6, we implement the algorithm to analyse also near-IR IFU observations obtained with KMOS and SINFONI. Further applications of this fitting code can be found in: Venturi et al. (2018), Mingozzi et al. (2019) and Marconcini et al. (2023) to MUSE data of nearby AGN from the MAGNUM survey (PI: A. Marconi); in Marasco et al. (2020) and Marasco et al. (2023) to MUSE observations of nearby AGN and starburst dwarf galaxies, respectively; in Cresci et al. (2023) for the analysis of near-IR IFU *JWST/NIRSpec* of an obscured quasar at $z \sim 1.6$. In the following, we illustrate the basics of our fitting procedure (see Marasco et al. 2020 and Tozzi et al. 2021 for more details), whereas specific changes implemented for each dataset being analysed are presented in the corresponding science chapters.

Our fitting procedure aims at studying the spatial distribution and kinematics of spatially resolved emission, with the main focus on line emission from gas originating on 1–10 kpc scales, associated with distinct kinematics. Possible kinematic components are: AGN NLR, galaxy disk rotation, tidal streams, and AGN-driven outflows, which play a major role within this thesis. Our fitting strategy consists of three key steps:

- *Phase I.* We build a template model for the bright BLR emission using an integrated, high-S/N spectrum.
- *Phase II.* The BLR template built in phase I is used to map spaxel-by-spaxel the unresolved BLR contribution to the total emission across the entire FoV, along with stellar and/or AGN continuum emission. The resulting BLR and continuum model cubes are then subtracted from the data cube.
- *Phase III.* In the remaining ‘subtracted’ cube, we finally perform a refined modelling, spaxel-by-spaxel, of faint gas emission lines originating on galaxy scales.

In the following, we provide a more detailed description of each main step of our fitting procedure. We will refer to emission lines produced by gas on galaxy scales as ‘narrow’, in order to distinguish them from the typical ‘broad’ emission lines (FWHM>2000 km s^{-1}; e.g. Osterbrock 1981) originating from within dense and highly turbulent AGN BLR.

I. Modelling the BLR emission The fitting code starts with modelling the bright BLR emission in a spectrum extracted from the nuclear region, while fitting other spectral components as well. Generally, possible contributing components to be fitted are: stellar and/or AGN continuum emission, broad BLR emission lines, and narrow emission lines from more diffuse gas on galaxy scales. The code builds the BLR model as a sum of two independent components: broad (isolated) permitted emission lines (mostly hydrogen), and several broad, blended Fe II emission lines significantly contributing to rest-frame optical emission. To run this full fit, the standard version of the fitting code employs the software PPXF (Cappellari and Emsellem, 2004, Cappellari, 2017), which can easily handle large libraries of templates, such as stellar and BLR Fe II templates. While we adopt different stellar templates depending on the targeted rest-frame emission (i.e. optical or near-IR), the procedure by default uses the semi-analytic templates of Kovačević et al. (2010) to reproduce rest-frame optical broad Fe II emission from AGN BLR. Moreover, PPXF gives the possibility of including an additive n-degree polynomial to either adjust the continuum shape to the observed data, or account for any additional continuum component such as AGN continuum. Regarding line emission, a Gaussian profile of same kinematics (i.e. central velocity and velocity dispersion) is fitted to all broad emission lines, whereas multiple Gaussian components are often required to properly model narrow emission lines, with each set of narrow Gaussian components still constrained to have the same kinematics. When present, PPXF fits [O III]$\lambda\lambda$4959,5007, [O I]$\lambda\lambda$6300,64 and [N II]$\lambda\lambda$6549,83 as doublets with a fixed flux ratio of 3 between the brighter and fainter components. In the end, the best-fit BLR template is stored and passed to phase II (see below).

II. Mapping the unresolved BLR emission across the FoV Since BLR emission is typically unresolved in our data, we expect its spatial variations to follow the Point Spread Function (PSF) of our observations. Therefore, we allow the BLR template obtained in phase I to change only in amplitude across the FoV and proceed to fit with PPXF the whole data cube. For the modelling of narrow emission lines, we use multiple Gaussian components and adopt a Kolmogorov-Smirnov (KS) test as a statistical approach to select spaxel-by-spaxel the minimal, optimal number of Gaussian components to aptly reproduce emission line profiles (see Marasco et al. 2020 for details). Typically, one Gaussian component is sufficient to model emission lines in low-S/N spaxels, whereas two or three (even four, see Chapter 4) Gaussian components are necessary to reproduce the most complex line profiles in high-S/N spaxels. Stellar continuum and/or AGN continuum[12] are fitted spaxel-by-spaxel following the same prescriptions as in phase I. After running the modelling of the full data cube, we subtract spaxel-by-spaxel BLR and continuum emission, thus obtaining a cube containing only residual narrow emission lines due to diffuse gas. Hereafter, we will refer to this cube as ‘subtracted cube’ (or ‘subtracted spectra’).

III. Modelling the narrow emission lines In phase III, we focus on the refined modelling of the narrow emission lines remaining after the subtraction of BLR and continuum emission. In fact, although they are already modelled by PPXF in phase II, re-fitting these lines on the cleaned dataset brings two main advantages. First, we now have fewer free

---

[12] Being typically unresolved in our data, AGN continuum emission can be just modelled in phase I through a polynomial fit and, then, included in the unresolved BLR template, which is re-scaled in flux spaxel-by-spaxel in phase II. Otherwise, PPXF can model it spaxel-by-spaxel via a n-degree polynomial at this stage of the procedure.

parameters since we do not have to model the complex BLR and continuum emission. Secondly, we can bypass the PPXF limitations of using solely Gauss-Hermite functions and select any desired functional form to fit the data, constraining or not different emission lines to the same kinematics. In the case of the datasets presented in this thesis, we find that a multi-Gaussian representation of the detected line profiles is satisfactory. Similarly to the phase II modelling, the procedure runs multiple Gaussian fittings, each time increasing the number of Gaussian components[13], and then selects the optimal number of components required via a KS test. Finally, the procedure allows us to isolate line emission associated with high-velocity outflowing gas, from that tracing the gas bulk motion within the host galaxy. For that, we implement different classification criteria, depending on the complexity of line profiles (see details in each science chapter).

1.4 Goals and strategy of this thesis

In this chapter we have provided an overview of the rich AGN phenomenology and their key role played in galaxy evolution. We have described AGN structure, from their inner powering engine - an accreting BH - to more external regions, and summarised the main different AGN components, each emitting in a specific waveband but overall covering the whole electromagnetic spectrum. We also showed that the AGN unified model can explain most of the observed AGN spectral features, but increasing observational evidence points to the limits of this standard picture, thus favouring alternative scenarios. Besides their complex phenomenology, AGN are now widely accepted to be crucial ingredients in the evolution of galaxies via AGN feedback mechanisms, which strongly influence galaxy properties. In particular, we have focused on AGN-driven outflows, considered the main responsible for the SF quenching in more massive galaxies, and invoked by theoretical models to explain observed scaling relations revealing a strict co-evolution of BHs with their host galaxies.

This PhD thesis fits into this broad picture of AGN properties and related mechanisms, making large use of IFU data of local and $z \sim 2$ AGN to spatially trace AGN-driven outflows as well as faint local signatures of AGN activity. The first two science chapters address issues related with the detection of faint, elusive AGN. In Chapter 2, we use optical He II line emission to trace AGN hidden in star-forming galaxies from the IFU MaNGA survey, typically missed by the standard optical BPT selection, with important application to high

---

[13] At this stage, the maximum number of Gaussian components required to reproduce the most complex line profiles often exceeds that employed in phase II, since the removal of BLR and continuum emission may unveil fainter asymmetries in line profiles.

redshift. Sometimes, elusive AGN can also reveal themselves thanks to CL transitions, as addressed by Chapter 3. Here, we report the recent discovery of a new optical CL AGN, showing evidence for a double type-transition in its multi-epoch spectra. The remaining three science chapters instead aim at investigating AGN-driven outflows at both low redshift (Chapter 4), where the higher spatial resolution and sensitivity enable a more detailed study, and $z \sim 2$, the crucial epoch for AGN feedback (Chapters 5 and 6). In all these chapters, we use IFS observations carried out with different ground-based facilities at the VLT. In Chapter 4, we combine optical MUSE and near-IR KMOS data of a local AGN galaxy to trace ionised and warm molecular components of outflows, respectively. In Chapters 5 and 6 instead, we trace ionised outflows in $z \sim 2$ AGN using near-IR IFU observations, where rest-frame optical emission is found redshifted. In particular, Chapter 5 investigates the connection of large-scale ionised outflows with X-ray nuclear UFOs, as their inner powering engine; whereas Chapter 6 unveils an interesting difference in ionised outflow kinematics between type-1 and type-2 AGN.

Chapter 2

Unveiling hidden AGN in MaNGA star-forming galaxies with He IIλ4686

In this chapter, we address the limits of standard optical emission-line diagnostics and use optical He IIλ4686 line emission as an effective tracer of hidden AGN in MaNGA star-forming galaxies. In view of exploring unprecedented high redshifts with JWST and new ground-based facilities, developing novel emission-line diagnostics is fundamental to discover AGN residing in highly star-forming and metal-poor environments. Adapted from Tozzi et al. (2023), MNRAS, 521, 1264.

Huge efforts have been invested in compiling large and complete AGN samples, including both high-luminosity quasars and low-luminosity AGN galaxies, to understand their physical properties and establish their role in galaxy evolution. Based on the distinctive characteristics of AGN (e.g. accretion rate and obscuration state), various techniques have been developed to search for AGN in different spectral bands, from hard X-rays to mid-IR and radio, as revised in Sect. 1.1.3. The most common and widely used optical method relies on BPT diagrams (Baldwin et al., 1981, Veilleux and Osterbrock, 1987), based on the combined [O III]/Hβ and [N II]/Hα line ratios (with [S II]/Hα or [O I]/Hα as alternatives), which allow to identify the dominant ionisation mechanism, distinguishing mainly between AGN and star formation.

Ten years ago, an alternative diagnostics was presented by Shirazi and Brinchmann (2012), the so-called He II diagram, where the [O III]λ5007Å emission line flux is replaced by He IIλ4686Å (hereafter [O III] and He II, respectively) in the ratio with the Hβ line flux. Given the higher ionisation potential of He II ($E_{\rm ion}(He^{+})$ = 54.4 eV) compared to [O III] ($E_{\rm ion}(O^{++})$ = 35.2 eV), the He II diagnostics is more sensitive to AGN activity and better differentiates between ionisation due to AGN and star formation. In particular, it allows to identify low-luminosity AGN in star-forming (SF) galaxies, where the AGN emission may be overwhelmed by intense star formation and, therefore, missed by the standard BPT-based selection, as pointed out by Schawinski et al. (2010). Bär et al. (2017) indeed used the He II diagram to search for nuclear activity in local galaxies in the SDSS Data Release 7 (SDSS DR7; York et al. 2000, Gunn et al. 2006, Abazajian et al. 2009).

Although the He II line emission is an optimal tracer of AGN activity, there are several limitations associated with its use. First of all, it is a faint emission line, which is the reason why the published studies on the topic are few and all limited to the local Universe. Moreover, it can also be of stellar origin. The He II line is indeed frequently observed in HII regions, associated with young stellar populations and, in particular, with evolved and massive Wolf-Rayet (WR) stars. However, in presence of WR stars, the He II line appears blended with several metal lines, forming the so-called 'blue-bump' around λ4650Å (Brinchmann et al., 2008). Indeed, several studies have also found evidence for substantial He II emission in low-metallicity, SF dwarf galaxies (e.g. Umeda et al., 2022). In the case of dwarf galaxies some authors have also proposed other ionising sources, such as X-ray binaries (e.g. Schaerer et al., 2019) and fast radiative shocks (Garnett et al., 1991, Thuan and Izotov, 2005, e.g.). However, recent observations have revealed the presence of AGN in several dwarf galaxies (e.g. Mezcua et al., 2016, Mezcua and Domínguez Sánchez, 2020, Schutte and Reines, 2022), therefore indicating that AGN ionising photons may be responsible for the He II emission even in these systems.

Most searches for AGN using optical spectroscopy have so far relied on single-fibre observations (such as the SDSS). As pointed out in Wylezalek et al. (2017), the SDSS optical fibres cover the central $\sim 3''$ region of galaxies, where AGN radiation might be either diluted by other dominant ionisation processes (like star formation), or hidden by obscuring material and gets unveiled on larger scales, missed by the $3''$-apertures of SDSS. In consequence, the central AGN may not be detected in the central integrated spectrum of its host, leading to an incorrect classification of the galaxy as non-active. Thanks to IFU observations (as mentioned in Sect. 1.3), it is now possible to search for weak (less diluted) and off-centre AGN signatures, such as cases of AGN offset from the centre due to a recent merger with a non-active galaxy, or of a second off-centre AGN in dual AGN systems (Greene et al., 2011, Comerford et al., 2012, Comerford and Greene, 2014, Hainline et al., 2016, Mannucci et al., 2022). Another possibility might also be a recently turned off AGN (Shapovalova et al., 2010, McElroy et al., 2016), whose relic ionisation remains visible at large distance from the centre (Keel et al., 2012, 2015).

In this chapter, we combine the power of integral field spectroscopy using data from the MaNGA survey (Bundy et al., 2015) with the He II diagnostics to identify AGN host candidates. By comparing the AGN samples selected by the He II emission and the standard BPT diagrams, we find that the former is crucial to detect elusive AGN residing in highly SF galaxies, which are completely missed by the standard BPT classification, therefore increasing the total number of AGN in our parent sample. In this work, we adopt a flat ΛCDM cosmology with $\Omega_{\rm m,0} = 0.3$, $\Omega_{\Lambda,0} = 0.7$ and $H_0 = 70$ km s^{-1} Mpc^{-1}.

2.1 Sample selection and classification

2.1.1 MaNGA data

Our sample is based on the fifteenth data release (DR15) of the MaNGA survey (Mapping Nearby Galaxies at APO; Bundy et al. 2015, Drory et al. 2015, Law et al. 2015, Yan et al. 2016, Wake et al. 2017). MaNGA is an optical fibre-bundle IFU (see Sect. 1.3.1) spectroscopic survey, part of the fourth phase of the SDSS (SDSS-IV; Blanton et al. 2017). The MaNGA DR15 catalogue consists of spatially resolved data of about 4600 local ($z \sim 0.03$) galaxies with a spectral resolution $R \sim 3000$ over the wavelength range of $\sim 3600 - 10300$ Å , using multiple (from 19 to 127) fibre bundles. The median effective spatial resolution of MaNGA data is of $2.54''$ FWHM (Law et al., 2016), corresponding to ~ 2 kpc at $z \sim 0.05$, and the pixel scale is of $0.5''$. In our analysis, we use spatially resolved data and measurements of galaxies (e.g. data and model cubes, emission-line flux maps) provided by the MaNGA data-analysis pipeline (DAP; Belfiore et al. 2019, Westfall et al. 2019), and take global properties (e.g. star formation rate, stellar mass) integrated within the FoV, from the MaNGA Pipe3D value added catalog (Sánchez et al., 2016).

2.1.2 Spatially resolved emission line diagrams

With the aim of comparing the efficacy of BPT and He II diagrams in selecting AGN galaxies, we start dealing with spatially-resolved measurements of emission-line flux of all MaNGA spaxels. From the MaNGA DAP we select spaxels with a signal-to-noise (S/N) ratio higher than 3 in [O III], [N II], Hβ and Hα for the BPT diagram (BPT spaxels), whereas we require S/N > 5 in He II and S/N > 3 in [N II], Hβ and Hα for the He II diagram (He II spaxels). We apply a higher S/N cut for the He II, compared to that for the other lines, in order to conservatively select only spaxels with a secure He II detection and to avoid cases of putative He II line emission that is actually consequence of a strong residual of the stellar continuum or to contamination from a foreground galaxy (these cases are discussed later in Sect. 2.1.3.1.)

These S/N cuts lead to ~2.1 million and ~15200 spaxels for the BPT and He II diagrams, respectively (out of a total of more than 4.3 million MaNGA spaxels). The large discrepancy (i.e. ~2 orders of magnitude) in the number of high-S/N spaxels resulting from the two separate S/N cuts (i.e. the BPT-selected versus He II–selected spaxels) reveals how faint and rare the detection of the He II emission line is, even in the spectra of local galaxies.

To compute line ratios, we use dust-corrected emission line fluxes resulting from the Gaussian line modelling performed within the MaNGA DAP, except for a few galaxies which instead need a complete or partial spectral re-fitting. In the case of these objects, we take single-spaxel emission line fluxes obtained from our re-modelling (see Sect. 2.1.3.2).

2.1.2.1 BPT and He II diagnostic diagrams

The top panels of Fig. 2.1 show the [O III]/Hβ versus [N II]/Hα version of the BPT (left panel) and the He II (right) diagnostic diagrams of MaNGA spaxels.

Regions in the two diagrams corresponding to different ionisation mechanisms are delimited by demarcation lines. In the BPT diagram, the Ke01 and Ka03 lines represent the theoretical extreme starburst line (Kewley et al., 2001) and the empirical upper limit to the SF region (Kauffmann et al., 2003), respectively; the S07 line instead separates LINERs from AGN ionising sources according to Schawinski et al. (2007). Similarly, we plot separating curves in the He II diagram as determined in Shirazi and Brinchmann (2012): the solid and dashed lines are defined as the limiting curves above which more than 50% and 10% of the He II flux, respectively, is expected to come from an AGN. We classify spaxels as AGN-like only when they lie in the pure AGN regions of their respective diagrams: in the BPT, these are the spaxels falling above both the Ke01 and S07 lines, referred to as BPT AGN spaxels (empty/filled blue circles); while in the He II diagram, the He II AGN spaxels are those above the 50% AGN line (empty/filled red squares). Filled symbols represent BPT and He II AGN spaxels meeting the additional requirement of having S/N(He II) > 5 and S/N([O III]) > 3, respectively. Whereas there is a substantial difference in number between filled (~3440 spaxels) and empty (~37700 spaxels) blue circles, almost all He II spaxels fulfilling the S/N threshold in He II (~12000 spaxels) have also S/N > 3 in [O III] (~11700 spaxels). The grey shading in the background represents the total sample of MaNGA spaxels as selected by the S/N cut, namely the total BPT (left) and He II (right) spaxels as previously defined.

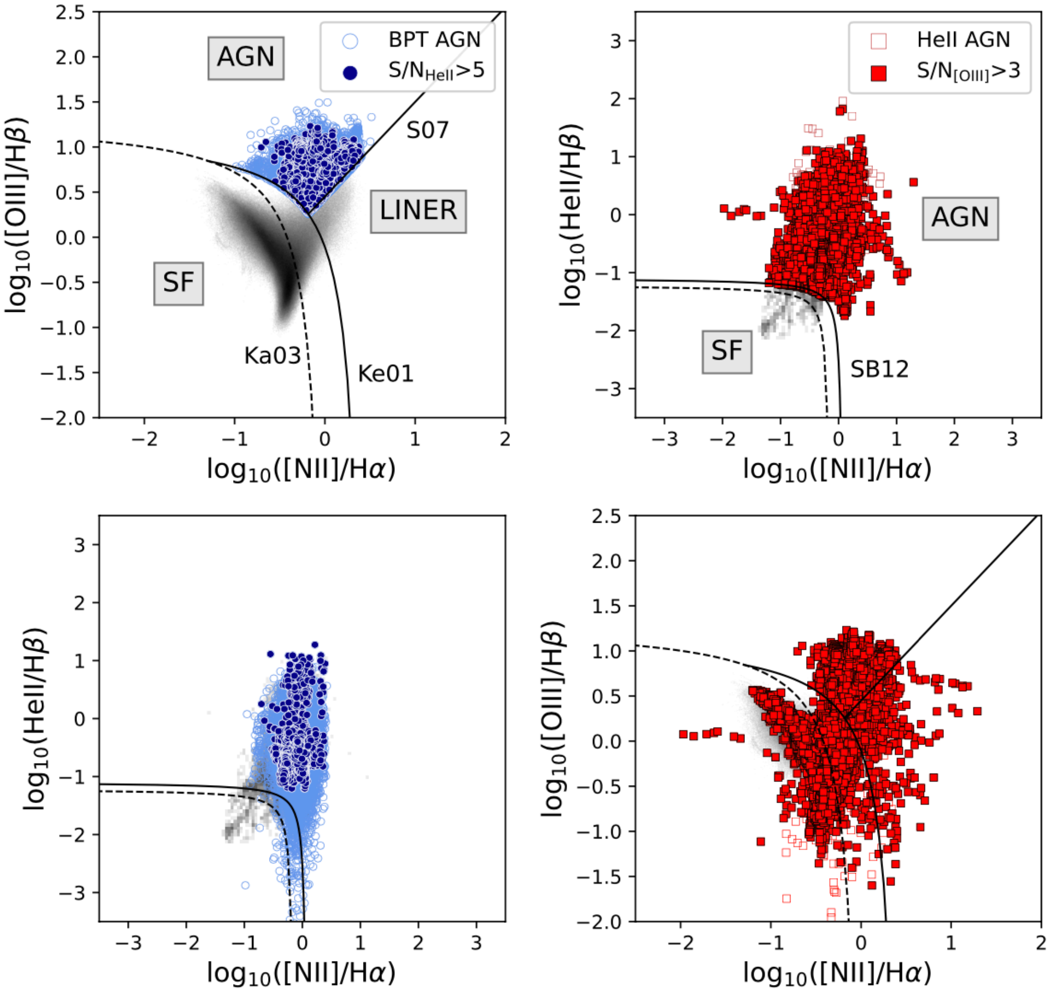

Fig. 2.1 *Spatially resolved emission line diagnostics diagrams. Top panels. BPT (left) and* He II *(right) diagrams for MaNGA DR15 spaxels. The BPT AGN region is delimited by the Ke01 line, defined in Kewley et al. (2001) as the extreme starburst line, and the S07 line separating AGN from LINER ionising sources (Schawinski et al., 2007). In the* He II *diagram the dashed and solid SB12 lines represent the limit above which 10% and 50% of the* He II *emission, respectively, is expected to come from an AGN (Shirazi and Brinchmann, 2012). In each diagram the grey shading represents MaNGA spaxels satisfying the S/N threshold (Sect. 2.1.2). Spaxels falling in the AGN region of the BPT and* He II *diagrams are shown as circles (BPT AGN) and squares (*He II *AGN), respectively. Filled symbols represent the two categories meeting the additional requirement of having S/N(*He II*) > 5 (~3440 spaxels) and S/N([*O III*]) > 3 (~11700 spaxels), respectively. Bottom panels. Distribution of BPT AGN and He*II *AGN spaxels in the* He II *(left) and BPT diagram (right), respectively. BPT AGN are mostly all confirmed by the* He II *diagram, while* He II*-selected AGN spread largely also in the SF region of the BPT diagram.*

2.1.2.2 Comparing the two diagnostic diagrams

Similarly to the analysis performed on integrated emission line flux ratios in Bär et al. (2017), in the bottom panels of Fig. 2.1 we compare the spatial distributions of AGN spaxels identified with one diagnostic diagram, within the parameter space of the other diagnostic. More precisely, we show the distribution of BPT-selected AGN spaxels in the He II diagram (empty/filled blue circles, bottom left panel) and the distribution of He II-selected AGN spaxels in the BPT diagram (empty/filled red squares, bottom right panel). Except for a very few cases, almost all BPT AGN spaxels fall above the 10% AGN demarcation line of the He II-diagram, and 82% of the total BPT AGN spaxels is located even above the 50% AGN line in the He II diagram. Such a fraction increases to 100%, if we consider only BPT AGN spaxels with also S/N(He II) > 5 (filled blue circles). Therefore, the He II-classification overall recovers the BTP-classified AGN. Unlike the BPT AGN spaxels in the He II diagram, the He II AGN spaxels are scattered across the BPT plane and extend well into the SF region, with only 29% of them meeting classification criteria for BPT AGN. Hence, Fig. 2.1 clearly demonstrates the power of He II diagnostic in identifying regions with significant contribution to ionisation from an AGN, which may be erroneously classified as entirely due to star formation.

2.1.3 Selecting AGN host galaxies in MaNGA

We define a criterion to identify AGN host galaxies based on their content of AGN spaxels as classified by the emission line diagnostic diagrams in Fig. 2.1. We identify as BPT (He II) AGN galaxy candidates those objects with at least 20 AGN spaxels meeting the S/N threshold, defined for the BPT (He II) diagram in Sect. 2.1.2. The minimum requirement of 20 AGN spaxels approximately corresponds to one spatial resolution element in MaNGA, in case of adjacent spaxels. We check contiguity among spaxels at a later stage of the analysis (see Sects. 2.1.3.1 and 2.1.3.4).

With this definition we obtain populations of BPT and He II AGN galaxy candidates based on the BPT and He II spaxels classification, respectively. Among the He II AGN population, some galaxies are also BPT-selected AGN (hereafter BPT&He II AGN); while others are identified as AGN only by the He II diagram (hereafter He II-only AGN), with the majority of their spaxels located in BPT SF region.

Details on the demography of the different AGN populations are provided at the end of Sect. 2.1.3.3, after refining our selected sample of AGN galaxies.

2.1.3.1 Excluding cases of dubious He II line emission

As already mentioned, the main problem related to the use of the He II emission line is its faintness, limiting its clear detection to only a small sample of MaNGA galaxies. From our preliminary selection we obtain 178 He II AGN galaxy candidates, most of which must be rejected because the He II emission line at S/N>5 (suspiciously reported by the MaNGA DAP even in spaxels in the galaxy outskirts) does not appear to be real. By visually inspecting single-spaxel spectra using Marvin[1] (Cherinka et al., 2019) and He II DAP maps, we indeed find, in ~50% of the selected galaxies, spaxels with a putative high-S/N He II, where the He II emission line is actually resulting from either noise, artifacts or strong residuals after the stellar continuum subtraction.

To identify and exclude these galaxies from our He II AGN sample, for each galaxy we plot the He II flux map and create the ‘subtracted cube’, that is the MaNGA data cube after subtracting the DAP stellar continuum model. From the subtracted cube and the DAP emission line model cube[2] of each galaxy, we then extract the spectrum and the cumulative emission line model using two different central apertures (i.e. $2.5''$ and $5.5''$). By visually examining both the He II flux maps and the integrated spectra, we finally exclude cases of He II non-detection from our preliminary selected sample.

We additionally report on five cases of contamination by a foreground galaxy (8084-12701, 8158-1901, 8158-1902, 8987-6101, 9194-6104), producing an emission line (likely Hβ) around the He II wavelength in the rest-frame of the target galaxy and, therefore, misinterpreted as the He II line by the DAP. These five galaxies are therefore excluded.

2.1.3.2 Need for re-modelling some MaNGA data cubes

By visually inspecting extracted spectra along with their cumulative emission line model (as previously explained in Sect. 2.1.3.1), we also find 16 MaNGA data cubes of He II AGN galaxies badly fitted by the MaNGA DAP (Table 2.1). We therefore re-model all them by means of our fitting code described in Sect. 1.3.3.

As described in Sect. 1.3.3, our fitting procedure first models the full data cubes with PPXF (Cappellari and Emsellem, 2004, Cappellari, 2017), creating dedicated templates for each contributing spectral component: namely, stellar continuum, AGN continuum, and line emission from AGN BLR and NLR. Then, the fitting code allows the user to subtract from the data the total continuum (i.e. stellar plus AGN continuum) and the unresolved BLR emission, thus creating a subtracted cube containing only spatially-resolved narrow

---

[1] Online, interactive tool to search for, access and visualise MaNGA data (https://dr15.sdss.org/marvin/).

[2] Both stellar continuum and emission line models are stored in the MaNGA model cube produced by the MaNGA DAP.

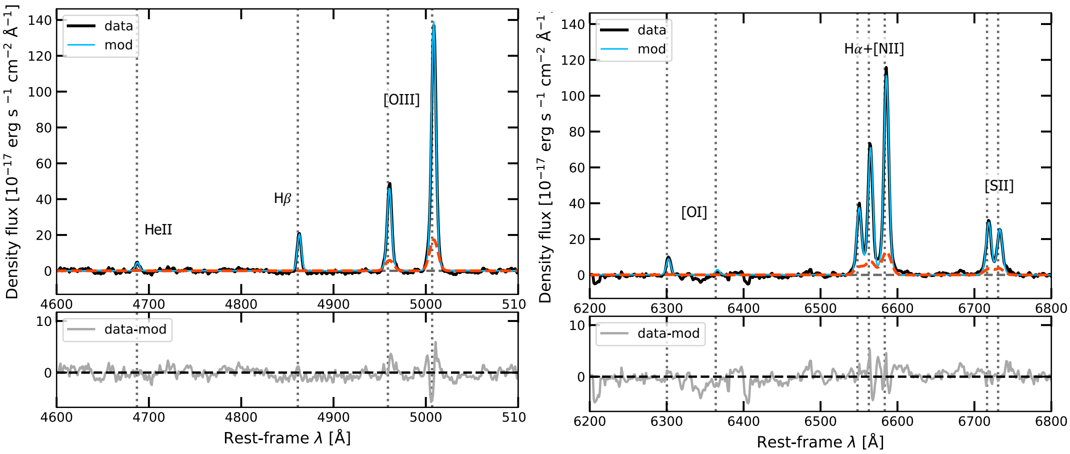

Fig. 2.2 *Best-fit results from our spectral re-modelling of the main emission lines in the MaNGA galaxy 9026-9101:* He II, Hβ *and* [O III] *emission lines in the upper panel, whereas* [O I], [N II], Hα *and* [S II] *in the lower panel. In each panel, the subtracted data (black) and the total emission-line model (lightblue) are extracted from a central* $2.5'' \times 2.5''$ *aperture. Two Gaussian components are required to accurately model the narrow-line emission in this galaxy, one of which is separately shown in orange. Below each main panel, we show corresponding residuals.*

emission lines. At this point, a refined multiple Gaussian modelling of narrow emission lines can be performed, with no longer contamination from continuum and/or unresolved emission.

Among the 16 badly fitted MaNGA data cubes, six galaxies are likely type-1.8 AGN since their Balmer hydrogen lines clearly exhibit a very broad component originating in the AGN BLR, which the MaNGA DAP is not designed to reproduce. We therefore fully re-fit these six data cubes (labelled as ‘full’ in Table 2.1), starting from the modelling of stellar continuum and including also a very broad Gaussian component ($\sigma > 1000$ km s^{-1}) in the model of permitted lines (i.e. Balmer hydrogen lines and He II), to account for the BLR contribution to total line emission. We model stellar continuum with the MILES extended stellar population templates (Röck et al., 2016), and AGN continuum through a 1st-degree polynomial. In the remaining ten data cubes instead, no BLR line emission is present and stellar continuum has been correctly modelled by the MaNGA DAP. We hence create the corresponding subtracted data cubes (as defined in Sect. 2.1.3.1) and re-model emission lines only. In eight data cubes, the inaccurate best-fit model is limited to the faint He II emission line, while the other brighter emission lines have been correctly modelled. So, in these cases we re-fit the He II emission line only (labelled as ‘He II’ in Table 2.1), to obtain a more reliable flux. Two galaxies instead require a re-modelling of their entire subtracted cube, hence we re-fit all emission lines (‘all lines’ in Table 2.1). In Fig. 2.2, we plot as representative example the best-fit results of the main emission lines in

Table 2.1 *List of refitted MaNGA data cubes. For each refitted data cube, the columns are arranged in the following order: (1) plate-ifu ID of the corresponding galaxy, (2) type of remodelling, (3) maximum number of Gaussian components adopted to model narrow emission line profiles in single-spaxel spectra; (4)* He II*-based classification (AGN or SF) after our remodelling, and (5) identification of* He II*-only AGN. In column (2) we distinguish among full refitting of MaNGA data cubes (full), modelling of all emission lines in MaNGA continuum-subtracted data cubes (all lines), and re-modelling of the* He II *emission line only (*He II).

Plate-ifu ID	Refitting type	ncomp max	He II classification	He II-only AGN
7815-6104	full	3	AGN	no
8146-1901	He II	1	AGN	yes
8320-9101	all lines	2	SF	-
8341-12704	full	3	AGN	no
8341-12705	He II	1	SF	-
8458-3702	He II	1	SF	-
8465-3701	He II	1	AGN	yes
8615-3701	full	AGN	3	yes
8715-3702	full	AGN	3	no
8934-3701	He II	1	SF	-
8940-6102	He II	2	AGN	yes
9026-3701	He II	1	SF	-
9026-9101	all lines	2	AGN	no
9487-3702	full	3	AGN	no
9487-9102	full	3	AGN	yes
9883-3701	He II	1	SF	-

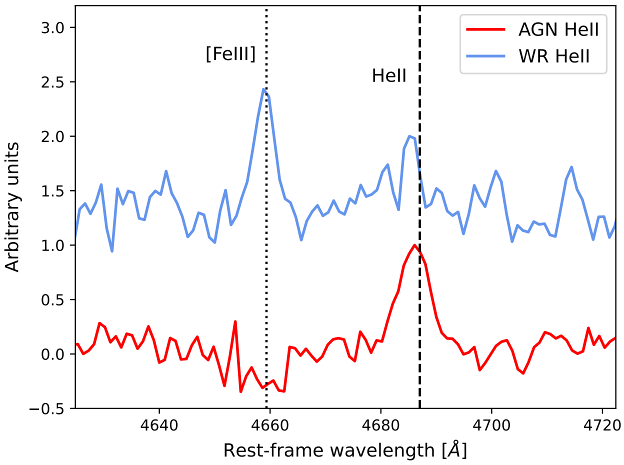

Fig. 2.3 *Representative examples of* He II *emission line associated with WR stars (blue) and with an AGN (red), respectively. The former is extracted from a WR region in the galaxy 8458-3702 (previously classified as a WR galaxy by Liang et al. 2020) and shows typical signatures of WR emission (i.e. blue bump around* He II *and bright* [Fe III] λ*4658); the latter from the nuclear region of the galaxy 8257-12701, identified as* He II*-only AGN, clearly exhibiting a peaked* He II *emission line, AGN classified by the* He II *diagram.*

the MaNGA galaxy 9026-9101, as obtained from our spectral re-modelling: the subtracted data (black) and the total emission-line model (lightblue) have been extracted from a central 2.5″×2.5″ aperture. To accurately model the narrow-line emission in this galaxy, we use two Gaussian components, one of which is separately shown (orange) in Fig. 2.2.

After the re-modelling, we create flux maps of the main emission lines and correct line fluxes for dust extinction (Calzetti et al., 2000). At this point, six galaxies (8320-9101, 8341-12705, 8458-3702, 8934-3701, 9026-3701, 9883-3701) are no longer classified as AGN galaxies (but as SF galaxies) according to the He II diagram, so we exclude them. In Table 2.1, we list the refitted MaNGA data cubes along with the type of remodelling and the maximum number of Gaussian components used to model narrow emission line profiles in single-spaxel spectra. For each galaxy, we also indicate whether the He II AGN classification is confirmed after the remodelling, and identify He II-only AGN galaxies among such confirmed cases.

2.1.3.3 Search for type-1 AGN and He II due to WR stars

We finally look for type-1 AGN in the overall (BPT and/or He II) AGN sample, and for central He II emission due to WR stars among He II AGN galaxies. To identify both categories we compare the average velocity dispersion $\langle\sigma\rangle$ of different emission lines within a 5.5″ central aperture. In particular, we classify as type-1 AGN those with $\langle\sigma(\mathrm{H}\alpha)\rangle > 2\,\langle\sigma([\mathrm{O\,III}])\rangle$

or $\langle\sigma(\mathrm{H}\beta)\rangle > 2\,\langle\sigma([\mathrm{O\,III}])\rangle$, resulting in 13 galaxies. We decide to exclude the type 1 AGN since we are primarily interested in AGN likely missed by the BPT classification, while these are very clear, luminous AGN. Furthermore, their data cubes should be refitted (just like the type-1.8 AGN described in Sect. 2.1.3.2) and the determination of their SFR and stellar masses would be more uncertain.

Regarding He II emission due to WR stars, we find clear evidence for blue blump in three galaxies He II-classified as SF after our remodelling (8458-3702, 8934-3701, 9883-3701), identified as WR galaxies by Liang et al. (2020). In Fig. 2.3, we show for comparison two spectra over the He II wavelength range, respectively extracted from a WR region in the galaxy 8458-3702 (blue), and from the nuclear region of the galaxy 8257-12701 (red), classified as He II-only AGN in our census. Whereas the former spectrum clearly exhibits a blue bump around the He II line along with a bright [Fe III] λ4658 typically associated with WR stars (e.g. Rogers et al. 2021), the latter distinctly shows a peaked He II emission line, classified as AGN-like by the He II diagram.

However, we point out that this study does not aim at a rigorous identification of WR regions within MaNGA galaxies but, mostly, at excluding cases of clear WR He II emission originating in the galaxy centre, but misclassified as AGN-like based on the He II diagnostic. For this reason, we search in the remaining He II AGN sample for signatures of blue bump only within a central 5.5″ aperture, by requiring $\langle\sigma(\mathrm{He\,II})\rangle > 2\,\langle\sigma([\mathrm{O\,III}])\rangle$ and $\langle\sigma(\mathrm{He\,II})\rangle > 500\ \mathrm{km\ s^{-1}}$ (indicative lower limit taken from Brinchmann et al. 2008). We thus tentatively detect one case of blue bump in the central region of the galaxy 8250-6101. Yet, given the marginal detection of such bump compared to the narrow, nebular He II emission line, we decide to retain this in our AGN sample.

2.1.3.4 Final refined AGN sample

Figure 2.4 summarises the demography of the AGN population (and subpopulations), consisting of 459 AGN host candidates in total (~10% in MaNGA DR15), as resulting from our selection criterion. Out of the total AGN galaxies, 432 are BPT-selected AGN (94%), whereas 81 are He II-selected AGN (18%). In the He II AGN subsample, 54 objects are classified as AGN galaxies also by the BPT (12% and 67% of the total and He II AGN samples, respectively). There are instead 27 He II-only AGN candidates (6% and 33% of the total and He II AGN samples, respectively), missed by the BPT AGN classification. There are finally 378 BPT AGN (82%), with no He II detection (BPT AGN noHe II).

In Figs. 2.5 and 2.6, we show spatially resolved maps of every selected He II-only AGN galaxy, displaying the spaxel classification according to BPT and He II diagrams, respectively. Bold labels indicate galaxies whose MaNGA data cubes needed some spectral

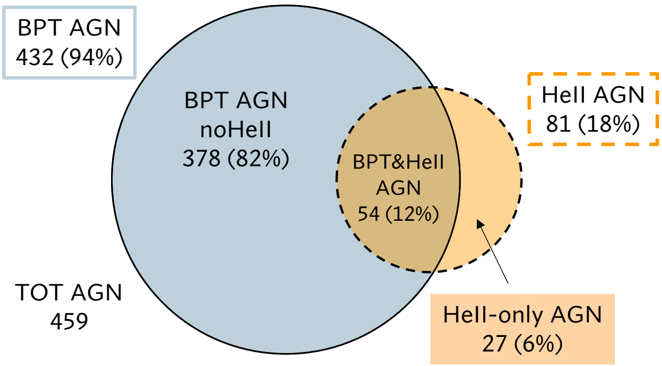

Fig. 2.4 *Chart summarising the demography of the AGN population selected in MaNGA. In total, we identify 459 AGN galaxy candidates by combining the two diagnostics: 432 (94% out of our total AGN population) are BPT-classified AGN, while the* He II *diagram selects 81 (18%) galaxies as AGN. 54 galaxies are selected by both diagrams (BPT&*He II *AGN), corresponding to 12% of the total AGN population, and 27 galaxies (6% of the AGN population) are instead classified as AGN only by the* He II *diagnostic (*He II*-only AGN). Finally, there are 378 BPT AGN (82%), with no* He II *detection (BPT AGN* noHe II*).*

remodelling (listed in Table 2.1). In BPT maps (Fig. 2.5), we use distinct colours to distinguish different ionisation mechanisms (Kewley et al., 2001, Kauffmann et al., 2003, Schawinski et al., 2007): star formation (blue), LINER (green), composite mechanisms (grey), and AGN (red, globally absent). With the exception of very few isolated red spaxels in galaxy outskirts (totally negligible), the BPT diagnostic detects no AGN-like emission in these galaxies, in agreement with our BPT-based classification of these objects as non-active galaxies.

In a similar way, we use different colours to indicate regions ionised by distinct mechanisms according to the He II diagram (Fig. 2.6): star formation (blue) and AGN, for which we distinguish between a stronger (red, above the 50% curve; see Fig. 2.1 and Sect. 2.1.2.1) and weaker (orange, above the 10% curve) AGN contribution to the He II (Shirazi and Brinchmann, 2012). In both BPT and He II maps, solid black lines are contour levels of Hα line flux corresponding to 1%, 10%, 50% and 80% values of the respective emission peak, and a black cross marks the galaxy centre. Coloured spaxels are those meeting the S/N threshold, as defined at the beginning of Sect. 2.1.2. In addition, we apply MaNGA DAP masks associated with the flux each emission line, which explains why in a few maps of Fig. 2.6 the number of red (strong AGN) spaxels is smaller than the 20-spaxel threshold adopted for our preliminary selection of AGN galaxies (Sect. 2.1.3). Yet, we retain such galaxies in the He II AGN sample since they however show centrally-located, He II-classified AGN emission.

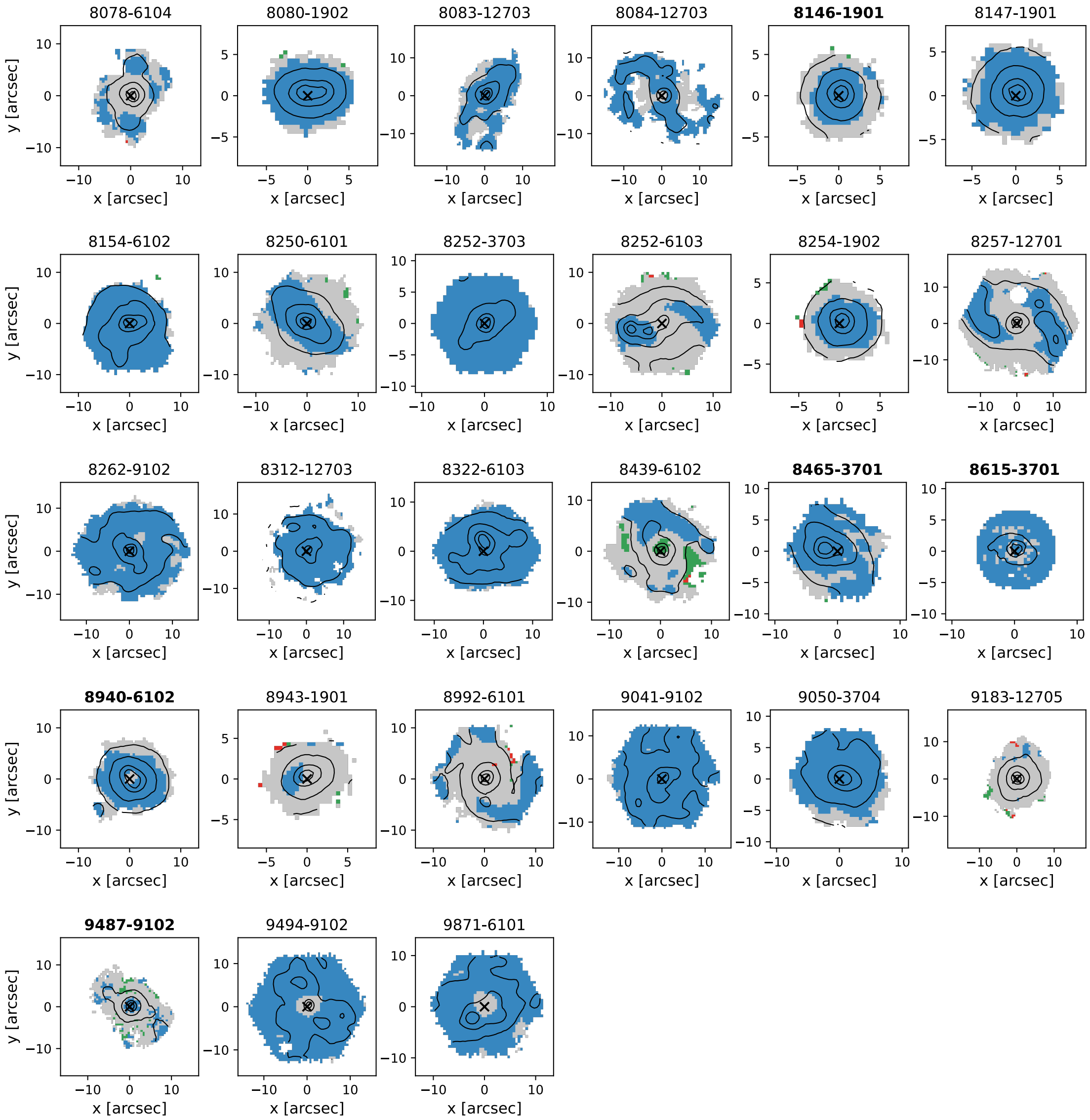

8078-6104 8080-1902 8083-12703 8084-12703 **8146-1901** 8147-1901

8154-6102 8250-6101 8252-3703 8252-6103 8254-1902 8257-12701

8262-9102 8312-12703 8322-6103 8439-6102 **8465-3701** **8615-3701**

8940-6102 8943-1901 8992-6101 9041-9102 9050-3704 9183-12705

9487-9102 9494-9102 9871-6101

Fig. 2.5 *Spatially resolved BPT maps of the 27* He II*-only AGN galaxies resulting from our selection (Sect. 2.1.3.4). Distinct colours identify regions ionised by different mechanisms (Kewley et al., 2001, Kauffmann et al., 2003, Schawinski et al., 2007): star formation (blue), LINER (green), composite processes (grey), and AGN (red, globally absent). Black lines are contour levels of* Hα *line flux corresponding to 1%, 10%, 50% and 80% values of the emission peak, and the black cross marks the galaxy centre. Coloured spaxels are those meeting the S/N threshold (Sect. 2.1.2), and not masked by the MaNGA DAP. Bold labels indicate galaxies whose MaNGA data cubes needed some spectral remodelling (see Table 2.1).*

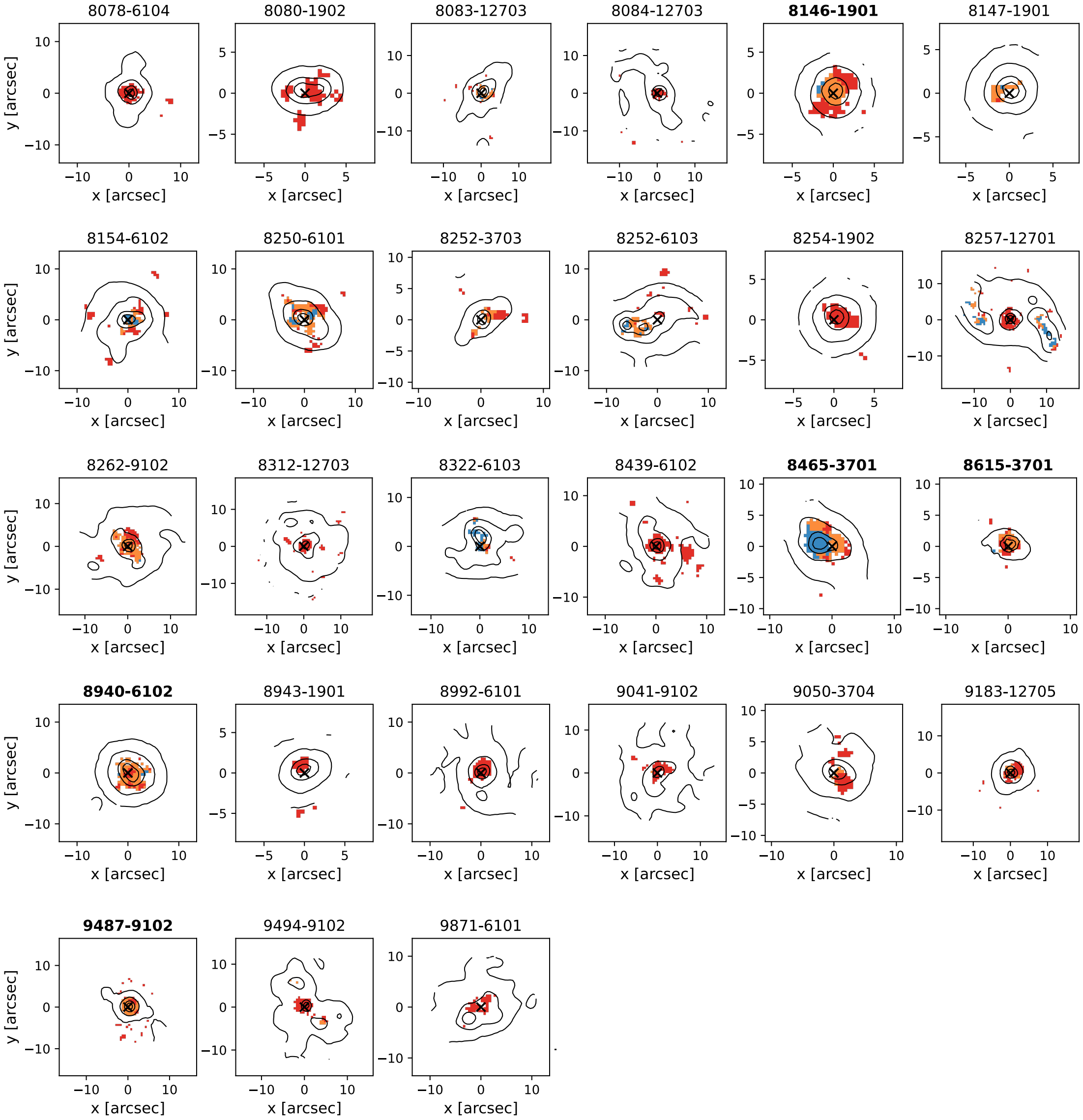

Fig. 2.6 *Spatially resolved* He II *maps of the 27* He II*-only AGN galaxies resulting from our selection (Sect. 2.1.3.4). Distinct colours identify regions ionised by different mechanisms (Shirazi and Brinchmann, 2012): star formation (blue), strong AGN (red, above the 50% curve; see Fig. 2.1 and related text), and weak AGN (orange, above the 10% curve). Black lines, black cross and bold labels have the same meaning as in Fig. 2.5. Coloured spaxels fulfil the S/N threshold (Sect. 2.1.2), and are not masked by the MaNGA DAP.*

Overall, spatially resolved diagnostic maps shown in Figs. 2.5 and 2.6 supports the presence a central AGN and confirms the identification of these objects as He II-only AGN. By crossmatching our sample of He II-only AGN with the AGN catalogue reported by Comerford et al. (2020), we find that 11 out of 27 (41%) He II-only AGN are identified as AGN based on their radio observations (10 objects) and/or mid-IR colours (2), further supporting the use of He II to select AGN missed in usual BPT diagnostics. Moreover, Comerford et al. (2020) classify as AGN also the galaxy 8615-3701, due to the presence of broad emission lines in its SDSS spectrum. This object is indeed one of the MaNGA galaxies we identified as intermediate-type AGN and, for this, fully refitted in Sect. 2.1.3.2.

2.1.4 Verifying the AGN-like nature of He II line emission

We take advantage of the spatially resolved information of MaNGA to verify the AGN-like nature of the detected He II line emission. In Fig. 2.7, we plot the radial distribution (distance from the centre in units of effective radius, R_e) of the AGN-like BPT (lightblue) and He II (grey) spaxels. In agreement with the AGN interpretation, the AGN-like He II emission mainly originates in the galaxy center. In fact, the BPT AGN spaxels are on average at a distance of ~ 1.2 R_e (dashed lightblue line) and located up to ~ 3 R_e from the galaxy centre; while the He II AGN spaxels are exclusively found at shorter distances, where the S/N is high enough to detect He II, with a mean (dashed grey line) and maximum radial distance of ~ 0.56 R_e and ~ 2 R_e, respectively.

As a final check on the correct selection of AGN-like spaxels, hence on the overall identification of He II-only AGN galaxies, in Fig. 2.8 we plot He II/Hβ ratio as a function of equivalent width (EW) of Hβ (left panel), Hα (middle panel) and [O III] (right panel) lines, for all spaxels of He II-only AGN fulfilling the S/N threshold (they are plotted in Fig. 2.6), defined in Sect. 2.1.2. In addition, we show the dependence on the [N II]/Hα ratio using different colourbars according to their He II-based classification as SF (star symbols, blue colourbar), strong AGN (squares, red colourbar), or weak AGN (triangles, yellow-to-orange colourbar). The He II/Hβ ratios overall decrease at increasing line EWs, with the largest EWs associated SF spaxels, consistently with EW(Hβ) values inferred for SDSS SF galaxies showing WR signatures (Shirazi and Brinchmann, 2012). Such SF spaxels, featured by low-He II/Hβ and high-EW values, also exhibit the lowest [N II]/Hα ratios in agreement with those typical of SF galaxies (Cid Fernandes et al., 2011). In addition to have higher He II/Hβ ratios (as already pointed out by the He II diagram), AGN spaxels are instead overall characterised by larger EW(Hα) (> 10 Å) and higher [N II]/Hα ratios (log([N II]/Hα) $\gtrsim -0.4$), consistently with the AGN classification by Cid Fernandes et al. (2011). The few

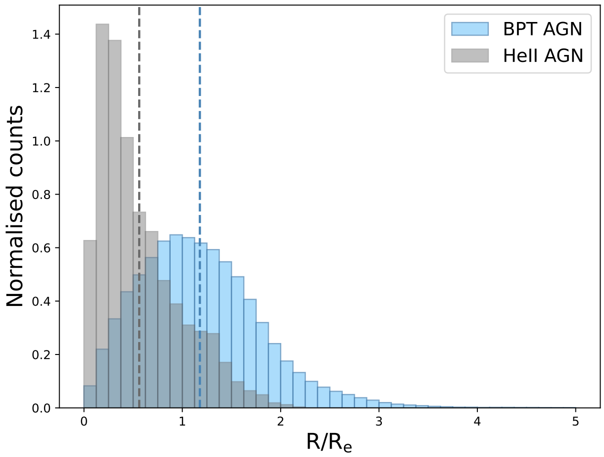

Fig. 2.7 *Normalised distributions of radial distance (in units of effective radius, R_e) from the galaxy centre for the spaxels separately classified as BPT AGN (lightblue) and* He II *AGN (grey). The* He II *AGN spaxels are concentrated in the centre, with a mean radial distance of* $\sim 0.56\ R_e$ *(dashed grey line), compared to the BPT-classified AGN spaxels (*$\sim 1.2\ R_e$*, dashed lightblue line).*

spaxels with slightly lower [N II]/Hα ratios have however too large He II/Hβ ratios to be due to pure star formation.

The right panel (i.e. He II/Hβ against EW([O III])) highlights the existence of a separate population of spaxels at lower values of EW([O III]). Such a spaxel population might either identify cases of AGN nuclear continuum detected to some extent, or central spaxels showing some scattered nuclear emission. We will further investigate this aspect in a future study.

2.2 Properties of the AGN host galaxies

In Fig. 2.9 we plot the star formation rate – stellar mass diagram (SFR – M$_*$; Noeske et al. 2007, Elbaz et al. 2011, Lee et al. 2015), separately for the distinct AGN sub-populations, namely the BPT AGN (left panel, blue points), the He II AGN (middle, red squares) and the He II-only AGN (right, orange triangles) samples, with the grey shading in the background showing the distribution of SDSS galaxies, whose SFR and M$_*$ measurements are taken from the MPA/JHU catalogue[3]. To separate the different regions in the plane of SF, green valley (GV) and quiescent (Q) galaxies, we use the demarcation lines from Hsieh et al. (2017). Measurements of SFR and M$_*$ have been taken from the MaNGA Pipe3D catalogue. In particular, we adopt the integrated SFR estimates derived from single stellar population

---

[3] Available at http://www.mpa-garching.mpg.de/SDSS/DR7/.

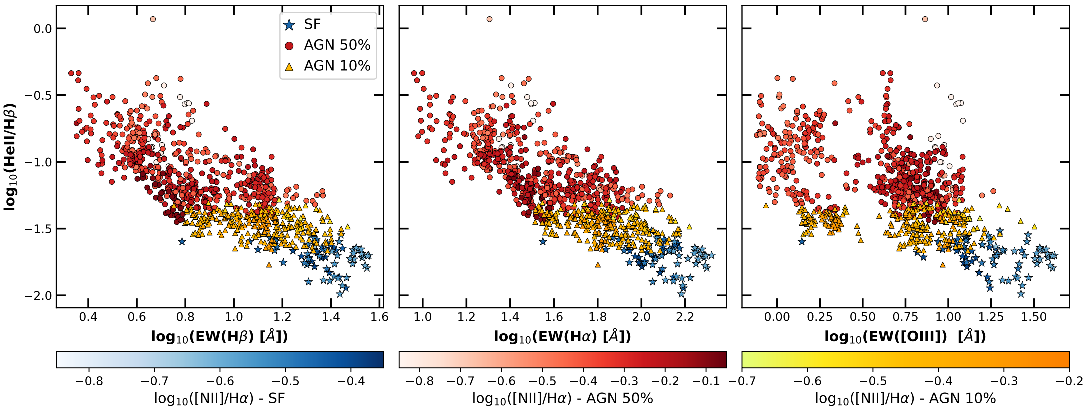

Fig. 2.8 He II/Hβ *ratio as a function of EW(*Hβ*) (left panel), EW(*Hα*) (middle panel) and EW(*[O III]*) (right panel) for all spaxels of* He II*-only AGN (plotted in Fig. 2.6), fulfilling the S/N threshold defined in Sect. 2.1.2. We also show the dependence on the* [N II]/Hα *ratio using different colourbars according to their* He II*-based classification as SF (star symbols, blue colourbar), strong AGN (squares, red colourbar), or weak AGN (triangles, yellow-to-orange colourbar). The* He II/Hβ *ratios overall decrease with line EWs, with the largest EWs found in SF spaxels, consistently with EW(*Hβ*) values inferred for SDSS SFGs showing WR signatures (Shirazi and Brinchmann, 2012). Such low-*He II/Hβ *and high-EW(*Hβ*) SF spaxels also exhibit the lowest* [N II]/Hα *ratios in agreement with those typical of SFGs (Cid Fernandes et al., 2011).*

(SSP) models provided by Pipe3D, which are computed from the amount of stellar mass formed in the last 32 Myr. Since we are dealing with AGN galaxies, SSP-based SFRs are indeed expected to be more accurate than Hα-based SFRs (SSP- and Hα-based SFR values are consistent within 50% for SFGs), given the likely significant AGN contamination to the Hα emission.

Each panel of Fig. 2.9 reports the percentage of AGN galaxies of the respective sub-sample lying in the SF, GV and Q regions. The BPT AGN mainly fall in the GV (45%), with a considerable fraction (29%) of AGN residing in quiescent galaxies. The He II AGN instead tend to lie on the Main Sequence (MS, 74%), although they are still scattered across the GV (25%). Finally, the He II-only AGN exhibit the interesting property of being all in MS galaxies. All these findings are consistent with those obtained by Bär et al. (2017) using single-fiber SDSS measurements. However, it is important to note that our selected He II-only AGN reside in massive galaxies ($M_* \gtrsim 10^{10}$ $M_\odot$). This gives us confidence that we are not including star forming dwarf galaxies, where the AGN presence may be more questionable and the He II emission may originate from different sources, such as hot massive stars in metal-poor systems (e.g. Umeda et al., 2022).

The discovery through the He II diagnostics of an AGN sub-population residing in massive MS galaxies and missed by the BPT classification points to the unique ability of the He II emission line diagnostic to find elusive AGN hosted by actively SF galaxies. This

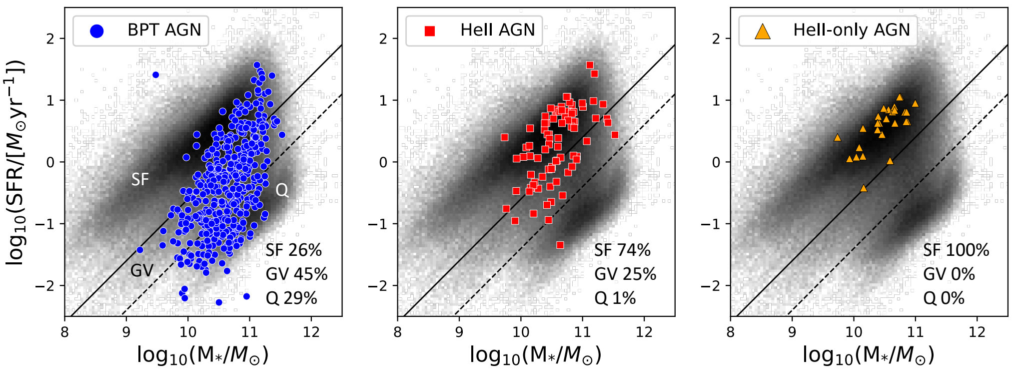

Fig. 2.9 *SFR –* M_* *diagram separately for the different AGN populations: the BPT-selected AGN (left, blue points), the* He II*-selected AGN (middle, red squares) and the* He II*-only AGN (right, orange triangles). The gray shading shows the distribution of SDSS galaxies and the demarcation lines separating SF, GV and Q galaxies are taken from Hsieh et al. (2017). Each panel reports the AGN percentage lying in the three distinct regions. While BPT-selected AGN mostly fall in the GV as found by previous studies, the* He II*-selected AGN are on the SF Main Sequence, with the*He II*-only AGN exclusively residing on the SF Main Sequence.*

hence highlights the possible relevant role of the He II line emission in the systematic rest-frame optical search for AGN especially at very high redshift, where the star formation in MS galaxies is expected to be higher.

In Fig. 2.10 we compare the He II line luminosity ($L_{\mathrm{He\,II}}$) in He II-only AGN to that of BPT&He II AGN selected by both diagnostics. The He II line luminosity (as well as other commonly used lines, such as [O III]) is indeed known to correlate with the AGN intrinsic luminosity as traced, for instance, by their hard X-ray emission (Berney et al., 2015). Therefore, it can be used as a proxy for the AGN luminosity. For this purpose, we compute the total $L_{\mathrm{He\,II}}$ in a given galaxy from the total He II line flux obtained by summing the He II flux contained in S/N(He II)>5 spaxels. Similarly to what obtained in Bär et al. (2017), we find that the He II-only AGN are less luminous than the BPT&He II ones, with a mean He II luminosity (in units of erg s^{-1}) of 39.6 (dashed orange line) and 39.9 (dashed black line) in logarithmic scale, respectively. The mean values inferred in Bär et al. (2017) for SDSS galaxies are larger (40.7 and 41.1, respectively) but also separated by a comparable difference of a few dex. This difference in $L_{\mathrm{He\,II}}$ is likely due to the fact that the SDSS survey spans a higher redshift range and therefore includes, on average, more luminous AGN than MaNGA.

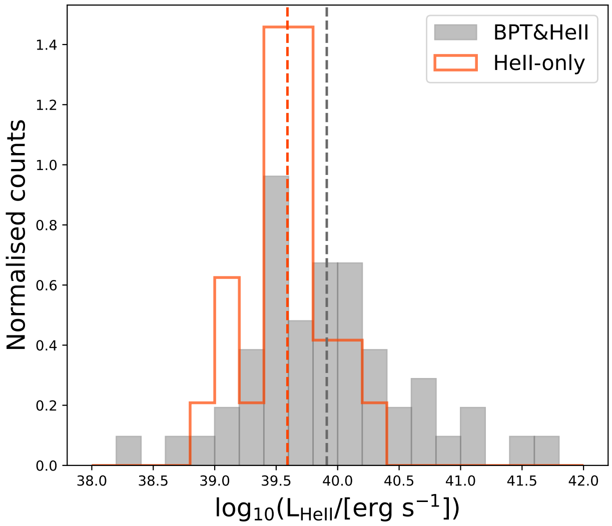

Fig. 2.10 *Normalised histogram of the* He II *line luminosity in the BPT&*He II *(grey-shaded) and* He II*-only AGN (orange line). The resulting mean* He II *luminosity of the two AGN populations are respectively of 39.9 (dashed grey line) and 39.6 (dashed orange) in logarithmic scale.*

2.3 Discussion

2.3.1 Estimating the number of undetected He II-only AGN

Previously, we showed that there are 27 galaxies (i.e. 6% of the total selected AGN sample) classified as AGN only on the basis of the He II diagram. Such He II-only AGN represent about 33% of the overall He II-selected AGN population and, interestingly, reside primarily in massive ($M_* \gtrsim 10^{10}$ $M_\odot$) MS galaxies, where star formation activity plays a primary role as an ionising source. The intense star formation in the galaxy, combined with the low-luminosity nature of these AGN, can therefore lead to the missed BPT-AGN selection. Being more sensitive to AGN emission, the He II diagnostics allows us to unveil this low-luminosity AGN sub-population and to perform a more complete census of the total AGN population.

However, as already mentioned, the main issue related to the use of the He II diagnostics is the faintness of such an emission line. Among our total selected AGN population (459), we indeed detect the He II line in 81 objects only. It is therefore important to estimate how many He II AGN we are missing in the MaNGA sample because of detection limits, so to obtain a less biased estimate of the AGN population. A fraction of this overall undetected He II AGN population is expected to be among the selected BPT AGN which show no He II line emission (cerulean region in Fig. 2.4, 378 objects). Therefore, these

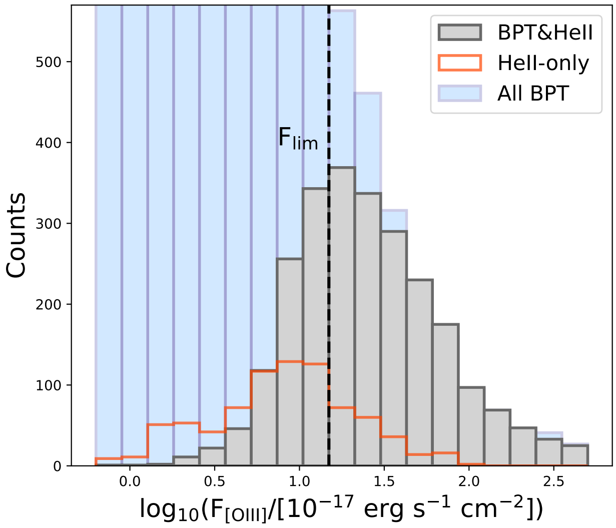

Fig. 2.11 *Distribution of the* [O III] *flux (estimated from the total flux of spaxels at radii* $R < 0.6\ R_e$*) for the different AGN subsamples: both BPT*&He II *classified AGN (filled grey),* He II*-only classified AGN (orange contours), and all BPT-classified AGN (filled lightblue). The vertical, black dashed line represents, for the BPT-classified AGN, the* [O III] *flux adopted as detection limit (*$F^{\rm lim}_{\rm [O\,III]} \sim 1.5 \times 10^{-16}$ *erg s*$^{-1}$ *cm*$^{-2}$*) for them to also have an* He II *detection and AGN classification.*

are already counted in the total AGN census, whereas we want to estimate the number of missing He II-only AGN in MaNGA, not yet included in our total selected AGN sample.

With this aim, we first estimate the MaNGA detection limit for the He II line emission by using the brighter [O III] line emission as a proxy. Figure 2.11 shows the distribution of the [O III] emission line flux contained in single spaxels within a central aperture of radius of 0.6 R_e, separately, for the AGN subsample selected by both diagrams (filled grey histogram; S/N([O III])>3 and S/N(He II)>5), the He II-only AGN population (orange contours; S/N([O III])>3 and S/N(He II)>5), and the overall BPT-selected AGN (filled lightblue; S/N([O III])>3). By comparing the He II-only and BPT&He II distributions, the former is shifted towards smaller values of [O III] flux compared to the latter. This behaviour is expected since in the He II-only AGN the star formation dominates over the AGN, thus producing smaller [O III]/Hβ ratios consistent with ionisation due to star formation. The BPT&He II is coincident with the overall BPT AGN selected population above $\log(F_{\rm [O\,III]}/10^{-17} {\rm erg\ s^{-1}}) > 1.5$. This is interesting, as it indicates that at high [O III] fluxes all BPT-selected AGN are also He II-selected. However, at lower fluxes the two populations start to depart and the BPT&He II distribution shows a clear cutoff at a flux of $F^{\rm lim}_{\rm [O\,III]} < 1.5 \times 10^{-16}$ erg s^{-1} cm^{-2} (vertical black dashed line), while the distribution of all standard BPT AGN keeps increasing to lower [O III] fluxes. The cutoff in the BPT&He II

Table 2.2 *Demography of AGN galaxies included in the BPT-selected (first row) and* He II*-only-selected (second row) AGN subsamples. For each subsample, we report the total number of detected objects, and among these the number below ($N_{\mathrm{below-F_{lim}}}$) and above ($N_{\mathrm{above-F_{lim}}}$) our adopted detection limit ($F_{\mathrm{lim}} = 1.5 \times 10^{-16}$ erg s^{-1} cm^{-2}. We show the total BPT-selected AGN population as sum of two distinct contributions, namely, the BPT&*He II *AGN sample and the BPT AGN with* noHe II *detection (no*He II*).*

	Total detected	-	$N_{\mathrm{below-F_{lim}}}$	$N_{\mathrm{above-F_{lim}}}$
BPT AGN	432	BPT&He II	29	25
		noHe II	376	2
He II-only AGN	27	-	22	5

population is clearly due to the requirement of having He II detected. Therefore, we take the cutoff value (1.5×10^{-16} erg s^{-1} cm^{-2}) as the limiting [O III] flux (F_{lim}) beneath which the He II emission is likely missed because of the sensitivity of MaNGA observations.

To count how many He II-only AGN are missed below this limit, we assume that the ratio of He II-only to all BPT AGN below the [O III] flux limit is the same as above the limit, namely:

$$N^{\mathrm{He\,II-only}}_{\mathrm{below-F_{lim}}} = \frac{N^{\mathrm{He\,II-only}}_{\mathrm{above-F_{lim}}}}{N^{\mathrm{BPT}}_{\mathrm{above-F_{lim}}}} \times N^{\mathrm{BPT}}_{\mathrm{below-F_{lim}}} = 75, \tag{2.1}$$

where $N^{\mathrm{He\,II-only}}_{\mathrm{above-F_{lim}}} = 5$, $N^{\mathrm{BPT}}_{\mathrm{above-F_{lim}}} = 27$, and $N^{\mathrm{BPT}}_{\mathrm{below-F_{lim}}} = 405$, as inferred by comparing for each object the average [O III] flux in spaxels within 0.6 R$_{\mathrm{e}}$ with F_{lim}. The resulting demography is summarised in Table 2.2. Among the 75 He II-only AGN below our adopted limit, 22 are however detected. Therefore, the undetected He II-only AGN below F_{lim} are expected to be 53 in total, thus leading to a final overall AGN sample consisting of 512 galaxies. However, we argue that the estimate of 53 missing He II-only AGN must be considered as a lower limit to the real number, since such value has been inferred under the assumption that the ratio of He II-only AGN to BPT AGN is the same at all stellar masses. Instead, we know that BPT AGN mainly reside in GV and Q galaxies, which are typically more massive than SF Main Sequence galaxies, the primary hosts of He II-only AGN.

2.3.2 Implications for the AGN census and quenching scenarios

As final step of this work, in Fig. 2.12 we study how the AGN demography in the SFR – M$_*$ plane changes with respect to the initial BPT-based census (first bar chart), after the inclusion of the He II-selected AGN (second), and further after the inclusion of the 53 estimated missing He II-only AGN (third). Each bar chart shows percent fraction of

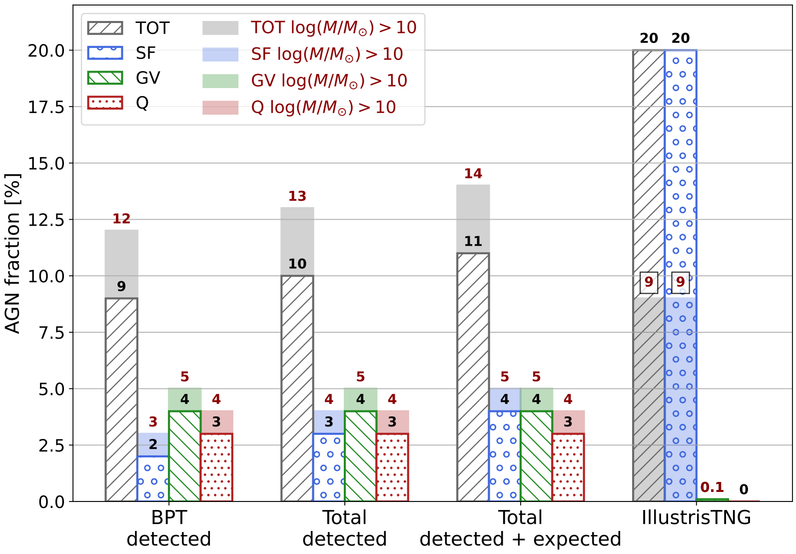

Fig. 2.12 *Bar charts summarising the demography in the SFR – M_* plane of the AGN samples selected by just the BPT (first bar chart), by combining the BPT and* He II *diagnostics (second), and after including the AGN population expected to be missing (53) in the* He II*-only AGN sample because of sensitivity limits (third); finally, the predictions from the IllustrisTNG cosmological simulation (fourth). Each grouped bar chart shows percent fractions, computed with respect to the overall MaNGA sample, of the total AGN (grey) population and, separately, of the AGN residing in SF (blue), GV (green) and Q (red) galaxies. The filled bars (with red labels) represent the same categories but only for the galaxies more massive than $M_* > 10^{10}\ M_\odot$.*

the total AGN population (grey) and, separately, of the SF Main Sequence (blue), GV (green) and Q (red) AGN sub-samples, with respect to the total MaNGA DR15 galaxies (4656). The filled bars represent the same categories but considering only galaxies more massive than $M_* \gtrsim 10^{10}$ M$_\odot$ (3297 massive galaxies in MaNGA DR15), since almost all (93%) He II-only AGN are found in this stellar mass range. With respect to our initial BPT AGN census, the He II diagnostics leads to an increase by 6% and 24% in our total and SF Main Sequence detected AGN samples, respectively, further highlighting the poor BPT efficiency at unveiling AGN in SF galaxies. On the contrary, the GV (4%) and Q (3%) AGN fractions in MaNGA are not affected at all, being all the selected He II-only AGN located on the MS. We assumed the same to be valid for all the 53 He II-only AGN expected to lie below the MaNGA detection limit. The inclusion of these 53 objects entails an increase by about 12% in our total (BPT and/or He II) AGN sample, and by about 38% in our SF (Main Sequence) AGN population. These expected new figures represent 11% and 4% in the overall MaNGA DR15 sample, respectively, corresponding to 14% and 5% for the more massive case ($M_* \gtrsim 10^{10}\ M_\odot$). Overall our new census implies a modest increase in the overall census of AGN with respect to the classical BPT classification (from 9% to 11%), but the number of AGN on the SF Main Sequence is *doubled*.

A substantial number of AGN in SF galaxies compared to GV and Q galaxies points to a picture where significant star formation and BH accretion are coeval, with a large amount of gas simultaneously available for both star formation and BH feeding. Such a correlation between star formation and BH accretion rates is also predicted by cosmological hydrodynamical simulations (Piotrowska et al., 2022, Ward et al., 2022), such as IllustrisTNG (Marinacci et al., 2018, Naiman et al., 2018, Nelson et al., 2018, Pillepich et al., 2018, Springel et al., 2018), SIMBA (Davé et al., 2019) and, to a lesser extent, by EAGLE (Schaye et al., 2015). To illustrate this in our context, in Fig. 2.12 we also show the predictions of IllustrisTNG for the redshift z=0 AGN population (fourth bar chart) for comparison with our observational results. In the simulation, we select as AGN hosts those galaxies with an Eddington ratio $\lambda_{\rm Edd}$ in the top 20% of all Eddington ratios ($\lambda_{\rm Edd} > 0.016$), and classify them in SF, GV and Q galaxies according to the same prescription used with MaNGA data (i.e. Hsieh et al. 2017). When comparing our observational results (first to third bar charts) with the simulation predictions, we can clearly see that the discrepancy in the fraction of total and SF (MS) AGN starts is mitigated only when adding the He II-only AGN to the BPT-selected sample. At the same time, we note that the AGN feedback prescription implemented in IllustrisTNG necessarily dictates an association between high AGN accretion rates and their location on the star forming Main Sequence. In this model, AGN feedback is only successful at suppressing global SFR in galaxies when it switches into the 'kinetic' mode at low accretion rates. In consequence, simulated black holes with high $\lambda_{\rm Edd}$ are expected to almost exclusively reside in galaxies with active star formation.

Finally, we highlight that the existence of a considerable AGN population in SF galaxies compared to GV and Q galaxies can have important implications for AGN quenching scenarios (Schawinski et al., 2009). In fact, the remarkably larger fraction of AGN found in GV and Q galaxies in past studies has always favoured either the scenario in which the AGN phase is long-lived enough (~1 Gyr) to suppress star formation, and then evolve towards the green valley and the red sequence, or the scenario in which AGN are able to immediately quench star formation but becoming detectable only with a delay of about 100 Myr. Our discovery of a substantial AGN population in SF galaxies, instead might suggest the scenario in which AGN do not really quench star formation directly nor instantaneously, but suppress start formation indirectly, on much longer timescales (~1 Gyr) via 'preventative' feedback (Fabian, 2012, Bluck et al., 2020, Trussler et al., 2020, Piotrowska et al., 2022), namely, by injecting energy into the halo, preventing accretion of fresh gas, and hampering star formation as a consequence of starvation.

2.4 Conclusions

We have used the He II diagnostics (Shirazi and Brinchmann, 2012) to detect AGN activity in galaxies observed in the MaNGA survey, hence with spatially-resolved spectroscopy, and compare the resulting population with the AGN detected via the standard BPT diagrams. The main conclusions from our study are summarised below.

1. By comparing the spatially-resolved BPT and He II diagrams of MaNGA spaxels (Fig. 2.1), we find that whereas the He II diagnostics globally recover the BPT AGN classification, only 29% of the He II-selected AGN spaxels are classified as AGN by the BPT diagram.

2. Based on the spaxel classification according to the two diagnostics, we obtain a total sample of 459 AGN host galaxies in MaNGA, out of which 432 (94%) are BPT-selected AGN, whereas 81 (18%) are He II-selected AGN (Fig. 2.4). In the He II AGN sample, 27 objects (6%) are classified as AGN by the He II diagnostics only (He II-only AGN), out of which 11 (41%) are identified as AGN based on radio observations (10) and/or mid-IR colours (2) (Comerford et al., 2020). This further supports the He II diagnostic as useful tracer of AGN missed in usual BPT diagnostics.

3. The He II AGN-like emission is overall centrally located (within 0.6 R_e) in all He II-selected AGN galaxies (Fig. 2.7), thus supporting the AGN-like ionisation of such He II emitting regions. Moreover, the high He II/Hβ and [N II]/Hα ratios combined with large EWs (EW(Hα) > 10 Å) (Fig. 2.8), compared to pure SF galaxies (Cid Fernandes et al., 2011), further supports our correct identification of the 27 He II-only AGN as real active galaxies.

4. All He II-only AGN reside in SF Main Sequence galaxies (Fig. 2.9) and are less luminous than the BPT-selected AGN, on average (Fig. 2.10). These lower-luminosity AGN are overwhelmed by the intense star formation radiation and, therefore, miss the BPT AGN classification. Furthermore, the He II-only AGN are mainly found in massive galaxies ($M_* \gtrsim 10^{10}\ M_\odot$). This rules out the possibility that we are including SF dwarf galaxies, whose He II emission might be due to hot massive stars and X-ray binaries, especially in case of metal-poor environments (Umeda et al., 2022).

5. Being the He II an extremely faint emission line, we expect several more AGN to be below the He II detection limit in MaNGA (Fig. 2.11). Under simplifying assumptions, we estimated a lower limit to the missing population of undetected He II-only AGN (53 objects), all assumed to reside in SF galaxies like the objects we detect.

6. Our inferred, revised AGN census indicates that 11% of galaxies (in MaNGA DR15) host an AGN, of which 4% on the SF Main Sequence, 4% in the Green Valley and 3% in Quiescent galaxies (Fig. 2.12). We note that on the SF Main Sequence the number of AGN is doubled with respect to the simple BPT classification. If we restrict the census to galaxies more massive than $M_* \gtrsim 10^{10}\ M_\odot$, then we infer that the AGN population rises to 14%, of which 5% on the SF Main Sequence, with the the Green Valley (5%) and Quiescent (4%) AGN populations unaffected.

7. The presence of a substantial number of AGN in SF galaxies compared to GV and Q galaxies is consistent with expectations of cosmological simulations (Piotrowska et al., 2022, Ward et al., 2022). It may also have important implications on quenching scenarios, possibly supporting the picture where AGN feedback on star formation is not instantaneous (i.e. inefficiency of the ejective mode) but, if anything, has a delayed, preventive quenching effect, likely via halo heating.

With a view to exploring high redshifts at unprecedented high resolution and sensitivity with *JWST* and upcoming VLT facilities (ERIS and MOONS), novel emission-line diagnostics are fundamental to investigate the ionisation conditions of the high-redshift Universe, featured by highly SF and/or metal-poor environments. As our observational study has demonstrated for actively SF galaxies, photoionisation models (Nakajima and Maiolino, 2022) also show that BPT are likely to incorrectly identify the dominant ionisation mechanism in metal-poor galaxies at $z \gtrsim 4-5$, highlighting instead the efficiency of optical He IIλ4686 and UV He IIλ1640. The crucial role of He II diagnostic in the search for hidden AGN at high redshift is indeed confirmed by first *JWST/NIRSpec* observations in $z > 3$ galaxies, exhibiting prominent He II line emission which reveals their AGN nature (Maiolino et al., 2023b, Perna et al., 2023, Übler et al., 2023). Finally, we point out the greater feasibility of the He II diagnostics compared to other BPT-alternative AGN tracers, such as the rarer and fainter optical coronal lines (e.g. [Ar X]λ5533, [S XII]λ7609, [Fe XI]λ7982, [Fe XIV]λ5303; Gelbord et al. 2009, Molina et al. 2021, Negus et al. 2021, 2023, Reefe et al. 2022).

Chapter 3

The optically elusive, changing-look active nucleus in NGC 4156

This chapter reports on the discovery of the optical CL active nucleus of the galaxy NGC 4156, showing how CL transitions can make clearly visible even this well-known optically 'dull' AGN. By comparing optical spectra from different epochs, we observe spectral changes pointing to a double type transition, and speculate on its possible origin. Thanks to the appearing of broad[1] *BLR Hα and Hβ components, we also provide first single-epoch estimates of BH mass, bolometric luminosity and Eddington ratio for NGC 4156. Based on data acquired with other undergraduate students of the Università degli Studi di Firenze, at the Telescopio Nazionale Galileo on La Palma (Canary Islands). Adapted from Tozzi et al. (2022), A&A, 667, L12.*

As reviewed in Sect. 1.1.2, AGN galaxies are commonly classified into type-1 and type-2 systems, depending on the presence or not of broad BLR emission lines (FWHM > 2000 km s^{-1}) in their optical spectra. According to the standard AGN model (Sect. 1.1.2.1), these two AGN classes are are consequence of a dusty and gaseous torus differently oriented towards the observer, which shields BLR emission in type-2 (obscured) AGN but not in type-1 (unobscured) AGN (Antonucci, 1993, Netzer, 2015). Intermediate types (1.5 or 1.8) can then result from the combination of viewing angles and a clumpy distribution of the obscuring material of different optical depths (Goodrich, 1989).

In recent years, the discovery of an increasing number of CL AGN undergoing type transitions within a few years or months has highlighted the limits of the standard paradigm (Sect. 1.1.2.3). In the optical, CL AGN are typically identified through the appearance

---

[1] In this chapter, the adjective 'broad' always refers to broad-line emission (FWHM > 2000 km s^{-1}), originating in the AGN BLR, as opposed to 'narrow' indicating narrow-line emission from AGN NLR.

(disappearance) of broad BLR components in Hα and Hβ line profiles in previously known type-2 (type-1) AGN (e.g. Denney et al. 2014, Shappee et al. 2014, Raimundo et al. 2019). The local Seyfert NGC 1566 is one of the first CL AGN ever discovered (Pastoriza and Gerola, 1970). Its variability has been widely studied from the optical, to the UV and X-ray energies, revealing a dramatic variability of emission line profiles and recurrent brightening events (Alloin et al., 1986, da Silva et al., 2017, Oknyansky et al., 2019, Oknyansky, 2022). The changing state of NGC 1566 was interpreted as the result of a luminosity increase, which causes the sublimation of dust in the line of sight, previously obscuring part of the BLR. However, in spite of the increasing number of newly discovered CL AGN (a few tens), the physical mechanism at their origin is still under debate.

In this chapter, we present the serendipitous discovery of the galaxy NGC 4156 as a new intriguing CL AGN. NGC 4156 is a face-on, barred spiral galaxy (SBc; Nieto and Tiennot 1984) at $z = 0.0226$ (for a luminosity distance of 100 Mpc, Alam et al. 2015), whose AGN nature is implied by X-ray observations (Elvis et al., 1981, Guainazzi et al., 2005). Based on its optical narrow-line emission, NGC 4156 has been classified as a LINER (low-ionisation nuclear emission-line region; Kennicutt 1992, Nisbet and Best 2016) galaxy, with no definitive optical AGN signatures. In particular, the SDSS Data Release 6 (Adelman-McCarthy et al., 2008) spectrum of NGC 4156, taken in 2004, is devoid of both a bright AGN continuum and broad Hα and Hβ components. The mass of the supermassive BH in NGC 4156 is estimated to be $\log(M_{\rm BH}/{\rm M}_\odot) \approx 7.7$ (Nisbet and Best, 2016) via the $M_{\rm BH} - \sigma_*$ relation (McConnell and Ma, 2013), with the stellar velocity dispersion σ_* measured in the SDSS data ($\sigma_* = 155.2\,{\rm km\,s^{-1}}$). Radio emission from NGC 4156 was also detected during the Very Large Array (VLA) FIRST survey (Wadadekar, 2004), with a radio flux density at an observed frequency $\nu_{\rm obs} = 1.4$ GHz of 2.93 mJy, corresponding to a radio luminosity $L_{1.4\,{\rm GHz}} \approx 10^{37.7}\,{\rm erg\,s^{-1}}$. The radio source is estimated to lie 1.04$''$ apart from the AGN location (Wadadekar, 2004).

Elvis et al. (1981) was the first to report the detection by the Einstein Observatory High Resolution Imager of compact, probably variable, X-ray emission of roughly 10^{42} erg s^{-1} in the optically ‘dull’ NGC 4156 galaxy. The optical spectrum taken with the Multiple Mirror Telescope was displaying the weakest emission line fluxes of any known X-ray active galaxy at that time but a H$\beta/L_{\rm X}$ ratio, however, was observed to be consistent with previous results.

In April 2019, we observed NGC 4156 within an observing campaign led by undergraduate students of the University of Florence (UNIFI, Italy) at the Telescopio Nazionale Galileo (TNG) located at the Roque de Los Muchachos (La Palma, Canary Islands). The optical spectrum acquired with the spectrograph DOLORES (Device Optimized for the

LOw RESolution) has given the first clues about the ongoing state transition of NGC 4156 from a type-2 towards a type-1 AGN (see Fig. 3.1). Therefore, new TNG/DOLORES observations of NGC 4156 have been recently performed (PI: E. Lusso), with longer exposure times and at higher spectral resolution, aimed at confirming the CL AGN nature of NGC 4156 and at robustly modelling the broad-line component of Hα and Hβ to estimate the BH mass and the accretion rate of the source. This chapter presents these TNG/DOLORES observations obtained in 2019 and 2022, which together lead to the discovery of NGC 4156 undergoing a double changing-look transition: first, from a type-2 (in 2004) towards a type-1 (i.e. type-1.5 in 2019), and then backwards towards a type-2 (i.e. type-1.8 in 2022).

3.1 TNG/DOLORES observations of NGC 4156

First TNG/DOLORES observations of NGC 4156 were carried out on April 28th 2019, as part of a multi-year campaign planned and performed by UNIFI undergraduate students in Physics and Astronomy, within a course of introductory observational astrophysics (Lusso et al., 2022) I took part in during my Master's studies. To date, this program has targeted 89 nearby ($z < 0.2$), bright active and non-active spiral galaxies to perform both imaging and low-resolution spectroscopy with different facilities. Since 2010, 74 galaxies have been observed at the 1.5m Cassini telescope in Loiano (operated by the INAF Bologna, Italy), 2 at the 1.8m Copernico telescope in Asiago-Ekar (INAF Padova, Italy), and 13 at the 3.6m TNG telescope. These observations aimed at measuring galaxies' apparent diameter (from imaging) and redshift (from spectroscopy), to estimate the Hubble parameter H_0. Additional goals were to get estimates of SFR and $M_{\rm BH}$, in case of AGN galaxies.

Within this observing program, we acquired spectroscopy of NGC 4156 with DOLORES using the low-resolution LR-B grism ($R \sim 580$), covering the wavelength range 3000–8400 Å. In these observations, NGC 4156 was targeted together with the brighter, nearby galaxy NGC 4151, by placing the $1''$-slit along the direction joining the two nuclei, with an exposure time (300 s) tailored to the latter, the primary (brighter) target of the observations. The seeing varied between $0.5''$ and $1.5''$.

Whereas NGC 4151 data were reduced in 2019 immediately (showing no unexpected features), the first data reduction for NGC 4156 was performed in 2022, revealing unexpected hints on its transition from a type-2 to a type-1 AGN. After such a discovery, we followed up the galaxy on May 28th 2022 with DOLORES using the $1.5''$ slit and two different spectral setups: (i) LR-B grism with an exposure time of 1200 seconds; (ii) VHR-R grism (6300–7700 Å; $R \sim 2500$) with exposure time of 1800 seconds. The average seeing was $1.5''$.

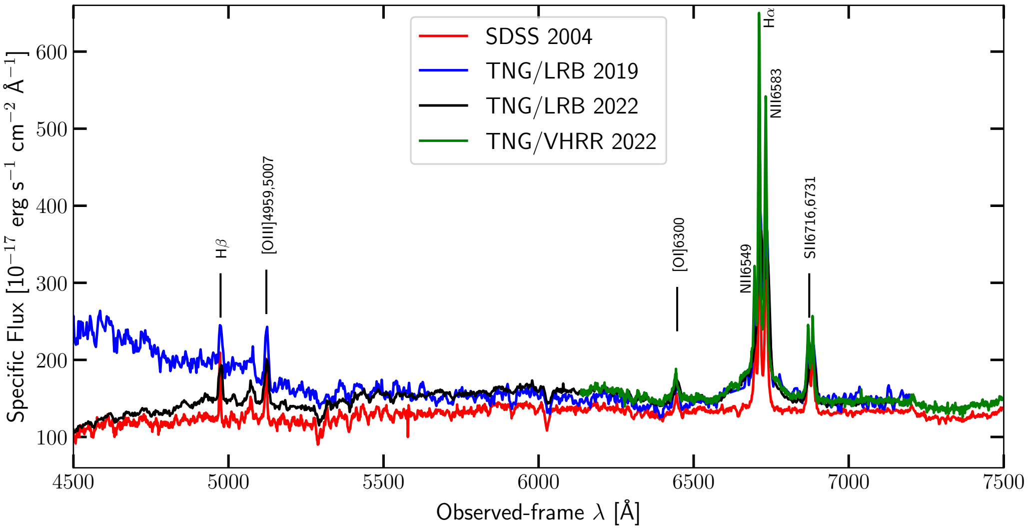

Fig. 3.1 *Comparison of the SDSS 2004 spectrum (red) with the spectra acquired at the TNG. The TNG/LR-B data observed in 2019 and 2022 are represented by blue and black lines, respectively; while the TNG/VHR-R 2022 spectrum by a green line. Data are shown in the observed frame.*

3.1.1 Data reduction

We reduced the LR-B TNG spectra of NGC 4156 taken in 2019 and 2022 with the open source data reduction pipeline PypeIt (Prochaska et al., 2020, 2022, v1.9). The data reduction follows the standard procedure, including bias subtraction and flat fielding, removal of cosmic rays, sky subtraction, extraction of the 1D spectrum and wavelength calibration. Wavelength calibration was derived from the combined helium, neon and mercury arc-lamps in the vacuum frame, and a quadratic polynomial function was used to fit the pixel-wavelength data. The resulting dispersion from the wavelength calibration is $\Delta\lambda = 2.72$ Å/pixel for both spectra with an rms < 0.1 pixel and ≈ 0.15 pixel for the 2019 and 2022 data sets, respectively. The nuclear integrated spectra were extracted using a pseudo-slit of $1.5'' \times 4''$ centered on the galaxy centre (PA = 39° and PA = 0° for the 2019 and 2022 data, respectively). A standard star with known spectral type was observed during both the 2019 (HD 121409) and 2022 (Feige 66) observing nights to account for telluric absorption and flux calibration, whose data were reduced with the same pipeline.

The reduction of the VHR-R data was performed with a custom-made pipeline, since this grism is not currently supported in PypeIt. The custom pipeline uses some routines from MAAT (MATLAB Astronomy and Astrophysics Toolbox, Ofek, 2014). It includes all the standard corrections listed above for PypeIt. The wavelength calibration was performed as for the LR-B data. The resulting dispersion is $\Delta\lambda = 0.78$ Å/pixel. The telluric correction and the flux calibration were performed with the IDL software XTELLCORR (Vacca et al., 2003). The nuclear integrated spectrum was extracted using a pseudo-slit of 1.5″ × 4″ centered on the galaxy center (PA = 0°). To test the robustness of our pipeline, we also reduced the 2019 and 2022 LR-B data, obtaining results fully consistent with the PypeIt output.

The final 1D TNG LR-B and VHR-R observed spectra are shown in Fig. 3.1 together with the archival SDSS data. From a first visual comparison, the TNG/2019 spectrum clearly shows a broad Hα component (FWHM≈4000 km s^{-1}) unlike the SDSS spectrum, and a similar broad component seems to be present for the Hβ emission line as well. Additionally, the TNG/2019 spectrum displays a rise of the continuum at $\lambda < 5500$ Å, likely due to thermal emission from the accretion disc around the supermassive BH. Interestingly, the rising continuum is no longer detected in the TNG/2022 data, whilst the broad Hα component is still clearly observed. We will discuss these results in Sect. 3.4.

3.2 Spectral analysis

We fit the four 1D spectra of NGC 4156 (i.e. the SDSS 2004, the TNG/LR-B 2019, and the TNG/LR-B and VHR-R 2022) with both our fitting code (described in Sect. 1.3.3, here employed in a simplified version to handle single 1D spectra) and `QSFit` (Calderone et al., 2017). Specifically, the SDSS data and the two LR-B spectra are fitted over the wavelength range 4500–8000 Å, while the VHR-R one over the range 6250–6800 Å. Being the results obtained from the two fitting algorithms fully consistent, we adopt the best-fit results from our fitting code, which allows to fix emission-line components of different lines to the same kinematics (useful to model broad-line emission; see Sect. 3.2.1).

As described in Sect. 1.3.3, we first model full spectra with `pPXF` (Cappellari and Emsellem, 2004, Cappellari, 2017), building dedicated templates for the various spectral components: namely, stellar continuum, AGN continuum, and emission lines from the AGN BLR and NLR. After that, we subtract from the data the overall continuum (i.e. stellar and AGN continuum) and BLR emission, and perform a more accurate modelling of narrow emission lines only, aiming at checking whether narrow-line emission is subject to variability as well. Details on the two steps of the spectral modelling are provided below.

Figures 3.2–3.5 show the best-fit modelling of the four available full spectra: data are shown in black, with the total best-fit model and individual model components drawn on top in red and different colours (see plot legend), respectively. In all spectra, we model the stellar continuum (orange) using the MILES extended stellar population models (Röck et al., 2016); whereas we employ the semi-analytic templates of Kovačević et al. (2010) to reproduce broad Fe II emission lines (light green) originating in the AGN BLR, when

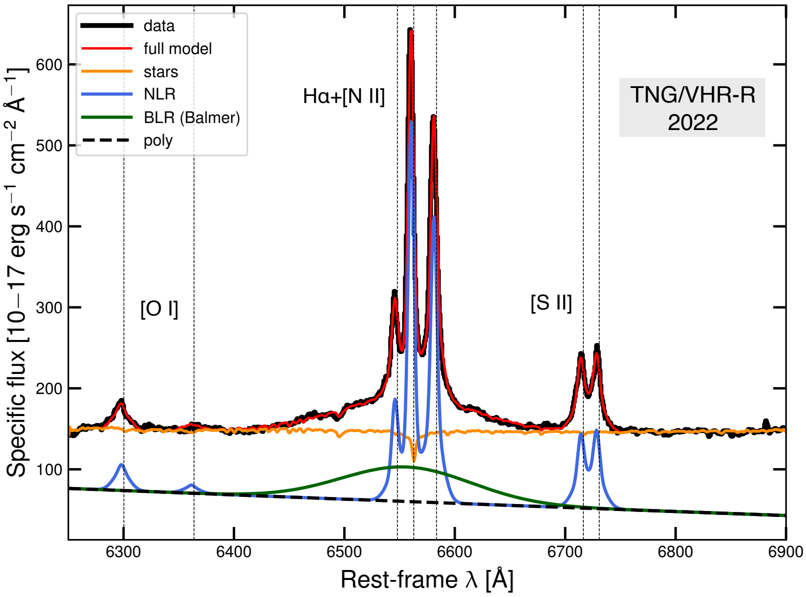

Fig. 3.2 *Best-fit modelling with `pPXF` of the full TNG/VHR-R spectrum of NGC 4156. Data are shown as solid black line along with the full best-fit model (red) and the separate models for each spectral component (different colours, see the legend). A 1st-degree polynomial is here used to reproduce the AGN contribution to the continuum emission.*

detected. As shown in Fig. 3.3, a prominent Fe II component is required to properly model the steep increase of the continuum emission in the bluest part of the LR-B 2019 spectrum, but it is absent in the other spectra, except for a paltry contribution to the total emission around 5300Å in the LR-B 2022 spectrum (Fig. 3.4).

As mentioned in Sect. 1.3.3, `pPXF` gives the possibility of including an additive nth-degree polynomial to either adjust the continuum shape to the observed data, or account for any additional continuum component. Whereas a 1st-degree polynomial is sufficient to properly reproduce the faint AGN continuum in the SDSS and VHR-R spectra (black dashed line in Figs. 3.5 and 3.2, respectively), it is not appropriate for the steeply rising continuum in the bluest part of the 2019 spectrum (see Fig. 3.3). Therefore, we specifically create a set of broken power law templates with independently-variable slopes ($F_\lambda \propto \lambda^\alpha$, with $-3.5 < \alpha_1, \alpha_2 < 0$). To reduce the number of templates, we fix the break point of all templates to 5800 Å, as resulting from the 2019 best-fit obtained with `QSFit`. In the LR-B 2022 data instead, the AGN continuum cannot be well constrained, being overwhelmed by the almost flat stellar continuum over the entire wavelength range 4500–8000 Å (Fig. 3.4). Nonetheless, we expect an AGN continuum component to be present as well, since the LR-B 2022 continuum remains at a higher flux level with respect to the SDSS 2004 one (see Fig. 3.1), which cannot be due to a variation in the stellar component. The comparison

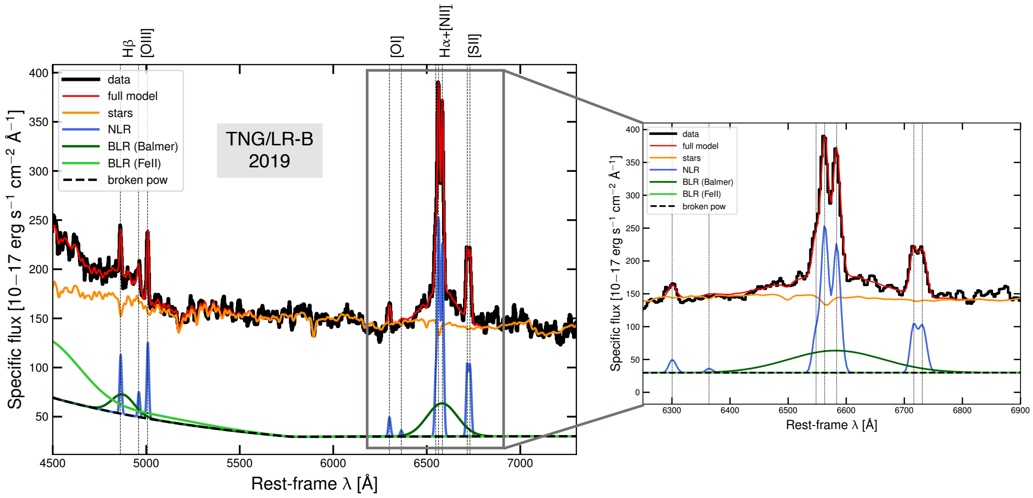

Fig. 3.3 *Left. Same as Fig. 3.2 for the TNG/LR-B 2019 spectrum. A broken power law (black dashed line) has been here used to approximate the AGN continuum. Right. Zoom-in over the spectral window 6250–6900 Å around the Hα line.*

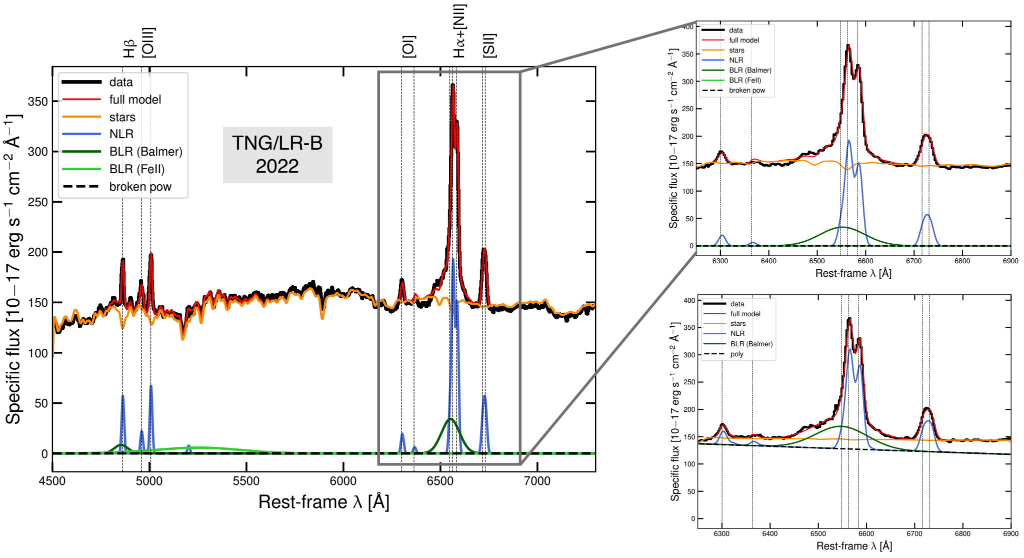

Fig. 3.4 *Left. Same as Fig. 3.2 for the TNG/LR-B 2022 spectrum. The AGN continuum is totally unconstrained and overwhelmed by the host galaxy emission. Upper right. Zoom-in over the spectral window 6250–6900 Å around the Hα line. Lower right. Best-fit results from the re-modelling over the narrower wavelength range (i.e. 6250–6900 Å) of the VHR-R data. The comparison between the two right panels shows how sensitive the broad components are to the continuum level (see Sect. 3.2.1), which in turns strongly depends on the spectral range selected for the fit.*

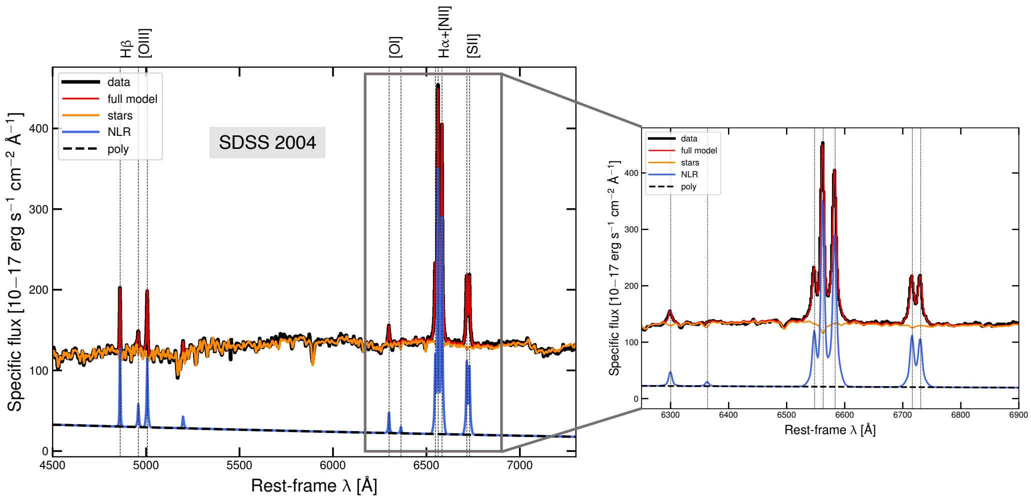

Fig. 3.5 *Left. Same as Fig. 3.2 for the SDSS 2004 spectrum. A slight 1st-degree polynomial (dashed black line) is fitted to the weak AGN continuum, while no BLR components are detected. Right. Zoom-in over the spectral window 6250–6900 Å around the Hα line, clearly showing the total absence of a broad Hα component.*

between the 2022 LR-B and VHR-R best-fit results for the AGN continuum further points out the degeneracy of this template in the 2022 data, especially its strong dependence on the fitted wavelength range (cfr. Figs. 3.2 and 3.4).

The main emission lines detected in the covered wavelength range are the Balmer hydrogen lines Hα and Hβ, and the forbidden lines [O III]$\lambda\lambda$4959,5007, [O I]$\lambda\lambda$6300,64, [N II]$\lambda\lambda$6549,83, and [S II]$\lambda\lambda$6716,31. In this chapter hereafter, we will refer to the brighter doublet component (i.e. [O III]λ5007, [O I]λ6300 and [N II]λ6583) as [O III], [O I] and [N II], respectively. Two narrow (σ of a few hundreds km s^{-1}) Gaussian components are necessary to properly reproduce the NLR contribution to each emission line (lightblue line); whereas an additional broad ($\sigma > 2000$ km s^{-1}) Gaussian component is included to account for any possible BLR contribution to the Hα and Hβ line profiles (dark green line; not present at all in the SDSS spectrum, Fig. 3.5). Each set of (broad or narrow) Gaussian components is constrained to have the same kinematics (i.e. same v and σ).

In Tables 3.1-3.4, we summarise the main line-emission properties for the four examined optical spectra of NGC 4156, as inferred from our spectral analysis: observed flux F, equivalent width (EW) and velocity dispersion σ. All best-fit parameters are shown along with their statistical errors resulting from the fit, which are likely to underestimate the real uncertainty. This is true especially for the broad Hα and Hβ measurements (Table 3.1), which strongly depend on the best-fit model of continuum emission (discussed in Sect. 3.2.1).

Table 3.1 *Observed flux, EW and σ of broad BLR Hα and Hβ components, as resulting from our modelling of the full spectra with* pPXF. *The row '2022/LR-B†' lists the parameters for the broad Hα obtained from the re-modelling of the LR-B 2022 spectrum over the VHR-R wavelength range (i.e. 6250–6900 Å).*

Year	$F^{\rm B}_{\rm H\beta}$ [10^{-15} erg s^{-1} cm^{-2}]	$\rm EW^{B}_{H\beta}$ [Å]	$F^{\rm B}_{\rm H\alpha}$ [10^{-15} erg s^{-1} cm^{-2}]	$\rm EW^{B}_{H\alpha}$ [Å]	$\sigma^{\rm B}_{\rm H\alpha,\beta}$ [km s^{-1}]
2004/SDSS	-	-	-	-	-
2019/LR-B	37.1±0.2	22.2±0.4	62.6±0.2	42.0±0.7	3690±16
2022/LR-B	9.2±0.3	6.5±0.6	37.1±0.4	24±2	2110±30
2022/LR-B†	-	-	56.8±0.4	38±4	2460±30
2022/VHR-R	-	-	64.6±0.2	42.9±0.3	2694±17

3.2.1 Modelling of broad-line emission

In Table 3.1, we list the main properties inferred for the broad BLR components of Hα and Hβ emission lines. By comparing results obtained for the two 2022 spectra, we notice that the broad Hα flux and EW values measured in the VHR-R 2022 spectrum are larger by a factor of ~1.7 than the corresponding LR-B 2022 values. Such a difference is due to the different resolution and fitted wavelength range. The higher-resolution VHR-R data indeed allow us to detect and model even the shallower wings of the broad Hα, and also to better decompose the Hα+[N II] line complex. In fact, by re-modelling the LR-B 2022 spectrum only over the VHR-R wavelength range (i.e. 6250–6900 Å; see lower right panel of Fig. 3.4), we obtained a best-fit globally similar to the VHR-R one: the level of the AGN continuum has changed, being now reproduced by a similar 1st-degree polynomial, and the broad Hα component has become consistent with its corresponding VHR-R counterpart. The best-fit results for the broad Hα from this re-modelling are labelled as 2022/LR-B† in Table 3.1. This simple check demonstrates how sensitive the broad BLR components are to the level of the total continuum, which in turn strongly depends on the fitted wavelength range (compare the right panels of Fig. 3.4).

On other hand, the 2022 broad Hβ flux is smaller by a factor of ~4 than in 2019 (consequently, the EW as well). This apparent dimming is likely consequence of degeneracy effects between the faint broad Hβ and the other spectral components (such as Fe II) which significantly contribute in the Hβ wavelength range. These are mainly the AGN continuum and Fe II emission in the 2019 spectrum; and the stellar continuum in the LR-B 2022 data. Moreover, the modelling of the faint broad Hβ is further complicated by dust extinction, expected to affect the Hβ wavelength range more than that around Hα, which is also intrinsically brighter than Hβ. Constraining the broad Hβ to the same kinematics of the brighter, broad Hα helped us better disentangle the broad Hβ component, although it has not solved the problem definitely. In fact, it is likely that we have overestimated

Table 3.2 *Observed flux, EW and σ of the NLR emission in Hα and Hβ profiles, as inferred from our refined modelling of the subtracted spectra (Sect. 3.2.2).*

Year	$F^{\rm N}_{\rm H\beta}$ [10^{-15} erg s^{-1} cm^{-2}]	$\rm EW^{N}_{H\beta}$ [Å]	$\sigma^{\rm N}_{\rm H\beta}$ [km s^{-1}]	$F^{\rm N}_{\rm H\alpha}$ [10^{-15} erg s^{-1} cm^{-2}]	$\rm EW^{N}_{H\alpha}$ [Å]	$\sigma^{\rm N}_{\rm H\alpha}$ [km s^{-1}]
2004/SDSS	6.2±0.3	5.1±0.2	220±10	28.5±0.6	21.4±0.3	230±10
2019/LR-B	8±3	4.8±0.1	310±40	36±11	24.3±0.3	300±40
2022/LR-B	8.9±1.6	6.3±0.1	360±90	32±5	21±6	310±90
2022/VHR-R	-	-	-	37.4±0.6	24.8±0.1	220±10

Table 3.3 *Same as Table 3.2 for the [O III] emission line.*

Year	$F_{\rm [O\,III]}$ [10^{-15} erg s^{-1} cm^{-2}]	$\rm EW_{[O\,III]}$ [Å]	$\sigma_{\rm [O\,III]}$ [km s^{-1}]
2004/SDSS	7.6±0.3	6.2±0.4	290±10
2019/LR-B	10.6±3	6.3±0.1	310±40
2022/LR-B	12±2	8.4±0.1	440±90
2022/VHR-R	-	-	-

the 2019 broad Hβ flux, as suggested by the unreliably small value of the broad Balmer Decrement (BD; $[{\rm H}\alpha/{\rm H}\beta]^{\rm B,2019} \sim 1.7$) compared to that computed for the narrow components ($[{\rm H}\alpha/{\rm H}\beta]^{\rm N,2019} = 4.5 \pm 1.4$) and the theoretical one (~ 2.87). Similarly, we caution on the 2022 broad Hβ measurements, although leading to an apparently reasonable value of broad BD ($[{\rm H}\alpha/{\rm H}\beta]^{\rm B,2022} = 4 \pm 2$, which implies a significant level of dust extinction) when combined with the corresponding broad Hα flux.

3.2.2 Modelling of narrow-line emission

To check whether any variability affects the narrow-line emission as well, we rely on the refined modelling of the subtracted spectra (phase III; see 1.3.3), obtained after subtracting the overall continuum and BLR (Fe II and broad Balmer components) emission from the data. As in the first modelling with PPXF, [O III], [O I] and [N II] are fitted as doublets with a fixed flux ratio of 3 between the two components. This refined modelling confirms that

Table 3.4 *Same as Table 3.2 for the main forbidden emission lines within $\Delta\lambda$ =6400–6800 Å.*

Year	$F_{\rm [N\,II]}$ [10^{-15} erg s^{-1} cm^{-2}]	$\rm EW_{[N\,II]}$ [Å]	$\sigma_{\rm [N\,II]}$ [km s^{-1}]	$F_{\rm [S\,II]6716}$ [10^{-15} erg s^{-1} cm^{-2}]	$\rm EW_{[S\,II]6716}$ [Å]	$\sigma_{\rm [S\,II]6716}$ [km s^{-1}]	$F_{\rm [S\,II]6731}$ [10^{-15} erg s^{-1} cm^{-2}]	$\rm EW_{[S\,II]6731}$ [Å]	$\sigma_{\rm [S\,II]6731}$ [km s^{-1}]
2004/SDSS	28.8±0.5	22.0±0.3	280±10	9.1±0.4	7.0±0.3	270±10	9.4±0.4	7.2±0.3	290±10
2019/LR-B	30±10	21.0±0.2	300±40	11±5	7.8±0.1	290±40	11±4	7.9±0.1	300±40
2022/LR-B	29±5	18.7±0.6	360±90	76±2	5.1±0.4	330±90	8±4	5.4±0.7	320±90
2022/VHR-R	34.9±0.4	24.2±0.1	270±10	9.7±0.4	6.7±0.1	290±10	10.7±0.4	7.4±0.1	290±10

two Gaussian components are confirmed to be enough to properly reproduce the narrow-line emission profiles in all spectra except for the LR-B 2022 one, which requires a third component to optimally reproduce simultaneously the narrow profiles of all emission lines. In doing so, we correctly model both a faint blue wing in the [O III] profile and the peak of the blended [S II] doublet, whose two components are instead well resolved in the LR-B 2019 due to the narrower slit (i.e. $1''$ against $1.5''$ in 2022), translating into a higher spectral resolution.

In Tables 3.2-3.4, we show the best-fit results obtained from the refined modelling of narrow-line emission in Hα and Hβ profiles (Table 3.2), as well as in all detected forbidden emission lines (Tables 3.3 and 3.4). Since narrow-line emission has been modelled with multiple Gaussian components, the narrow σ values ($\sigma^{\rm N}$) have been computed as moment-2 of the overall narrow line profile. In contrast with broad-line emission, narrow-line emission is not seen to vary across different epochs (see Sect. 3.3.2).

3.3 Results

The multi-epoch spectroscopic observations of NGC 4156 presented in this chapter has led to the discovery of its nature as CL AGN, as revealed by the appearance of BLR Hα and Hβ components in 2019, which suggests a global transition from a type-2 towards a type-1 since 2004. In addition, the appearing (in 2019) and subsequent disappearing (in 2022) of the blue rising continuum hints at a further evolution backwards to a type-2, overall making this galaxy extremely interesting to study.

The appearance of BLR emission offers us the possibility to infer first single-epoch estimates of fundamental AGN properties such as BH mass ($M_{\rm BH}$), bolometric luminosity ($L_{\rm bol}$), Eddington ratio ($\lambda_{\rm Edd} = L_{\rm bol}/L_{\rm Edd}$), and characteristic radius of the BLR ($R_{\rm BLR}$) using optical spectroscopic data. Considering all the issues related with the modelling of the faint broad Hβ component in low-resolution (LR-B) spectra (discussed in Sect. 3.2.1), all inferred AGN properties rely on the VHR-R measurements of the brighter broad Hα (Sect. 3.3.1). Moreover, all the luminosity/flux values presented in the following are corrected for intrinsic dust extinction (Calzetti et al., 2000): for the 2019 estimates we adopt the 2019 NLR BD ($[{\rm H}\alpha/{\rm H}\beta]^{\rm N,2019} = 4.5 \pm 1.4$), whereas for the 2022 ones the 2022 BLR BD ($[{\rm H}\alpha/{\rm H}\beta]^{\rm B,2022} = 4 \pm 2$). A 50% uncertainty has been considered on the BLR BD value to account for the systematic errors due to the uncertainty on the BLR components, strongly depending on the continuum best-fit (see Sect. 3.2.1). As a consequence, the narrow-line measurements are expected to be affected as well although to a lesser extent (~30% uncertainty assumed on the NLR BD).

3.3.1 Single-epoch estimates of AGN properties

We derive the single-epoch estimate of $M_{\rm BH}$ from the VHR-R 2022 data, whose higher resolution enables more accurate measurements of the broad Hα component. Following the prescription by Greene and Ho (2005), we estimate $M_{\rm BH}$ to be equal to $(1.4 \pm 0.1) \times 10^8$ M$_\odot$ (i.e. $\log(M_{\rm BH}/{\rm M}_\odot) \sim 8.1$) from the VHR-R $\sigma^{\rm B}_{\rm H\alpha}$ ($\simeq 2690$ km s^{-1}) and broad Hα luminosity ($L^{\rm B}_{\rm H\alpha} \sim 1.9 \times 10^{41}$ erg s^{-1}). Such a value is remarkably similar to the one predicted by the $M_{\rm BH} - \sigma_*$ relation based on the SDSS data.

For the 2019 and 2022-epoch estimates of $L_{\rm bol}$, we apply an optical bolometric correction at 4400Å of 5.0 (Duras et al., 2020) to the AGN continuum luminosity (λL_{4400}). Given the difficulty in constraining the AGN continuum directly from the spectral modelling (discussed in Sect. 3.2), we compute λL_{4400} by making the following assumption. Since we do not expect that the stellar continuum has varied since 2004, we subtracted the best-fit stellar continuum obtained from the 2004 spectrum to the LRB 2019 and 2022 ones. We then consider any additional emission at 4400 Å as the AGN continuum. From the values of λL_{4400} ($\lambda L^{2019}_{4400} \simeq 4.8 \times 10^{43}$ erg s^{-1} and $\lambda L^{2022}_{4400} \simeq 4.1 \times 10^{42}$ erg s^{-1}), we obtain the bolometric luminosity values of $L^{2019}_{\rm bol} = (2.4 \pm 1.2) \times 10^{44}$ erg s^{-1} and $L^{2022}_{\rm bol} = (2.1 \pm 1.1) \times 10^{43}$ erg s^{-1}, where 50% errors are driven by the uncertainty on the bolometric correction. From the inferred values of $M_{\rm BH}$ and $L_{\rm bol}$, we compute the Eddington ratio corresponding to the epochs 2019 and 2022, $\lambda^{2019}_{\rm Edd} \simeq 0.015$ and $\lambda^{2022}_{\rm Edd} \simeq 0.001$, respectively.

Elitzur et al. (2014) proposed that the AGN broad-line emission follows an evolutionary sequence from type-2 to type-1 (and backwards), through intermediate states, as the supermassive BH accretion rate increases (decreases). Such spectral evolution is described by the parameter $L_{\rm bol}/M^{2/3}_{\rm BH}$ ($L_{\rm bol}$ and $M_{\rm BH}$ in units of erg s^{-1} and M$_\odot$, respectively), where values larger than 35 are typical of BLR emission. From a qualitative comparison with Fig. 1 in Elitzur et al. (2014), we expect NGC 4156 to be compatible with a type-1.2/1.5 in 2019 ($\log(L^{2019}_{\rm bol}/M^{2/3}_{\rm BH}) \simeq 39.0$), whereas more with a type-1.8 in 2022 ($\log(L^{2022}_{\rm bol}/M^{2/3}_{\rm BH}) \simeq 37.9$), given the factor of ~10 of difference between our 2019 and 2022 $L_{\rm bol}$ estimates. The rough type-1.8 classification for the 2022 epoch is also supported by the 2022 value of $L^{\rm B}_{\rm H\alpha} \sim 10^{41}$ erg s^{-1} (Stern and Laor, 2012). This suggests that in 2019 and 2022 we might have observed NGC 4156 in two distinct intermediate phases of its round-trip evolution along the type sequence.

We finally estimate $R_{\rm BLR}$ from the AGN continuum luminosity at 5100 Å (λL_{5100}) via the Hβ reverberation time lag calibrated by Bentz et al. (2013), as

$$\log(R_{\rm BLR}/1\,\text{lt-day}) = 1.527 + 0.533 \log(\lambda L_{5100}/10^{44} {\rm erg\,s^{-1}}), \tag{3.1}$$

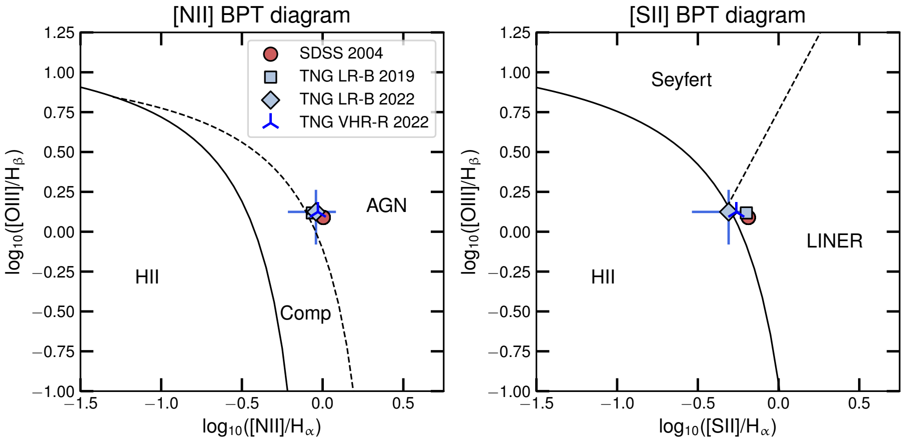

Fig. 3.6 *[N II]- and [S II]-BPT diagrams with line-flux ratio measurements for the 4 spectra of NGC 4156: archival SDSS 2004 (circle) and our TNG LR-B 2019 (square), LR-B 2022 (diamond) and VHR-R 2022 (blue marker) spectra. The VHR-R 2022 points have been obtained by combining the measurements of x-axis and y-axis ratios from the VHR-R and LR-B 2022 spectra, respectively. Solid and dashed black lines, separating between different ionisation regimes, are taken from Kewley et al. (2001, 2006) and Kauffmann et al. (2003). For clarity, we plot only the error bars relative to the TNG/LR-B 2022 measurements, comparable to the TNG/LR-B 2019 ones, while the SDSS 2004 (< 9%) and TNG/VHR-R (< 6%) are too small to be appreciated.*

By taking our best constrained value of λL_{5100}, that is from the 2019 best-fit model of AGN continuum ($\lambda L_{5100} \simeq 1.3 \times 10^{43}$ erg s^{-1}), we find $R_{\rm BLR} \sim 11$ light days. Since the NLR likely extends up to a few hundreds of parsecs (see Eqs. 1, 2 and 3 Bennert et al., 2002), the narrow lines are expected to vary on a timescale much longer than the time frame spanned by these observations (2004–2022), consistently with no significant change observed in the narrow-line emission of NGC 4156 since 2004 (see Sect. 3.3.2).

3.3.2 Constant (ambiguous) narrow-line emission in NGC 4156

As shown in Sect. 3.2.2, no significant variation of narrow-line emission has occurred from 2004 to 2022 as opposed to BLR emission. As a consequence, all narrow-line ratios confirm the previous classification of NGC 4156 as a Seyfert/LINER galaxy (Nisbet and Best, 2016), occupying all the same intermediate region of BPT diagrams (see Fig. 3.6). In Fig. 3.6 we show the [N II]- (left panel) and [S II]-BPT diagrams (right panel) with the line-flux ratio measurements obtained for the 4 available optical spectra: the archival SDSS data, and our TNG spectra acquired in 2019 (LR-B) and 2022 (LR-B and VHR-R). The VHR-R 2022 points combine the measurements of x- and y-axis ratios from the VHR-R and LR-B 2022 spectra, respectively. For clarity of the plots, we only represent the errorbars on the TNG/LR-B 2022 measurements, which are compatible with the LR-B 2019 ones, whereas the SDSS 2004 ($< 9\%$) and TNG/VHR-R 2022 ($< 6\%$) uncertainties on the flux ratios are too small to be appreciated in the two diagrams. The solid and dashed black lines are defined in Kewley et al. (2001, 2006) and Kauffmann et al. (2003), and separate regions in the diagrams dominated by a different source of ionisation. In the [N II]-diagram, all points lie in the AGN region but they are still consistent within the uncertainty with the composite region, where ionisation can be due to either SF (i.e. HII regions) or an AGN, or a combination thereof. The situation is very similar in the [S II]-BPT diagram, with all the 4 measurements compatible with the previous LINER classification, but also consistent with an AGN (Seyfert) or SF as primary ionising source. As a consequence of this inconclusive BPT-based classification, the appearance of broad Hα and Hβ components represent the first clearl optical signatures of the AGN residing in NGC 4156.

3.4 Discussion and conclusions

In this chapter, we have presented our serendipitous discovery of NGC 4156 as a CL AGN, undergoing a double type transition: first, from a type-2 towards a type-1 (1.5 in 2019), and now getting back to a type-2 (1.8 in 2022). Optical TNG data taken in 2019 have indeed revealed the appearance of a BLR component in the Hα and Hβ line profiles, together with a rising blue continuum. The BLR components have been confirmed by our 2022 follow-up observations, whereas the rising continuum has disappeared. In both 2019 and 2022, the broad Hα is bright and well detected, whilst the broad Hβ emission line is barely detected and harder to identify, especially in 2022 (see Sect. 3.2). This suggests that in 2019 and 2022 we have caught NGC 4156 in two intermediate states (Osterbrock, 1981) of its 2-to-1 type round-trip evolution (Elitzur et al., 2014).

The spectral evolution and type transitions observed in the optical over the last twenty years might be the result of variable dust absorption, shielding the central AGN along the line of sight, or changes in the accretion rate. To test the variable absorption scenario, we compute the crossing time ($t_{\rm cross}$) of an intervening screen orbiting the BLR. Assuming a Keplerian orbit of radius $R_{\rm cloud} = 3R_{\rm BLR}$ (LaMassa et al., 2015) and our Hα-based $M_{\rm BH}$ estimate, we obtain $t_{\rm cross} \sim 4$ years. Since NGC 4156 has not yet fully transitioned back to a type-2 in a time of 3 years (i.e. 2019-2022), the shielding of the nucleus seems to be a viable scenario. Even though we have approximated estimates of the NLR BDs in all epochs, such values are not necessarily representative of the BLR extinction, which is unknown in 2004 and 2019, and might also affect the continuum. We can only estimate the 2022 BLR BD, considering a ~50% systematic uncertainty (as discussed at the beginning of Sect. 3.3).

On the other hand, the inferred 2019 and 2022 values of L_{bol} and λ_{Edd} suggest a decreased accretion activity in NGC 4156, which might explain the recent flattening of the continuum emission. Moreover, a systematic analysis of a large number of intermediate-type AGN with $L_{\mathrm{bol}} < 10^{44}$ erg s^{-1} (e.g. Stern and Laor, 2012) has demonstrated that these systems should be classified as low-luminosity unobscured AGN rather than as obscured type-2 objects and, consequently, any observed change possibly ascribed to a variable accretion rate. In spite of the unlikely nature of NGC 4156 as a fully unobscured AGN (BD> 3.5 in all epochs), its 2019/2022 emission is consistent with that of optically-selected type-1 AGN in the $L_{[\mathrm{O\,III}]} - L^{\mathrm{B}}_{\mathrm{H}\alpha}$ plane (Fig. 8 in Stern and Laor, 2012). Except for the 2019 bright phase, the low-luminosity AGN nature of NGC 4156 is also supported by the low contrast between the AGN and the host galaxy, with the latter overwhelming the AGN continuum in 2004 and 2022 data.

Further insights into the observed variability of this source may arise at X-ray energies. At the time of our 2022 TNG follow-up, there were no archival X-ray pointed observations of NGC 4156, which, however, falls in the field of NGC 4151 in 9 different *XMM-Newton* observations (from 2000 to 2012). A preliminary analysis of these data reveals some degree of X-ray variability of NGC 4156. Interestingly, new *XMM-Newton* data (June 2022, PI: E. Lusso) show no clear signs of absorption. Therefore, if absorption is the main responsible for the observed change in the optical, such obscuring material is not attenuating the flux at higher energies. We defer a more detailed analysis of the X-ray properties of NGC 4156 to a dedicated publication.

In conclusion, the discovery of NGC 4156 as a CL AGN makes this galaxy worthy of further investigations. Ongoing optical and X-ray monitoring of this galaxy with the Asiago telescope (PI: L. Casetti) and *XRT-Swift* (PI: R. Middei), respectively, will allow us to constrain the duty cycle of the nuclear activity and to shed light on the mechanism driving the type transition in NGC 4156, clarifying the role played by variable dust absorption. Such a monitoring will also reveal whether (and possibly when) the galaxy will revert to a type-2 AGN. Polarization monitoring campaigns might also bring crucial information on the geometry and composition of the nuclear reprocessing regions as well as on the AGN inclination (e.g. Goodrich, 1989, Hutsemékers et al., 2019, Marin and Hutsemékers, 2020).

Chapter 4

Comparing MUSE and KMOS panoramic IFU spectroscopy of NGC 6240

This chapter presents unpublished results on an ongoing multi-phase IFU study of the local galaxy merger NGC 6240, known to host a double AGN. Combined MUSE Wide Field Mode and KMOS mosaic observations offer an unprecedented panoramic view of the optical and near-IR emitting gas, which allows us to study the properties of multiple gas phases, with a primary focus on ionised and warm molecular gas and their corresponding outflow components. These will be complemented in future with the mapping of the neutral atomic gas phase, and compared with the cold CO-molecular phase studied in previous works.

Merger and interactions of gas-rich galaxies are thought to be crucial triggers for both nuclear activity and starbursts (e.g. Kennicutt and Keel 1984, Norman and Scoville 1988, Barnes and Hernquist 1996, Genzel et al. 1998), thanks to the enormous concentration of gas funneled into the merger nucleus. The resulting starburst and AGN can then also influence each other: winds driven by starbursts can indeed provide the necessary fuel to 'feed' the central accreting BH (e.g. Canalizo and Stockton 2001), and gravitational torques can remove angular momentum from shocked galactic gas (Barnes and Hernquist, 1991, 1996), allowing further accretion of gas on the BH, which finally activates a bright AGN. Most of merging systems are luminous infrared galaxies (e.g. Sanders and Mirabel 1996), with the brightest ones referred to as Ultra-Luminous Infrared Galaxies (ULIRGs; $L_{\rm IR} > 10^{12}$ L$_\odot$), powered by strong starburst (Genzel et al., 1998) and/or AGN (Nardini et al., 2010). While in the local Universe ULIRGs most commonly occur in (rare) gas-rich major mergers (Veilleux et al., 2002), they represent a widely spread population of galaxies at high redshift, where the rate of merging events is higher and the gas reservoir of galaxies larger.

Therefore, ULIRG systems in the local Universe are unique laboratories to get important insight of: ongoing major mergers (so common at high redshift but rare locally), through which galaxies evolve and grow in mass; and the complex and powerful mechanisms featuring systems at the cosmic noon ($z \sim 2$; Madau and Dickinson 2014). Being similar in properties to high-redshift luminous and dusty galaxies, local ULIRGs also offer the opportunity to investigate properties of outflows and their feedback effects on kpc scales. In the past, several works have proven the existence of multi-phase (ionised, neutral, and molecular) outflows in ULIRGs (e.g. Veilleux et al. 2013, Arribas et al. 2014, Cicone et al. 2014, Cazzoli et al. 2016, Fluetsch et al. 2019, 2021), but have mostly focused on a specific gas phase or employed observations at a spatial resolution larger than 1 kpc, not high enough to trace outflows accurately. High-resolution and multi-wavelength observations are therefore necessary to get a detailed, full picture of outflows (e.g. Emonts et al. 2017, Pereira-Santaella et al. 2018, Perna et al. 2020, Cicone et al. 2020; as discussed in Sect. 1.2.3).

Starbursts, AGN radiation, and shocks produced by fast outflows are all mechanisms potentially responsible for gas ionisation and excitation in ULIRGs. In this respect, near-IR observations can potentially greatly enhance the study of the physical conditions of the ISM in these sources. Indeed, being rich of gas, local ULIRGs allow us to detect also near-IR faint H_2 emission lines, tracing warm molecular gas ($T \sim 100$ K), and [Fe II]$\lambda 1.64 \mu$m line emission, one of the main tracer of shock excited gas. Similarly to optical BPT diagrams, differentiating among various gas ionisation mechanisms (see Sect. 1.1.3 and Chapter 2), near-IR emission-line ratios can be combined to investigate excitation properties of warm molecular gas, and to identify the presence of shocks (e.g. Mouri 1994, Larkin et al. 1998, Riffel et al. 2013, Colina et al. 2015), as employed in several works (e.g. Ramos Almeida et al. 2009, Mazzalay et al. 2013, Scharwächter et al. 2013, Maiolino et al. 2017, Riffel et al. 2020, 2021a,b).

Despite the recognised importance of galaxy mergers as discussed above, their complex and short-lived nature prevents us from a clear understanding of the entire process, even at low redshift (i.e. $z < 0.1$). A rare opportunity to study the transient phase between the first encounter and the final coalescence of two interacting galaxies is NGC 6240, one of the most impressive galaxy mergers in the local Universe ($z = 0.02448$; Downes et al. 1993), known to host (at least) a double AGN (see Sect. 4.1 and references therein). This chapter presents unpublished results from an ongoing work, aiming at completing the first study of the large-scale (tens of kpc) kinematics and spatial distribution of ionised, neutral atomic, and warm molecular gas in NGC 6240, by combining archival MUSE Wide Field Mode (WFM) and KMOS mosaic observations at the Very Large Telescope

(VLT). We will study ionisation and excitation gas properties, and trace different gas phase components of outflows. Results from literature on X-ray UFOs (Mizumoto et al., 2019) and CO-based cold molecular outflows (Saito et al., 2018) will be compared to our findings on warm molecular and ionised gas phases, to finally get one of the most completed multi-phase description of AGN outflow achieved so far. In this thesis, we hence present first inferred results on ionised and warm molecular phases, based on MUSE and KMOS IFU observations.

4.1 NGC 6240: a local merger hosting a double AGN

NGC 6240 is considered the prototypical galaxy merger in the local Universe ($z = 0.02448$; Downes et al. 1993), caught in the rare transient phase between the first encounter and the final coalescence of two merging gas-rich spirals (e.g. Fosbury and Wall 1979, Tacconi et al. 1999, Engel et al. 2010). This galaxy has been investigated at all wavelengths (e.g. Max et al. 2005, Feruglio et al. 2013, Nardini et al. 2013, Wang et al. 2014, Scoville et al. 2015, Ilha et al. 2016, Yoshida et al. 2016, Müller-Sánchez et al. 2018, Fabbiano et al. 2020, Treister et al. 2020, Fyhrie et al. 2021, Medling et al. 2021, Paggi et al. 2022).

At a distance of 97 Mpc (Genzel and Cesarsky, 2000), NGC 6240 represents the local counterpart of gas-rich merging galaxies widely populating the high-redshift Universe. With $L_{\mathrm{IR}} \approx 10^{11.8}\ L_{\odot}$ (Wright et al., 1984), NGC 6240 falls just short of the formal limit defining the ULIRG class. *HST* images show a large-scale morphology dominated by tidal arms characteristic for mergers past first passage (Gerssen et al., 2004). Two distinct galaxy nuclei, with a projected separation of about 1 kpc are seen at optical (e.g. Gerssen et al. 2004, Rafanelli et al. 1997, Kollatschny et al. 2020), IR (e.g. Scoville et al. 2000, Koss et al. 2018) and radio wavelengths (e.g. Beswick et al. 2001, Gallimore and Beswick 2004, Max et al. 2007). In the optical through IR, the angular separation between the two nuclei decreases toward longer observing wavelengths, suggesting heavy dust extinction in the nuclear region. Each nucleus has been discovered to host an heavily obscured AGN, detected in hard X-rays with *Chandra* (Komossa et al., 2003), at 5 GHz (Gallimore and Beswick, 2004) and at 3-5 μ (Risaliti et al., 2006, Sani et al., 2008). Yet, Lutz et al. (2003) and Armus et al. (2006) estimate that AGN contribute less than half (perhaps only 25%) of the total luminosity of NGC 6240. To date, we do not know the exact location of the optical/IR counterpart of the two radio AGN, since these are separated by about $1.5''$ (~700; e.g. Max et al. 2007), while the two bright near-IR/optical spots by about $1.8''$ (~900 pc; e.g. Koss et al. 2018).

NGC 6240 presents one of the strongest near-IR H_2 line emission found in any galaxy, with a luminosity $L_{H_2} \sim 10^9 L_\odot$ (Joseph et al., 1984). Several studies have mapped H_2 line emission in the inner (~1 kpc) region (e.g. Tanaka et al. 1991, van der Werf et al. 1993, Sugai et al. 1997, Tecza et al. 2000, Ohyama et al. 2003, Bogdanović et al. 2003, Max et al. 2005, Engel et al. 2010, Ilha et al. 2016), pointing at shock excitation as dominant mechanism. Based on the relative intensity of H_2 and CO(2–1) emission, Ohyama et al. (2003) conjecture that the shocks occur due to a superwind outflowing from the southern nucleus colliding with the molecular gas concentration. Using archival K-band IFU AO-assisted data (acquired with NIFS at the Gemini North telescope), Ilha et al. (2016) found evidence for different H_2 excitation mechanisms taking place: whereas shocks might be dominant between the two nuclei, the H_2 line emission seems to be mainly due to thermal processes in correspondence of and close to both two nuclei, possibly originating from gas heating by X-ray AGN radiation.

4.2 KMOS and MUSE observations of NGC 6240

In this section, we present unpublished H- and K-band KMOS observations (PI: G. Cresci) and archival MUSE WFM of NGC 6240. In Sect. 4.2.1, we also describe the reduction of KMOS datasets, while we took from the ESO archive the MUSE WFM data cube already reduced. Figure 4.1 shows over an optical *HST* image of NGC 6240 the FoV of our H- and K-band KMOS mosaics (32.5″ × 16.3″; red rectangle) and of the archival MUSE WFM data (60″ × 60″; blue square) employed in this work.

4.2.1 Near-IR *H*- and *K*-band KMOS small mosaic

H- and K-band KMOS observations of NGC 6240 were acquired in small mosaic mode (see Fig. 4.1), using the eight available KMOS IFUs to fully map NGC 6240 over a 32.5″ × 16.3″ region (pixel scale of 0.2″), through nine consecutive telescope pointings with H and K gratings, respectively. H- and K-band KMOS grating cover 1.46–1.85 μm and 1.93–2.46 μm, with a spectral resolving power $R \sim 4000$ and $R \sim 4200$, respectively. Part (i.e. two thirds) of K-band observations were acquired in September 2013 (PI: G. Cresci, program ID 60.A-9461(A)) as part of the KMOS Science Verification (SV). The K-band mosaic was then completed in April/May 2015, along with the full acquisition of the H-band mosaic (PI: G. Cresci, program ID 0.95.B-0145(A)). The nine consecutive pointings composing each KMOS mosaic were obtained in two integrations of 380 sec (for a total of 760 sec) with the H-band grating, and a single integration of 720 sec in K band. Within each observing

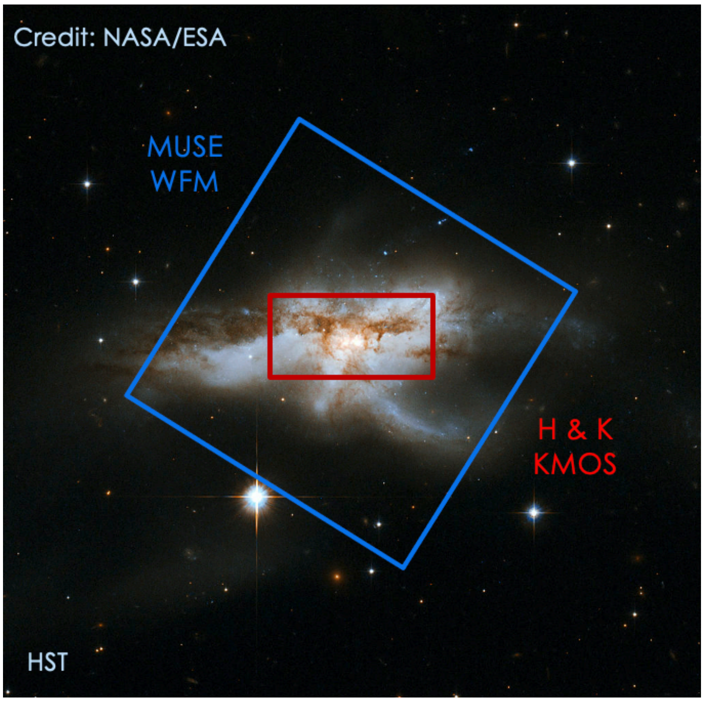

Fig. 4.1 *Optical HST image of NGC 6240 overlapped with red and blue contours indicating the FoV of our H- and K-band KMOS mosaics* ($32.5'' \times 16.3''$) *and archival MUSE WFM data* ($60'' \times 60''$) *employed in this work.*

block (OB), a pattern O-S-O-O-S-O, alternating object (O) and sky (S) frames, was followed to minimise sky subtraction residuals. The airmass varies between 1.12 and 1.27 (1.15 and 1.77) among different exposures within the H-band (K-band) dataset. Standard stars were observed for telluric correction and flux calibration: three distinct A-type stars were observed shortly before or after each science K-band OB, being taken in distinct nights; two B-type stars were targeted during the two nights in which H-band OBs were acquired.

We reduce the data using the ESO Reflex KMOS pipeline (v. 3.0.1). We correct both H- and K-band observations for atmospheric transmission measured from corresponding standard star observations, by selecting the following options `use_molecfit/calctrans = false` and `telluric_and_response_correction = 0` in the Reflex workflow. Sky subtraction is optimised by setting to `true` both `sky_tweak` and `stretch` parameters of the recipe `kmos_sci_red`. Finally, we combine (`kmos_combine` recipe) all single reconstructed reduced cubes (relative to distinct IFUs from different OBs), with the parameter `edge_nan = true` which sets the edge values of each cube to Nan before combining them, to minimise unwanted border effects when dithering. H-band reconstructed cubes are combined in the full mosaic recovering the correct shifts from the WCS information stored in the header of every IFU (`method = header`). Instead, we combine K-band reconstructed cubes using `method = user`, where shifts are specified by the user and

Table 4.1 *Observations of NGC 6240 used in this chapter. From left, columns list: IFU spectrograph, grating (in case of KMOS data), observed wavelength range, FoV, pixel scale, total exposure time ($t_{\rm exp}$), instrumental PSF ($\theta_{\rm PSF}$) corresponding to each dataset, measured as FWHM of a 2D Gaussian profile fitted to the light distribution of observed stars. For KMOS mosaics, we report the average $\theta_{\rm PSF}$ value measured from dedicated PSF stars observations, targeted in distinct nights; for MUSE data, we measure it from a bright star lying within the MUSE FoV.*

Spectrograph	Obs date	grating	λ range [Å]	FoV [arcsec^2]	pix scale [pix/$''$]	$t_{\rm exp}$ [s]	$\theta_{\rm PSF}$ [arcsec]
KMOS	2013 Sept 25, 27 2015 Apr 29	K	19300–24600	32.5 × 16.3	0.2	720	0.56
KMOS	2015 May 17, 28	H	14600–18500	32.5 × 16.3	0.2	760	0.45
MUSE	2016 Jun 10, 11	-	4800–9300	60 × 60	0.2	4800	0.87

given in input to the recipe. This is necessary since the K-band cubes from the third OB require a 4-pixel shift along the horizontal direction, with respect to WCS coordinates, to be correctly aligned with other cubes.

We point out the presence of horizontal blank stripes in the final reduced H- and K-band mosaic data cubes. These are consequences of a reconstruction issue due to a mismatch of calibration frames with respect to the science exposures. Unfortunately, such an effect was not known (hence not corrected) at the time of these observations.

From reduced images of the standard stars, we measure the mean PSF associated to H- and K-band KMOS mosaics, by fitting a 2D-Gaussian to the observed flux distribution. We thus obtain a mean PSF ($\theta_{\rm PSF}$) of $0.45''$ and $0.56''$ in H and K bands, respectively, measured as FWHM of the 2D Gaussian profile.

4.2.2 Optical MUSE Wide Field Mode observations

We downloaded the publicly available, reduced MUSE WFM data from the ESO Science Portal. Such observations were taken in June 2016 within the observing program 0.95.B-0482 (PI: E. Treister), in two consecutive nights. The MUSE WFM maps a $60'' \times 60''$ FoV (see Fig. 4.1) with a 0.2 pixel scale, and covers the wavelength range 4300–9800 Åwith a resolving power varying from $R = 1770$ (at 4800 Å) to $R = 3590$ (at 9300 Å). The final reduced MUSE data cube is the result of the combination of two distinct OBs, consisting of two (NDIT) integrations of 1200 sec each, for a total exposure of 4800 sec (i.e. 2 OBs × 2 NDIT ×1200 sec). We measure the PSF of these MUSE observations as FWHM of a 2D-Gaussian fitted to the light distribution of a bright star within MUSE FoV ($\theta_{\rm PSF} = 0.87''$).

In Table 4.1, we summarise main characteristics of KMOS (H- and K-band) and MUSE observations of NGC 6240, used in this chapter.

4.3 Data analysis

We analyse all three datasets of NGC 6240 observations with our fitting code described in Sect. 1.3.3. In the next subsections, we provide details on the spectral fitting separately for optical MUSE data cube and near-IR KMOS mosaics. Given the higher spectral/spatial resolution of KMOS, which is also less affected by dust extinction with respect to MUSE observations, we use near-IR emission lines to measure the redshift of the southern nucleus of NGC 6240[1]. From the peak of the brightest near-IR emission lines (i.e. [Fe II]λ1.64 and H_2(1-0)S(1); see Sect. 4.3.2), we measure a redshift of $z - 0.0242$. This redshift is used in the following to shift spectra from observed to rest frame and to set galaxy systemic velocity, with respect to which all line velocities are computed.

4.3.1 MUSE WFM data cube

Considering the large amount of obscuring material, we see no BLR emission from NGC 6240. Therefore, we skip phase I of our fitting procedure (see sect. 1.3.3), and start from phase II with the modelling via `pPXF` (Cappellari and Emsellem, 2004, Cappellari, 2017) of full MUSE spectra over the optical rest-frame range 4700–9300 Å. The main spectral components we detect in this optical range: stellar continuum and emission lines from diffuse ionised gas. Figure 4.2 displays three distinct spectra extracted with a $0.6'' \times 0.6''$ aperture, centred on different regions of the FoV marked with coloured crosses in the right-hand map. Different highlighted regions correspond to: the southern and northern nuclei (black and pink cross, respectively), and a more external region (light blue), where stellar continuum emission is no longer detected, but line emission is still bright. On the right, we show an integrated flux map obtained by collapsing spectral channels of Hα+[N II] emission lines (i.e. rest-frame 6520–6620 Å); a mean level of continuum emission has been subtracted, measured from two spectral ranges (i.e. rest-frame 6410–6510 Å and 6630–6680 Å) adjacent to the line multiplet.

Since we initially aim at properly modelling continuum emission separately from emission lines to finally remove it, we perform the `pPXF` fit on binned spaxels using a Voronoi tessellation (Cappellari and Copin, 2003), obtained by requiring a mean S/N>20 per spectral channel on continuum emission within the rest-frame range 5250–5450 Å, where no emission lines are found. For the stellar continuum, we use the MILES extended stellar population models (Röck et al., 2016), and add an additive 3rd-degree polynomial to better model the continuum shape. In our modelling, we mask the spectral region (rest-

---

[1] Unfortunately, the northern nucleus falls in one of the blank stripes of KMOS mosaics mentioned in Sect. 4.2.1 (see also Sect. 4.3.2 and Fig. 4.5).

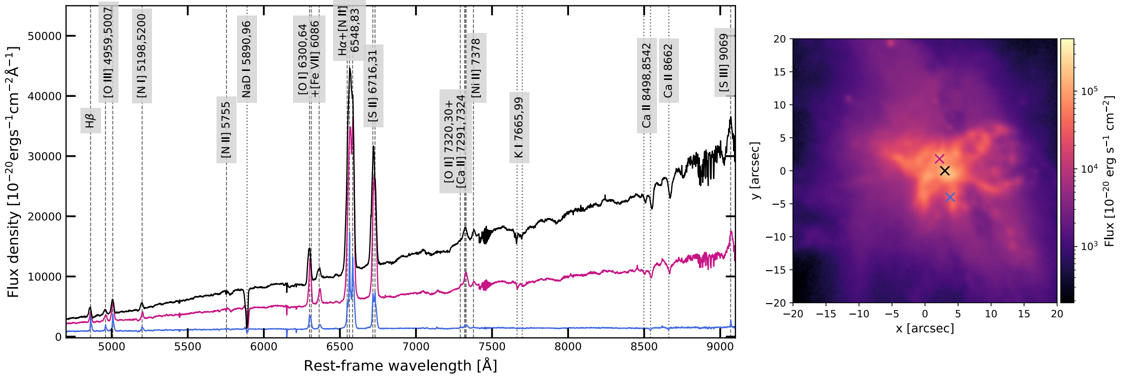

Fig. 4.2 *MUSE spectra of NGC 6240, extracted with a* 0.6″ × 0.6″ *aperture centred on three different positions on the FoV (marked with coloured crosses in the right-hand map), corresponding to: the southern and northern nuclei (black and pink, respectively), a more external region (light blue) where stellar continuum emission is no longer detected. On the right, we show an integrated flux map obtained by collapsing spectral channels of the bright* Hα+[N II] *multiplet (i.e. rest-frame 6520–6620 Å); a mean level of continuum emission has been subtracted, measured from two spectral windows (i.e. rest-frame 6410–6510 Å and 6630–6680 Å) adjacent to the line multiplet.*

frame 5850–5920 Å) around the line multiplet of He Iλ5876 line emission and absorption Na ID$\lambda\lambda$5890,96 line doublet. In fact, unlike Ca IItripletλ8498,8542,8662 triplet absorption well reproduced by stellar templates, the Na ID$\lambda\lambda$5890,96 line doublet exhibits a strong absorption, which reveals a significant gas contribution, in addition to that from stellar atmosphere. The Na ID absorption feature also remarkably varies in shape across the FoV, showing prominent blue and/or red wings, which point to the presence of neutral atomic outflows in NGC 6240. Since the He I+Na ID emission/absorption line multiplet is a spectral feature very complex to model (see e.g. Perna et al. 2020), we will model it in future separately to investigate also neutral atomic gas in NGC 6240, and trace outflows in this gas phase.

Within the fitted rest-frame wavelength range (i.e. 4700–9300 Å), we detect many emission lines (see Fig. 4.2): hydrogen Balmer lines Hα and Hβ, and several forbidden lines among which [O III]λ4959,5007, [O I]λ6300,64, [N II]λ6548,83, [S II]λ6716,31 line doublets and [S III]λ9069. Emission line profiles are extremely diverse and complex from spaxel to spaxel, requiring up to four Gaussian components to accurately model simultaneously all emission lines and properly reproduce detailed high-S/N line profiles. Via a KS test (see Sect. 1.3.3), we then select the optimal (minimum) number of components to model line emission in each spaxel, finding that three or four components are selected in most spaxels, given the complexity of gas kinematics in NGC 6240.

After removing stellar continuum emission, we focus on the refined modelling of emission line profiles in the resulting MUSE subtracted cube. Four Gaussian components are confirmed to be necessary to simultaneously reproduce all emission line profiles, accounting for very complex shapes and asymmetries. Therefore, as done in the previous modelling of full spectra with `pPXF`, we fit all subtracted spectra with a number of Gaussian components ranging from 1 to 4, and then select the statistically best multi-Gaussian modelling via a KS test. In the line fitting, brighter emission lines (i.e. Hα, Hβ, [O III]λ4959,5007, [O I]λ6300, [N II]λ6548,83, [S II]λ6716,31) are fitted first, with Gaussian profiles variable in flux and kinematics (i.e. flux, mean velocity v and velocity dispersion σ as free parameters); then, fainter ones (i.e. [N I]λ5198,5200, [N II]λ5755, [O II]λ7320,30, [Ca II]λ7291,7324, [Ni II]λ7378, [S III]λ9069) are fitted with Gaussian components fixed to the best-fit v and σ values obtained for bright lines, hence re-scaled only in flux. Given the large number of emission lines detected, such an approach reduces the number of free parameters, and also avoids that fainter low-S/N emission lines might influence the best-fit kinetic parameters.

The complexity and diversity of the emission line profiles across the MUSE FoV reflect the intricate gas kinematics in NGC 6240, as a result of different kinetic components possibly contributing in this galaxy: disk rotation, AGN NLR, tidal streams and outflows. A detailed and accurate identification spaxel-by-spaxel of each component contribution to total line emission is hard to achieve, and also beyond the purpose of our study, which primarily aims at investigating outflows in NGC 6240. Therefore, we define the following criterion to identify Gaussian components likely associated with ionised outflow emission (classified as ‘broad’), isolating them from all other components (generically referred to as ‘narrow’). Such a preliminary classification will be then confirmed by the resulting kinematics (see Sect. 4.4.1). Our classification criterion relies on the fact that outflows are typically responsible for broader and higher-velocity line emission (see Sect. 4.4.1) compared to the other possible components, usually producing narrow line emission close to galaxy systemic velocity or compatible with disk rotation. Hence, we first define a threshold value of velocity dispersion ($\sigma_{\rm max}$ = 250 km s^{-1}) to automatically classify as narrow all components with $\sigma < \sigma_{\rm max}$. Those with $\sigma > \sigma_{\rm max}$ are instead subject to further checks. In each spaxel requiring multiple components, we identify the one closest in velocity to stars and calculate its displacement from stellar velocity ($\Delta\ V_{\rm min}$); if not yet, this component is classified as narrow. Remaining components are then identified as narrow if their absolute velocity displacement from stars is less than $|\Delta\ V_{\rm min}|$+50 km s^{-1}, where the additional 50 km s^{-1} shift allows for further small discrepancies.

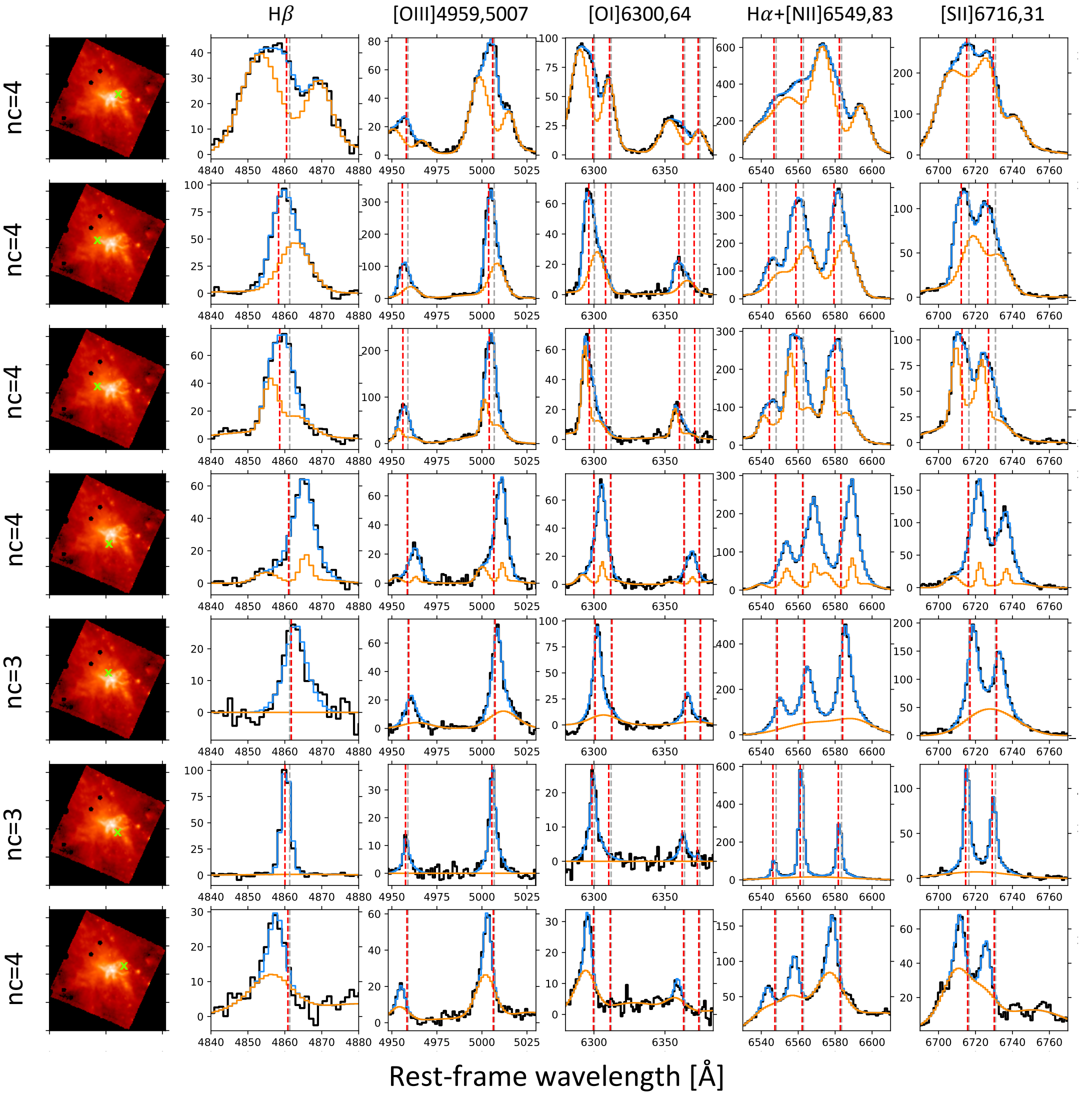

Fig. 4.3 *MUSE subtracted spectra of NGC 6240, extracted from random spaxels (green cross in first-column* Hα maps*) with a S/N>20 on all emission lines shown. For all spectra, we draw the total emission-line model (light blue), and total broad model (orange) as sum of all broad-classified components. Vertical red and grey dashed lines correspond to stellar and galaxy systemic (set to 0 km s^{-1}) velocities (coinciding in some cases).*

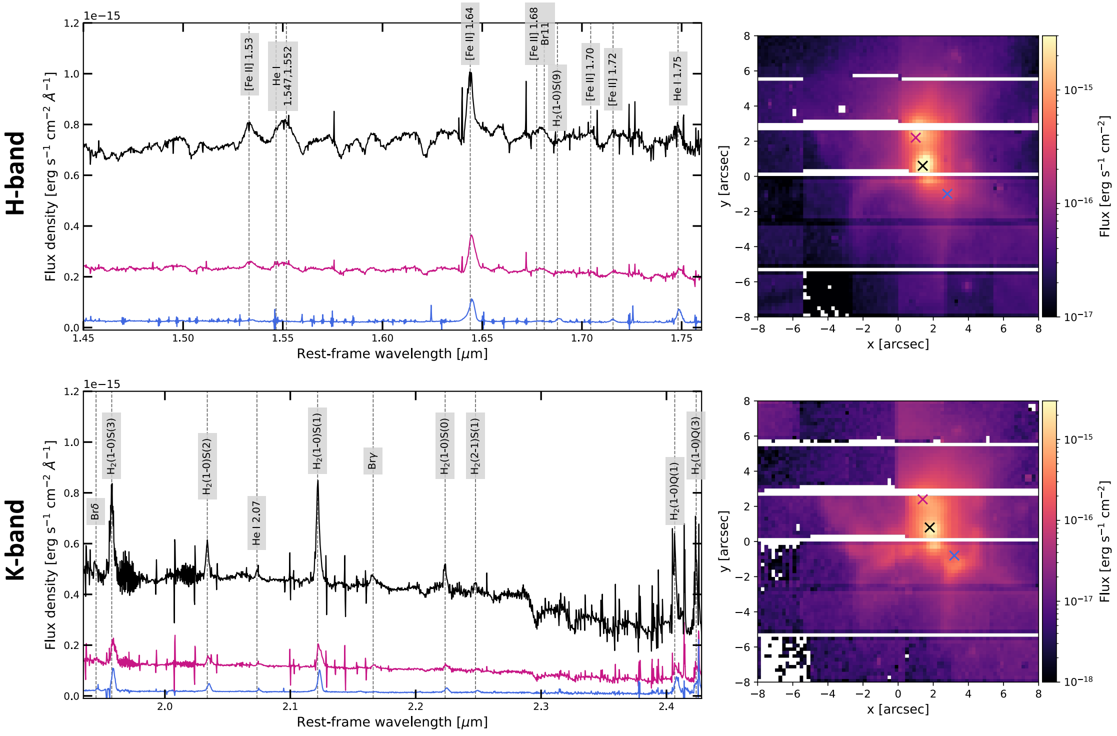

Fig. 4.4 *H- and K-band KMOS data of NGC 6240 in upper and lower panels, respectively. The left panels show full spectra extracted with a* $0.6'' \times 0.6''$ *aperture from three different regions (coloured crosses in right-hand maps): the southern and northern nuclei (black and pink, respectively), and a more external region (light blue) with only emission lines detected. On the right, are shown flux maps obtained by collapsing spectral channels around* [Fe II]$\lambda 1.64$ *and* H_2(1-0)S(1) *(i.e. within rest-frame 1.638–1.649* μm *and 2.119–2.126* μm *ranges) in H and K band, respectively. Horizontal white stripes are a reconstruction issue due to a mismatch between calibration and science frames (see Sect. 4.2.1).*

In Fig. 4.3, we show subtracted spectra extracted from random spaxels (marked with a green cross in first-column Hα maps) with a high S/N (>20) on all emission lines shown (see labels on each column displaying spectra). Only spectral ranges of brighter emission lines are shown to highlight the resulting decomposition into broad and narrow components: the orange line shows the total broad-component model, while the light blue line is the total emission-line (i.e. broad + narrow components) model. Vertical red and grey dashed lines correspond to stellar and galaxy systemic velocities (they overlap in some plots).

4.3.2 KMOS *H*- and *K*-band data

In Fig. 4.4, we show *H*- and *K*-band spectra of NGC 6240, extracted from KMOS data cubes using a $0.6'' \times 0.6''$ aperture centred on the northern and southern nuclei (pink and black, respectively), and on an off-nuclei region, where we detect only line emission. Right-hand maps have been obtained by collapsing the emission contained in spectral channels around [Fe II]λ1.64 and H_2(1-0)S(1) emission lines (i.e. within rest-frame 1.638–1.649 μm and 2.119–2.126 μm ranges) in H- and K-band data cubes, respectively. Horizontal white stripes are a consequence of a reconstruction issue due to an undesired mismatch between calibration and science frames. Unfortunately, the centre of the northern nucleus falls exactly in one of these blank stripes. So, we extract an integrated spectrum from the bright northern region, as close as possible to the expected location of the northern nucleus (pink cross in upper-right map). As shown in left-hand panels, H-band spectra present several [Fe II] and He I lines, among which the [Fe II]λ1.64 and He Iλ1.75 are brightest ones, respectively. We also detect a couple of faint atomic (Br11) and molecular (H_2(1-0)S(9)) hydrogen lines. In K-band spectra instead, we observe a wealth of roto-vibrational transitions of molecular hydrogen. The brightest ones are H_2(1-0)S(1), H_2(1-0)S(3), H_2(1-0)S(2) emission lines; also H_2(1-0)Q(1) and H_2(1-0)Q(3) lines appear quite bright, but fall in a noisy region of most KMOS spectra. Additionally, we detect atomic Brδ and Brγ hydrogen lines, as well as He Iλ2.07 emission line. Around 2.3μm, CO 2.29μm band absorptions are well visible.

We fit KMOS H- and K-band data cubes separately, over the rest-frame wavelength range of 1.48–1.81 μm and 1.93–2.34 μm, respectively. As done with MUSE data cube, we apply a Voronoi tessellation requiring an average S/N>5 per spectral channel within 1.556–1.641 μm and 2.132–2.245 μm (rest-frame) in H- and K-band spectra. We model stellar continuum emission via the single stellar population (SSP) models at high spectral resolution from Maraston and Strömbäck (2011). Due to possible residual effects from data reduction, we also include in the `pPXF` fit an additive 3rd-degree polynomial (as done for MUSE data), and a 10-degree multiplicative polynomial to help SSP models reproduce continuum emission at best (e.g. Baldwin et al. 2018). Unlike optical counterparts, near-IR emission lines require up to three Gaussian components as a likely consequence of the lower S/N of KMOS data compared to MUSE, in spite of the higher nominal spectral resolution of near-IR KMOS spectra ($R \sim 4000$ against $R \sim 3000$ of MUSE).

After the removal of the best-fit continuum model, we notice that, especially in nuclear H-band spectra, the level of residual continuum emission is not constantly to zero as expected, and significant (both positive and negative) residuals are present (see Fig. 4.5). This is likely due to residual effects from data reduction, which prevent us from an accurate modelling of faint emission lines lying close to these residual contaminant features (e.g. [Fe II]λ1.68 and Br11 in H-band spectra). Similarly, we do not re-fit emission lines falling in particularly noisy spectral regions (e.g. H_2(1-0)Q(1) and H_2(1-0)Q(3) in most of *K*-band spectra).

To increase the S/N and better model emission lines, we first smooth the subtracted data cubes with a Gaussian kernel of width $\sigma = 0.2''$. Then, we fit emission lines with a variable number of Gaussian components, ranging from one to three, and select the statistically best multi-Gaussian modelling via a KS test (see Sect 1.3.3). We use the same criterion as adopted for MUSE data to isolate 'broad' components, associated with outflowing gas, from 'narrow' ones. For *K*-band spectra, we keep the same $\sigma_{\rm max} = 250$ km s^{-1} as used in the optical; while we find that a slightly larger threshold (i.e. $\sigma_{\rm max} = 300$ km s^{-1}) leads to a more reasonable decomposition of Gaussian components, as checked by visually inspecting the resulting classification in several representative spaxels. Likely, this is a consequence of a worse continuum subtraction on *H*-band spectra with respect to *K* band (see Fig. 4.5), as already pointed out.

Figure 4.5 displays our best-fit modelling of main emission lines detected in KMOS *H*-(left) and *K*-band (right) subtracted spectra. Data are shown in black, with the total (i.e. broad + narrow) emission line (light blue) and total broad-component model (orange) drawn on the top. Spectra shown in the upper panels have been extracted from the brightest spaxel centred on the southern nucleus, while those in the lower panels are from a more external off-nucleus spaxel. Grey shadings indicate regions of residual sky emission, masked during the emission-line modelling. As already discussed, significant negative/positive residuals from continuum subtraction are present, especially in the *H*-band nuclear spectrum, which prevents us from modelling faint emission lines lying nearby (e.g. [Fe II]λ1.68 and Br11).

4.4 Preliminary results

In this section, we present preliminary results on the properties of optical and near-IR emitting gas, as traced in MUSE and KMOS observations, respectively. In Sect. 4.4.1 we investigate the morphology and kinematics of distinct gas phases and compare them to each other; while in Sects. 4.4.2 and 4.4.3 we investigate optical and near-IR gas properties, such as gas ionisation/excitation mechanisms via spatially resolved emission-line diagnostics.

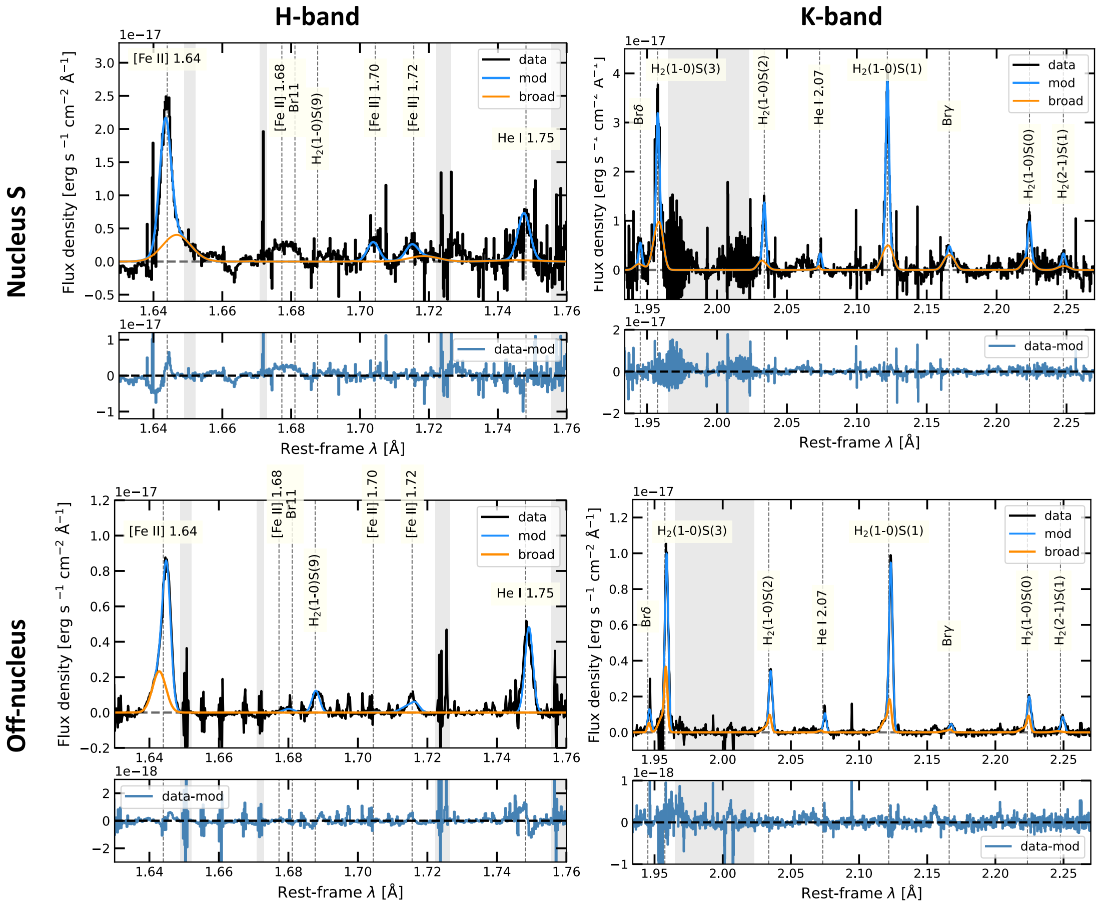

Fig. 4.5 *KMOS H- (left) and K-band (right) subtracted spectra of NGC 6240, from the brightest spaxel centred on the southern nucleus (upper panels), and from a more external, off-nucleus spaxel (lower). Data are shown in black, with total (i.e. broad + narrow) emission-line (light blue) and total broad-component model (orange) drawn on the top. Grey shadings indicate regions of residual sky emission, masked during the emission-line modelling.* [Fe II]λ1.68 *and* Br11 *in H-band spectra are not modelled, because of near/overlapping contaminant residuals which would affect best-fit results. Below each subtracted spectrum, an additional panel shows final residuals (i.e. data–model, shown in the corresponding upper panel).*

4.4.1 Gas morphology and kinematics

Useful insight into the morphology and kinematics of distinct gas phases can be obtained from the brightest emission lines detected in optical MUSE and near-IR KMOS observations.

4.4.1.1 Optical emitting gas

In Figs. 4.6 and 4.7, we show moment-0 (intensity field), moment-1 (velocity field), and moment-2 (velocity dispersion field) of [O III] and Hα line emission, respectively, as traced in optical MUSE WFM data of NGC 6240. From left, maps shown in different columns refer to total (i.e. narrow + broad) line emission, narrow and broad components separately, displaying only pixels with S/N>3. In each map, the location of the two active nuclei is marked by two crosses. The [O III] broad moment-0 map features a bright emission originating in the centre and extending away up to about 15 kpc, which corresponds to regions of high velocity and velocity dispersion. In particular, both east and west of the two nuclei we find a couple of well definite, elongated kinetic structures showing the highest velocity and velocity dispersion values ($|v| \sim 400$ km s^{-1}, $\sigma \sim 600$ km s^{-1}) observed across the MUSE FoV. Interestingly, both eastern and western pairs of high-velocity regions consist each of a blueshifted and a redshifted component of comparable absolute velocity ($|v| \sim 400$ km s^{-1}). On the contrary, narrow [O III] emission exhibits a more temperate kinematics, with smaller moment-1 and moment-2 values (i.e. $|v| < 200$ km s^{-1} and $\sigma \sim 100-200$ km s^{-1}). This becomes more evident in Hα maps, shown in Fig. 4.7, where the higher S/N of Hα compared to [O III] allows us to trace ionised gas over the full FoV of MUSE. In particular, the narrow Hα moment-1 map unveils a velocity gradient (with $|v| < 200$ km s^{-1}) along the northeast-southwest direction (coinciding with that joining the two nuclei), likely associated with disk rotation, as well as winding tidal streams, clearly visible also in the total moment-1 map. The narrow Hα component shows values of $\sigma \sim 100-200$ km s^{-1} over the entire MUSE FoV, well below the typical values found in the broad moment-2 map ($\sigma \gtrsim 400$ km s^{-1} in most spaxels).

The different kinematics found for broad and narrow line emission supports our correct classification of Gaussian components, with the former associated with fast outflowing ionised gas, while the latter tracing nearly systemic gas motions. The outflow interpretation of broad line components is further supported by the location of the high-velocity blueshifted/redshifted regions, which extend symmetrically from the galaxy centre out of the rotating disk plane of the merger. They exhibit the peculiar property of appearing as pairs of a blushifted component and a redshifted one both east and west of the two

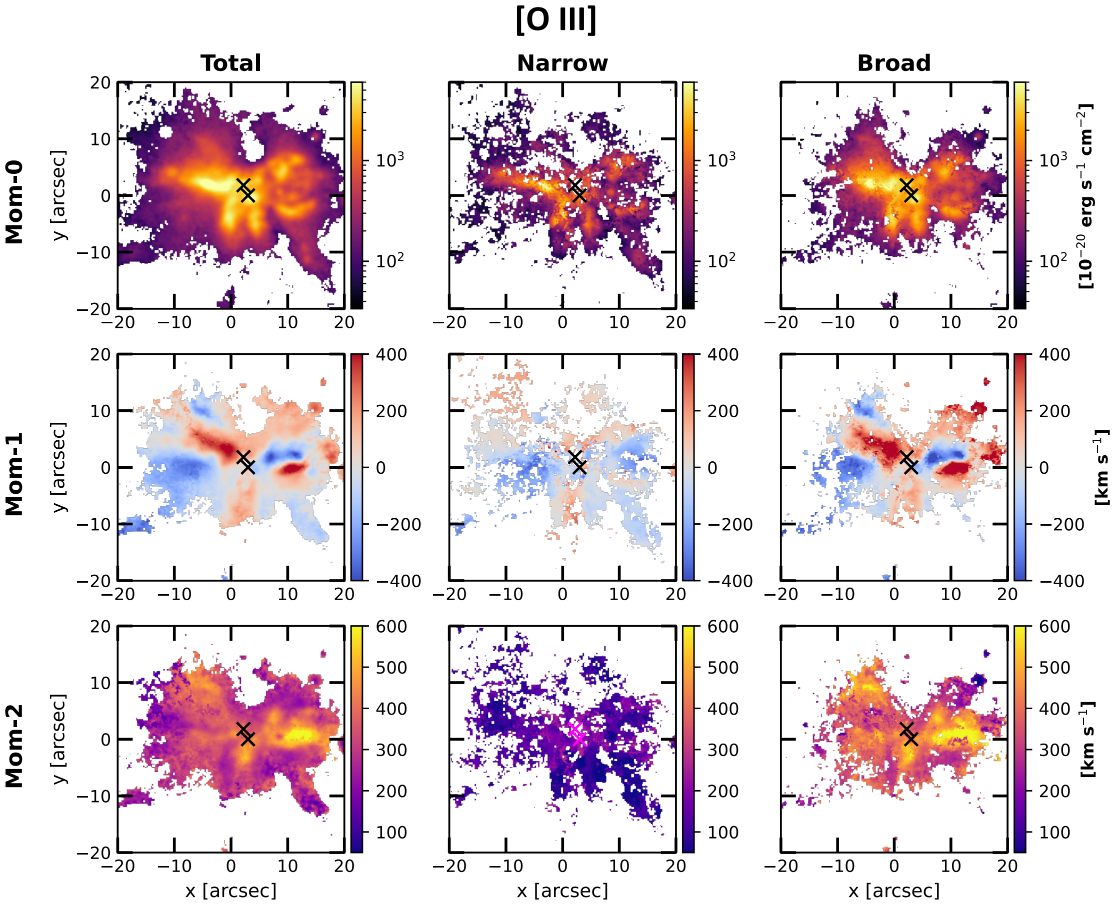

Fig. 4.6 *Moment-0 (intensity field), moment-1 (velocity field), and moment-2 (dispersion field) maps of* [O III] *line emission in NGC 6240, as traced in MUSE optical data. We show maps for total line emission, and separately for narrow and broad components, reporting only pixels with S/N>3. In each map, two crosses indicate the location of the two active nuclei. While narrow moment-1 and moment-2 exhibit values of* $|v| < 200$ *km s*$^{-1}$ *and* $\sigma 100-200$ *km s*$^{-1}$*, broad maps feature well-definite regions with high velocity and velocity dispersion values (*$|v| \sim 400$ *km s*$^{-1}$ *and* $\sigma \sim 600$ *km s*$^{-1}$*), associated with fast ionised outflows.*

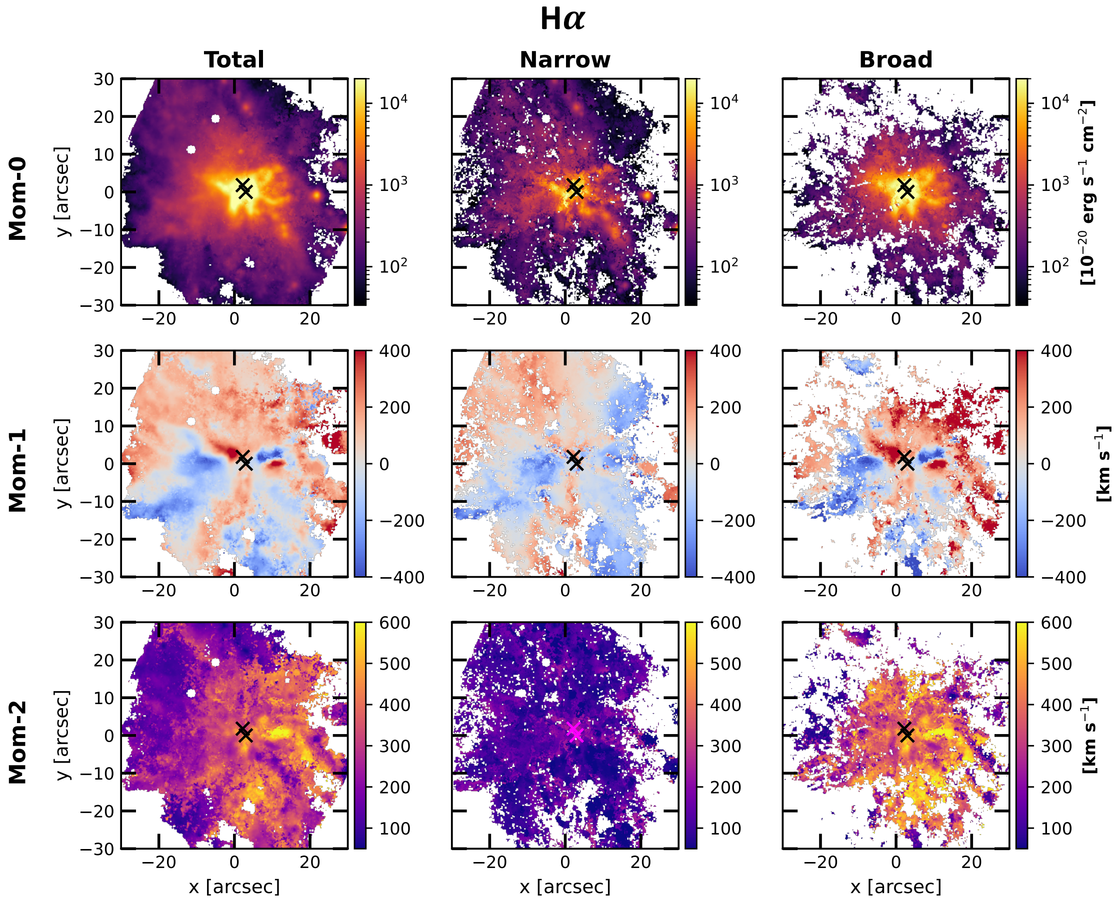

Fig. 4.7 *Same moment-0, moment-1 and moment-2 maps as in Fig. 4.6 but relative to* Hα *line emission in NGC 6240, as traced in MUSE optical data. Thanks to its higher S/N compared to* [O III] *emission line,* Hα *line emission extends at a larger distance from the centre and traces nearly systemic gas motions, such as disk rotation along northeast-southwest direction and tidal streams.*

nuclei. These collimated kinetic structures seem to be not associated with tidal streams and resemble conical geometries typical of ionisation cones, as observed in prototypical Seyfert galaxies (e.g. Fischer et al. 2013, Venturi et al. 2018). All this points to an AGN-driven origin of these outflows, although the low spatial resolution of MUSE WFM data prevents us from a clear interpretation these pairs of blueshifted/redshifted outflowing structures. In fact, it is not clear whether they originate from one of the two nuclei, or they are the resulting effect of both. As a consequence, the blueshifted and redshifted structures observed on each side of the galaxy plane might be either two distinct outflows, or different (approaching/receding) sides of the same conical outflow. In both cases, it is likely that the bulk of the outflowing gas lies in the plane of the sky, which would explain the relatively small projected velocities observed for these outflows. The joint analysis of optical MUSE NFM and near-IR *JWST/NIRSpec* observations at higher spatial resolution (~50–80 mas) of the inner kpc region of NGC 6240, in progress within our research group (Ceci et al., in prep.), will help us distinguish between possible different scenarios.

Although AGN-driven outflows seems to be most likely interpretation in terms of both location, symmetry and collimated kinetic morphology, tidal interaction might even play some role in originating these high-velocity structures. Furthermore, due to the high star formation rate of NGC 6240 (SFR>100 $M_\odot yr^{-1}$, as inferred from UV and IR luminosity measurements; Howell et al. 2010), we cannot rule out a contribution to powering outflows from starbursts at this stage of the analysis, based on purely kinetic arguments. NGC 6240 is indeed known to host a giant (extending up to ~90 kpc) Hα nebula (Yoshida et al., 2016), whose complex structure, composed of numerous filaments, loops, bubbles, and knots, points to the presence of intense winds driven by starbursts. Interestingly, the high-velocity structures detected in our data appear being elongated at the center of the Hα bubble (Yoshida et al., 2016, Müller-Sánchez et al., 2018), possibly suggesting that the outflow is inflating a cavity in the ISM (e.g. Cresci et al. 2023). In Sect. 4.4.2, optical emission-line diagnostics will help us shed light on the powering mechanisms of these ionised outflows.

Based on previous combined optical *HST* imaging and ground-based long-slit spectroscopy, Müller-Sánchez et al. (2018) claimed the existence of two outflows of distinct origin in NGC 6240: an AGN-driven outflow well detected in [O III] to the northeast, and a starburst-driven outflow observed in Hα (but not in [O III]) to the northwest, associated with the Hα nebula (Yoshida et al., 2016). While the AGN/starburst origin will be better discussed in next sections, we here notice that northeastern outflow previously traced in [O III] corresponds in terms of location, morphology and kinematics ($v \sim 350$ km s^{-1}, $\sigma \sim 500$ km s^{-1} inferred by Müller-Sánchez et al. 2018) to the eastern redshifted high-velocity kinetic structure detected by MUSE. Additionally, MUSE IFU data have revealed a wealth of new structures, too faint to be detected in previous *HST* imaging, such as the eastern blueshifted high-velocity high-velocity structure and the western blushifted/redshifted counterparts, located at the basis of the Hα bubble detected by *HST* (Müller-Sánchez et al., 2018), which are likely to be associated with AGN ionisation cones, similarly to the eastern redshifted bright high-velocity structure. Therefore, this leaves open the possibility of an AGN-driven contribution to outflows also in the eastern region of NGC 6240, as also suggested by BPT diagrams (discussed later in this section; see Fig. 4.13).

4.4.1.2 Near-IR emitting gas

Similarly to the optical moment maps shown in Figs. 4.6 and 4.7, Figs. 4.8 and 4.9 display moment maps relative to the brightest near-IR emission lines detected in KMOS observations of NGC 6240: H_2(1-0)S(1) (Fig. 4.8) in *K* band, tracing warm molecular gas; and [Fe II]λ1.64 (Fig. 4.9) in *H* band, a good tracer of shock-excited gas. Maps of H_2(1-0)S(1) and [Fe II]λ1.64 have been obtained from independent spectral modellings of *K*- and *H*-band data cubes (see Sect. 4.3.2).

In spite of the worse quality compared to MUSE data, our KMOS mosaics provide an unprecedented panoramic IFU view of near-IR emitting gas on galaxy scales, as opposed to previous near-IR IFU studies which all focused only on the inner kpc region of NGC 6240 (Ilha et al., 2016, Müller-Sánchez et al., 2018). Moment-1 maps of total H_2(1-0)S(1) and [Fe II]λ1.64 line emission show well-definite regions of strongly redshifted and blueshifted velocities east and west of the two nuclei, corresponding to the high-velocity structures of ionised gas detected by MUSE (discussed later in this section; see Fig. 4.10). As expected, broad line components of H_2(1-0)S(1) and [Fe II]λ1.64 are responsible for such high-velocity near-IR emitting regions, as shown by corresponding broad maps featuring values of $|v| \sim 300-400$ km s^{-1} and $\sigma \sim 400$ km s^{-1} for H_2 ($|v| \sim 400-500$ km s^{-1} and $\sigma \sim 300-400$ km s^{-1} for [Fe II]) in these regions. Unlike MUSE data, where narrow line emission reveals disk rotation and tidal streams, near-IR narrow components do not point to any clear kinetic structure, but however display lower velocities ($|v| \lesssim 200$ km s^{-1}) and velocity dispersion values ($\sigma \lesssim 200$ km s^{-1}), which supports our correct classification of Gaussian components during the spectral modelling of KMOS data.

To highlight kinetic differences and similarities between optical ionised and near-IR emitting gas, in Fig. 4.10 we compare total moment-1 maps of near-IR emission lines with total moment-1 level contours of [O III] line emission. More specifically, left and right panels display total moment-1 maps of H_2(1-0)S(1) and [Fe II]λ1.64 line emission,

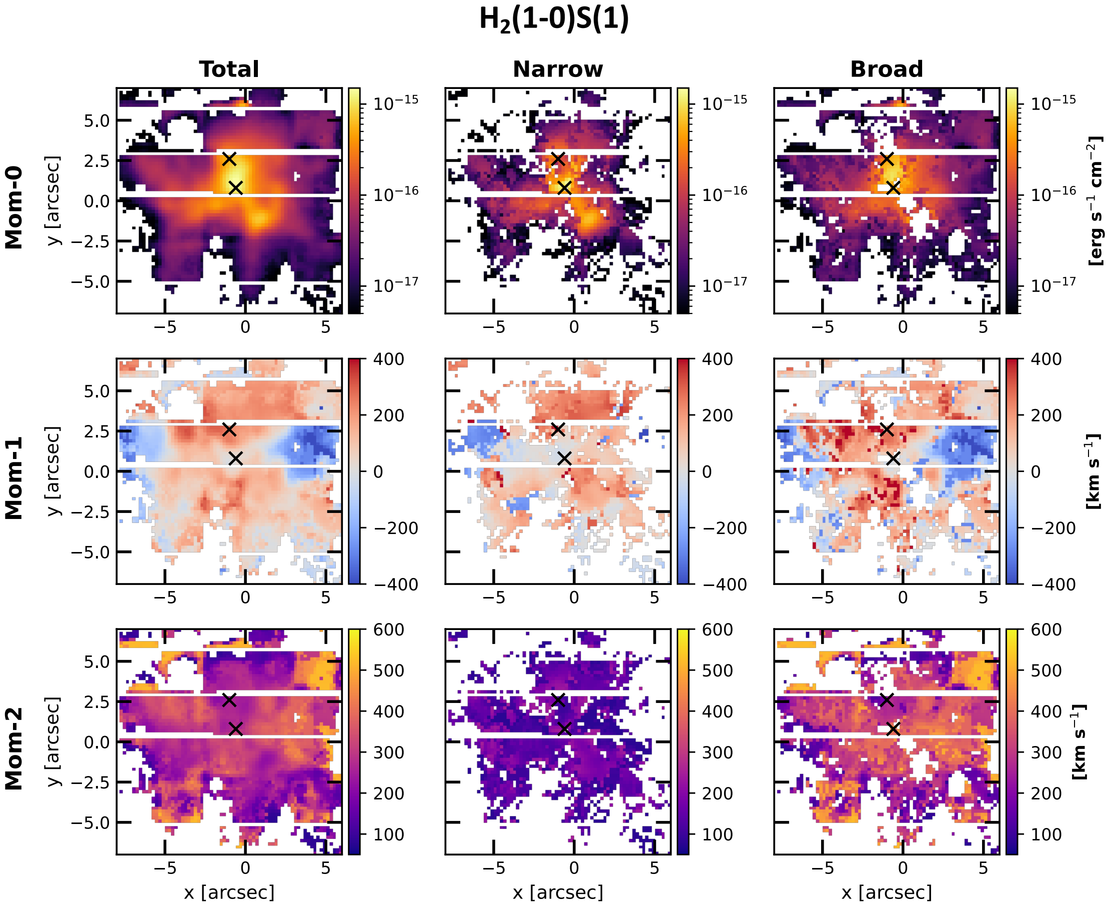

Fig. 4.8 *Moment-0 (intensity field), moment-1 (velocity field), and moment-2 (dispersion field) maps of* H_2(1-0)S(1) *line emission in NGC 6240, the brightest emission line in KMOS K band. Maps overall display the morphology and kinematics of warm molecular gas, separately for total line emission, narrow and broad components. A S/N>3 has been applied to all maps, and the location of the two nuclei is marked with two crosses. Broad* H_2(1-0)S(1) *line emission feature higher moment-1 and moment-2 values (*$|v| \sim 400$ *km s*$^{-1}$*,* $\sigma \sim 400-500$ *km s*$^{-1}$*) than its narrow counterpart, especially perpendicularly to direction joining the two nuclei, as observed in MUSE maps (Figs. 4.6 and 4.7).*

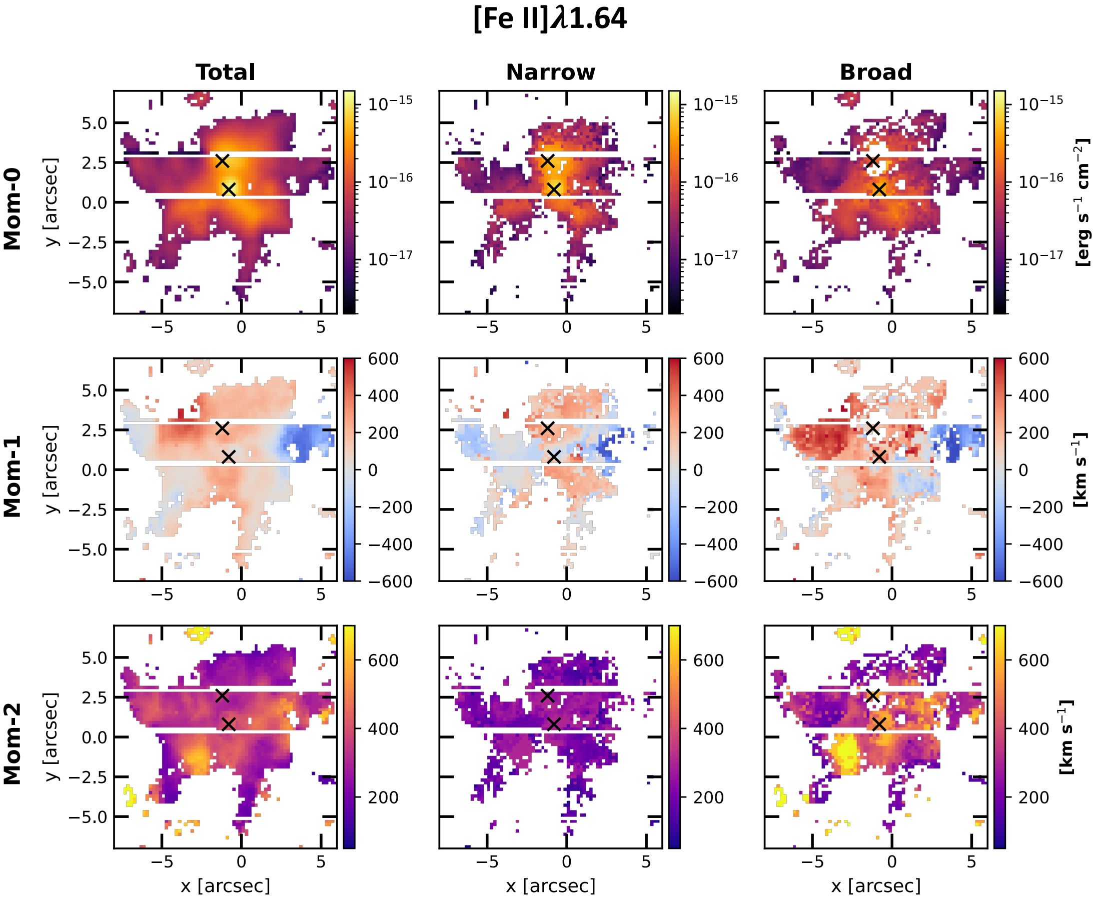

Fig. 4.9 *Moment-0, moment-1, and moment-2 maps of* [Fe II] λ1.64 *line emission in NGC 6240, the brightest emission line in KMOS H band, tracing near-IR ionised gas possibly associated with shocks. As in Figs. 4.8, we display the morphology and kinematics of [Fe* II*] line emission, separately for total line emission, narrow and broad components. A S/N>3 has been applied to all maps, and the location of the two nuclei is marked with two crosses. Obtained from the spectral analysis of the KMOS H-band data cube, independently from the K-band dataset, broad moment-1 [Fe* II*] map highlights two well definitive regions of* $|v| \sim 500$ *km* s^{-1}*, perpendicularly to the direction, similarly to what observed in MUSE maps (see Figs. 4.6 and 4.7 and KMOS K-band maps.*

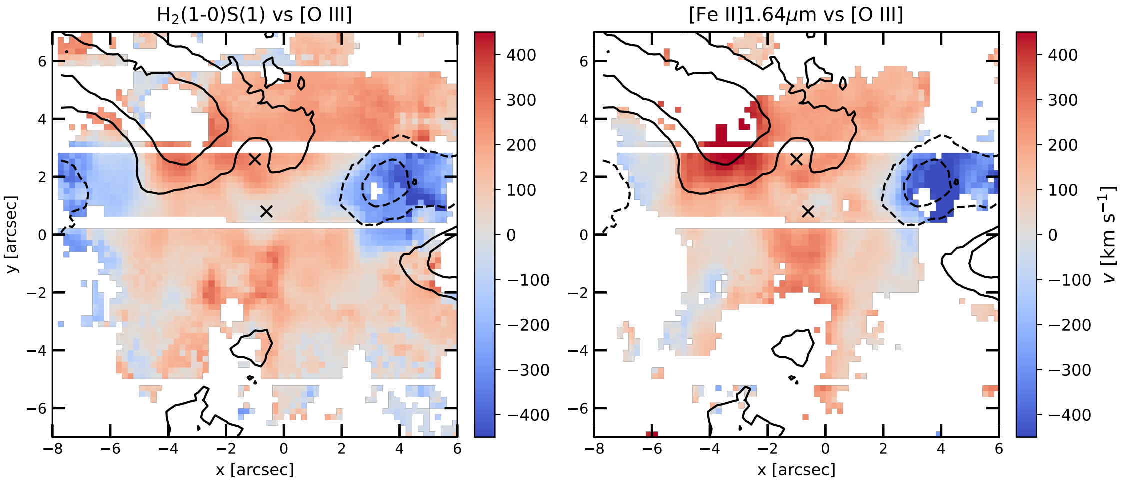

Fig. 4.10 *Comparison of total moment-1 maps of near-IR emission lines -* H_2(1-0)S(1) *(left) and* [Fe II]λ1.64 *(right) - with total moment-1 level contours of* [O III] *-traced ionised gas, corresponding to negative (dashed) and positive (solid) velocities of* $|v| = 300$ *km s*$^{-1}$ *and* $|v| = 150$ *km s*$^{-1}$*. Although the worse quality of KMOS data, [O* III*] dashed and solid contours spatially coincide with near-IR regions of highest blue and red velocities (*$|v| = 400$ *km s*$^{-1}$*), implying an overall common kinematics followed by optical and near-IR emitting gas.*

respectively, both overlapped with [O III] level contours tracing negative (dashed) and positive velocities (solid) of $|v| = 300$ km s^{-1} and $|v| = 150$ km s^{-1}. In spite of the worse quality of KMOS data, [O III] dashed and solid contours spatially overall coincide with near-IR emitting regions of highest blue and red velocities, implying a common kinematics for the optical and near-IR emitting gas.

In Fig. 4.11, we also show total moment-0 flux maps of the main lines detected in KMOS *H*- (i.e. He Iλ1.75) and *K*-band (all the others) data cubes of NGC 6240, with a S/N>3 cut. Along with [Fe II]λ1.64 and H_2(1-0)S(1), most of these emission lines (e.g. Brγ and H_2 lines) are fundamental to study excitation gas properties via near-IR emission-line diagnostics (see Sect. 4.4.3). Main near-IR emission lines overall trace the same gas morphology and structures, although H_2-traced warm molecular gas shows line emission extending from the southern nucleus to the northern companion, while emission from other lines (i.e. Brγ, He I and [Fe II]) is centrally located on the two nuclei and faint between the two. Similarly, the gas clump southwest of the southern nucleus appears brighter in H_2 lines than the other lines (e.g. [Fe II], He I), suggesting that indeed the H_2 lines trace a different gas phase, partially decoupled from the bulk of the ionised gas.

Finally, we do not show maps of Brδ line emission since we notice that it is blended with H_2(2-1)S(5) at 1.945μm. Therefore, in the following we will not correct near-IR fluxes for dust extinction, due to the unreliability of Brγ/Brδ ratios.

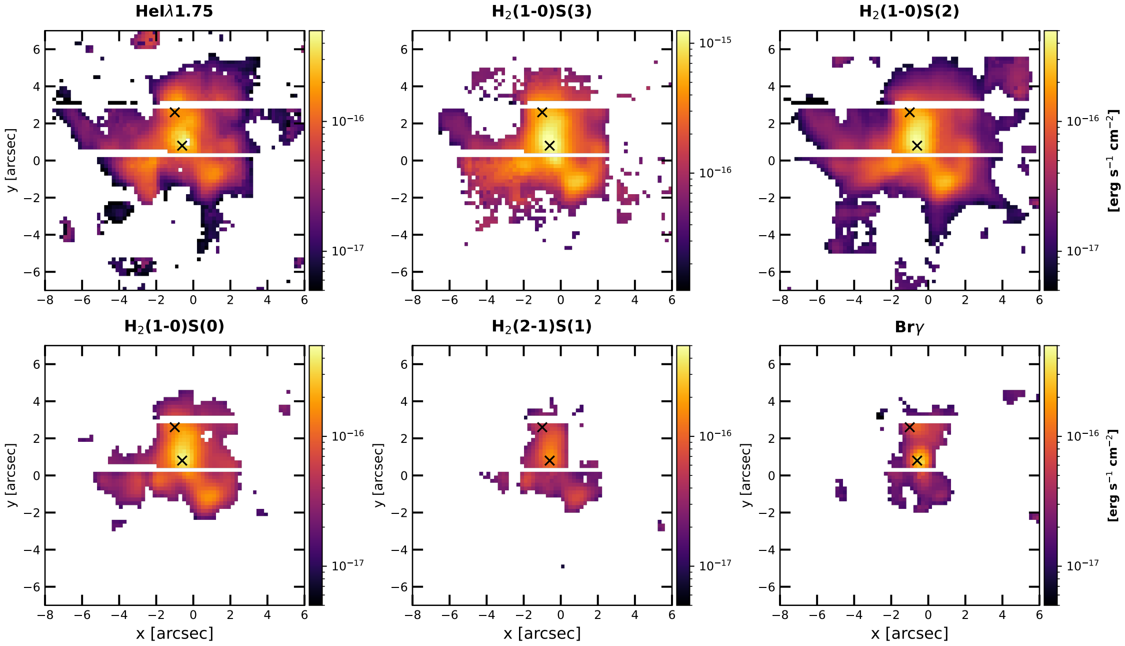

Fig. 4.11 *Moment-0 flux maps of the main emission lines detected in KMOS H- (i.e.* He I λ1.75*) and K-band (all the others) data cubes of NGC 6240, with a S/N>3 cut. Near-IR emission lines overall trace the same large-scale gas structures and morphology, with some differences on smaller scales.* H_2 *emission lines indeed appear brighter than the other lines both between the two nuclei and in the gas clump southwest of the southern nucleus.*

4.4.2 Ionised gas properties

Thanks to the high sensitivity of MUSE WFM data, we can infer spatially resolved optical emission-line ratios which allow us to get insights of the properties of ionised gas in NGC 6240 up to kpc scales, such as electron density $n_{\rm e}$ (left panel of Fig. 4.12) from [S II]λ6717/[S II]λ6731 flux ratio (Sanders et al., 2016), ionisation parameter q (middle panel) from [S III]$\lambda\lambda$9069,9532/ [S II]$\lambda\lambda$6717,31 (Díaz et al., 2000), and dust extinction A_V (right panel) from the Balmer Decrement Hα/Hβ (Calzetti et al., 2000). Spatially resolved maps of all these physical quantities, computed from total line ratios, are shown in Fig. 4.12, with contour levels corresponding to $|v| = 300$ km s^{-1} of broad [O III] line emission, which identifies the location of ionised outflows. A S/N>3 on corresponding emission lines employed has been applied to every map.

Interestingly, $n_{\rm e}$ and q maps reveal a highly ionised ridge of low-density gas ($n_{\rm e} \sim 50-100$ cm^{-3}) between the main eastern outflow components. Such a high-ionisation region has been already observed in terms of [O III]/Hβ ratios from narrow-band optical *HST* images by Medling et al. (2021), who interpreted it as due to direct AGN photoinisation (ionisation mechanisms will be further explored via BPT diagrams later in this section; see Fig. 4.13). In addition to this, MUSE WFM data clearly shows that this high-ionisation region spatially anti-correlates with the location of the two redshifted and blueshifted eastern ionised outflows, and is featured by a lower gas density ($n_{\rm e} \sim 50-100$ cm^{-3}) compared to surrounding regions. All this indicates that AGN radiation follows the path of least resistance between the two outflow components, which may be either two separate outflows or represent the receding and approaching components of the same outflow of empty conical geometry. Unfortunately, the situation is less clear to the west, where [S II] line emission is fainter (i.e. S/N<3) and does not allow us to get reliable estimates of $n_{\rm e}$ in most outflow region (blank spaxels in the $n_{\rm e}$ map of Fig. 4.12).

As shown in Sect. 1.1.3 (and in Chapter 2 in more detail), optical emission-line ratios can be also used to explore ionisation mechanisms, distinguishing among different possible ionising sources. In Fig. 4.13, we show spatially resolved [S II] and [N II] BPT diagrams (left panels) of NGC 6240, obtained by combining optical total line ratios from MUSE data. Line ratios have been corrected using A_V extinction previously obtained from Hα/Hβ ratios (see A_V map in Fig. 4.12). Black solid lines in both diagrams indicate the extreme starburst line from Kewley et al. (2001), a theoretical upper limit on SF line ratios; the black dashed curve in the [S II] BPT marks the boundary between Seyferts and LINERs (Kewley et al., 2006), while in the [N II] BPT between star-forming galaxies and AGN as defined in Kauffmann et al. (2003). In addition to the classical subdivision among H II, LINER and AGN ionisation (shown in different colours), in both [S II] and [N II] diagrams we colour of

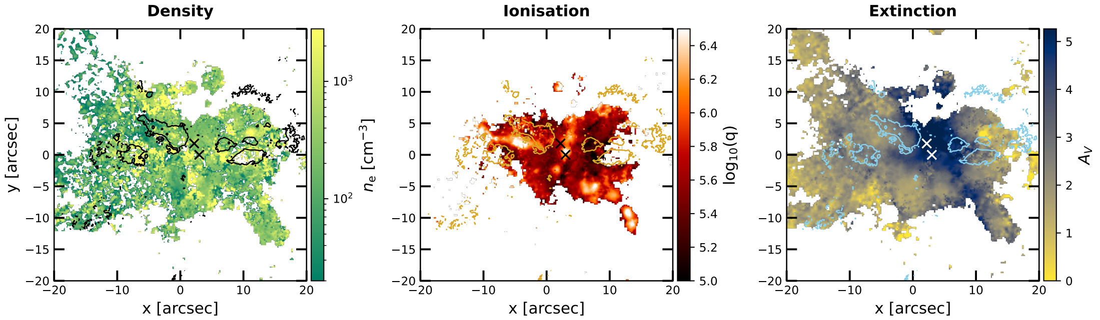

Fig. 4.12 *Ionised gas properties as derived from total optical emission-line ratios detected in MUSE WFM data of NGC 6240. From left, are shown spatially resolved maps of: electron density* n_e *(Sanders et al., 2016), ionisation parameter* q *(Díaz et al., 2000), and dust extinction* A_V *(Calzetti et al., 2000). On top, contour levels corresponding to* $|v| = 300$ *km s*$^{-1}$ *of broad* [O III] *line emission trace the location of ionised outflows. Between the two major eastern outflow regions,* n_e *and* q *maps reveal a highly ionised ridge of low-density gas (*$n_\mathrm{e} \sim 50-100$ *cm*$^{-3}$*). The central region of NGC 6240 surrounding the two nuclei is found to be extremely extincted with* $A_V \gtrsim 4$.

purple those spaxels with highest [S II]/Hα and [N II]/Hα line ratios, respectively, likely associated with most extreme shock ionisation. In magenta, we also mark spaxels forming the highest-[O III]/Hβ extremity of the AGN region in the [N II] BPT. Spaxels lying within the same BPT region have been coloured using the same colour scale, with darker colours corresponding to higher x-axis ratios. Right panels instead show spatially resolved [N II] and [S II] BPT maps, colour-coded according to corresponding BPT classification (see left panels). Both [N II] and [S II] BPT maps have the same contour levels as in Fig. 4.12 drawn on the top, tracing ionised outflows.

According to the [S II] BPT, most of the line emission of NGC 6240 is classified as LINER (green and purple spaxels), with the exception of a few H II regions in the galaxy outskirts (blue spaxels), and Seyfert-like ionisation in correspondence of the high-ionisation ridge-line detected in the q map of Fig. 4.12, featured by $-0.3 <$log([S II]/Hα)< 0.1 (red spaxels) in addition to high log([O III]/Hβ) (>0.2) ratios, further pointing to the high ionisation of these spaxels. The far end of the high-ionisation ridge also exhibits the largest [O III]/Hβ ratios (log([O III]/Hβ)>0.6, pink spaxels in the [N II] BPT), while compact small regions of extreme LINER-like ionisation (largest x-axis ratios, purple spaxels in both BPTs) are found to the west, close to high-velocity regions of outflow emission. Besides the few small regions of extremely high line ratios just discussed (pink and purple spaxels), the overall classification based on the [N II] BPT is consistent with AGN ionisation, with some extended composite regions along the southeast and southwest filaments. Such a composite classification likely results from the combination of both AGN and SF ionisation, being these regions mostly H II-selected according to the [S II] BPT. SF is also identified as

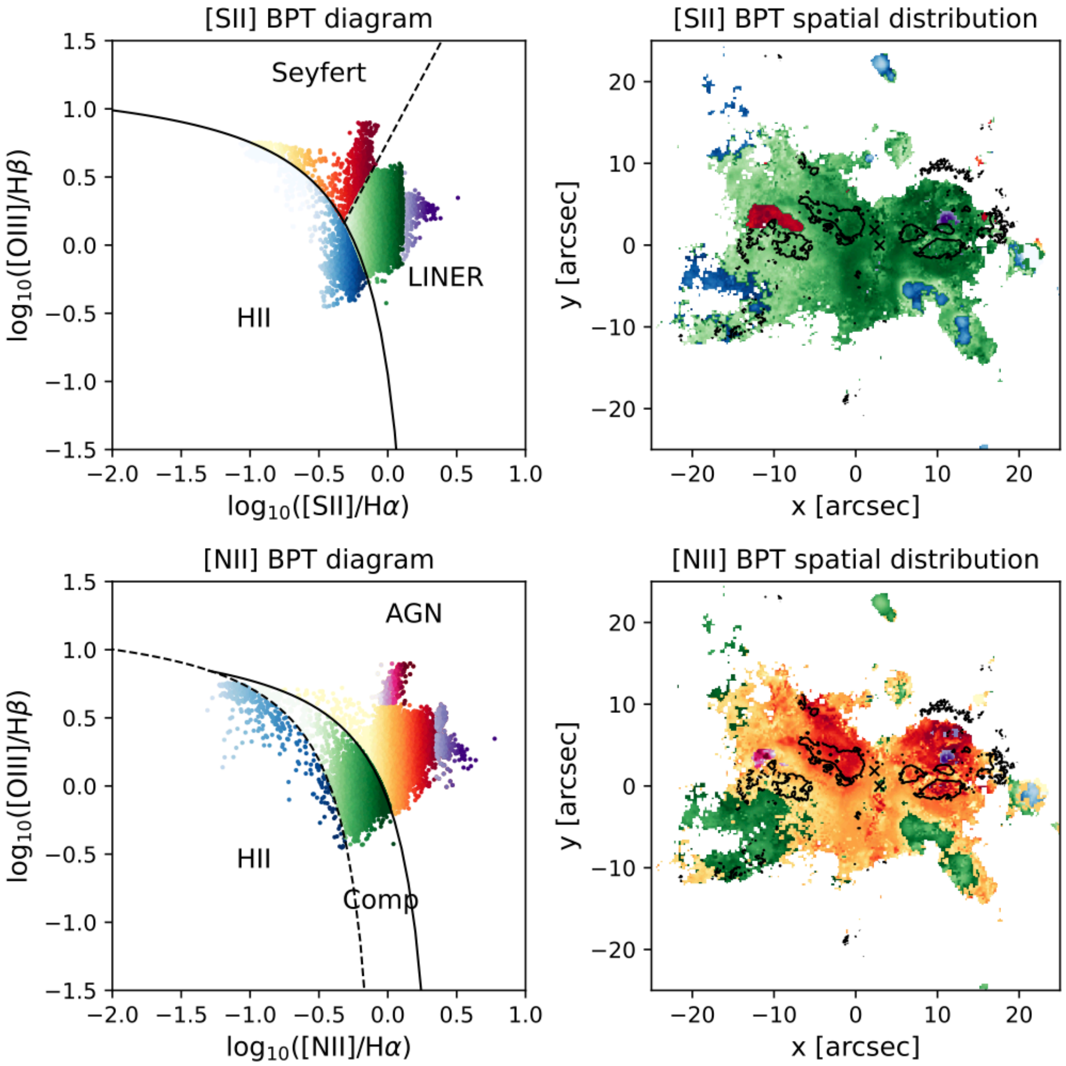

Fig. 4.13 *Left panels:* [S II] *(upper) and* [N II] *(lower) BPT diagrams of NGC 6240, as derived from MUSE data by combining optical total emission-line ratios. In both diagrams, a black solid curve indicates the extreme starburst line inferred by Kewley et al. (2001); while black dashed line marks the boundary between Seyferts and LINERs (Kewley et al., 2006), and between star-forming galaxies (i.e.* H II *regions) and AGN in the* [N II] *BPT (Kauffmann et al., 2003). Also, we colour of purple in both diagrams those spaxels of highest x-axis line ratios, likely associated with more extreme shock ionisation, and of magenta in the* [N II] *BPT those forming the highest-*[O III]/Hβ *extremity of AGN-classified spaxels. Darker colours of the same colourscale (i.e. same* [S II]/[N II] *BPT classification) indicate higher x-axis ratios. Right panels: spatially resolved* [S II] *(upper) and* [N II] *(lower) BPT maps, colour-coded according to the corresponding BPT classification resulting from left-hand panels. Same broad* [O III] *moment-1 contour levels as in Fig. 4.12 trace ionised outflows. The high-ionisation ridge located between eastern outflow components appears as a well-definite collimated region of pure AGN ionisation according to* [S II] *BPT (red spaxels), with the* [N II] *BPT revealing the highest* [O III]/Hβ *ratios located at the far end of the ridge. To the west, compact purple regions, likely tracing shocks, are found in the surroundings of ionised outflow emission.*

the main mechanism responsible for ionisation in the most western gas clump. Finally, we notice that regions of high-velocity outflow emission are all classified as AGN (LINER) according to the [N II] ([S II]) BPT, consistently with the dominant mechanism largely identified across the galaxy. This points to no clear distinction between the origin of eastern and western ionised outflows as opposed to what previously suggested by Müller-Sánchez et al. (2018), who proposed them to be AGN- and starburst-driven, respectively, since they did not detect [O III] line emission west of the nuclei in optical *HST* imaging of NGC 6240.

Our BPT-based findings are overall consistent with the previous results found by Medling et al. (2021), obtained by combining optical narrow-band *HST* images and IFU observations from the Wide-Field Spectrograph (WiFeS) on the ANU 2.3m Telescope (spatial resolution of ~1.5″). In spite of the worse quality of their data compared to MUSE, Medling et al. (2021) indeed found that line-emission from different regions of NGC 6240 is consistent with AGN (LINER) ionisation according to the [N II] ([S II]) BPT, with the high-ionisation ridge line still matching the same classification as that of the other regions but featuring well larger [O III]/Hβ ratios. Thanks to the higher quality (i.e. higher spatial resolution and S/N) of MUSE WFM data of NGC 6240, we have got new crucial insights of the properties of this peculiar high-ionisation region, from its well definite collimated geometry and extremely low gas density, to its spatial anti-correlation with ionised outflows and clear AGN-like ionisation. All this provides further evidence in favour of the interpretation of the high-ionisation ridge previously proposed by Medling et al. (2021), as due to direct AGN photoinisation. In fact, such ridgeline seems to point directly to the southern nucleus and results to be aligned with the rotation axis of its nuclear disk (Medling et al., 2011, 2014). Yet, the spatial resolution achieved by MUSE WFM is not high enough to exclude any ionising contribution to this ridge from the northern nucleus. MUSE WFM observations have delivered us new piece of information on the properties of this region, revealing that AGN radiation field might follow the path of least resistance (i.e. lower gas density) which is interestingly found to anti-correlate spatially with ionised outflows.

4.4.3 Near-IR emission-line diagnostics

As mentioned in Sect. 1.1.3 and at the beginning of this chapter, near-IR emission-line ratios provide crucial diagnostics to investigate gas excitation mechanisms, distinguishing among possible different heating sources (i.e. SF, AGN, LINER; see Sect. 4.4.3.1), and between thermal and non-thermal excitation processes (see Sect. 4.4.3.2). Moreover, as they are less affected by dust extinction, near-IR tracers allow us to probe the ISM emission from regions inaccessible in the optical. In this section, we hence use such near-

IR diagnostics in a spatially resolved manner, to shed light on the excitation properties of the near-IR emitting gas in NGC 6240 on kpc scales. Near-IR based results will be then compared with our findings on ionised gas, obtained previously in Sect. 4.4.2, to check whether near-IR and optical emission-line diagnostics lead to compatible results or unveil different excitation/heating mechanisms. Unfortunately, such an optical/near-IR comparison will be limited to the inner central region of NGC 6240, where the necessary near-IR emission lines are detected at sufficiently high S/N (details in Sects. 4.4.3.1 and 4.4.3.2). We point out that all near-IR emission-line ratios used in the following are not corrected for dust extinction via Brγ/Brδ ratios, due to the blending of Brδ and H_2(2-1)S(5) lines, which prevents us from modelling Brδ accurately.

4.4.3.1 The [Fe II]/Brγ – H_2(1-0)S(1)/Brγ diagram

Combined near-IR [Fe II]/Brγ and H_2(1-0)S(1)/Brγ line ratios have been largely employed in literature to identify the main source of gas heating (e.g. Maiolino et al. 2017, Riffel et al. 2020, 2021a,b), distinguishing among SF, AGN and LINER (e.g. Riffel et al. 2013, Colina et al. 2015). In Fig. 4.14, we study the distribution of total [Fe II]/Brγ and H_2(1-0)S(1)/Brγ line ratios of NGC 6240, as derived from KMOS *H*- and *K*-band observations. Left panels show the near-IR [Fe II]/Brγ – H_2(1-0)S(1)/Brγ diagram, with dashed lines representing boundaries between distinct excitation sources as defined in Riffel et al. (2013), namely: SF, AGN, LINER and transient objects (TOs). In the upper left panel, spaxels with S/N>2 on all employed emission lines have been coloured using different colour scales depending on the IR region of the diagram where they lie (see plot legend); darker colours of the same colour scale indicate larger H_2(1-0)S(1)/Brγ x-axis ratios. All these spaxels have been then mapped in the upper right panel with the same colour coding to check their spatial location. Due to the faintness of the Brγ emission line in our KMOS observations, and due to the blending of Brδ with H_2 emission, we can unfortunately probe gas excitation conditions only in the more central region of NGC 6240, within few kpc from the nuclei. Yet, in this central region, we find distinct regions of spaxels, classified as due to distinct processes. A small compact region, centrally located on the southern nucleus, results in being AGN excited according to the IR classification by Riffel et al. (2013), while surrounding central regions are largely identified as either LINER or TOs. IR AGN-classified spaxels are also found in more external regions: they all show AGN-like line ratios similar to those observed in correspondence of the southern nucleus, except for the most distant ones (~6$''$ from the centre to west), featuring lower H_2(1-0)S(1)/Brγ ratios, closer to the SF region of the IR diagram, which suggest a weaker AGN ionisation. Finally, we point out that all plotted line ratios are observed measurements not corrected for dust

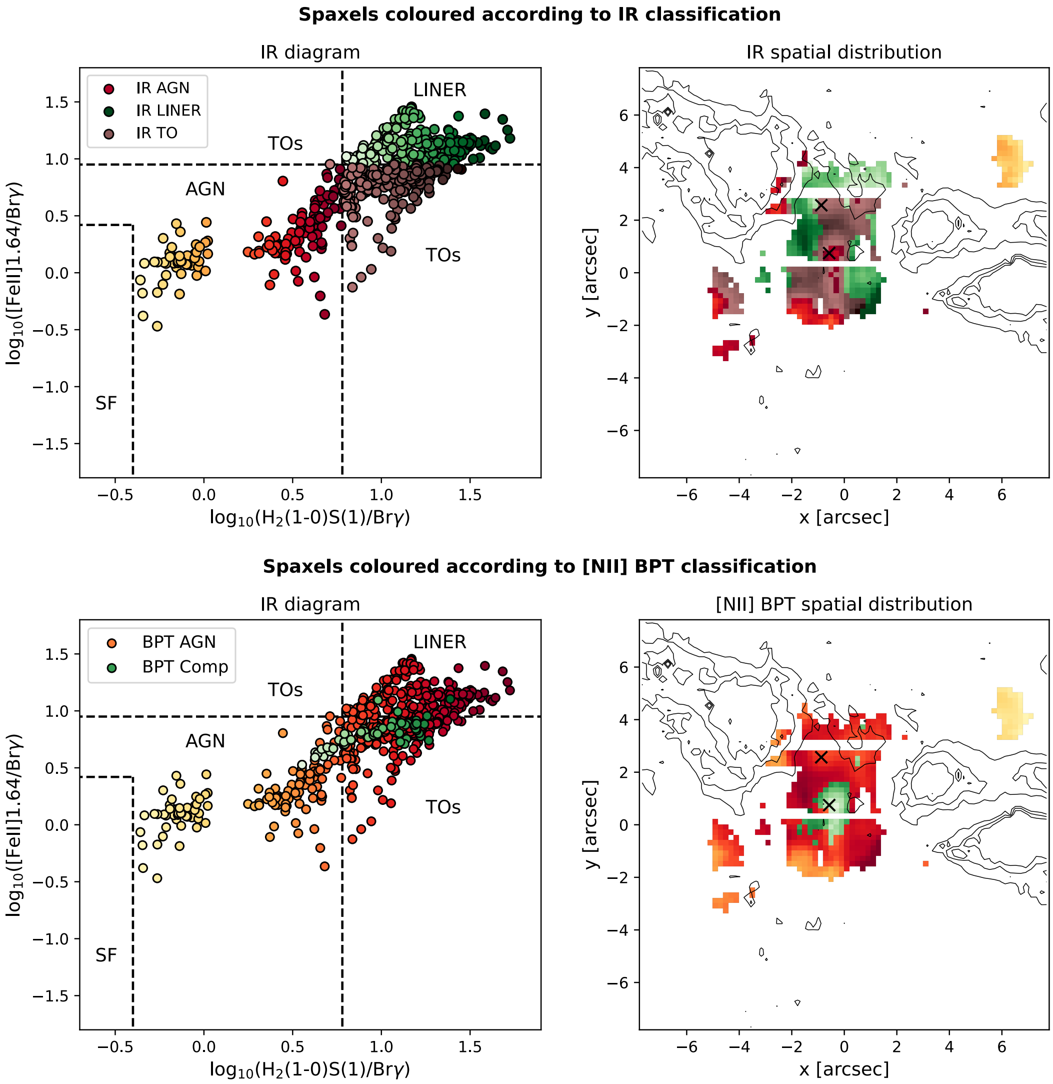

Fig. 4.14 *Upper panels: near-IR* [Fe II]/Brγ – H_2(1-0)S(1)/Brγ *diagram (left) and spatially resolved map (right) of the resulting IR classification for spaxels with S/N>2 on all employed near-IR emission lines, as detected in KMOS observations of NGC 6240. Different colour scales represent spaxels lying in different regions of the IR diagram, demarcated by dashed lines as defined by Riffel et al. (2013), namely: SF (no data points), AGN (yellow-to-red), transient objects (TOs; brown), LINER (green); darker colours of the same colour scale indicate higher* H_2(1-0)S(1)/Brγ *ratios. Same colour coding has been used to map spaxels in the right-hand plot, where black contours correspond to levels of increasing absolute velocity (200, 300, 400 km s*$^{-1}$*) relative to broad* [O III] *line emission, tracing ionised outflows. Lower panels: same pair of plots as in the upper panels but with S/N>2 spaxels colour-coded according to their optical AGN (yellow-to-red) or composite (green) classification based on* [N II] *BPT, while they are all LINER-selected by the* [S II] *BPT. By comparing results from optical BPT and near-IR diagnostics, we do not find any clear match between the two resulting classifications. Near-IR emission lines might be useful to probe the nature of excitation/ionisation sources in more extincted regions, where optical BPT have limited access.*

extinction. Therefore, they might underestimate the real flux-ratio measurements, with possibly more data points lying in the LINER region, although dust extinction is expected to affect near-IR wavelengths less than optical ones.

In the lower panels of Fig. 4.14 we display the same pair of plots as above, but spaxels here are coloured according to their optical classification based on the [N II] diagram. Considering the same S/N>2 (driven by Brγ), we plot the same spaxels from the inner central region as in the upper panels, which are exclusively classified as either AGN (red) or composite (green) according to the [N II] BPT. The distribution of [N II] BPT AGN and composite spaxels in the IR [Fe II]/Brγ – H_2(1-0)S(1)/Brγ plane does not point to any clear spatial separation between the two optical spaxels' populations, with both extending from the IR AGN region, through IR TOs, to IR LINERs. Any possible match between optical and near-IR classification is further disfavoured if we consider that all these plotted spaxels are identified as LINER by the [S II] BPT (see corresponding region in the upper right panel of Fig. 4.13), while both AGN and LINER spaxels are separately identified via IR diagnostics. Being less affected by dust extinction, near-IR emission lines might indeed be useful in unveil ionisation/excitation sources in more obscured regions, which cannot be probed deeply enough by optical BPT diagnostics.

Our results seem to be overall consistent with previous ones based on near-IR Gemini NIFS IFU observations of the inner kpc region of NGC 6240, presented by Ilha et al. (2016). They indeed found H_2(1-0)S(1)/Brγ and [Fe II]λ2.07/Brγ pointing to AGN X-ray heating close to both nuclei, while to shocks in the region between the two nuclei. Due to the presence of blank horizontal stripes, unfortunately we cannot probe the region surrounding the northern nucleus.

Since narrow and broad (outflow) line components are expected to be associated with distinct kinetic components, in Fig. 4.15 we plot separately near-IR line ratios relative to narrow (pink crosses) and outflow (grey circles) components in the near-IR [Fe II]/Brγ – H_2(1-0)S(1)/Brγ diagram, considering a S/N>2 on narrow/outflow components of all emission lines employed. As pointed out for total line ratios shown in Fig. 4.14, narrow/outflow line ratios here plotted are likely to slightly underestimate real ratio values, being not corrected for dust extinction. Nonetheless, we find that outflow points are overall located at lower line ratios, consistent mostly with AGN or TO excitation. Narrow measurements are instead distributed across the TO and LINER regions. This might indicate that direct AGN radiation might be the dominant responsible for the excitation of gas funneled within outflows, which in turn might shock against the surrounding nearly-systemic galactic medium, thus leading to narrow line ratios more consistent with LINER

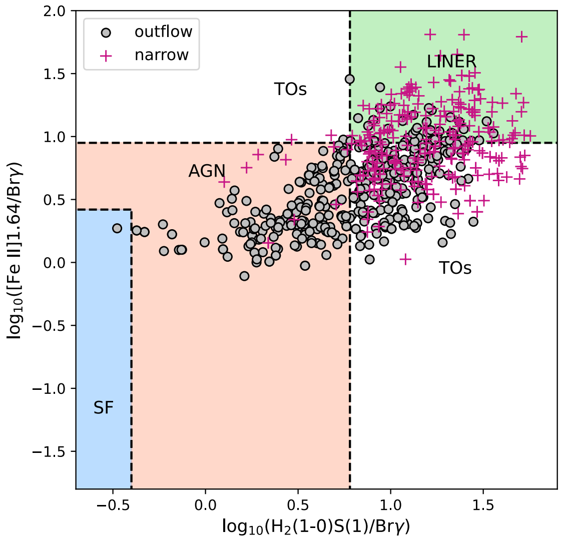

Fig. 4.15 *Near-IR* [Fe II]/Brγ – H_2(1-0)S(1)/Brγ *diagram separately for outflow (grey circles) and narrow (pink crosses) emission-line ratios, with S/N> 2 on narrow/outflow line components. Regions of different excitation mechanisms have been marked with different colours following the classification by Riffel et al. (2013). The distribution of outflow points is shifted towards lower line ratios more consistent with AGN-like excitation, while narrow measurements are more compatible with LINER. The latter might be due to shocks produced by fast outflowing gas excited by direct AGN radiation.*

excitation. Another possibility is that narrow line emission due to AGN ionising photons is filtered by dust (e.g. Mingozzi et al. 2019), thus leading to LINER-like line ratios.

4.4.3.2 The H_2(1-0)S(2)/H_2(1-0)S(0) – H_2(2-1)S(1)/H_2(1-0)S(1) diagram

In addition to the near-IR [Fe II]/Brγ – H_2(1-0)S(1)/Brγ diagram, in this section we combine H_2 emission-line ratios to further investigate gas excitation mechanisms. In Fig. 4.16, we show the near-IR H_2(1-0)S(2)/H_2(1-0)S(0) – H_2(2-1)S(1)/H_2(1-0)S(1) diagram used in previous works to distinguish among thermal and non-thermal excitation processes (e.g. Mouri 1994, Ramos Almeida et al. 2009, Mazzalay et al. 2013, Riffel et al. 2013, 2021a,b). Upper panels show the near-IR H_2 diagram (left) and corresponding spatially resolved map (right) of spaxels with a S/N>2 on all emission lines, as detected in KMOS observations of NGC 6240. Spaxels are coloured of yellow to red at increasing y-axis ratio values. Regions of thermal (yellow shading) and non-thermal (purple shading) excitation are delimited, respectively, by vertical dashed and dotted lines from Mouri (1994). In the near-IR H_2 diagram we additionally plot model predictions for thermal UV (purple crossed-solid line; Sternberg and Dalgarno 1989), X-ray (yellow crossed-solid line; Lepp and McCray 1983, Draine and Woods 1990) and shock (cyan star; Brand et al. 1989), and non-thermal

UV fluorescence (purple crosses; Black and van Dishoeck 1987). Black contours in the right-hand map represent the same absolute velocity levels as in Fig. 4.14, tracing ionised outflow emission.

We find the distribution of H_2 line ratios of NGC 6240 to be well located within the thermal region of the diagram. In particular, the bulk of points is compatible with thermal shock excitation, consistently with findings from previous near-IR studies (e.g. Tecza et al. 2000, Ohyama et al. 2003, Max et al. 2005, Engel et al. 2010) pointing to shocks as the dominant excitation mechanism taking place in NGC 6240. In particular, we notice that more central regions of NGC 6240 feature lower y-axis ratios compared to more external spaxels, with the lowest H_2(1-0)S(2)/H_2(1-0)S(0) ratios (yellow) found in correspondence of the southern nucleus. Larger ratios (orange/red) in more external regions instead are also consistent with thermal X-ray excitation from AGN. This seems to be overall consistent with the near-IR classification resulting from the near-IR [Fe II]/Brγ – H_2(1-0)S(1)/Brγ plane in Sect. 4.4.3.1 (see Fig. 4.14), where LINERs are identified as the main mechanism in the central region - with the exception of the southern nucleus exhibiting an AGN-like excitation -, whereas AGN excitation is found in more external spaxels. As pointed out in Sect. 4.4.3.1, observed H_2 line ratios might however slightly differ from their intrinsic (i.e. dust-corrected) values.

Finally, lower panels display the same plots as the upper ones, with the difference that spaxels are coloured according to their [N II] BPT classification into either AGN (yellow-to-red) or composite (green) line emission. BPT composite spaxels lie close to thermal shock predictions, while AGN spaxels extend also to larger y-axis ratios, near predictions for thermal X-ray excitation. Yet, no clear separation between distinct BPT-classified categories of spaxels overall comes out from this diagram, suggesting that this near-IR diagnostic and BPT diagrams probe different gas phases which are not necessarily subject to the same dominant mechanisms.

4.5 Conclusions and future steps

In this chapter, we presented preliminary results from the analysis of the combined IFU panoramic spectroscopy of NGC 6240 obtained with optical MUSE WFM and near-IR KMOS mosaic observations. Contrary to most of the previous IFU works targeting this galaxy, the larger FoV of our data allows an unprecedented spatially resolved multi-phase study of the large-scale outflows in this peculiar object, in both ionised, neutral atomic and warm molecular phases. While we will trace the neutral atomic phase via NaD I line absorption (e.g. Perna et al. 2020), in this chapter we have presented preliminary

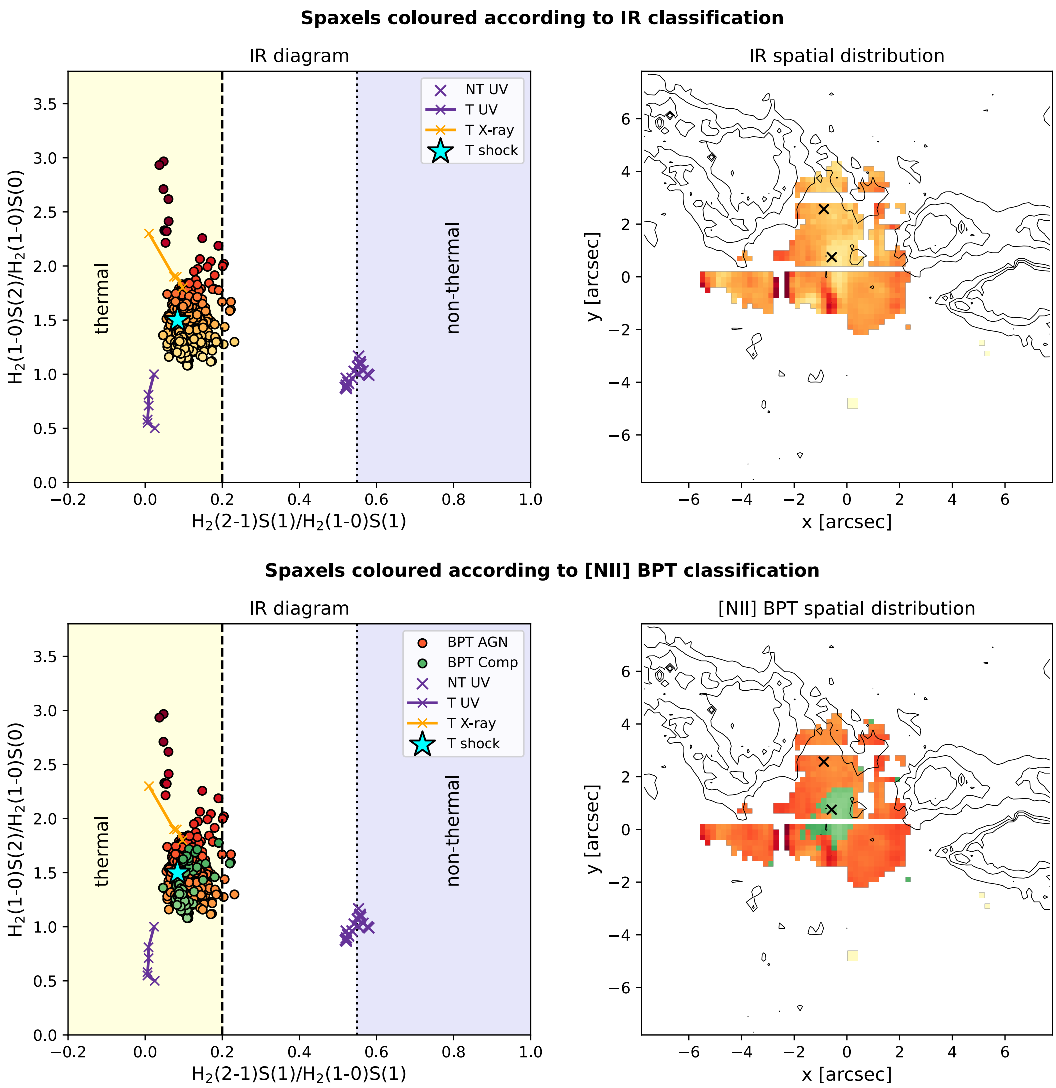

Fig. 4.16 *Upper panels: near-IR* $H_2(1\text{-}0)S(2)/H_2(1\text{-}0)S(0)$ – $H_2(2\text{-}1)S(1)/H_2(1\text{-}0)S(1)$ *diagram (left) and spatially resolved map (right) of spaxels with a S/N>2 on all emission lines, as detected in KMOS observations of NGC 6240. Spaxels are coloured of yellow to red at increasing y-axis ratios. Vertical dashed and dotted lines mark the boundary of thermal (yellow shading) and non-thermal (purple shading) excitation processes (Mouri, 1994), respectively. Along with observational measurements, we plot in the IR diagram model predictions for thermal (T) UV (purple crossed-solid line; Sternberg and Dalgarno 1989), X-ray (yellow crossed-solid line; Lepp and McCray 1983, Draine and Woods 1990) and shock (cyan star; Brand et al. 1989), and non-thermal (NT) UV fluorescence (purple crosses; Black and van Dishoeck 1987). Same contour levels as in Fig. 4.14 trace ionised outflows in the right-hand map. The distribution of* H_2 *line ratios lies in the thermal region of the diagram, pointing to thermal shock excitation as the dominant mechanism taking place in NGC 6240, especially in more central regions. In more external regions, we also find larger ratios consistent with thermal X-ray. Lower panels: same plots as above but spaxels colour-coded according to their optical* [N II] *BPT AGN (yellow-to-red) or composite (green) classification. BPT composite spaxels are clustered around thermal shock predictions, while AGN spaxels extend up to higher y-axis ratios, close to thermal X-ray model predictions. Besides this, no clear separation between BPT-classified spaxels comes out from this diagram.*

results on ionised outflows, as traced via optical Hα and [O III] line emission, and warm molecular outflows via near-IR H_2 transitions. From the comparison between these two gas phases, we found that ionised and warm molecular outflows in NGC 6240 are co-spatial and exhibit a similar kinematics (see Fig. 4.10). Compared to warm molecular gas traced in KMOS observations, optical MUSE WFM data reveal a more complex kinematics of ionised kinematics, with pairs of blueshifted and redshifted outflow regions east and west of the two nuclei, as well as disk rotation and tidal features due to the ongoing merger (see Figs. 4.6 and 4.7). Contrary to what found by Müller-Sánchez et al. (2018), all ionised outflows detected appear to have an AGN-driven origin, considering their location outside the galaxy plane, elongated morphology pointing to the nuclear region, as well as emission-line ratios compatible with AGN ionisation (see Fig. 4.13).

The exquisite sensitivity of MUSE WFM has also allowed us to infer fundamental ionised gas properties, such as electron density n_e, ionisation q, dust extinction A_V, and dominant ionisation mechanisms via BPT diagrams (e.g. Osterbrock 1981, Veilleux and Osterbrock 1987). Spatially resolved maps of all these properties unveil an elongated high-ionisation ridgeline residing with eastern redshifted and blueshifted outflow components (see middle panel of Fig. 4.12). Interestingly, this ridgeline features a low gas density (i.e. $n_\mathrm{e} \sim 50-100\ \mathrm{cm}^{-3}$) compared to surrounding region (see left panel of Fig. 4.12), and is fully compatible with AGN-like ionisation based on BPT diagrams (see Fig. 4.13), as suggested by previous observations at lower spatial resolution and sensitivity (Medling et al., 2011). This high-ionisation ridge might be ionised by direct AGN radiation, which follow the path of least resistance (i.e. lower densities) within the two blueshifted and redshifted outflow regions. These might be either two separate outflows, or approaching/receding sides of the same outflow cone.

Moreover, both optical and near-IR line emission points to the key role played by shocks to ionise/excite gas in NGC 6240. Indeed, LINER-like ionisation is largely detected across the field, with more extreme shock-ionised regions surrounding the western outflows, as revealed by the largest optical [N II]/Hα and [S II]/Hβ ratios. Near-IR line emission gives further support to thermal shocks as one of the dominant excitation source of H_2 line emission in NGC 6240 (see Figs. 4.14 and 4.16). In particular, shock excitation seems to affect more narrow systemic line components than outflow ones, which are more consistent with AGN-like excitation (see Fig. 4.16). The comparison of the results from optical and near-IR emission-line diagnostics highlights the importance of using to latter to probe gas excitation/ionisation mechanisms of more dust-enshrouded ISM components, which cannot be investigated deeply enough by optical - more extincted - emission lines.

In future, we will complete the analysis by calculating outflow properties (e.g. velocity, mass rate) for different gas phases. In addition to ionised and warm molecular outflows, we will also map the neutral atomic phase of outflows via NaD I absorption lines, and complement our three-phase outflow description with archival ALMA data tracing the cold molecular component of outflows. We will compare the properties of outflows in these four distinct gas phases and shed light on their most likely nature as due to either AGN or starburst, or even a combination of both. The comparison of large-scale outflow energetics with that of nuclear X-ray winds (Mizumoto et al., 2019) will also help us distinguish among different acceleration mechanisms. This study will hence provide a unique view of spatially resolved properties of multi-phase outflows on kpc scales in a nearby impressive galaxy merger such as NGC 6240.

Chapter 5

Connecting X-ray UFOs with galaxy-scale ionised winds in two z∼1.5 lensed AGN

The work presented in this chapter aims at investigating the connection of galaxy-scale outflows with X-ray nuclear winds, to shed light on the acceleration mechanism of AGN-driven winds on kpc scales. We use VLT/SINFONI observations to trace the ionised phase of galaxy-scale outflows in two lensed quasars known to host X-ray UFOs at z∼1.5, that is close to the Cosmic Noon - the golden epoch of AGN feedback. Our inferred results considered along with those from similar studies provide interesting insights of the link between large-scale and nuclear outflows, in the framework of wind feedback models. Adapted from Tozzi et al. (2021), A&A, 649, A99.

Throughout Sect. 1.2, we have seen that X-ray UFOs (Sect. 1.2.3.1) are considered promising candidates as nuclear 'engine' powering more massive outflows on galaxy scales, as predicted by wind feedback models (e.g. King and Pounds 2015). According to these models, galaxy-scale outflows propagate in either a momentum-driven or an energy-driven regime, depending on the cooling efficiency in the shocked gas shell. Momentum-driven winds are expected to provide a low-efficiency feedback, whereas energy-driven counterparts involve larger gas mass and energy, hence they can efficiently either remove or heat the galactic gas via energy injection (see Sect. 1.2.2.1).

Whereas UFOs have been widely detected in the Local Universe (e.g. Tombesi et al. 2010, Gofford et al. 2013, Nardini et al. 2015), the search for UFOs at high redshift ($z > 1$) is hampered by resolution and/or sensitivity limits of the current observing facilities. In fact, there are currently only 14 AGN known to host X-ray UFOs at $z > 1$ (see Dadina et al. 2018, Chartas et al. 2021 on the list of published objects). Among these, twelve are gravitationally lensed systems (Hasinger et al. 2002, Chartas et al. 2003, 2007, 2009b, 2016, 2021, Dadina et al. 2018). Thanks to the magnified view of background sources, strong gravitational lensing is indeed a well-known, powerful tool to investigate properties of high-redshift, which has enabled new measurements and spatially resolved studies, which otherwise would not have been possible beyond the local Universe (e.g. Peng et al. 2006, Ross et al. 2009, Bayliss et al. 2017, Spingola and Barnacka 2020, Stacey et al. 2021).

To shed light on outflow acceleration mechanisms, we need to collect larger and larger samples of AGN with detection of both X-ray UFOs and large-scale outflows, so that we can compare wind energetics on nuclear and galaxy scales to finally test model predictions. In such a perspective, in this chapter we investigate the connection between nuclear UFOs and large-scale outflows for the first time - in two lensed quasars close to the peak of AGN activity ($z \sim 2$). In doing so, we combine VLT/SINFONI observations (analysed in Sect. 5.2) to trace ionised outflows via [O III]λ5007 line emission (Sect. 1.2.3.2) and measurements from the literature on X-ray, highlighting (and taking advantage of) of the rare strong gravitational lensing affecting these two objects. In this chapter, we adopt a ΛCDM flat cosmology with $\Omega_{\mathrm{m},0} = 0.27$, $\Omega_{\Lambda,0} = 0.73$ and $H_0 = 70$ km s^{-1} Mpc^{-1}.

5.1 Description of the quasars in this work

5.1.1 Selection of targets

Our sample consists of two $z \sim 1.5$ multiply lensed quasars, HS 0810+2554 and SDSS J1353+1138, observed with VLT/SINFONI (Eisenhauer et al., 2003) within as part of the observing program 0102.B-0377(A) (PI: G. Cresci). These objects were specifically selected for being known UFO hosts (Chartas et al., 2016, 2021), and having a redshift ($z \sim 1.5$ and $z \sim 1.6$ for HS 0810+2554 and SDSS J1353+1138, respectively) such that rest-frame optical [O III]λ5007 emission lies in the near-IR wavelength range observed by SINFONI. This selection in redshift leads to consider objects at epochs close to the Cosmic Noon ($z \sim 2$), with [O III]λ5007 redshifted to the near-IR J-band ($\lambda \sim$1.1–1.4 μm) of SINFONI for $z \sim 1.5$ targets (as those two examined in this work).

In total, there are 14 known high-redshift ($z > 1$) quasars with UFO detection (see Dadina et al. 2018, Chartas et al. 2021 for the full list). These are among the brightest - in terms of 2–10 keV luminosity ($L_{2-10\ \mathrm{keV}} > 10^{45}$ erg s^{-1}, except for PID352 $L_{2-10\ \mathrm{keV}} \sim 10^{44}$ erg s^{-1}) - quasars at high redshift. This is because they are: either intrinsically luminous (of the total 14-AGN sample, only HS 1700+6416 and PID352; Lanzuisi et al. 2012, Vignali et al. 2015); or subject to gravitational lens magnification (Hasinger et al., 2002, Chartas et al., 2003, 2007, 2009b, 2016, Dadina et al., 2018, Chartas et al., 2021). In both cases,

Table 5.1 *Properties of HS 0810+2554 and SDSS J1353+1138, the quasars examined in this chapter.* ^{a}*Redshifts are measured from the [O III] systemic component in integrated spectra extracted from the nuclear region of both sources (Sects. 5.2.1.1 and 5.2.2).*

Target name	α(J2000)	δ(J2000)	z^{a}	scale
HS 0810+2554	$08^{h}13^{m}31^{s}.3$	$+25°45'03''$	1.508 ± 0.002	8.67 kpc/$''$
SDSS J1353+1138	$13^{h}53^{m}06^{s}.34$	$+11°38'04''.7$	1.632 ± 0.002	8.69 kpc/$''$

X-ray observations of these objects have delivered high-quality spectra exhibiting clearly X-ray UFO absorption features, in spite of their high redshift ($z > 1$). Amongst this $z > 1$ UFO-host sample, APM 08279+5255 ($z \sim 3.9$; Hasinger et al. 2002) is the only $z > 1$ quasar with a clear detection of both nuclear UFOs and a galaxy-scale outflow detected in molecular phase (Feruglio et al., 2017). Recent ALMA observations have revealed the tentative detection (at ~3–5σ confidence level) of a molecular outflow also in HS 0810+2554 (Chartas et al., 2020). Therefore, this work will map for the first time ionised outflows in known UFO-hosts at $z > 1$, thus extending to three the number of $z > 1$ quasars for which it is possible to investigate the connection of nuclear UFOs with large-scale outflows (in at least one gas phase). HS 0810+2554 will be also the first quasar ever having a three-phase description of AGN winds, including nuclear UFOs: highly ionised (X-rays; Chartas et al. 2016, 2021), ionised (optical; this work) and molecular (millimetric; Chartas et al. 2020. In the following, we provide a short description of HS 0810+2554 and SDSS J1353+1138, with their main properties listed in Table 5.1.

5.1.1.1 HS 0810+2554

HS 0810+2554 is a radio-quiet, NAL (one of the few known NAL system with X-ray UFO detection; see Sect. 1.2.3.1) quasar at $z \sim 1.5$, which was discovered by Reimers et al. (2002). It consists of four lensed images in a typical fold lens configuration with the two southern, brightest images in a merging pair configuration (A+B), as shown in the *Hubble Space Telescope (HST)* image in Fig. 5.1 (left panel). The lens galaxy (labelled with G) is detected in the *HST* image, and its redshift is estimated to be $z_{\mathrm{l}} \sim 0.89$ from the separation and the redshift distribution of existing lenses (Mosquera and Kochanek, 2011). Quadruply lensed quasars occur in extremely strong lensing regimes (e.g. Narayan and Bartelmann 1996), when the compact and bright UV accretion disk and X-ray corona emission regions overlap the lens caustics. This leads to high magnification factors, whose values strongly depend on the image and lens positions. As a consequence, a small change in the input parameters to the lens models (image and lens positions) can lead to a significant change in the image magnifications. For HS 0810+2554, estimates of the magnification factor μ

in different spectral bands are found in the literature, in particular for the X-ray ($\mu \sim 103$; Chartas et al. 2016), optical ($\mu \sim 120$; Nierenberg et al. 2020), and radio emission ($\mu \sim 25$; Jackson et al. 2015).

HS 0810+2554 was singled out as an exceptionally X-ray bright lensed object during an X-ray survey of NAL AGN with outflows of UV absorbing material (Chartas et al., 2009a). More recent *Chandra* and *XMM-Newton* observations (Chartas et al., 2016) provided definitive X-ray proofs for the presence of a highly ionised, relativistic wind in the source nuclear region. The strongly blueshifted absorptions of highly-ionised metals (i.e. Fe XXV, Si XIV) indicate outflow velocity components within the range of $0.1-0.4\ c$. The VLT/UVES spectrum of HS 0810+2554 also shows blueshifted absorptions of C IV and N V doublets, which point to the existence of UV absorbing material moving with an outflowing speed of $v_{\rm CIV} = 19,400$ km s^{-1} (Chartas et al., 2014, 2016). Although classified as radio-quiet object, VLA observations at 8.4 GHz (Jackson et al., 2015) show that HS 0810+2554 hosts a radio core, thus demonstrating that it is not radio-silent.

HS 0810+2554 was also recently observed with ALMA in the mm-band (Chartas et al., 2020). The analysis of ALMA data has shown the tentative detection of high-velocity clumps of CO(J=3→2) emission, suggesting the presence of a massive molecular outflow on kpc scales. With our characterisation of the ionised gas phase of the outflow blowing in HS 0810+2554, we have - for the first time ever - a three-phase description of an AGN-driven wind at high redshift, from nuclear to the galaxy scales: the highly-ionised, ionised, and neutral molecular gas phases, thanks to a broadband spectral coverage ranging from X-ray to optical and mm bands.

5.1.1.2 SDSS J1353+1138

Unlike HS 0810+2554, widely observed in several spectral bands, SDSS J1353+1138 has been less intensively studied, as its discovery is more recent (Inada et al., 2006). This object was selected from the SDSS as a candidate double lensed quasar at $z \sim 1.6$. Inada et al. (2006) during the University of Hawai'i 88-inch Telescope (UH88) follow-up observations of SDSS J1353+1138, obtaining *V*, *R*, *I* and *H*-band images of the source. The two lensed images are well-distinguishable (see right panel in Fig. 5.1), with an angular separation of $\Delta \sim 1.40''$ (Inada et al., 2006).

More recently, on 2016 January 13, SDSS J1353+1138 was observed with *XMM-Newton*. The analysis of its X-ray spectrum (Chartas et al., 2021) revealed a significant absorption at ~ 6.8 keV (consistent with Fe XXV), indicating the presence of a $\sim 0.31c$ UFO.

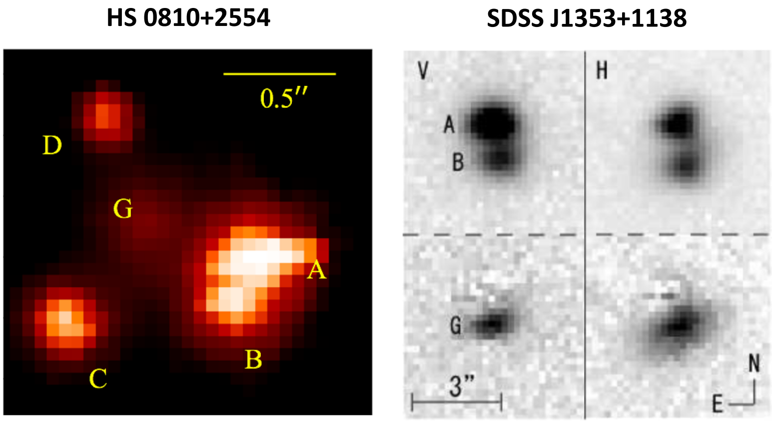

Fig. 5.1 *Lensed images of HS 0810+1154 (left) and SDSS J1353+1138 (right). Left. HST ACS F555W image of HS 0810+2554 showing the four magnified images of the background quasar in fold lens configuration: the C and D images are spatially resolved, while the pair A+B is blended together. At the centre, we can see the emission from the foreground lens galaxy. Right. V and H-band images from Inada et al. (2006) SDSS J1353+1138 taken at the UH88 telescope (upper panels) and corresponding images after the subtraction of A and B components (lower panels), clearly showing the lens galaxy (component G).*

5.1.2 SINFONI observations and data reduction

SINFONI observations of HS 0810+2554 and SDSS J1353+1138 were carried out on two different nights in February and March 2019, respectively, in the near-IR J-band ($\lambda \sim 1.1$–$1.4\ \mu$m) and with a spectral resolution $R = 2000$. The observations were performed in seeing-limited mode[1], using the $0.250'' \times 0.125''$ pixel scale which provides a total FoV of $8'' \times 8''$, essential to map gas dynamics on galaxy scales. The airmass varied during the observations of each target, spanning a range of ∼1.7–1.9 and ∼1.2–1.3 for HS 0810+2554 and SDSS J1353+1138, respectively. The data were obtained in eight and sixteen integrations of 300s each, for a total of 40 min for HS 0810+2554, and 80 min for SDSS J1353+1138. During each observing block, an ABBA pattern was followed: the target was put alternatively in two different positions of the FoV about 4.3″ apart, to perform sky subtraction through a nodding technique. A dedicated star observation to measure the PSF was not available in either case but the estimated angular resolution is ∼0.7″ (∼0.8″) for HS 0810+2554 (SDSS J1353+1138), based on the measured extent of the spatially unresolved BLR emission (see Sect. 5.2.3). Finally, a standard B-type star for telluric correction and flux calibration was observed shortly before or after the on-source exposures.

We reduce SINFONI data using the ESO SINFONI pipeline (v. 3.2.3). Before flux calibration and co-addition of single exposure frames, we correct for atmospheric dispersion

---

[1] The SINFONI AO module was not available at the time of the observations, since SINFONI had been already moved from UT4 to UT3 for the last few months of its research activity.

effects consisting in a significant change of the AGN continuum emission across the FoV of both sources. This is a consequence of the differential atmospheric dispersion at different wavelengths, which makes the measured spectra not as ‘straight’ as expected. In practical terms, as the wavelength increases, an increasingly larger fraction of emission gets deposited into adjacent pseudo-slits, producing a coherent spatial shift of the target as a function of λ. Additionally, possible flexures in the instrument may contribute to producing the observed shift. In order to limit the impact of these optical distortions, we spatially align the emission centroid channel-by-channel in each single-exposure, sky-subtracted cube by adopting the following procedure.

For each cube, we first determine, in every spectral channel, the average position of the emission centroid on the FoV through a 2D-Gaussian fit. Then we calculate the shift of the centroid mean position with respect to the centroid position in the first spectral channel, assumed as reference channel. In both spatial directions on the FoV, we find an increasing trend of the shift at increasing wavelengths, which we model with a two-degree polynomial to neglect the presence of some spikes, due to noisier channels. The spatial shift, totally observed from the bluest to the reddest spectral channel, spans the range of $\sim 0.5-1$ pixel among the various single-exposure cubes of both targets. As the spatial shifts are fractional in units of pixels, we adopt the Drizzle algorithm (Gonzaga et al., 2019, Fruchter and Hook, 2019) to optimise the alignment of every spectral channel in each raw single-exposure data cube.

Finally, we perform the flux calibration and the co-addition of the single-exposure cubes. The final sky-subtracted, flux-calibrated data consist of $100 \times 72 \times 2234$ data cubes, hence, each one including more than 7,000 spectra. Each spectrum is sampled by 2234 channels with a 1.25 Å channel width and covers the spectral range $\sim 1.1-1.4$ μm, corresponding to about 4400 – 5600 Å rest-frame wavelengths.

5.1.3 Lens models for the two quasars

As both objects are gravitationally lensed quasars, lens models are required to infer intrinsic (i.e. unlensed) outflow properties, such as its intrinsic radius and unlensed flux, which are key ingredients to derive outflow energetics.

Both quasars are lensed by a foreground elliptical galaxy and detailed lens models for both objects can be found in the literature. In particular, for HS 0810+2554, there are several lens models reported in literature obtained from observations performed in different spectral bands (e.g. from VLA-radio data in Jackson et al. 2015, from ALMA-mm data in Chartas et al. 2020). In this work, we adopt the most recent model for HS 0810+2554 obtained by Nierenberg et al. (2020), based on *HST*-WFC3 IR observations:

images and lens galaxy positions have been measured from direct F140W wide imaging (central wavelength ~1392 nm), while slitless dispersed spectra have been provided by the grism G141 (useful range: 1075–1700 nm). Assuming $z_\mathrm{l} \sim 0.89$ for the lens galaxy (Mosquera and Kochanek, 2011), Nierenberg et al. (2020) modelled the deflector mass distributions with a singular isothermal ellipsoid (SIE), plus an external shear to account for tidal perturbations from nearby objects.

Detailed lens models for SDSS J1353+1138 are presented in Inada et al. (2006) and Rusu et al. (2016), based on imaging observations in the i-band with the Magellan Instant Camera (MagIC) on the Clay 6.5m Telescope and in the K-band with the Subaru Telescope adaptive optics system, respectively. Inada et al. (2006) modelled the lens mass distribution using either a SIE model, or a singular isothermal sphere (SIS) model plus a shear component (γ), and estimated the lens redshift to be $z_\mathrm{l} \sim 0.3$ based on the Faber-Jackson relation (Faber and Jackson, 1976). The resulting total magnification factors μ are 3.81 and 3.75 from the SIS+γ and SIE model, respectively. Still assuming $z_\mathrm{l} \sim 0.3$, Rusu et al. (2016) found slightly lower values for total magnification: $\mu \sim 3.47$ (SIS+γ), $\mu \sim 3.42$ (SIE) and $\mu \sim 3.53$ (SIE+γ). We use all these magnification values from the literature to determine the unlensed flux carried by the ionised outflow in SDSS J1353+1138. Instead, for HS 0810+2554, we will provide an estimate of the ionised outflow magnification ($\mu_\mathrm{out} \sim 2$) starting from our data. Such values will be discussed further in Sect. 5.3.2.

5.2 Data analysis

5.2.1 Spectral fitting

For the spectral analysis of SINFONI data, we adopt the fitting procedure presented in Marasco et al. (2020) (see Sect. 1.3.3. Here, we implement the code to handle SINFONI data, introducing adjustments and new functionalities depending on the specific necessities of our data. In particular, we aim at performing a kinematic analysis of diffuse ionised gas, with primary focus on [O IIIλ5007 line emission (hereafter [O III]), the optimal tracer of ionised outflows, as mentioned at the beginning of this chapter (see also Sect. 1.2.3). Since reduced data cubes are produced by the ESO SINFONI pipeline with no noise cubes associated, we associate a single noise value to each channel in our SINFONI data cubes, computed as root mean square (rms) of the fluxes extracted spaxel-by-spaxel in a region with no significant emission from the target. Details on the spectral analysis of SINFONI data of HS 0810+2554 and SDSS J1353+1138 are provided below.

5.2.1.1 Phases I-II. Modelling full data cubes

As described in Sect. 1.3.3, we start with the spectral modelling of full SINFONI data cubes. The spectral components detected in our SINFONI data (hence, to be fitted) are: AGN continuum, BLR emission lines, and narrow emission lines from diffuse gas; instead, stellar continuum is undetected, being AGN continuum entirely dominant. In the rest-frame wavelength range observed by SINFONI ($\Delta\lambda$ ~4200–5600 Å), BLR emission consists of two components: broad Balmer hydrogen emission lines (Hβ in HS 08010+2554, Hβ and Hγ in SDSS J1353+1138) and several Fe II broad emission lines, whereas diffuse gas emission of the [O III] emission line doublet and the narrow components of Balmer hydrogen lines.

For the BLR modelling of HS 0810+2554 (phase I, see Sect. 1.3.3), we extract a high-S/N spectrum from an aperture of 0.3$''$ radius, centred on the observed blended emission of A+B images (see Fig. 5.1), and fit all the previously mentioned components simultaneously. We model the AGN continuum through a 1st-degree polynomial. The Fe II emission lines are modelled using the semi-analytic templates of Kovačević et al. (2010), while the BLR component of Hβ with two broad Gaussian components. Narrow emission lines are fitted through two Gaussian components. Given the complexity of BLR Hβ line profile in HS 0810+2554, we additionally associate spatially unresolved residuals from the fit to this component, following the approach detailed in Marasco et al. (2020). In case of SDSS J1353+1138, where the two lensed images (A and B in Fig. 5.1) are well distinguishable and spatially resolved, matters are complicated by the fact that we observe a significant change between nuclear spectra extracted from the two distinct images. As a consequence, this prevents us from considering a single BLR template. The procedure followed for the BLR modelling of SDSS J1353+1138 is described separately in Sect. 5.2.2.

After that, we fit the whole data cubes with PPXF (Cappellari and Emsellem, 2004, Cappellari, 2017), leaving the best-fit BLR template obtained in phase I to change only in amplitude across the FoV (phase II, see Sect. 1.3.3). To model narrow emission lines of both HS 0810+2554 and SDSS J1353+1138, we consider a number of Gaussian components ranging from 1 to 3 (finding the latter optimal to reproduce the most complex line profiles) and select in each spaxel the (minimum) optimal number of components via a KS test. Then, we subtract spaxel-by-spaxel BLR and AGN continuum emission, thus obtaining for each galaxy the corresponding subtracted cube.

5.2.1.2 Phase III. Modelling narrow emission lines in subtracted data cubes

As detailed in Sect. 1.3.3, the phase III of the fitting procedure focuses on the refined modelling of narrow emission lines that remain after the subtraction of BLR and AGN continuum emission components. The only residual significant emission in our subtracted data is the [O III] emission doublet, while the narrow components of Balmer hydrogen lines are very weak and marginally resolved. Therefore, we model residual narrow emission lines through multiple Gaussian components, adopting some reasonable constraints: the two emission lines of the [O III] doublet are fitted by imposing the same central velocity and velocity dispersion, with the intensity ratio $I(5007)/I(4959)$ fixed at 3 according to the theoretical expectations of the atomic theory; whereas, for weak narrow components of Balmer hydrogen lines, we assume the same [O III]λ5007 line shape and leave only the flux as a free parameter. This is a reasonable assumption as we expect that narrow Balmer hydrogen and [O III] emission lines come from regions with the same gas kinematics.

Similarly to the fit in phase II, we consider a number of Gaussian components ranging from 1 to 3, using a KS test as before to determine spaxel-by-spaxel the optimal number of components required. In both quasars, most line profiles are well reproduced by two Gaussian components: a narrow, bright component close to the systemic velocity, plus a broad blueshifted component to reproduce the [O III] blue wing observed in most of the FoV, which we identify with approaching outflow emission. In HS 0810+2554, three Gaussian components are required in some spaxels to reproduce properly the faint but still visible red wing in the [O III] line profile, tracing the fainter, redshifted outflow component receding from us. On the contrary, in SDSS J1353+1138, two Gaussian components are sufficient to model even the most complex line profiles, as we do not detect the [O III] red wing anywhere.

In order to study physical and kinematic properties of ionised outflows, we have to carefully identify [O III] emission associated with high-speed outflowing gas, disentangling it from [O III] emission due to the gas bulk motion within the host galaxy. To do so, we adopt the same selection criterion used in Marasco et al. (2020) to identify line emission due to ionised outflows in two local AGN. For each Gaussian component employed in the [O III] modelling in a given spaxel, we focus on the fraction of total line flux contained in the line wings with a velocity shift $|v - v_{\rm peak}|$ larger than a certain threshold width $w_{\rm th}$, where $v_{\rm peak}$ is the peak velocity of the line in each spaxel. If this fraction is higher than a given threshold fraction τ, the Gaussian component is classified as a possible 'outflow' component, to be confirmed by the following kinematic analysis (Sect. 5.3.1); otherwise, it is classified as a 'narrow' component, due to systemic gas motions in the host galaxy. We verify the decomposition in several representative spaxels to select the optimal threshold values. In HS 0810+2554, we use $\tau = 0.5$ and $w_{\rm th} = 300$ km s^{-1}: the Gaussian component reproducing the narrowest, brightest emission near the systemic velocity has been typically classified as narrow; while any additional Gaussian component

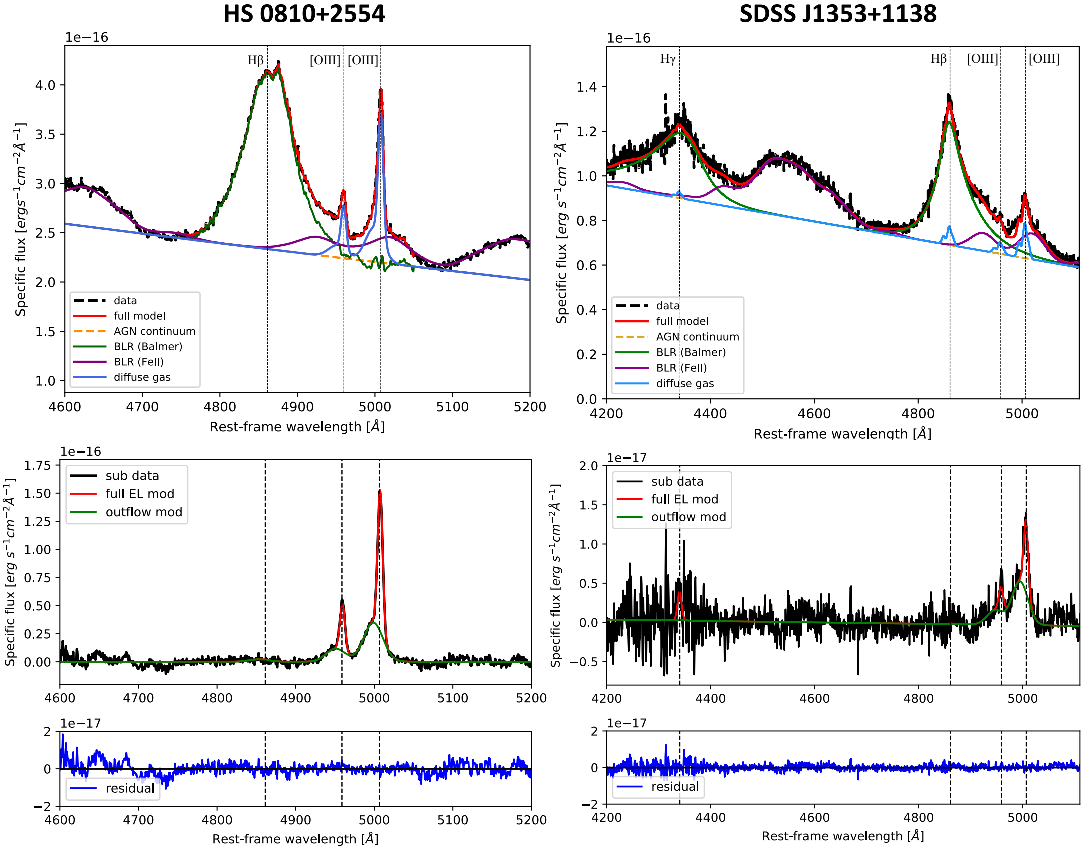

Fig. 5.2 *Representative scheme of our fitting procedure. Top panels. SINFONI J-band spectra of HS 0810+2554 (left) and SDSS J1353+1138 (right), zoomed in the spectral region of* [O III] *and Balmer hydrogen emission lines. Both spectra have been extracted using an aperture of ~0.44″-radius, centred on the peak of the AGN continuum emission (located on image A in SDSS J1353+1138). Black dashed lines show the data, while red solid lines show the best-fit models obtained in phase II of our analysis (see Sect. 5.2.1.1). The latter is partitioned into the contributions of various components: AGN continuum (yellow), BLR emission in Balmer hydrogen emission lines (green) and* Fe II *(purple), and narrow line emission from the diffuse gas (light blue) represented as sum of multiple Gaussian components. Middle panels: J-band spectra extracted from the subtracted cubes, with the same aperture used in the top panels. Subtracted data (black lines) are compared to the best-fit models (red lines) resulting from the refined emission-line (EL) modelling implemented in phase III (see Sect. 5.2.1.2). Green lines highlight the outflow component alone. Bottom panels. Residuals obtained by subtracting the full EL model from the subtracted spectra.*

used to model either the blue or the red wing in [O III] profile is identified as an outflow component. In SDSS J1353+1138, to get the expected classification we slightly relax the width threshold ($w_{\rm th} = 250$ km s^{-1}).

Figure 5.2 summarises our spectral-fitting strategy. Top panels show J-band spectra of HS 0810+2554 and SDSS J1353+1138, extracted from SINFONI data cubes with an aperture of ~0.44″-radius, centred on the peak of the observed emission (located on image A in SDSS J1353+1138). The best-fit models shown are obtained in the phase II of our spectral modellig (see Sect. 5.2.1.1). Since no distinctions between a possibly broad outflow and narrow systemic components are made at this stage of the procedure, the diffuse gas model is plotted as sum of multiple components. We notice that in HS 0810+2554, there is a faint, broad emission line at $\sim 4700-4750$ Å (rest-frame) present in the Fe II templates, which is not present in our data. However, this does not affect the overall fitting procedure, as the observed Fe II emission is reproduced well by the templates at all other wavelengths. The middle panels show the spectra extracted from the subtracted cubes using the same aperture as above, along with the results from the refined multi-Gaussian fit of diffuse gas emission lines (phase III, at the beginning of this subsection). In both subtracted spectra, the [O III] line profile exhibits a prominent, asymmetric blue wing that is already visible in the full spectra shown above. This strongly suggests the presence of high-speed outflowing material moving towards the observer, which we discuss in greater detail in Sect. 5.3.1.

5.2.2 Modelling a ‘double’ BLR in SDSS J1353+1138

As noted in Sect. 5.2.1.1, for SDSS J1353+1138, we find a significant change in the spectral shape within the wavelength range including Hβ and [O III] lines, while comparing the nuclear spectrum of the brighter image A (spectrum A) with that of the fainter image B (spectrum B), shown in upper and lower panels of Fig. 5.3, respectively. In particular, while in the former we can easily identify the [O III] line doublet, we do not detect any counterpart in the latter. Moreover, Hβ line profile in spectrum B is broader, with an evident brighter blue wing. Both effects are likely due to an overall increase in Fe II emission in image B, as Hβ line width is not expected to intrinsically vary between different lensed images. The anti-correlation between Fe II and [O III] emission in AGN spectra reflects a well-known effect known as Eigenvector-1 (Boroson and Green, 1992) and represents one of the most frequent differences among AGN properties. Although subject of many studies, a clear physical understanding of its origin is still lacking. Boroson and Green (1992) suggest that high column densities in the BLR enhance Fe II, while reducing the ionising radiation able to reach the NLR. In a spectral principal component analysis

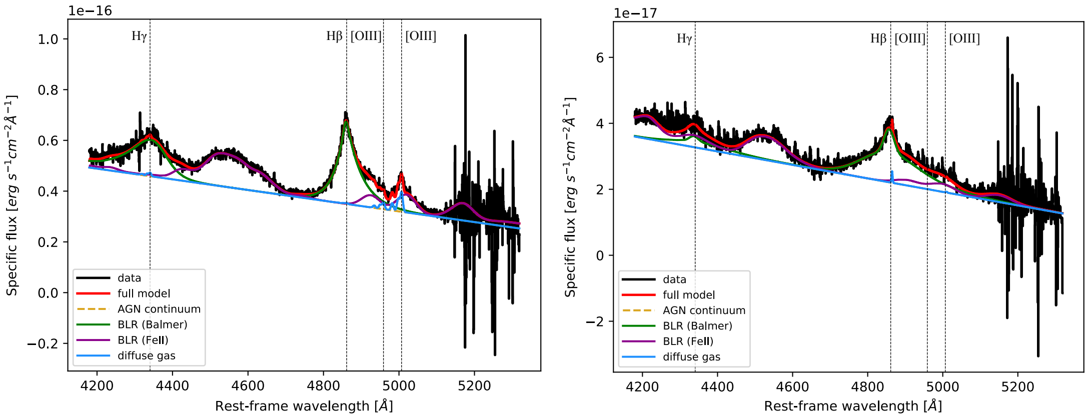

Fig. 5.3 *Best-fit models of nuclear spectra of SDSS J1353+1138 extracted from an aperture of 0.3$''$ radius, centred on image A (upper panel) and on image B (lower panel). The various spectral components, the total model and data are represented with different colours (see the plot legend). In spectrum A, a broken power law distribution is perfectly suited to reproduce the BLR* Hβ *profile, while in spectrum B, an additional broad Gaussian component was required to adequately reproduce the broad peak in the BLR* Hβ *line profile, which is entirely dominant over the barely detected* Hβ *narrow component (solid light-blue line). The two spectra clearly differ from each other mostly for the lack of* [O III] *detection and the presence of a prominent blue wing in the* Hβ *line profile in spectrum B.*

of AGN from SDSS, Ludwig et al. (2009) instead argue that the covering factor of the NLR likely cause the observed range in [O III] strength, while Ferland et al. (2009) suggest that the higher column densities required for the infall in more luminous AGN would additionally account for the observed correlation of Fe II strength with $L/L_{\rm Edd}$.

In spite of its still unclear origin, there are two main possible explanations for the observed significant variation in Fe II emission between the two lensed images. The first one is based on the typical short time scales (i.e. days, weeks; e.g. Kaspi et al. 2000) on which AGN BLR are seen to vary. Because of different paths followed by the light from the background quasar, the two lensed images are produced with a time delay of about 16 days (Inada et al., 2006). This temporal shift is comparable with the typical BLR variation timescale, therefore, it could be at the origin of the substantial change in BLR emission we observe. Given the short time scale probed here, this could carry interesting implications on AGN accretion variations and in the consequent response of the BLR gas. Alternatively, the observed variation could be the consequence of microlensing effects (e.g. see Nierenberg et al. 2020) produced by either single stars or low-mass dark matter halos intervening along the line of sight. Microlensing effects typically affect only the emission originated on small scales, while the emission from the NLR is insensitive. Of the two possibilities, the latter seems to be less likely, as we do not observe any significant counterpart variation in the strength of the BLR Hβ component, in addition to that observed in the Fe II strength. However, a remarkable simultaneous variation in both Hβ and Fe II strength is what we would expect in the case when the two emissions are strictly co-spatial, whereas we know that the BLR is stratified and that microlensing magnifies the emission from the most compact regions more strongly. Therefore, we do not exclude the microlensing hypothesis. A detailed analysis of the different BLR spectra from the two images is beyond the scope of this work and will be presented in a forthcoming paper. Therefore, in this work, we focus on how we accounted for this effect during the spectral analysis.

Consequently, in SDSS J1353+1138, we extract two distinct nuclear spectra, namely, spectrum A and B that are shown in Fig. 5.3 (left and right panel, respectively), using a $0.3''$ radius aperture centred on the emission peak of each lensed image, and fit them separately. In both spectra, we use a 1st-degree polynomial to model the AGN continuum that is still dominant over the stellar continuum. Unlike the BLR modelling of HS 0810+2554, the multiple Gaussian fit is not sufficient to reproduce the broader and complex profile of the broad Balmer emission lines, especially Hβ line emission in spectrum B. In fact, even though both Hβ prominent wings are likely due to the Fe II emission, as discussed above, the Fe II templates employed by the code are not able to reproduce such observed emission. Therefore, we model both wings as part of the broad Hβ line profile without any focus on their physical interpretation, as we are simply interested in identifying the overall BLR spectrum to finally remove it. For the modelling of the broad Balmer emission lines observed in SDSS J1353+1138 (i.e. Hβ and Hγ), we use a broken power law distribution convolved with a Gaussian profile (Nagao et al., 2006):

$$F(\lambda) = \begin{cases} F_0 \times \left(\frac{\lambda}{\lambda_0}\right)^{+\alpha}, & \text{for } \lambda < \lambda_0 \\ F_0 \times \left(\frac{\lambda}{\lambda_0}\right)^{-\beta}, & \text{for } \lambda > \lambda_0 \end{cases}, \tag{5.1}$$

where the free parameters of the fit, for each line, are the central wavelength λ_0, the two power law indices α and β, the normalisation F_0, and the width σ of the Gaussian kernel. In spectrum A (upper panel), Hβ and Hγ are modelled separately through the line profile described in Eq. (5.1). Spectrum B (lower panel) has required instead an additional broad Gaussian component to suitably reproduce both the more extended red wing and the broad peak ($\sigma \sim 800$ km s^{-1}) in Hβ profile. Moreover, we have constrained Hγ line profile through that of Hβ. Different Fe II templates have been selected in the BLR best-fit models for the two nuclear spectra. To model narrow emission line profiles, we use three Gaussian components in spectrum A, while a single Gaussian component in spectrum B, since we do not actually observe any narrow component.

Then, we fit the whole data cube following the procedure described in Sect. 5.2.1.1, with the main difference that in each spatial pixel, PPXF considers a linear combination of the two BLR models, weighing their relative contribution and providing their most suitable combination as the overall BLR model in that specific spaxel. In general, in those spaxels close to one of the lensed images, we basically get the BLR model directly obtained in the modelling of the respective nuclear spectrum; while a combination of the two BLR models in those spaxels ended up roughly between the two images, as expected.

5.2.3 Testing the spatially resolved emission of the ionised outflows

Before analysing the outflow kinematics across the FoV, we test whether the ionised outflow emission is spatially resolved. This is crucial for the calculation of the outflow energetics. As our observed data have missed a dedicated PSF star, we compare the spatial extent of the [O III] outflow emission with that of the BLR emission (both obtained from our spectral modelling, see Sect.5.2.1). In fact, being unresolved in our data, BLR emission is suitable for reproducing the instrumental response. We hence fit a 2D-Gaussian profile to the BLR flux map, obtained by integrating in wavelength our BLR model, to estimate the angular resolution of our seeing-limited observations. The resulting best-fit Gaussian profiles are not circularly symmetric, especially in the case of HS 0810+2554, whose profile is elongated in the NW-SE direction. Such an elongation is mostly due to lens stretching effects and to the blending of A and B images, rather than to a possible intrinsic asymmetry of the PSF. Therefore, for both sources we assume as representative of the true PSF extent the minor-axis angular size of the best-fit Gaussian profile, as this is heading in the direction where lens stretching effects are expected to be minimal. For HS 0810+2554 and SDSS J1353+1138, we estimate a PSF FWHM ($\theta_{\rm res}$) of $0.7''$ and $0.8''$, respectively. These near-IR values are slightly smaller than the optical seeing measurements obtained with the differential image motion monitor (DIMM) during the observations, namely, $0.9''$ and $1.0''$, respectively (Oya et al., 2016).

To test whether the detected ionised outflows are spatially resolved, we create flux maps of [O III] outflow and BLR emission and then produce corresponding ratio maps of [O III] outflow ($\text{[O III]}_{\rm out}$) flux to BLR flux. The resulting ratio maps obtained for both quasars are shown in left panels of Fig. 5.4. The increasing trend in $\text{[O III]}_{\rm out}$-to-BLR ratios with the distance from the central emission peak indicates that the [O III] outflows are spatially resolved in both objects. Moreover, the ratio map of HS 0810+2554 highlights the existence of a preferred NE-SW direction along which the highest ratio values are found. Such a direction is perpendicular to the blending direction of the images A+B. Unlike HS 0810+2554, the two lensed images of SDSS J1353+1138 are spatially well-resolved and not

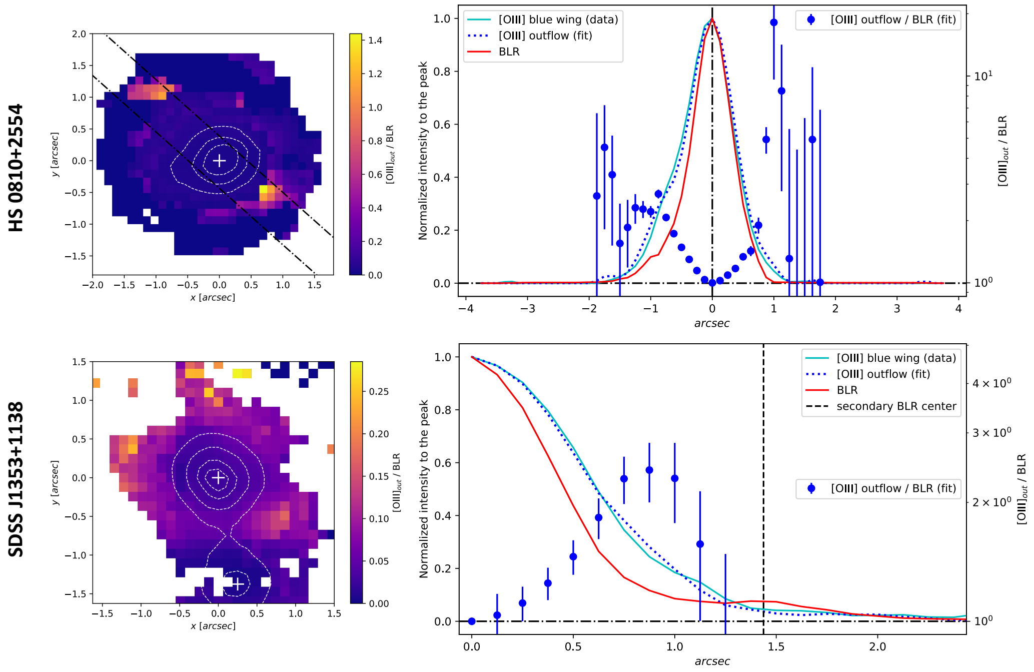

Fig. 5.4 *Spatially resolved ionised outflows in HS 0810+2554 (top) and in SDSS J1353+1138 (bottom). Left panels. Ratio maps of* [O III] *outflow flux to BLR flux (both from best-fit models). Coloured pixels refer to a S/N* $\gtrsim 2$ *(S/N* $\gtrsim 3$*) on the full* [O III] *emission line (i.e. narrow + outflow components) for HS 0810+2554 (SDSS J1353+1138). Location of the continuum emission peak of resolved lensed images is marked with a white '+', while white dotted lines indicate the contour levels of BLR emission at 75%, 50%, and 25% of its peak; for SDSS J1353+1138, we also show the level at 90%. Right panels. Normalised intensity profiles along the pseudo-slit (black dotted-dashed lines in the ratio map) and in circular annuli of increasing radius for HS 0810+2554 (top) and SDSS J1353+1138 (bottom), respectively: BLR model (red lines),* [O III] *outflow model (blue dotted lines) and* [O III] *blue wing from data (cyan lines). Blue points represent ratio values of* [O III] *outflow flux to BLR flux (referred to the right-hand logarithmic scale). Dashed black line in the plot of SDSS J1353+1138 corresponds to the radial distance of the centre of image B.*

affected by significant lens stretching effects. As a consequence, the [O III]$_{\rm out}$-to-BLR ratio map of SDSS J1353+1138 shows an isotropic pattern of increasing ratio values moving outwards from the centre of image A (we recall that we detect [O III] emission only from this image, as discussed in Sect. 5.2.2).

Spatially-resolved properties of outflows can be better appreciated by comparing spatial profiles. In particular, we infer spatial profiles of [O III] outflow and BLR emissions, as well as of their ratio, and study how they vary with increasing distance from the central peak of the overall emission. In HS 0810+2554, since [O III] emission is preferentially located along the NE-SW direction, we define a pseudo-slit in such a direction ($\theta \sim 130°$) with a width of five spaxels, along which to derive various spatial emission profiles. On the contrary, given the overall isotropic emission pattern in SDSS J1353+1138, we infer spatial profiles in circular annuli of increasing radial distance from the centre of image A (lower panel). All spatial profiles thus obtained are shown in the right panels of Fig. 5.4. Each one has been normalised to its own 0″-value, that is the value at the peak position of the overall emission. For [O III] outflow and BLR profiles, the 0″-value corresponds also to their own peak value. This is helpful in further confirming our previous conclusion that the [O III] outflows detected in both galaxies are spatially resolved, since [O III] outflow profiles are broader than the respective BLR profiles. A unique exception occurs in SDSS J1353+1138 at about 1.5″ from the centre, where we observe a clear bump in the BLR emission profile: this is due to the flux contribution from image B and, therefore, does not affect our previous conclusion. As a further test, we also infer the spatial emission profile of the [O III] blue wing - associated with outflowing gas - by collapsing the spectral channels in the subtracted data cube over the wavelength range 4976 − 5000 Å (4970 − 4996 Å) for HS 0810+2554 (SDSS J1353+1138). The two [O III] outflow profiles, obtained from the fit (blue dotted line) and from the spectrally-integrated (cyan solid line) subtracted data, agree very well.

To estimate the angular extent of ionised outflows on the image plane[2], we focus on the ratio values of [O III] outflow flux to BLR flux. These are plotted in logarithmic scale (on the right-hand side of the plots), after being rescaled to 1 in the central pixel. In this way, we can easily identify values larger than 1 as regions producing a significant [O III] outflow emission and, hence, determine the spatial extent of resolved ionised outflows. The associated errorbars have been computed by propagating the uncertainties on the [O III] and BLR fluxes in the spatial pixels involved. Uncertainty on fluxes has been in turn obtained by propagating the error (mostly due to the noise) associated with the spectral channels collapsed to get the total flux of that spatial pixel. At this point, we take the

---

[2] To be still corrected for lens effects.

maximum distance, including solely ratio values not consistent with 1, as both radius within which to spatially integrate the flux of the [O III] outflow component, and observed outflow radius ($R_{\rm obs}$) to be still corrected for SINFONI PSF and lens stretching effects.

To correct for PSF smearing, we apply the correction $R_{\rm PSF} = \sqrt{R^2_{\rm obs} - (\theta_{\rm res}/2)^2}$, where $R_{\rm PSF}$ is the PSF-corrected radius, $R_{\rm obs}$ is the radius observed in the image plane and $\theta_{\rm res}$ is our seeing estimate (0.7″ and 0.8″ for HS 0810+2554 and SDSS J1353+1138, respectively). In HS 0810+2554, we spatially integrate the [O III] outflow flux up to $R_{\rm obs} = 1.25''$, finding a total observed flux of $(3.73 \pm 0.05) \times 10^{-15}$ erg s^{-1} cm $^{-2}$ and $R_{\rm PSF} \sim 1.2''$. In SDSS J1353+1138, we take $R_{\rm obs} = 1.13''$ and assess a total observed flux of $(8.6 \pm 0.6) \times 10^{-16}$ erg s^{-1} cm^{-2} and $R_{\rm PSF} \sim 1.06''$ for the [O III] outflow[3].

5.3 Results

5.3.1 Distribution and kinematics of the ionised gas

The main purpose of the work presented in this chapter is to map the kinematics of [O III] emission, with a primary focus on the outflow component. Figures 5.5 and 5.6 show a global overview of the distribution and the kinematics of the ionised gas resulting from the modelling of the [O III] emission line in HS 0810+2554 and SDSS J1353+1138, respectively. The moment-0 (intensity field), moment-1 (velocity field), and moment-2 (dispersion field) maps for the narrow and the outflow components are shown separately, to better trace their distinct spatial and velocity distributions. All maps have been produced reporting only spatial pixels with a S/N equal or higher than 2 for HS 0810+2554 (Fig. 5.5), and higher than 3 for SDSS J1353+1138 (Fig. 5.6).

The candidate [O III]-outflow component is extended up to large distance from the galaxy centre of both systems, and it stands out for its strongly blueshifted velocities and high velocity dispersion values ($|v| \gtrsim 500$ km s^{-1} and $\sigma \gtrsim 600$ km s^{-1}, respectively; see moment-1 moment-2 maps in Figs. 5.5 and 5.6 relative to the outflow component). Such velocity dispersions are well above the values measured in typical star-forming systems at these redshifts ($\sigma \sim 100$ km s^{-1}, e.g. Cresci et al. 2009, Law et al. 2009) and, along with the overall blue-shifted motion, they provide clear evidence for large-scale outflows in these galaxies. Moreover, while in HS 0810+2554 the outflow and the narrow components have almost the same intensity across the FoV, we note that in SDSS J1353+1138, [O III] outflow

---

[3] The estimates for $R_{\rm PSF}$ are here provided with no uncertainty. We evaluate the error on the outflow intrinsic radius after correcting for lens effects in Sect. 5.3.2.

emission is brighter than [O III] narrow emission produced by the bulk of the gas of the host galaxy.

For the narrow component, expected to trace mostly systemic galactic motions, we obtain low velocity and velocity dispersion values ($|v| \lesssim 50$ km s^{-1}, $\sigma \lesssim 200$ km s^{-1} for HS 0810+2554, and $|v| \lesssim 100$ km s^{-1}, $\sigma \lesssim 300$ km s^{-1} for SDSS J1353+1138; see moment-1 and moment-2 maps in Figs. 5.5 and 5.6 relative to the narrow component) in the central region, where also the outflow emission is detected, which further supports our component decomposition during the spectral analysis of both quasars. In more external regions of HS 08101+2554, we observe slightly higher values of velocity dispersion ($\sigma \lesssim 300$ km s^{-1}), as the line profile is modelled with a unique Gaussian component, given that here the [O III] emission line is fainter and the S/N is lower. This could indicate that [O III] outflow emission is still present, but cannot be isolated from the [O III] narrow component because of its faintness and the worse S/N.

Similarly to Marasco et al. (2020) and given the complexity of the [O III] line profile across the FoV, we prefer adopting the following definitions of velocity and width for the outflow characterisation (e.g. see also Zakamska and Greene 2014, Carniani et al. 2015, Cresci et al. 2015a, 2023, Brusa et al. 2016), rather than moment-1 and moment-2 values. The latter are indeed more affected by geometrical projection and dust absorption effects. In each spatial pixel, we determine the 10th and 90th velocity percentiles (v_{10} and v_{90}) of the overall emission line profile (i.e. narrow + outflow components if present), as representative velocities of the approaching and receding outflow components, respectively. The null velocity value corresponds to the systemic velocity peak of the narrow component in the central spectrum. From v_{10} and v_{90}, we compute the line width W_{80}, defined as $v_{90} - v_{10}$. The W_{80} width is approximately equal to the FWHM for a Gaussian profile. Maps of v_{10}, v_{90} and W_{80} are shown in Fig. 5.7.

Maps of v_{10} show highly blueshfited velocities in most of the field of HS 0810+2554 and SDSS J1353+1138. In the former, a slightly steeper velocity gradient is present in the west direction from the centre, where we observe velocities as high as about −2170 km s^{-1}; in the latter, the outflow region is preferentially elongated in the NE-SW direction with highest velocity values (up to −2410 km s^{-1}) at the SW end of the strongly blueshifted region. In HS 0810+2554, we clearly detect also the redshifted component of the outflow in the two reddest regions of the v_{90} map, where the outflow is seen receding from us at velocities up to about 1730 km s^{-1} along the line of sight. Looking at the W_{80} maps, we observe extremely large values (1100 km s^{-1} $\lesssim v \lesssim$ 3500 km s^{-1}) in the outflow regions, which is consistent with other $z \sim 2$ AGN-driven outflows found in the literature (Carniani et al., 2015). Furthermore, by comparing [O III] outflow moment-1 and v_{10} maps of each

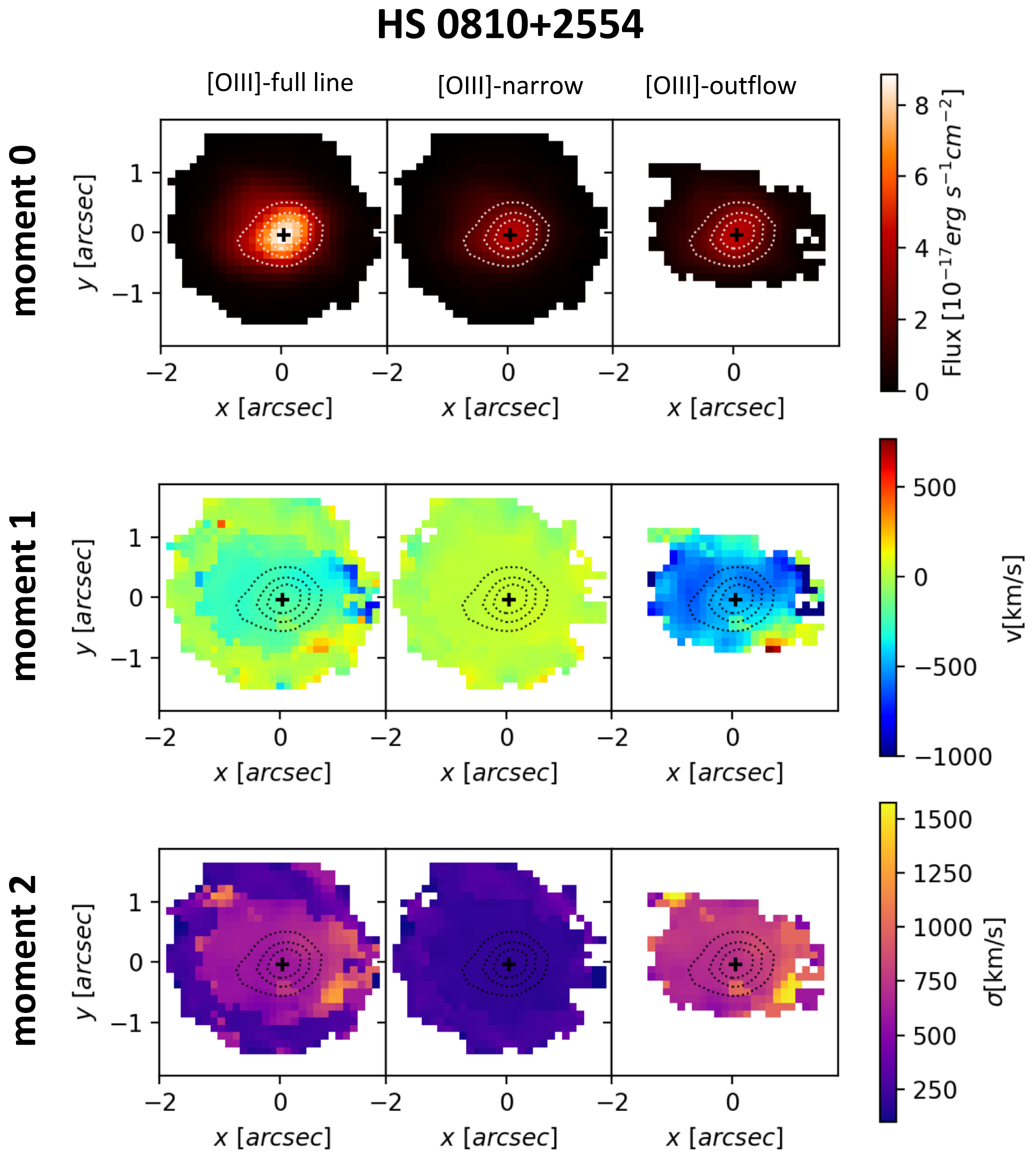

Fig. 5.5 *Moment-0 (intensity field), moment-1 (velocity field), and moment-2 (dispersion field) maps of the* [O III] *line emission in HS 0810+2554. The maps for the total, narrow and outflow components are shown separately, reporting only spatial pixels with a S/N equal or higher than 2. Black '+' indicate the AGN emission centroid, while dotted lines represent the contour levels of BLR emission at 75%, 50%, and 25% of its peak.*

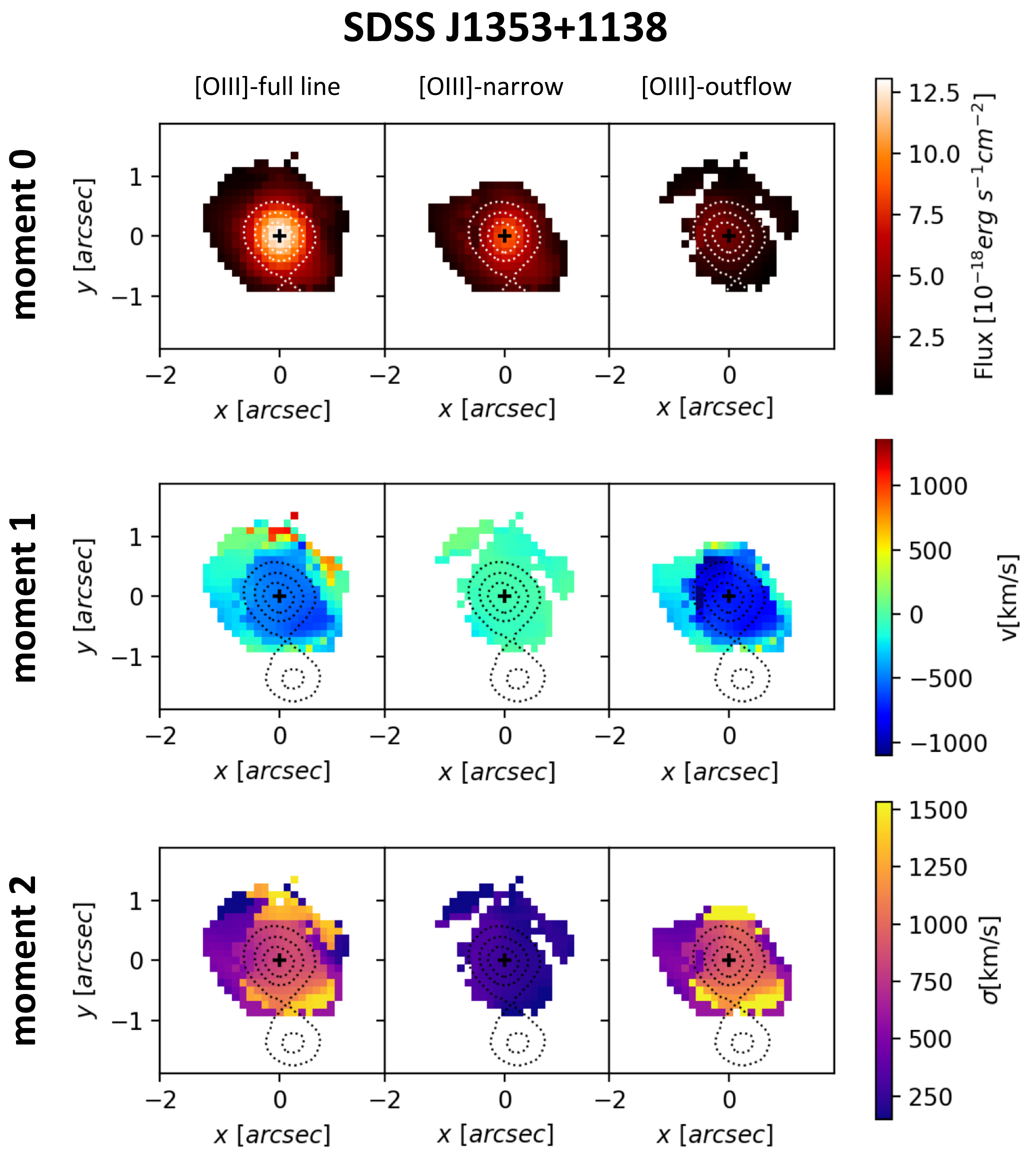

Fig. 5.6 *Moment-0 (intensity field), moment-1 (velocity field), and moment-2 (dispersion field) maps of the* [O III] *line emission in SDSS J1353+1138. The maps for the total, narrow and outflow components are shown separately, reporting only spatial pixels with a S/N equal or higher than 3. Black '+' indicate the AGN emission centroid, while dotted lines represent the contour levels of BLR emission at 75%, 50%, and 25% of its peak.*

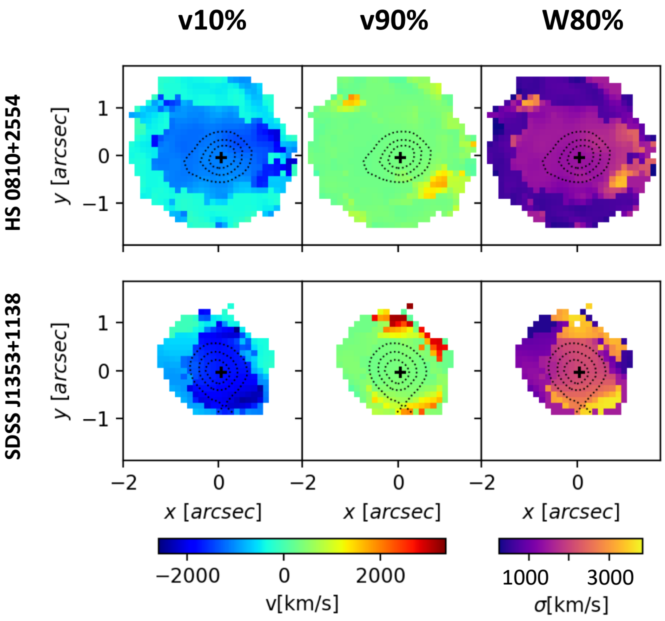

Fig. 5.7 *v_{10}, v_{90}, and W_{80} maps of the* [O III] *emission line in HS 0810+2554 (upper panels) and in SDSS J1353+1138 (lower panels). We have applied the same cut in S/N as in the moment maps of Figs. 5.5 and 5.6, namely, with a S/N equal or higher than 2 and for HS 0810+2554, and higher than 3 for SDSS J1353+1138.*

quasar, we note that the shape of the former reflects the bluest region in the v_{10} map, suggesting that any additional Gaussian component added to model the wings in the [O III] profile has been correctly classified as outflow component (compare also [O III] outflow moment-2 and W_{80} maps).

We rule out the possibility of alternative scenarios, such as galactic inflows or a galaxy merger event. In fact, in the few reported cases of their detection, galactic inflows have been observed mostly in absorption and with quite small bulk velocities ($\sim 200\,\mathrm{km\,s^{-1}}$) and velocity dispersions (e.g. Bouché et al. 2013). Moreover, for the inflowing gas theoretical modelling predicts a small covering factor (e.g. Steidel et al. 2010), making its direct observation rare especially at high redshift (e.g. Cresci et al. 2010). Finally, we exclude also the galaxy merger scenario since deep optical images of both HS 0810+2554 and SDSS J1353+1138 (see Fig. 5.1) do not show any continuum emission counterpart in correspondence of the outflow region, which could support such a scenario.

Finally, we stress that the obtained maps are relative to the lens plane and, thus, they do not account for gravitational lensing effects. While these are expected not to significantly affect the observed gas kinematics (hence, outflow velocity), they strongly alter the observed gas spatial distribution and surface brightness: fluxes are magnified and spatial dimensions are stretched. Therefore, the obtained maps cannot be used to infer directly outflow intrinsic radius and its total flux, which are key ingredients, along with outflow velocity, in the computation of outflow energetics. Therefore, we first need to quantify lensing effects, and then derive unlensed physical properties of the outflow. These aspects are discussed in Sect. 5.3.2.

5.3.2 Correcting outflow properties for lens effects

As discussed in Sect. 5.3.1, both spectral analysis and kinematic study have been performed in the lens plane. For this reason, we must correct for lens effects to determine the actual outflow extent and flux.

There are several adaptive-mesh fitting codes which, given a mass distribution for the lens and a surface brightness profile for the background source, fit the resulting forward lensed image to the observed data and use a statistics test (e.g. the minimum χ^2 method) to establish the best-fit models for both the lens and the source. These algorithms usually require the knowledge of the instrumental PSF to allow a correct comparison with the observed data. The output of these fitting codes is a 2D or 3D reconstruction (depending on the code used) of the unlensed source. In order to achieve an accurate reconstruction, it is also required that the lensed images are all detected and spatially resolved[4], as their position depends on the first derivative of the gravitational potential of the lens, while their flux on the second derivative (e.g. Jackson et al. 2015, Nierenberg et al. 2020). In other words, the knowledge of both position and flux of the multiple lensed images provides strong constraints on the lens and background source models.

Unfortunately, we cannot use such fitting codes to fully reconstruct the unlensed outflow in the source plane for either HS 0810+2554 or SDSS J1353+1138, since our data do not meet the necessary requirements. In fact, in the case of HS 0810+2554, the spatial resolution of SINFONI data is too low to resolve the various lensed images and, therefore, we recover just a partial reconstruction of the background outflow using the lens-fitting code from Rizzo et al. (2018) and adopting an approximated procedure (see Sect. 5.3.2.1). In SDSS J1353+1138 instead, the complete lack of [O III] detection in image B prevents us from attempting any background source reconstruction starting from our data, as no constraints can be put on this image.

5.3.2.1 Approximated reconstruction of the unlensed outflow in HS 0810+2554

As just mentioned, for HS 0810+2554 we obtain a partial 2D-reconstruction of the outflow emission in the source plane using the gravitational lens-fitting code by Rizzo et al. (2018),

---

[4] In addition or alternatively to single lensed images, fitting codes handle also lensed arcs.

which adopts the lensing operator described in Vegetti and Koopmans (2009). This depends, in particular, on lensing operators describing the lens as a power law plus a shear component (see Sect. 2.2 in Rizzo et al. 2018 for details).

We start with simulating possible intrinsic geometries of the outflow. We consider multiple conical configurations, differing in radius and aperture angle, while the position angle of the cone is kept fixed to $\theta \sim 130°$, that is the direction in which we observe the major [O III] outflow emission in the lens plane (see Sect. 5.2.3). To reduce further the number of free parameters characterising the outflow geometry, we fix the origin of all simulated cones to the position of the emission centroid of the unlensed outflow, obtained through a first tentative full 2D-reconstruction with the lens-fitting code by Rizzo et al. (2018) and a lens model fixed to that found in Nierenberg et al. (2020). In fact, although it cannot be used to infer the intrinsic extent of [O III] outflow due to the presence of residual effects from the PSF deconvolution, it still provides reliable constraints on the centre position of the background outflow emission. In doing so, each cone is modelled as a uniform distribution of homogeneous point-like sources, which are then individually lensed forward (i.e. singularly mapped and magnified in the lens plane) through the reconstruction algorithm by Rizzo et al. (2018), still keeping the lens model fixed to Nierenberg et al. (2020). As a result, we obtain the whole forward lensed image of each starting background cone, differing in radius and aperture angle.

To infer the intrinsic size of the outflow in HS 0810+2554, we select only those cones with a radius compatible with the detected [O III] outflow emission, by visually comparing the extent of the forward resulting lensed emission with the maximum distance of the [O III] outflow, once corrected for the SINFONI PSF, that is $R_{\rm max} = 9.5$ pixels[5]. In Fig. 5.8, we show an example of our forward lensing method: a background homogeneous cone with radius of 8 pixels and aperture of 60° (left), and its forward lensed image (right). The red solid circumference has a radius equal to $R_{\rm max} = 9.5$ pixels, that is the maximal extent reached by the observed (PSF-corrected) [O III] outflow emission (see caption of Fig. 5.8 for a detailed description). In this way, we find that the cones with a radius ranging from 6.5 to 9.5 pixels are compatible with $R_{\rm max}$. Taking the average of these more plausible radii and the maximum deviation from the mean as error, and converting into kpc units, we estimate the intrinsic outflow radius to be $R_{\rm out} = (8.7 \pm 1.7)$ kpc, with $z = 1.508 \pm 0.002$ being the redshift measured from the nuclear spectrum extracted during the BLR fitting (described in Sect. 5.2.1.1). We point out that our z measurement is consistent with

---

[5] For simplicity, being this an estimate of the outflow radius based on a qualitative comparison, we report projected distances in units of SINFONI pixels, here recalling that $R_{\rm max} \sim 8.7$ kpc corresponds to ~ 8 SINFONI pixels. At the end, we will provide the estimate of the intrinsic size of the outflow in physical units.

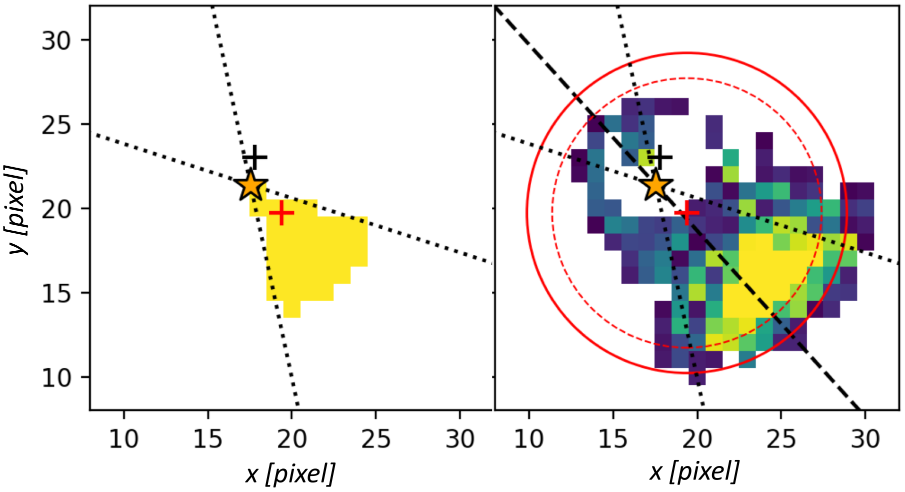

Fig. 5.8 *Example of forward lensing (Rizzo et al., 2018) of a background homogeneous cone with radius of 8 pixels and aperture of 60° (left) into the respective lensed image (right). In both images, the orange star, red and black '+' indicate, respectively, the position of the cone origin, the emission peak observed by SINFONI, and the lens centre. Red dashed and solid circumferences in the right panel have a radius, respectively, equal to the intrinsic cone size in the source plane (i.e. 8 pixel in the example shown here), and to the maximum extent of the observed (PSF-corrected)* [O III] *outflow emission (i.e.* $R_{\max} = 9.5$ *pixels). Both circumferences are centred on the observed emission peak (red '+'). Black dashed and dotted lines identify the position angle (~ 130°) and the aperture (here 60°) of the intrinsic cone. Note that the conical source does not intercept the lens centre, thus being subject to a low magnification.*

the centroids of the ALMA CO(J=3→2) and CO(J=2→1) emission lines of HS 0810+2554 reported in Chartas et al. (2020).

Finally, to estimate the lens magnification factor, we consider multiple aperture angles: 30°, 45°, 60°, and 90°, for each defined-radius cone, and calculate the magnification factor as the ratio of the total flux in the lens plane to the total flux in the source plane. All simulated conical configurations provide low magnification factors, weakly dependent on the assumed geometry of the cone (they differ by a factor ~1.4 at most). This follows from the fact that simulated cones do not intercept the lens caustics and extend to large scales, where the lens magnification is reasonably lower. Therefore, to determine the total mean magnification of the outflow in HS 0810+2554, we focus only on the magnification values obtained in correspondence to the established range of more plausible outflow radii, that is $6.5 - 9.5$ pixels. We hence average over these values, thus finding $\mu_{\rm out} = 2.0 \pm 0.2$, where the error is given by the maximum deviation from the mean.

5.3.2.2 Inferring unlensed size and flux of ionised outflows

Thanks to the partial 2D-reconstruction of the unlensed [O III] outflow in HS 0810+2554 obtained in Sect. 5.3.2.1, we find the outflow magnification factor and intrinsic radius to be $\mu_{\rm out} = 2.0 \pm 0.2$ and $R_{\rm out} = (8.7 \pm 1.7)$ kpc, respectively. By correcting for $\mu_{\rm out}$ the observed [O III] outflow flux (see Sect. 5.2.3), we obtain an unlensed outflow flux $F_{\rm out} = (1.9 \pm 0.2) \times 10^{-15} (2.0/\mu_{\rm out})$ erg $\rm s^{-1} cm^{-2}$. Our $\mu_{\rm out} \sim 2$ estimate is also close to what Chartas et al. (2020) found for a high-velocity CO-clump at a similar distance in ALMA data of HS 0810+2554. On the contrary, it remarkably differs (up to two orders of magnitude) from the other values from the literature presented in Sect. 5.1.1.1. This follows from the fact that the latter (i.e. high-magnification values) are estimates of lens magnification affecting emission from compact (UV disk and X-ray corona) regions, while our estimate is relative to a large-scale extended (~8 kpc) emission. Moreover, the reconstructed unlensed outflow does not intercept the lens caustics (see Sect. 5.3.2.1) and, hence, it misses the contribution from these highly-magnified regions.

On the contrary, the complete lack of [O III] detection in image B of SDSS J1353+1138 prevents us from achieving any reconstruction of the background source starting from SINFONI data, as mentioned at the beginning of this section. Therefore, we make simplified assumptions, referring to the lens models for SDSS J1353+1138 by Inada et al. (2006) and Rusu et al. (2016) (see Sect. 5.1.3), based on AGN plus host galaxy emission in *i*- and *K*-band images, respectively. Our assumptions rely on the fact that in SDSS J1353+1138 gravitational lensing effects are supposed to be smaller than in HS 0810+1154 (e.g. Narayan and Bartelmann 1996). As a consequence, compared to HS 0810+1154, for this object we

Table 5.2 *Directly measured properties of the* [O III] *ionised outflows in HS 0810+2554 and SDSS J1353+1138, and adopted outflow magnification factors. Starting from left, columns are defined as follows: maximum values observed in v_{10}, v_{90} and W_{80} maps ($v_{10}^{\max}$, $v_{90}^{\max}$ and $W_{80}^{\max}$, respectively), intrinsic outflow radius ($R_{\rm out}$), unlensed* [O III] *outflow flux ($F_{\rm out}$) corrected for the outflow magnification factor ($\mu_{\rm out}$), reported in the last column.*

AGN	$v_{10}^{\max}$ km s^{-1}	$v_{90}^{\max}$ km s^{-1}	$W_{80}^{\max}$ km s^{-1}	$R_{\rm out}$ kpc	$F_{\rm out}$ erg s^{-1}cm^{-2}	$\mu_{\rm out}$
HS 0810+2554	-2170 ± 70	1730 ± 60	3360 ± 110	8.7 ± 1.7	$(1.9 \pm 0.2) \times 10^{-15}$	2.0 ± 0.2
SDSS J1353+1138	-2410 ± 80	2270 ± 130	3850 ± 90	9.2 ± 1.1	$(2.4 \pm 0.3) \times 10^{-16}$	3.6 ± 0.4

expect: (1) a milder and almost isotropic stretching of physical dimensions, as we indeed observe; (2) smaller and less variable-in-space values of differential magnification. On the basis of the first argument, we neglect lens stretching effects and approximate the unlensed outflow angular size to $R_{\rm PSF} = 1.06'' \pm 0.13''$ (determined in Sect. 5.2.3). Regarding lens magnification instead, we expect total magnification factors of a few units, weakly dependent on the geometrical details of the flux distribution for background emissions with comparable spatial extent. Consequently, we take as a proxy for the total outflow magnification $\mu_{\rm out}$ the average between reported i-band (i.e. $\mu = 3.81$ and $\mu = 3.75$; Inada et al. 2006) and K-band values (i.e. $\mu = 3.47$, $\mu = 3.42$ and $\mu = 3.53$; Rusu et al. 2016) of total magnification factor, under the assumption of comparable unlensed physical sizes. Given the unknown real unlensed distribution of J-band outflow emission, we conservatively assume an uncertainty of 10% on our adopted $\mu_{\rm out}$ value, thus obtaining $\mu_{\rm out} = 3.6 \pm 0.4$. Correcting finally for lens magnification and converting to kpc units, we find the unlensed outflow flux and intrinsic radius to be $F_{\rm out} = (2.4 \pm 0.3) \times 10^{-16}(3.6/\mu_{\rm out})$ erg s^{-1}cm^{-2} and $R_{\rm out} = (9.2 \pm 1.1)$ kpc, using $z = 1.632 \pm 0.002$ as measured from the nuclear spectra extracted during the BLR modelling (described in Sect. 5.2.2).

In Table 5.2, we summarise the main outflow properties for HS 0810+2554 and SDSS J1353+1138 obtained up to this point. First columns show the maximum velocity values observed in v_{10}, v_{90} and W_{80} maps (see Sect. 5.3.1), respectively, labelled as $v_{10}^{\max}$, $v_{90}^{\max}$ and $W_{80}^{\max}$. Then, we report our lens-corrected estimates of $R_{\rm out}$ and $F_{\rm out}$, the latter corrected for the outflow magnification factor $\mu_{\rm out}$ shown in the last column. Most of these physical quantities are also employed in the computation of the outflow energetics in Sect. 5.3.3.

5.3.3 Outflow energetics

We derive physical properties of the large-scale ionised outflows in HS 0810+2554 and SDSS J1353+1138 from the observed [O III]λ5007 emission, following the prescriptions described in Cano-Díaz et al. (2012) as done also in Marasco et al. (2020). The [O III] line luminosity is given by:

$$L_{[\mathrm{O\,III}]} = \int_V \epsilon_{[\mathrm{O\,III}]} f \; dV, \tag{5.2}$$

where V is the volume occupied by the ionised outflow, f the filling factor of the [O III] emitting clouds in the outflow, and $\epsilon_{[\mathrm{O\,III}]}$ the [O III] line emissivity which, at the temperatures typical of the NLR ($\sim 10^4$ K), is weakly dependent on the temperature ($\propto T^{0.1}$) and can be written as:

$$\epsilon_{[\mathrm{O\,III}]} = 1.11 \times 10^{-9} E_{[\mathrm{O\,III}]} n_{\mathrm{O}^{2+}} n_{\mathrm{e}} \; \mathrm{erg\,s^{-1}cm^{-3}}, \tag{5.3}$$

with $E_{[\mathrm{O\,III}]}$ as the energy of the [O III] photons, $n_{\mathrm{O}^{2+}}$ and n_{e}, the volume densities of O^{2+} ions and electrons, respectively. Then, assuming that most of the oxygen in the ionised outflow is in the form of O^{2+}, it follows that:

$$\epsilon_{[\mathrm{O\,III}]} \approx 5 \times 10^{-13} E_{[\mathrm{O\,III}]} n_{\mathrm{e}}^2 10^{[\mathrm{O/H}]} \; \mathrm{erg\,s^{-1}cm^{-3}}, \tag{5.4}$$

where [O/H] gives the oxygen abundance in solar units. The mass of the outflowing ionised gas can be derived from the following expression:

$$M_{\mathrm{out}} = \int_V 1.27 m_{\mathrm{H}} n_{\mathrm{e}} f \; dV, \tag{5.5}$$

where m_{H} is the mass of the hydrogen atom and the factor of 1.27 follows from including the mass contribution of helium. By combining Eqs. (5.2) and (5.5), we get:

$$M_{\mathrm{out}} = 5.33 \times 10^7 \left(\frac{L_{[\mathrm{O\,III}]}}{10^{44}\ \mathrm{erg\ s^{-1}}}\right) \left(\frac{\langle n_{\mathrm{e}} \rangle}{10^3\ \mathrm{cm^{-3}}}\right)^{-1} \frac{C}{10^{[\mathrm{O/H}]}}\ \mathrm{M_\odot}, \tag{5.6}$$

where $\langle n_{\mathrm{e}} \rangle$ is the electron density averaged over the ionised outflow volume (i.e. $\langle n_{\mathrm{e}} \rangle = \int_V n_{\mathrm{e}} f \; dV / \int_V f \; dV$) and $C = \langle n_{\mathrm{e}} \rangle^2 / \langle n_{\mathrm{e}}^2 \rangle$ is the so-called ‘condensation factor’. Under the simplifying hypothesis that all ionising gas clouds have the same density, we get $C = 1$ and eliminate the outflow mass dependence on the filling factor of the emitting clouds.

To compute ionised outflow energetics, we make further simplifying assumptions for the outflow geometry and structure: we assume that the outflow has a (bi-)conical geometry with an opening angle Ω and a radial extent, R_{out}, and that it consists of a collection of ionised gas clouds, uniformly distributed within the cone and outflowing with a speed v_{out}. The mass outflow rate is given by:

$$\dot{M}_{\mathrm{out}} = \langle \rho \rangle \; v_{\mathrm{out}} \, \Omega R^2, \tag{5.7}$$

where $\langle\rho\rangle$ is the average mass density computed over the total volume V occupied by the conical outflow[6]. By substituting $\langle\rho\rangle$ in Eq. 5.7 with its definition in terms of $\dot{M}_{\rm out}$ (using Eq. 5.6) and V, we obtain:

$$\dot{M}_{\rm out} = 164 \left(\frac{L_{\rm [O\,III]}}{10^{44} {\rm erg\,s^{-1}}}\right)\left(\frac{\langle n_{\rm e}\rangle}{10^{3}{\rm cm^{-3}}}\right)^{-1}\left(\frac{v_{\rm out}}{10^{3}{\rm km\,s^{-1}}}\right)\left(\frac{R_{\rm out}}{\rm kpc}\right)^{-1}\frac{1}{10^{\rm [O/H]}}\ {\rm M_\odot\,yr^{-1}}, \tag{5.8}$$

where we have assumed $C = 1$. The mass outflow rate thus inferred does not depend on either the opening angle Ω of the outflow cone or the filling factor f of the emitting clouds.

Finally, we calculate the kinetic energy $E_{\rm kin}$, kinetic luminosity $L_{\rm kin}$ and momentum rate $\dot{p}_{\rm out}$ of the outflow by means of the following expressions:

$$E_{\rm kin} = 9.94\times10^{42}\left(\frac{M_{\rm out}}{\rm M_\odot}\right)\left(\frac{v_{\rm out}}{\rm km\ s^{-1}}\right)^2 {\rm erg}, \tag{5.9}$$

$$L_{\rm kin} = 3.16\times10^{35}\left(\frac{\dot{M}_{\rm out}}{\rm M_\odot\ yr^{-1}}\right)\left(\frac{v_{\rm out}}{\rm km\ s^{-1}}\right)^2 {\rm erg\,s^{-1}}, \tag{5.10}$$

$$\dot{p}_{\rm out} = 6.32\times10^{30}\left(\frac{\dot{M}_{\rm out}}{\rm M_\odot\ yr^{-1}}\right)\left(\frac{v_{\rm out}}{\rm km\ s^{-1}}\right) {\rm dyne}. \tag{5.11}$$

Equations 5.6–5.11 require the knowledge of different physical properties of the outflow, some of which can be derived, while others have to be assumed. These are: the oxygen abundance, which we fix to the solar abundance, and the electron density, which we assume to be $n_{\rm e} \sim 1000$ cm^{-3}, in agreement with the values measured in similar studies at high redshift (see e.g. Perna et al. 2017a, Förster Schreiber et al. 2019). The second assumption, in particular, affects the derived outflow energetics (Davies et al., 2020, Kakkad et al., 2020) but it is necessary though, since we cannot measure $n_{\rm e}$ directly from our data.

We now focus on the physical quantities we can calculate. In Sect. 5.3.2, we have provided values of intrinsic radius $R_{\rm out}$ and flux $F_{\rm out}$ of the ionised outflows detected in HS 0810+2554 and SDSS J1353+1138, traced by [O III] line emission. From $F_{\rm out}$, we infer the corresponding intrinsic [O III] line luminosity to then use in the mass outflow expression (Eq. 5.6). We thus find ($\mu_{\rm out}$-corrected) [O III] luminosity values of $L_{\rm [O\,iii]} = (2.8\pm0.3)\times10^{43}$ erg s^{-1} and $L_{\rm [O\,III]} = (4.4\pm0.6)\times10^{42}$ erg s^{-1} for HS 0810+2554 and SDSS J1353+1138, respectively.

To establish ionised outflows' velocity, we focus on the kinematic maps of v_{10} and v_{90} (Figs. 5.5 and 5.6). Our spectral analysis and study of the gas kinematics in HS 0810+2554

---

[6] We note that unless $f = 1$, in general $\langle\rho\rangle \neq 1.27 m_{\rm H}\langle n_{\rm e}\rangle$, with $\langle n_{\rm e}\rangle$ averaged over the volume occupied by the emitting clouds and not over the whole conical volume.

and in SDSS J1353+1138 have revealed the presence of an extended central region hosting outflowing gas directed towards us along the line of sight (Sect. 5.3.1), leading to very high v_{10} values. Moreover, in HS 0810+2554, we detect also a red [O III] wing in two smaller regions apart from the peak of the overall emission, corresponding to the high-velocity receding component of the ionised outflow. In this case, following Marasco et al. (2020), we define the outflow velocity as:

$$v_{\rm out} = \max\left(|v_{10}^{\rm max} - v_{\rm sys}|,\ |v_{90}^{\rm max} - v_{\rm sys}|\right), \tag{5.12}$$

where $v_{10}^{\rm max}$ and $v_{90}^{\rm max}$ are the maximum values observed, respectively, in the v_{10} and v_{90} maps (see Sect. 5.3.1), and $v_{\rm sys}$ is the bulk (or systemic) velocity of the galaxy, inferred from the nuclear spectrum used for the BLR fitting (in Sect. 5.2.1.1) and set to the value of 0 km s^{-1}, as described in Sect. 5.3.1. This definition is required by the unknown geometry and orientation of the outflow with respect to the line of sight: since we ignore the true angle of the outflow with respect to the line of sight, and given that the bulk of the outflow unlikely points towards the observer, we assume that the best representation of the outflow speed is provided by the velocity 'tail' of the line profile, that is, v_{10} and v_{90} in Eq. (5.12). These values are thought to be more suited to represent $v_{\rm out}$ than the mean (or median) velocity of the line, which strongly depends on projection effects and dust absorption (e.g. Cresci et al. 2015a).

The same argument holds also for the determination of the outflow velocity in SDSS J1353+1138. But in this case, possibly because of the different orientation with respect to the observer and higher dust absorption, we do not observe any asymmetric red wing in the [O III] profile produced by the receding part of the outflow (as stressed in Sect. 5.3.1). Therefore, for SDSS J1353+1138 we focus only on the blue tail of the [O III] line associated with the outflow, and hence assume $v_{\rm out} = v_{10}^{\rm max}$ as outflow velocity for SDSS J1353+1138.

We calculate the uncertainties on the quantities in Eqs. (5.6)-(5.11) via error propagation starting from inferred errors on $R_{\rm out}$, $L_{\rm [O\,iii]}$ and $v_{\rm out}$, and a typical uncertainty of 50% on $n_{\rm e}$ (e.g. Perna et al. 2017a, Förster Schreiber et al. 2019). The physical properties of the ionised outflows detected in HS 0810+2554 and in SDSS J1353+1138 are listed in Table 5.3, including also our estimates of kinetic efficiency and momentum-boost. The former is defined as the ratio of outflow kinetic luminosity $L_{\rm kin}$ (defined in Eq. 5.10) to AGN bolometric luminosity $L_{\rm bol}$ (corrected for lens magnification); while the latter is defined as the ratio of outflow momentum rate ($\dot{p}_{\rm out}$) to the momentum initially provided by AGN radiation pressure (i.e. $L_{\rm bol}/c$), approximately identified with the momentum rate of the X-ray UFO. The values of $L_{\rm bol}$ adopted in this work are $(2.5 \pm 0.9) \times 10^{45}$ erg s^{-1} and

$(39 \pm 2) \times 10^{45}$ erg s^{-1} for HS 0810+2554 and SDSS J1353+1138, respectively, which will be discussed in Sect. 5.4.1.

We find mass outflow rates of ~2 M$_{\odot}$ yr^{-1} and ~12 M$_{\odot}$ yr^{-1}, and kinetic efficiencies of $\sim 9 \times 10^{-5}$ and $\sim 700 \times 10^{-5}$ for SDSS J1353+1138 and HS 0810+2554, respectively. The values obtained for HS 0810+2554 are in good agreement with the predictions at $L_{\rm bol} \sim 2 \times 10^{45}$ erg s^{-1} of the $\dot{M}_{\rm out} - L_{\rm bol}$ and $L_{\rm kin} - L_{\rm bol}$ scaling relations (Carniani et al., 2015, Fiore et al., 2017) for the ionised outflow component. On the contrary, the inferred $\dot{M}_{\rm out}$ value for SDSS J1353+1138 is small (by a factor of ~ 100) compared to the predictions for the ionised outflow component at $L_{\rm bol} \sim 4 \times 10^{46}$ erg s^{-1}. Our findings are however relative only to the ionised phase of large-scale outflows, while a significant amount of outflowing gas may be in neutral molecular and/or atomic phase. Given the typical bolometric luminosities of our galaxies ($L_{\rm bol} \sim 10^{45} - 10^{46}$ erg s^{-1}), outflow mass rates predicted for the molecular component may indeed exceed our ionised gas measurements by a factor ~ 100. Chartas et al. (2020) have recently claimed the tentative detection of a massive ($M_{\rm out,\,mol} \sim 4 \times 10^{9}$ M$_{\odot}$) CO-molecular outflow in HS 0810+2554, with an overall mass rate and velocity of ~400 M$_{\odot}$yr^{-1} and 1040 km s^{-1}, respectively. Other gas phases might contribute and lead to a significant increase of total outflow mass and energetics. A possible contribution might come from neutral atomic outflows, although these are primarily observed in ULIRGs systems (see Sect. 1.2.3.3 and Chapter 4), showing both intense SF and AGN activity (e.g. Rupke et al. 2005, Cazzoli et al. 2016, Fluetsch et al. 2019, 2021). However, any contribution of additional gas phases may significantly increases the overall outflow mass and energetics (e.g. Cicone et al. 2014, Carniani et al. 2016, Fiore et al. 2017). Implications of all these results will be discussed in detail in Sect. 5.4.

5.4 Discussion

5.4.1 Connection with nuclear X-ray UFOs

The main purpose of this work is to shed light on the acceleration mechanism of ionised outflows on large scales. In this regard, we compare the energetics of galaxy-scale ionised outflows with the UFOs detected on nuclear scales, to test whether they are causally connected (i.e. whether they are subsequent phases of the same AGN-accretion burst). In case of a causal connection, we can go on to investigate the nature of the acceleration mechanism distinguishing between momentum-driven and energy-driven winds.

Whereas energetics measurements of large-scale ionised outflows in HS 0810+2554 and SDSS J1353+1138 have been inferred in Sect. 5.3.3, in this section we present X-ray measurements from the literature of the co-hosted UFOs, here used to determine the sub-pc scale wind energetics. For both quasars, we refer to Chartas et al. (2021), who presented the first X-ray spectral analysis of SDSS J1353+1138, and new UFOs measurements for HS 0810+2554 obtained from the most recent *Chandra* observation acquired in 2016 using the updated version of the photoionisation code *XSTAR* (Bautista and Kallman, 2001).

As done in Marasco et al. 2020, we follow Nardini and Zubovas (2018) to re-compute UFO energetics in a consistent way based on the same assumption we made in the calculation of the large-scale outflow energetics. We hence assume that the UFO is launched from the escape radius $r_{\rm esc} \equiv 2GM_{\rm BH}/v_{\rm UFO}^2$ of the BH and derive its mass outflow rate as:

$$\dot{M}_{\rm UFO} \simeq 0.3 \left(\frac{\Omega}{4\pi}\right)\left(\frac{N_{\rm H}}{10^{24}{\rm cm}^{-2}}\right)\left(\frac{M_{\rm BH}}{10^{8}{\rm M}_\odot{\rm yr}^{-1}}\right)\left(\frac{v_{\rm UFO}}{c}\right)^{-1} {\rm M}_\odot\ {\rm yr}^{-1}, \tag{5.13}$$

where Ω is the solid angle subtended by the UFO, $M_{\rm BH}$ the black hole mass, $N_{\rm H}$ the hydrogen gas column density, and $v_{\rm UFO}$ the wind speed. We take the values of $v_{\rm UFO}$ and $N_{\rm H}$ inferred by Chartas et al. (2021). For HS 0810+2554, these values (reported in Table 5.4) slightly differ from those previously published (i.e. $v_{\rm UFO,1} = 0.12^{+0.02}_{-0.01}c$, $N_{\rm H,1} = 3.4^{+1.9}_{-2.0} \times 10^{23}$ cm^{-3} and $v_{\rm UFO,2} = 0.41^{+0.07}_{-0.04}c$, $N_{\rm H,2} = 2.9^{+2.0}_{-1.6} \times 10^{23}$ cm^{-3} for the two distinct detected UFO components; Chartas et al. 2016), but are still in agreement. Adopted $M_{\rm BH}$ values are virial estimates based on Hβ for HS 0810+2554 (Assef et al., 2011) and on C IV for SDSS J1353+1138 (Chartas et al., 2021). The C IV-based measurement of $M_{\rm BH}$ for SDSS J1353+1138 has been corrected following the prescription published in Coatman et al. (2017) for C IV-based virial BH mass estimates, known to be systematically biased compared to BH masses derived from Balmer hydrogen lines. Finally, we assume for both UFOs a covering factor of $f = \frac{\Omega}{4\pi} = 0.4^{+0.2}_{-0.2}$, on the basis that about 40% of local AGN have been observed to host UFOs (Tombesi et al., 2010, Gofford et al., 2013). With all these ingredients, we calculate the mass rate $\dot{M}_{\rm UFO}$ (with Eq. 5.13), the momentum rate $\dot{p}_{\rm UFO}$ (i.e. $\dot{p}_{\rm UFO} = \dot{M}_{\rm UFO} v_{\rm UFO}$) and the momentum-boost (defined as $\dot{p}_{\rm UFO}/(L_{\rm bol}/c)$) of the nuclear winds. As uncertainty on all quantities, we take the minimum-maximum range of possible values, considering the values of $v_{\rm UFO}$, $N_{\rm H}$ and $M_{\rm BH}$ as inferred in Chartas et al. (2021). For $L_{\rm bol}$, we consider the average between the μ-corrected values obtained in Chartas et al. (2021) with two different methods: the 2-10 keV bolometric correction (Lusso et al., 2012) and the estimate from the continuum luminosity at 1450 Å (Assef et al., 2011, Runnoe et al., 2012).

Table 5.4 summarises physical properties of UFOs in HS 0810+2554 and SDSS J1353+1138, derived following the prescriptions in Nardini and Zubovas (2018), along with the physical quantities taken from Chartas et al. (2021). For HS 0810+2554 the values of $\dot{M}_{\rm UFO}$ and $\dot{p}_{\rm UFO}/(L_{\rm bol}/c)$ refer to the total UFO, as sum of the two detected UFO components moving

Table 5.3 *Derived properties of ionised outflows in HS 0810+2554 and SDSS J1353+1138, as derived from the analysis of* [O III] *line emission. From left, for the detected ionised outflows columns report the measured values of: velocity, mass, mass rate, kinetic energy, kinetic efficiency and momentum-boost. The values of* $L_{\rm bol}$ *are shown in Table 5.4.*

AGN	$v_{\rm out}$ km s^{-1}	$M_{\rm out}$ 10^6 M$_\odot$	$\dot{M}_{\rm out}$ M$_\odot$ yr^{-1}	$E_{\rm kin}$ 10^{56} erg	$L_{\rm kin}/L_{\rm bol}$ 10^{-5}	$\dot{p}_{\rm out}$ $L_{\rm bol}/c$
HS 0810+2554	2170 ± 70	15 ± 8	12 ± 6	7 ± 4	700 ± 500	1.9 ± 1.2
SDSS J1353+1138	2410 ± 80	2.4 ± 1.2	1.9 ± 1.0	1.4 ± 0.7	9 ± 7	0.022 ± 0.018

Table 5.4 *Physical properties of the UFOs in HS 0810+2554 and SDSS J1353+1138, as derived from X-ray measurements reported in Chartas et al. (2021) using prescriptions of Nardini and Zubovas (2018). (a)* $M_{\rm BH}$ *values are virial estimates based on* Hβ *in HS 0810+2554 (Assef et al., 2011), and on* C IV *in SDSS J1353+1138 (Chartas et al., 2021), respectively. The* C IV*-based measurement of* $M_{\rm BH}$ *in SDSS J1353+1138 has been corrected following the prescription for* C IV*-based virial BH mass estimates published in Coatman et al. (2017). (b) Values of* $L_{\rm bol}$ *are corrected for lens magnification and computed as average of the two independent estimates of AGN bolometric luminosity, obtained through the 2-10 keV bolometric correction (Lusso et al., 2012) and from the continuum luminosity at 1450 Å (Assef et al., 2011, Runnoe et al., 2012).*

AGN	log($M_{\rm BH}$) $^{\rm a}$ M$_\odot$	$L_{\rm bol}$ $^{\rm b}$ 10^{45} erg s^{-1}	$N_{\rm H}$ 10^{23} cm^{-3}	$v_{\rm UFO}$ c	f	$\dot{M}_{\rm UFO}$ M$_\odot$ yr^{-1}	$\dot{p}_{\rm UFO}$ $L_{\rm bol}/c$
HS 0810+2554	$8.62^{+0.22}_{-0.22}$	2.5 ± 0.9	$2.1^{+1.0}_{-1.1}$ $1.4^{+0.3}_{-0.5}$	$0.11^{+0.05}_{-0.03}$ $0.43^{+0.04}_{-0.05}$	0.4 ± 0.2	$1.2^{+4.2}_{-1.1}$	$3.9^{+17.6}_{-3.5}$
SDSS J1353+1138	$9.41^{+0.30}_{-0.30}$	39 ± 2	$3.9^{+2.4}_{-2.3}$	$0.34^{+0.02}_{-0.09}$	0.4 ± 0.2	4^{+9}_{-3}	$1.7^{+9.7}_{-1.6}$

at different speeds (for which we separately report $N_{\rm H}$ and $v_{\rm UFO}$ in Table 5.4), originally discovered in Chartas et al. (2016) and confirmed in Chartas et al. (2021).

Figure 5.9 shows the momentum-boost as a function of the outflow speed for HS 0810+2554 and SDSS J1353+1138. Given the two X-ray UFOs measurements (represented as circles), dashed horizontal and diagonal lines represent the predictions for a momentum-driven and an energy-driven scenario, respectively. Errorbars on UFOs points indicate the minimum-maximum range of possible values, as mentioned previously. In comparing with ionised outflow points (represented as squares), we observe that while the [O III] outflow of HS 0810+2554 is consistent (within the uncertainty) with the expectations for a momentum-driven mode, that of SDSS J1353+1138 is smaller by a factor of ~100 than the predictions for a momentum-driven propagation, therefore, it is far from any tentative connection with the UFOs on nuclear scale. We reiterate that our measurement is a lower limit, as we do not detect [O III] emission from the second lensed image and, moreover, we have approximated the outflow intrinsic radius to the observed one (just PSF-corrected). Nevertheless, even accounting for all these issues and approximations made, such a discrepancy between observations and theoretical

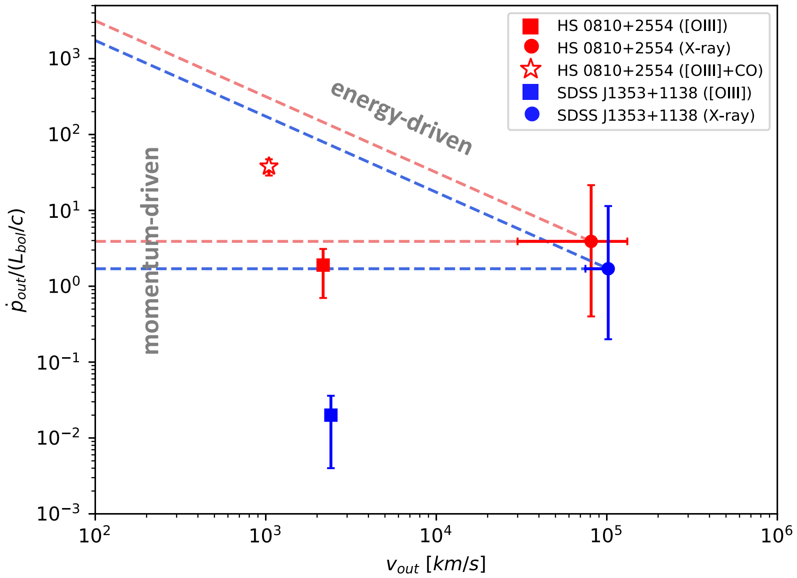

Fig. 5.9 *Momentum-boost versus wind velocity diagram for both UFOs (represented as circles) and galactic outflow components (represented as squares) of HS 0810+2554 (red) and SDSS J1353+1138 (blue). Dashed lines represent the predictions for a momentum-conserving regime (horizontal) and energy-conserving mode (diagonal). For HS 0810+2554, we also plot as a red star the measurement relative to the total (i.e. ionised + molecular) large-scale outflow.*

predictions can hardly be explained, as it amounts to about two orders of magnitude. Even associating half of the [O III] flux observed in image A to image B, on the basis of the flux ratio measurement of the two H-band images (Inada et al., 2006), we would obtain a momentum-boost larger than the previous one by only a factor ~ 1.5. Similarly, it is unlikely that we are underestimating the stretching effects so much as to overestimate $R_{\rm out}$ by a factor of $\sim$100. Therefore, we conclude that such a significant discrepancy must have a different origin. The more plausible hypotheses are: 1) either the likely presence of a massive molecular outflow in this galaxy that our work is not accounting for; or 2) the possibility that the observed UFO is caused by an extraordinary burst episode (see e.g. Zubovas and Nardini 2020) in the BH accretion activity of SDSS J1353+1138, while the large-scale outflow must be considered as the resultant effect of AGN activity averaged over longer timescales (Woo et al., 2017). For this object, Chartas et al. (2021) estimate a photon index $\Gamma \sim 2.2$, which is typical of narrow-line type-1 AGN (Leighly, 1999, Vaughan et al., 1999) and a typical signature of highly accreting systems (Huang et al., 2019). The Eddington ratio $\lambda_{\rm Edd}$ (defined as $L_{\rm bol}/L_{\rm Edd}$, see Sect. 1.1.1) estimated for SDSS J1353+1138 is $\lambda_{\rm Edd} = 0.20 \pm 0.02$ (Chartas et al., 2021), which is larger by a factor $\sim$3 than that inferred for HS 0810+2554 ($\lambda_{\rm Edd} = 0.07 \pm 0.03$; Chartas et al. 2021). Such results could support the recent post-burst scenario. Certainly, each hypothesis does not necessarily exclude the other and the real situation can be a combination of the two (effects).

The small values of momentum-boost ($\sim 0.02-2$) and of kinetic efficiency ($\sim 9-700 \times 10^{-5}$), inferred for the ionised outflows in SDSS J1353+1138 and HS 0810+2554, could be explained by an overall scarcity of [O III] (not only for the outflow component) in highly accreting AGN, observed in other local galaxies with similar properties (e.g. Sulentic et al. 2000). In our two quasars, the poor outflow energetics is indeed due mainly to small values of outflow mass, and not to particularly low velocities. Such a scenario is related to the Eigenvector-1 effect: while sources accreting at high rates (close to the Eddington limit) are actually the most promising candidates for hosting an active UFO (e.g. Nardini et al. 2019), they usually present a very bright Fe II emission and a faint, outshined [O III] emission. As a consequence, [O III] line emission may be not ideal to trace the ionised phase of large-scale outflows in AGN accreting at high rates, since the bulk of the ionised gas could be in the form of different chemical species.

It is also possible we underestimated the uncertainty of the [O III] outflow in HS 0810+2554, mostly due to our approximated procedure in the unlensed reconstruction. Moreover, given the recent tentative detection of a more massive CO-outflow on large scales claimed in Chartas et al. (2020), such a small value of momentum-boost for the ionised outflow is not as unexpected given that it accounts only for the ionised gas traced by the [O III] emission. Hence, we also determine the momentum-boost of the total (i.e. ionised plus molecular) large-scale outflow ($p_{\mathrm{out,tot}}/(L_{\mathrm{bol}}/c) \sim 38$), assuming its velocity to be equal to the mass-weighted average between the ionised and CO-molecular outflow velocities ($v_{\mathrm{out,tot}} \sim 1044$ km s^{-1}). Given the two orders of magnitude of difference between ionised and molecular outflow masses, the mass-weighted velocity is essentially the molecular outflow velocity ($v_{\mathrm{out,tot}} = 1040$ km s^{-1}; Chartas et al. 2020).

In Fig. 5.9, we report the CO + [O III] point with its uncertainty. Once the contribution of the molecular component is included, the energetics of the overall large-scale outflow in HS 0810+2554 is compatible with an energy-driven scenario of wind propagation, within the (large) UFO uncertainty. However, deeper observations are required to confirm the CO-outflow detection and to constrain its energetics.

5.4.2 Comparison with other AGN hosting UFOs

Our study has revealed that the energetics of the galaxy-scale ionised outflow in HS 0810+2554 is consistent with the expectations of a momentum-driven regime, whereas in SDSS J1353+1138, the ionised outflow does not seem to be related with the detected UFO event on sub-pc scales. However, the exiguity of our two-AGN sample prevents us from

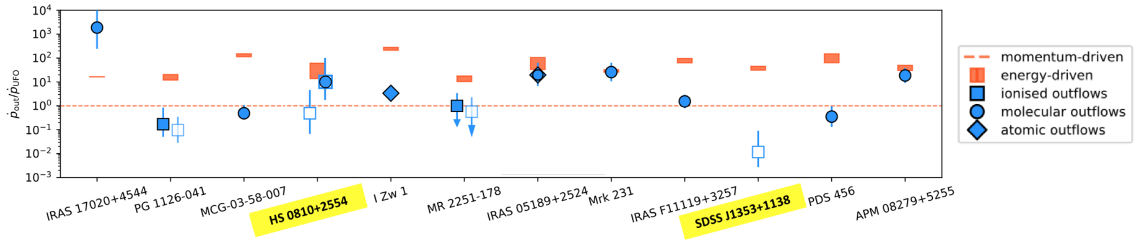

Fig. 5.10 *Ratio of galaxy-scale to sub-pc scale outflow momentum rates for different AGN hosting UFOs. Measurements for individual objects are shown in blue with the respective errorbars, using different markers according to the gas phase of the observed large scale outflow. The galaxy points are ordered by increasing* $L_{\rm bol}$*. The horizontal dashed line shows the prediction for a momentum-driven wind (*$\dot{p}_{\rm out}/\dot{p}_{\rm UFO} = 1$*), while the orange rectangles indicate individual predictions for energy-driven winds. Filled and empty squares represent ionised outflow measurements based on* Hα *and* [O III] *emission, respectively. For HS 0810+2554, our* [O III]*-based measurement is shown both alone and combined with the CO-measurement of the molecular outflow (Chartas et al., 2020), with the respective symbol and combination of symbols (see the plot legend).*

testing the predictions of theoretical models, as well as making general considerations on the nature of the mechanism powering AGN winds on large scales. For this reason, we consider our results along with those of a sample of well-studied AGN, hosting both UFOs and galactic outflows, we collected in Marasco et al. (2020). This AGN-sample consists of two local objects, MR225-178 and PG 1126-041, analysed in Marasco et al. (2020) to trace the ionised phase of large-scale outflows, similarly to this work, but at low redshift; and, other AGN (all local but one) having reliable UFOs and molecular or atomic outflow measurements. In terms of redshift, the only exception is the lensed quasar APM 08279+5255 at $z \sim 3.9$ (Hasinger et al., 2002), found to host a molecular outflow in an energy-driven regime (Feruglio et al., 2017). In addition to HS 0810+2554 and SDSS J1353+1138, this is the only other case at high redshift, for which it has been possible so far to study the connection between nuclear and galaxy-scale winds. This highlights once again the importance of gravitational lensing as a powerful tool to overcome the limits imposed by current observations.

In Marasco et al. (2020), we re-computed the UFO mass rate (and wind energetics, consequently) for each quasar of their gathered sample, starting from the known estimates for $M_{\rm BH}$, $N_{\rm H}$, and $v_{\rm UFO}$. All measurements for molecular outflows have been re-scaled to the same luminosity-to-mass conversion factor $\alpha_{\rm CO} = 0.8$ (K km s^{-1}pc^2)$^{-1}$ M$_\odot$, typical of quasars, starburst and submillimeter galaxies (Downes and Solomon, 1998, Bolatto et al., 2013, Carilli and Walter, 2013). The main AGN parameters, as well as X-ray wind and large-scale outflow properties of the known AGN-sample are listed in Table B.1 in Marasco et al. (2020).

Figure 5.10 represents the updated version of Fig. 9 in Marasco et al. (2020), including now the measurements obtained for HS 0810+2554 and SDSS J1353+1138. The plot shows the ratios between galaxy-scale and sub-pc scale outflow momentum rates ($\dot{p}_{\rm out}$ and $\dot{p}_{\rm UFO}$, respectively), ordered according to the increasing $L_{\rm bol}$ of the AGN galaxy. This is an alternative way (with regard to Fig. 5.9) to compare observational results with theoretical predictions for each AGN and to distinguish between the two main regimes. The energetics of the large-scale outflow in 10 out of 12 AGN results to be consistent (or nearly consistent) with either a momentum-driven or an energy-driven regime: in seven (six) and three (four) objects, respectively, if we exclude (include) the contribution of the tentatively detected molecular outflow in HS 0810+2554. This globally confirms the conclusion drawn by Marasco et al. (2020) that models of either momentum- or energy-driven outflows describe the mechanism of wind propagation on galaxy-scales very well. The only two exceptions are SDSS J1353+1138 and IRAS 17020+4544, representative of the two extreme opposite situations in which the energetics on large and nuclear scales seem to be completely unrelated. As discussed in Sect. 5.4.1, the low value of $\dot{p}_{\rm out}/\dot{p}_{\rm UFO}$ in SDSS J1353+1138 could be due to the presence of a massive molecular outflow, which our work does not account for. Alternatively, it could indicate that SDSS J1353+1138 has recently undergone a burst episode of its AGN activity. In terms of high AGN variability, the high value of $\dot{p}_{\rm out}/\dot{p}_{\rm UFO}$ inferred for IRAS 17020+4554 could be explained by invoking a past higher BH accretion activity compared to present day, but observations reveal that IRAS 17020+2554 is now accreting at a substantial fraction of its Eddington rate ($\lambda_{\rm Edd}$ ~ 0.7; Longinotti et al. 2015). Finally, we do not observe any remarkable trend in $\dot{p}_{\rm out}/\dot{p}_{\rm UFO}$ values with $L_{\rm bol}$, nor any evident dependence of wind acceleration mechanism on galaxy redshift upon separately inspecting the results obtained for the high-redshift (our two objects plus APM 08279+5255) and low-redshift quasars (the remaining ones) in the sample.

5.5 Conclusions

Galaxy-wide outflows powered by AGN activity are thought to play a fundamental role in shaping the evolution of galaxies, as they allow us to reconcile theoretical models to observations. However, even though observations have widely confirmed their presence in both local and high-redshift galaxies, a clear understanding of the mechanism which accelerates these powerful, galaxy-scale winds is still lacking. To test the predictions of the current theoretical models, we need to compare, in a given object, the energetics of sub-pc winds with that of galaxy-wide outflows. Optimal sources in attempting the make a connection between different scales are the powerful quasars near the peak of AGN activity ($z \sim 2$), where AGN feedback is expected to be more effective.

In such a perspective, this work has focused on two $z \sim 1.5$ multiple lensed quasars, specifically selected to host UFOs (HS 0810+2554 and SDSS J1353+1138) and observed with the near-IR integral field spectrometer SINFONI. Thanks to strong lens magnification and to the spatially resolved SINFONI data, which trace the dynamics of the ionised gas phase through rest-frame optical emission lines, it has been possible, for the first time, to attempt to make the connection between the sub-pc winds and large-scale ionised outflows in two quasars near the peak of AGN activity. The only other well-studied case at high redshift is APM 08279+5255 ($z \sim 3.9$), which has been suggested to host a molecular outflow in energy-conserving regime (Feruglio et al., 2017). Moreover, the recent analysis of ALMA data of HS 0810+2554 has revealed the tentative detection of CO-molecular outflow (Chartas et al., 2020). Therefore, the characterisation of the ionised phase of the outflow in HS 0810+2554 provides the first three-phase description of an AGN-driven wind at high redshift, from X-ray to optical and mm bands, corresponding to highly ionised, ionised, and molecular gas phases, respectively.

In the following, we summarise the main results obtained in this chapter:

1. We studied the gas kinematics to identify the presence of outflowing gas by tracing the emission of the forbidden line doublet [O III]$\lambda\lambda$4959,5007, whose line profile is highly asymmetric in presence of outflows, with a typical broad, blueshifted wing corresponding to high speeds along the line of sight. In both AGN, we detected the presence of extended ($\sim$ 8 kpc) ionised outflows moving up to $v \sim 2000$ km s^{-1} in the image lens plane.

2. After correcting for gravitational lens effects, we found that the ionised outflow in HS 0810+2554 is consistent within the uncertainty with the predictions for a momentum-driven regime and with an energy-driven propagation once the contribution of the molecular outflow is included. On the contrary, the ionised outflow in SDSS J1353+1138 appears to be unrelated to the nuclear scale energetics, likely requiring either the presence of a massive molecular outflow or a high variability among the AGN activity.

3. By comparing our inferred results with those of the small sample of known AGN from the literature, each hosting both sub-pc scale UFOs and neutral or ionised winds on galaxy scales, we found that the momentum- and energy-driven frameworks describe all the observed targets very well, with the exception of SDSS J1353+1138 and IRAS 17020+4544. Therefore, these driving mechanisms appear to explain how

the energy released by the AGN activity is coupled with the galactic ISM, thus driving the wind propagation on a large scale.

Altogether, the observations presented in this work provide important pieces of information on the long sought-after ‘engine’ of large-scale outflows and feedback at the Cosmic Noon, highlighting once again the power of IFS in this type of study. Follow-up CO observations of these sources will be necessary to confirm the molecular outflow detection and to constrain its energetics in HS 0810+2554, and to test whether a massive molecular outflow is responsible for the mismatch between the wind energetics at different scales observed in SDSS J1353+1138.

Chapter 6

Fast & Furious: type-2 AGN host faster ionised winds than type-1 at z~2 in SUPER

In this chapter, we present spatially resolved VLT/SINFONI spectroscopy of z~2 type-2 AGN from SUPER (Survey for Unveiling the Physics and Effect of Radiative feedback), showing evidence of fast ionised winds ($v \gtrsim 600$ km s^{-1}) on 1–3 kpc scales, traced via [O III]λ*5007 line emission. Interestingly, our analysis reveals that type-2 AGN host faster ionised winds compared to SUPER type-1 systems within the same range of bolometric luminosity* ($L_{\rm bol} \sim 10^{44.8-46.5}$ *erg s*$^{-1}$)*. We speculate that these X-ray selected type-2 AGN represent the 'blow-out' phase predicted by galaxy evolutionary models, where a larger presence of obscuring material might ultimately favour the acceleration of large-scale ionised outflows via radiation pressure on dust. Based on Tozzi et al. (2023), to be submitted.*

To date we have plenty of observational evidence of multi-phase AGN-driven outflows from low to high redshift (see Sect. 1.2.3 also Chapters 4 and 5), with the high-redshift search primarily focused on bright distant sources, being easier to detect and to investigate. However, a number of questions still remain open due to the lack of clear observational evidence confirming definitely model predictions (as discussed in Sect. 1.2), which motivates us to continue our research. Among these observationally-untested theoretical predictions, there is the evolutionary sequence through different obscuring states followed by AGN galaxies (e.g. Hopkins et al. 2006, Menci et al. 2008; see Sect. 1.1.2.2). According to this picture, AGN galaxies go through a first dust-enshrouded phase, where the central nucleus is obscured by dust and gas, thus fuelling both supermassive BH growth and SF efficiently. All this sets the stage to the so-called 'blow-out' phase (e.g. Hopkins et al. 2008), during which powerful AGN-driven winds sweep away obscuring material and make the central AGN visible and unobscured.

Although *JWST* has opened a new window on unprecedented high redshifts (i.e. $z > 4$), the Cosmic Noon (z~2) still represents the golden epoch where to catch AGN feedback in action, and can be deeply investigated also with ground-based AO-assisted facilities. The completed ESO Large Programme SUPER (Survey for Unveiling the Physics and Effect of Radiative feedback; PI: V. Mainieri, ID: 196.A-0377), carried out with VLT/SINFONI has collected AO-assisted IFU data of a representative sample of X-ray AGN ($L_X \gtrsim 10^{42}$ erg s^{-1} at z~2, over a wide range of bolometric luminosity ($L_{\rm bol} \sim 10^{44-48}$ erg s^{-1}), selected in unbiased way with respect to the chance of hosting outflows (selected sample presented in Circosta et al. 2018). SUPER primarily aims at investigating AGN ionised outflows and studying their physical properties as a function of fundamental AGN and host galaxy parameters (e.g. bolometric luminosity, stellar mass, star formation rate), to finally assess the impact of outflows on their host.

This chapter continues the series of publications dedicated to SUPER[1], presenting the latest results obtained for the type-2 AGN subsample. We will analyse SINFONI observations of SUPER type-2 AGN and search for evidence of large-scale ionised outflows using [O III]λ5007Å line emission as tracer. The inferred results on type-2 ionised outflows will be then compared those detected in SUPER type-1 AGN (Kakkad et al., 2020), aiming at studying possible differences between type-1 and type-2 AGN populations. A ΛCDM flat cosmology with $\Omega_{\rm m,0} = 0.3$, $\Omega_{\Lambda,0} = 0.7$ and $H_0 = 70$ km s^{-1} $\rm Mpc^{-1}$ is adopted throughout this work.

6.1 The SUPER survey

The sample presented in this chapter is part of the SUPER survey, a completed ESO Large Programme (ID: 196.A-0377; PI: V. Mainieri) awarded 280 hours of SINFONI observing time with AO, to obtain near-IR IFU observations of 39 blindly selected X-ray AGN at $z \sim 2$ (see Circosta et al. 2018 for details on selection criteria an the original selected 39-AGN sample). The main scientific goals of SUPER are: (i) providing a first unbiased investigation of ionised gas conditions in z~2 AGN, with an unprecedented spatial resolution of ~ kpc thanks to SINFONI AO; (ii) inferring the impact of outflows on active SF; and (iii) linking outflow properties (e.g. velocity, mass rate) with fundamental AGN and host galaxy parameters (e.g. bolometric luminosity, stellar mass, star formation rate). Since part of the survey was executed in visitor mode rather than service mode, a considerable fraction

---

[1] Link to visit the SUPER webpage (http://www.super-survey.org/).

of time got lost because of bad weather conditions and a few selected targets (6 objects) were not observed. The final observed sample therefore consists of: 21 type-1 AGN and 12 type-2 AGN. Whereas SINFONI observations of the type-1 sample have been already analysed and published in Kakkad et al. (2020), we here present type-2 AGN datasets.

6.1.1 The type-2 AGN subsample

SUPER has targeted 12 type-2 AGN in total: six sources are from the *Chandra* Deep Field-South (CDF-S; Luo et al. 2017); whereas other six from the COSMOS-Legacy survey (Civano et al., 2016). Before being observed by SINFONI, they were selected to be type-2 systems based on the absence of BLR emission in archival rest-frame UV spectra (Cicone et al., 2018); then, the absence in SINFONI spectra of BLR components in rest-frame optical Balmer hydrogen lines (Hα and Hβ, less affected by extinction than rest-frame UV emission lines) has confirmed their spectral classification as type-2 AGN. In Table 6.1, we list some main properties of the 12 observed type-2 AGN, including spectroscopic redshift z; bolometric luminosity $L_{\rm bol}$, stellar mass M_*, and SFR, all derived from SED fitting (Circosta et al., 2018); 2–10 keV X-ray luminosity $L_{2-10\ \rm keV}$ and hydrogen column density $N_{\rm H}$ inferred from archival X-ray spectra (Circosta et al., 2018). Redshift values have been obtained from SINFONI rest-frame optical spectra (see Sect. 6.2.1), except for sources being undetected or marginally detected (five in total) in our SINFONI data (see Sect. 6.1.2). Redshift of these sources have been measured from archival rest-frame UV spectra (marked with †).

6.1.2 Observations and data reduction

SUPER targets were observed with SINFONI between November 2015 and December 2018, as part of the ESO Large Programme 196.A-0377 (PI: V. Mainieri), in both service and visitor mode. All SINFONI observations were planned to be carried out in AO mode in both *H* band, targeting Hβ and [O III]$\lambda\lambda$4959,5007Å emission lines, and *K* band, targeting Hα, [N II]$\lambda\lambda$6549,83Å, and [S II]$\lambda\lambda$6716,31Å.

Observations of ten out of 12 type-2 AGN were performed in AO-assisted mode with no tip-tilt star (i.e. in Seeing Enhancer mode), using both *H* and *K* gratings (R ~3000 and R ~4000, respectively); whereas the remaining two objects were observed with no-AO (cid_1253 with *H* and *K* gratings, cid_971 with the *HK* grating, R ~1500), to optimize the reduced fraction of time available during the visitor mode observing run because of bad weather conditions. For AO-assisted observations, we adopted a plate scale of $3'' \times 3''$ with a spatial sampling of $0.05'' \times 0.1''$, then re-sampled to $0.05'' \times 0.05''$ in the final data cube.

Table 6.1 *Main properties of the 12 observed type-2 AGN from SUPER. From left, columns report: coordinates of the optical counterpart of the target (J2000); spectroscopic redshift z; galaxy stellar mass M_*, star formation rate (SFR), AGN bolometric luminosity $L_{\rm bol}$, all with 1σ uncertainties, derived from SED fitting (Circosta et al., 2018); 2–10 keV X-ray luminosity $L_{2-10\ \rm keV}$ and hydrogen column density $N_{\rm H}$ with 90% confidence level errors, measured from archival X-ray data (Circosta et al., 2018). Redshift values have been measured from rest-frame optical SINFONI spectra (Sect. 6.2.1), except for sources undetected or marginally detected in SINFONI observations (Sect. 6.1.2)). For these objects, we report the spectroscopic redshift measured from archival rest-frame UV spectra (marked with †).*

Field & Target ID	RA (hh:mm:ss)	DEC (dd:mm:ss)	z	log M$_*$ [M$_\odot$]	SFR [M$_\odot$ yr^{-1}]	log $L_{\rm bol}$ [erg s^{-1}]	log $L_{2-10\ \rm keV}$ [erg s^{-1}]	log $N_{\rm H}$ [cm^{-2}]
CDF-S XID36	03:31:50.77	−27:47:03.41	2.255	10.68 ± 0.07	184 ± 9	45.70 ± 0.06	$43.84^{+0.31}_{-0.63}$	> 24.1
CDF-S XID57	03:31:54.40	−27:56:49.70	2.298 †	10.49 ± 0.11	< 34	44.26 ± 0.18	$44.04^{+0.17}_{-0.24}$	$23.30^{+0.32}_{-0.39}$
CDF-S XID419	03:32:23.44	−27:42:54.97	2.143	10.89 ± 0.02	42 ± 4	45.54 ± 0.05	$43.84^{+0.29}_{-0.44}$	$24.28^{+0.19}_{-0.31}$
CDF-S XID427	03:32:24.20	−27:42:57.51	2.303 †	10.87 ± 0.08	< 72	44.60 ± 0.13	$43.20^{+0.06}_{-0.06}$	$22.43^{+0.24}_{-0.34}$
CDF-S XID522	03:32:28.50	−27:46:57.99	2.309 †	10.42 ± 0.02	492 ± 25	45.02 ± 0.02	$43.51^{+0.76}_{-0.87}$	> 22.5
CDF-S XID614	03:32:33.02	−27:42:00.33	2.453	10.78 ± 0.08	247 ± 12	44.97 ± 0.13	$43.61^{+0.18}_{-0.18}$	$24.25^{+0.19}_{-0.18}$
COSMOS cid_1057	09:59:15.00	+02:06:39.65	2.210	10.84 ± 0.07	85 ± 4	45.91 ± 0.06	$44.53^{+0.26}_{-0.30}$	$23.98^{+0.24}_{-0.28}$
COSMOS cid_451	10:00:00.61	+02:15:31.06	2.444	11.21 ± 0.05	< 125	46.44 ± 0.07	$45.18^{+0.23}_{-0.19}$	$23.87^{+0.19}_{-0.15}$
COSMOS cid_2682	10:00:08.81	+02:06:37.66	2.437	11.03 ± 0.04	< 93	45.48 ± 0.10	$44.30^{+0.96}_{-0.27}$	$23.92^{+1.01}_{-0.20}$
COSMOS cid_1143	10:00:08.84	+02:15:27.99	2.443	10.40 ± 0.17	108 ± 18	44.85 ± 0.12	$44.83^{+0.43}_{-0.36}$	$24.01^{+0.77}_{-0.29}$
COSMOS cid_971	10:00:59.45	+02:19:57.44	2.473 †	10.60 ± 0.12	< 96	44.71 ± 0.24	$43.87^{+0.36}_{-0.38}$	< 23.68
COSMOS cid_1253	10:01:30.57	+02:18:42.57	2.147 †	10.99 ± 0.25	280 ± 194	45.08 ± 0.18	$43.92^{+0.29}_{-0.31}$	$23.22^{+0.47}_{-0.39}$

Instead, for the two targets observed in seeing-limited mode during the visitor-mode runs we selected the largest FoV ($8'' \times 8''$), corresponding to a pixel scale of $0.25'' \times 0.25''$ in the final reduced data cube. Before or after each observing block, a dedicated PSF star was observed to derive an estimate of the final AO PSF FWHM (reported in Table 6.2).

For a detailed description of both our observational strategy and reduction procedure, we refer to the second SUPER paper (Kakkad et al., 2020). Here, we just summarise the main steps of the reduction procedure applied to SINFONI data cubes. We reduced all observations using the ESOREX pipeline (3.1.1), which returns a distortion-corrected and wavelength-calibrated data cube of the science target, as well as of the PSF and telluric stars. We then removed background sky emission via the `IDL` routine 'skysub.pro' (Davies, 2007), and used our own custom-made `python` routines to perform flux calibration (based on Piqueras López et al. 2012) and to reconstruct the final data cube for each observed target. As a final check, we compared the synthetic photometry measured from SINFONI integrated spectra with both archival photometric measurements (Circosta et al., 2018), and the synthetic photometry from KMOS integrated spectra, when available (Scholtz et al., in prep.). From this comparison, we estimated a typical relative uncertainty on the flux calibration of our SINFONI data of about 20% for all employed bands.

In Table 6.2, we show some main parameters of SINFONI observations of the 12 SUPER type-2 AGN. For each target, we specify the observing mode (AO/noAO), and list

Table 6.2 *SINFONI observations of the 12 type-2 AGN from SUPER. For each target, we indicate the observing mode (AO/noAO), and list the following parameters for each adopted grating (H, K, HK): absolute (AB) magnitude measured from SINFONI integrated spectra, total exposure time ($t_{\rm exp}$), spatial resolution ($\theta_{\rm PSF}$), computed as PSF FWHM, and emission lines (EL) being detected. Boldface characters indicate targets detected with a spatially integrated S/N>2 on* [O III]*; when detected at S/N<2,* [O III] *and* Hα *are accompanied by a '†' symbol. For targets marked with '*', a correction factor (~ 2) was required to match the previous synthetic measurements (Circosta et al., 2018).*

Target	Obs mode	*H* band				*K* band			
		mag (AB)	$t_{\rm exp}$ [hr]	$\theta_{\rm PSF}$ [$''$] ($\theta_{\rm PSF}$ [kpc])	EL	mag (AB)	$t_{\rm exp}$ [hr]	$\theta_{\rm PSF}$ [$''$] ($\theta_{\rm PSF}$ [kpc])	EL
XID36	AO	21.45	5.3	0.29 × 0.26 (2.4 × 2.1)	Hβ, [O III]	21.13	2.0	0.15 × 0.15 1.2 × 1.2	Hα, [N II], [S II]
XID57	AO	-	3.0	0.32 × 0.30 (2.6 × 2.5)	-	-	1.0	0.33 × 0.27 (2.7 × 2.2)	-
XID419	AO	22.69*	0.8	0.47 × 0.52 (3.9 × 4.3)	[O III]	21.85*	1.0	0.24 × 0.22 (2.0 × 1.8)	Hα, [N II]
XID427	AO	22.72	1.0	0.23 × 0.20 (1.9 × 1.6)	-	21.90*	1.0	0.28 × 0.20 (2.3 × 1.6)	Hα †
XID522	AO	-	1.0	0.25 × 0.20 (2.0 × 1.6)	-	-	1.0	0.25 × 0.19 (2.0 × 1.6)	-
XID614	AO	22.41*	11.5	0.38 × 0.37 (3.1 × 3.0)	Hβ, [O III]	21.79	3.5	0.27 × 0.28 (2.2 × 2.3)	Hα, [N II]
cid_1057	AO	21.80*	2.0	0.32 × 0.30 (2.6 × 2.5)	Hβ, [O III]	20.91	0.7	0.46 × 0.43 (3.8 × 3.6)	-
cid_451	AO	21.73	5.0	0.28 × 0.30 (2.3 × 2.4)	[O III]	21.69*	2.0	0.28 × 0.27 (2.3 × 2.2)	Hα, [N II]
cid_2682	AO	21.58	5.6	0.33 × 0.28 (2.7 × 2.3)	[O III]	21.01*	1.8	0.28 × 0.25 (2.3 × 2.0)	Hα, [N II]
cid_1143	AO	22.44	5.5	0.41 × 0.38 (3.3 × 3.1)	Hβ, [O III]	22.66	2.0	0.30 × 0.30 (2.4 × 2.4)	Hα †
cid_1253	noAO	22.45	4.0	0.68 × 0.63 (5.6 × 5.2)	[O III] †	21.61	1.0	0.66 × 0.61 (5.5 × 5.1)	Hα †
		HK band							
		mag (AB)		$t_{\rm exp}$ [hr]		$\theta_{\rm PSF}$ [$''$] ($\theta_{\rm PSF}$ [kpc])		EL	
cid_971	noAO	-		1.8		0.42 × 0.39 (3.4 × 3.2)		-	

the following parameters for the corresponding adopted grating (*H*, *K*, *HK*): absolute (AB) magnitude measured from SINFONI integrated spectra, total exposure time ($t_{\rm exp}$), spatial resolution ($\theta_{\rm PSF}$), and emission lines (EL) being detected. The spatial resolution $\theta_{\rm PSF}$ has been computed as FWHM of a 2D-Gaussian profile fitted to the total flux distribution of the PSF star observed in *H* and *K* bands. The brightest emission lines are [O III] and Hα in *H* and *K* bands, respectively: when detected with a total S/N<2 in SINFONI integrated spectra, these lines are marked with †. Seven type-2 sources are detected in [O III] line emission with a total, spatially integrated S/N>2 (target IDs in boldface in Table 6.2). Five of these have also Hα+[N II] detected with a S/N>2, whereas in cid_1057 and cid_1143 Hα is totally undetected and marginally (S/N<2) detected, respectively. In two sources (namely, XID427 and cid_1253), we detect [O III] and/or Hα (i.e. only Hα in XID427, both [O III] and Hα in cid_1253) just marginally (i.e. S/N<2), whereas the remaining three targets (i.e. XID522, XID57 and cid_971) are totally undetected in SINFONI observations. These undetections or poor detections in *H*- or *K*-band datasets are a consequence of lower integration time, due to observing time lost because of bad weather conditions, which particularly penalised SUPER type-2 objects, being also the faintest sources of the SUPER sample ($L_{\rm bol} < 10^{46}$ erg s^{-1}).

The rest of this chapter will focus on the seven type-2 AGN with [O III] detected at S/N>2 (listed in boldface in Table 6.2), for which it is possible to perform a spatially-resolved, spectral analysis of [O III] line emission, aiming at searching for ionised outflows signatures.

6.2 Data analysis

In this section, we analyse SINFONI *H*-band data cubes of the seven type-2 AGN well detected (S/N>2) in [O III] (listed with boldface labels in Table 6.2), to spatially map [O III] line emission and its kinematics, looking for evidence of high-velocity outflowing gas (Sect. 6.2.1). Unfortunately, the quality of *K*-band data is worse (i.e. lower S/N) for most objects, which prevents us from an accurate mapping of *K*-band line emission across the SINFONI FoV. However, in Sect. 6.2.2 we use combine integrated measurements of Hα and Hβ flux from *K* and *H*-band data, respectively, to estimate dust extinction. Being these targets obscured (type-2) AGN, correcting for dust extinction is a crucial step to get reliable estimates of outflow energetics (see Sect. 6.3.2).

6.2.1 Spectral fitting

For the spectral fitting of SINFONI *H*-band data cubes, we adopt the fitting code presented in Sect. 1.3.3, and fit all cubes in the rest-frame optical wavelength range of 4800–5200Å. Being distant type-2 AGN, their SINFONI spectra show neither BLR emission nor strong (AGN and/or stellar) continuum, but consist of only ‘narrow’ (FWHM$\lesssim$2000 km s^{-1}) emission lines, either originating from AGN NLR or due to a different kinematics (i.e. outflow, disk rotation). In addition to [O III]$\lambda\lambda$5007,4959Å emission line doublet (detected in all seven examined sources), we also detect faint Hβ line emission in four *H*-band data cubes.

As a first step, we increase the S/N of SINFONI data by means of a Gaussian smoothing, avoiding carefully deteriorating further the instrumental PSF. Therefore, we smooth each data cube with a Gaussian kernel of width $\sigma_{\rm smooth} \sim 0.1 - 0.2''$, that is as larger as possible, but still smaller than the instrumental PSF (see Table 6.2, $\sigma_{\rm smooth} < \theta_{\rm PSF}/2.35$). After this, we model spaxel-by-spaxel the observed line emission via multiple Gaussian components, following the prescriptions summarised below:

- We fit two Gaussian components to the [O III]$\lambda\lambda$5007,4959Å line doublet, with a fixed flux ratio of 3, and same kinematics (i.e. velocity v and velocity dispersion σ). Hereafter, we refer to the brighter doublet component (i.e. [O III]λ5007Å) simply as [O III].

- When detected, faint Hβ line emission is modelled with v and σ fixed to the best-fit values obtained for [O III], hence with flux as a free parameter only.

- In each spaxel, we reiterate the line modelling using variable number of Gaussian components, ranging from one to a maximum number which best reproduces complex line profiles in high S/N spaxels. We then select the optimal (minimum) number of Gaussian components required in each spaxel via a Kolmogorov-Smirnov test on the residuals. Five *H*-band datasets require up to two Gaussian components; cid_1057 up to three components, given the presence of both blue and red [O III] wings detected; instead, one component is sufficient to model single-spaxel line emission in XID419.

- We also add a 1st-degree polynomial to reproduce any faint continuum emission over the entire fitted wavelength range.

Overall, several spectra require multiple Gaussian components to reproduce simultaneously both narrow, low-velocity line emission and broad, high-velocity wings in [O III] line profile. Whereas the latter are considered the typical signature of fast outflowing gas (discussed in Sect. 6.3.1), narrow, low-velocity line emission is typically due to nearly systemic gas motions (e.g. NLR, disk rotation). For this reason, we compute the redshift of each source from the peak of [O III] narrow line emission. In particular, we extract H-band integrated spectra from a small (i.e. radius of $1''$) aperture centred on the overall H-band emission peak (corresponding to [O, III] emission peak) and set to 0 km s^{-1} the peak of the [O, III] narrow line component. We estimate an uncertainty of $\Delta\ z = 0.001$ on our [O III]-based measurements of z, due to SINFONI H-band spectral resolution (R ~3000).

6.2.2 Integrated *H* and *K*-band spectra

Since the targets here examined are type-2, obscured AGN ($N_{\rm H} \gtrsim 10^{24}{\rm cm}^{-2}$; Circosta et al. 2018), it is important to correct flux/luminosity measurements for dust extinction. In particular, in Sect. 6.3.2 we will need to correct for dust extinction [O III] luminosity associated with outflowing gas, to estimate intrinsic energetics of ionised outflows. Below, we describe how we estimate rest-frame optical dust extinction from spatially integrated Hα/Hβ ratios for the seven examined type-2 AGN.

To accurately correct for dust extinction, we should: (i) account for spatial variations of Hα/Hβ across the FoV using spaxel-by-spaxel measurements; (ii) consider extinction effects exclusively on the outflow component, which may differ from those affecting the bulk of the ionised gas or any other kinematic component (e.g. disk rotation, AGN NLR). Yet, the S/N on Hα and Hβ is not high enough for such an accurate, spatial mapping of dust extinction. Indeed, their detection is mostly limited to central brighter spaxels, with Hβ undetected in three sources (even in integrated spectra), whereas Hα is totally undetected in cid_1057 and marginally (S/N<2) detected in cid_1143. Therefore, we extract integrated K and H-band spectra of each object to increase the S/N Hα and Hβ, so as to estimate (or put constraints on) dust extinction. The only target of the 7-AGN examined sample for which this is not possible is cid_1057, being totally undetected in Hα. Therefore, in the following we describe first how we estimate (or constrain) from integrated spectra dust extinction in the remaining six objects, and then assumptions adopted for cid_1057.

We extract integrated K- and H-band spectra of each object using an aperture of ~$0.25''$-radius centred on the source (see Figs. 6.1, 6.2, 6.3), and fit them following the same prescriptions described in Sect. 6.2.1. In particular, Gaussian profiles fitted to Hα and [N II]$\lambda\lambda$6549,83 are constrained to have the same velocity and velocity dispersion, with the additional constraint of a fixed flux ratio of 3 on the two [N II] doublet components. In XID36, we model also faint [S II]$\lambda\lambda$6716,31 line emission, following the same prescriptions adopted for Hβ in H-band datasets. In most cases, one Gaussian component is enough to reproduce K-band emission lines; XID36 and cid_451 instead require an additional broader component (σ ~800 km s^{-1} in XID36, σ ~400 km s^{-1} in cid_451). In Figs. 6.1 and 6.2, we show H- and K-band spectra extracted with a 0.25″-radius aperture from SINFONI data cubes, after subtracting a 1st-degree polynomial used to reproduce any residual faint continuum emission. Data are shown in black, with total emission-line model drawn on the top in red. In case of multi-Gaussian fitting, we plot separately components used to reproduce narrow, systemic line emission (lightblue), and broad high-velocity line emission (green), likely associated with fast outflowing gas. In Fig. 6.3, we also show an integrated H-band spectrum of cid_1057, extracted with the same 0.25″-radius aperture. In this source, the [O III] emission line exhibits an asymmetric profile which is well reproduced by three Gaussian components: one to reproduce systemic, narrow line emission (lightblue component in Fig. 6.3), two to model blue and red wings detected in [O III] (in different green colours).

Since we do not detect broad, high-velocity emission in Hβ profile, possibly associated with outflows, in any object (in Hα only in XID36 and cid_451), we use integrated total-line flux ratios (i.e. Hα/Hβ) to obtain an estimate of total dust extinction (Calzetti et al., 2000) and use it as an estimate of the one affecting the outflow emission. For XID36, XID614 and cid_1143, with both hydrogen lines detected, we estimate A_V and relative uncertainty via error propagation. For cid_1143, due to the low S/N on Hα and Hβ, we obtain a value of A_V consistent with 0 (i.e. no extinction) within the uncertainty ($A_V = 1.2 \pm 1.8$). Since A_V must be non-negative, we adopt $A_V = 1.2^{+1.8}_{-1.2}$. In XID419, cid_2682 and cid_451 instead, where we do not detect Hβ, we estimate a lower limit to A_V, considering a $2\sigma_{\rm noise}$ upper limit to Hβ flux. Finally, for cid_1057, the only source totally undetected in Hα, we consider an A_V value computed as the average of the three A_V measurements obtained for XID36, XID614 and cid_1143, taking the maximum distance of these estimates from the mean as uncertainty (i.e. $A_V = 1.8 \pm 1.0$). In Table 6.3, we list all A_V values adopted to correct observed outflow [O III] fluxes for each source.

6.3 Results

6.3.1 Ionised gas kinematics: evidence of spatially resolved outflows

Our spectral modelling of [O III] line emission has revealed clear prominent [O III] wings across the FoV of four galaxies (i.e. XID36, cid_1143, cid_451, cid_1057; see Figs. 6.1-6.3), pointing to the presence of gas moving at high speed with respect to the galaxy systemic

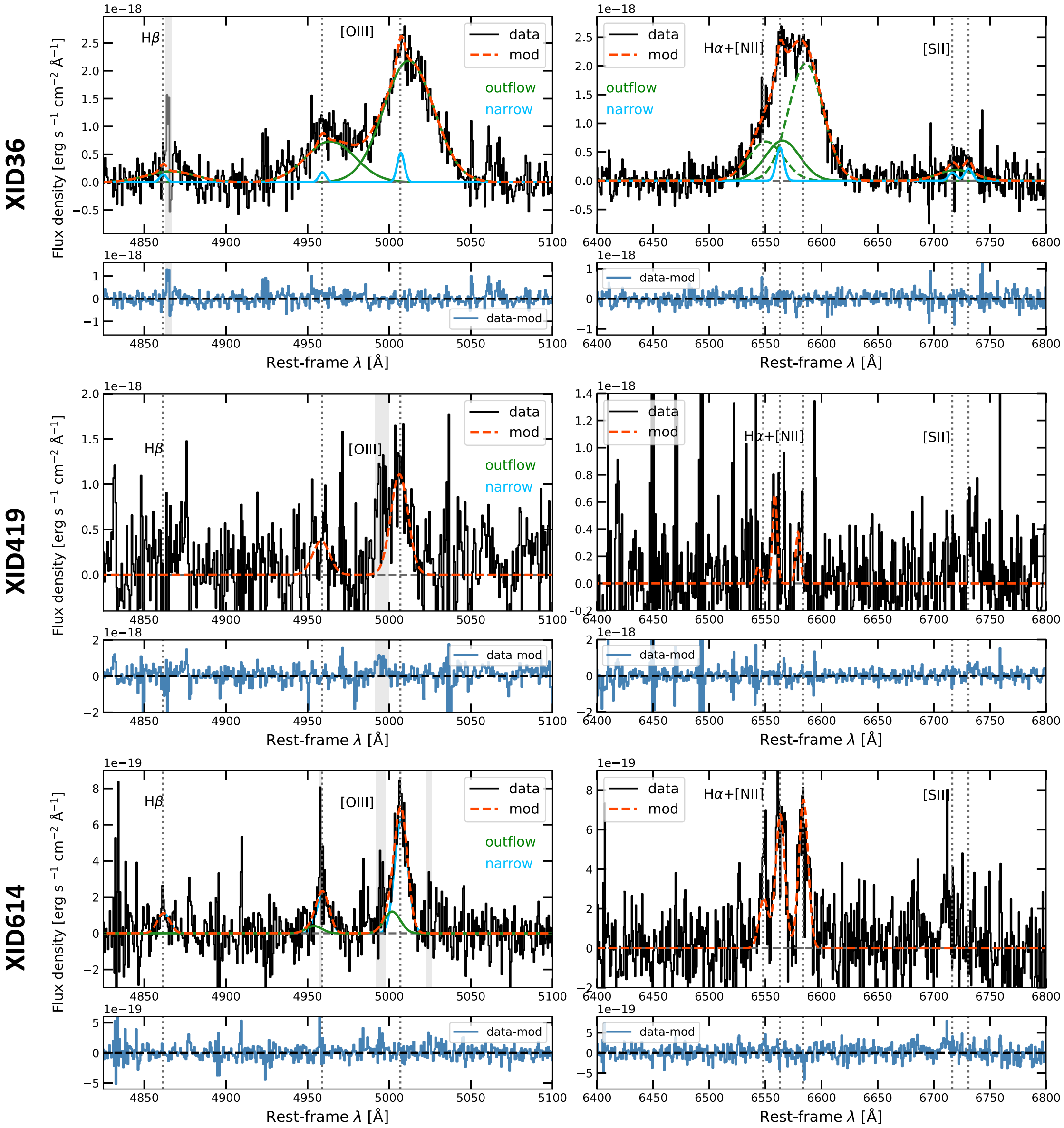

Fig. 6.1 *Integrated H- and K-band spectra extracted from SINFONI data cubes of XID36 (top), XID419 (middle) and XID614 (bottom), with a 0.25″-radius aperture, after subtracting a 1st-degree polynomial used to reproduce any residual faint continuum emission. Data are shown in black, with total emission-line model drawn on the top in red. For multi-Gaussian modellings, we plot separately components used to reproduce narrow, systemic line emission (lightblue), and broad high-velocity line emission (green), likely associated with fast outflowing gas. Shaded grey regions indicate channels of sky emission (masked during the modelling), while vertical dotted lines mark emission line rest-frame wavelengths at redshifts, as computed in Sect. 6.2.1. Below each main panel, a second one shows corresponding residuals (i.e. data–model).*

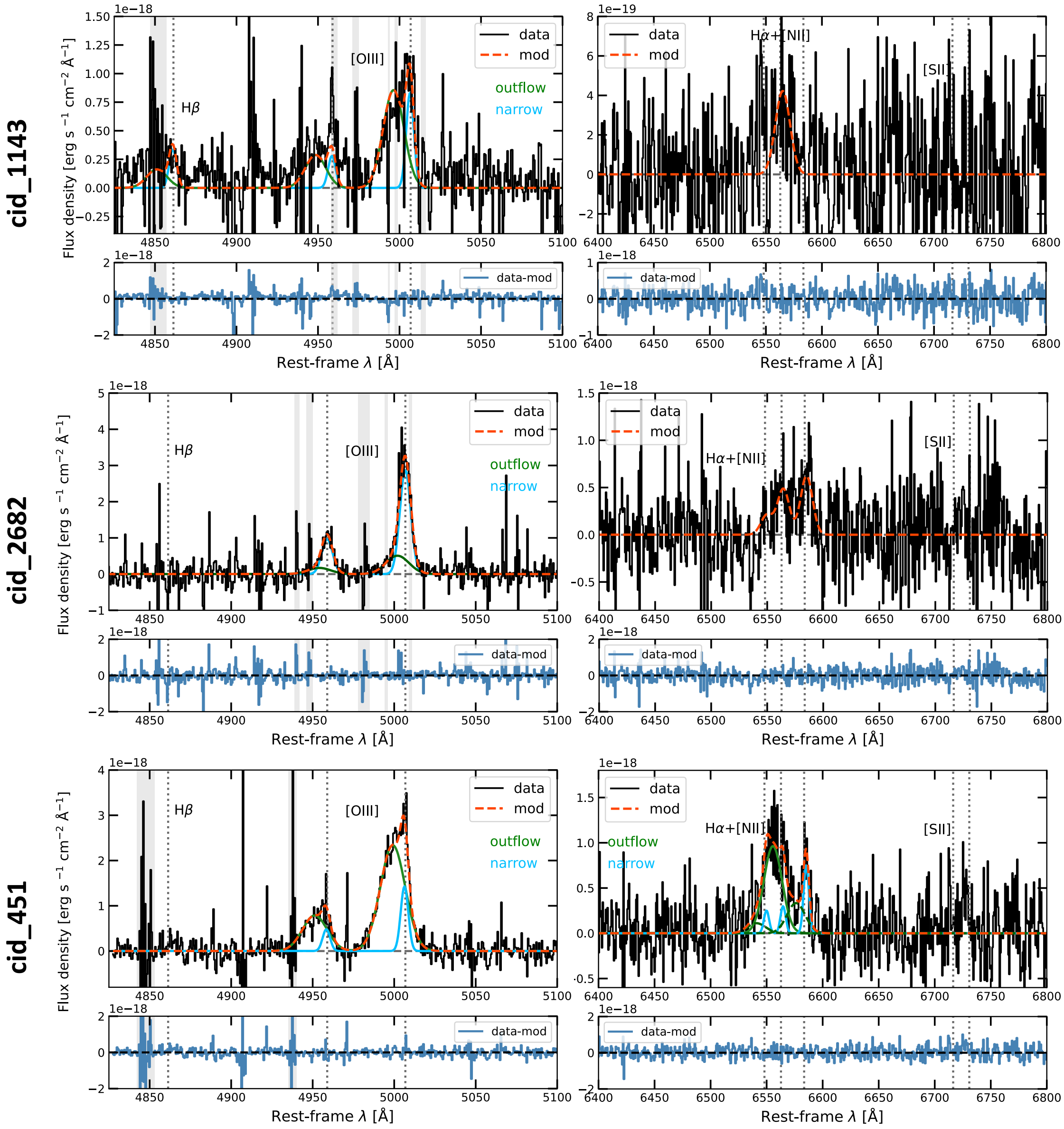

Fig. 6.2 *Integrated H- and K-band spectra extracted from SINFONI data cubes of cid_1143 (top), cid_2682 (middle) and cid_451 (bottom), with a 0.25″-radius aperture, after subtracting a 1st-degree polynomial used to reproduce any residual faint continuum emission. Same as in Fig. 6.2. In K-band spectrum of cid_1143, we fit only* Hα *line emission due to the low S/N (S/N<2) of this dataset.*

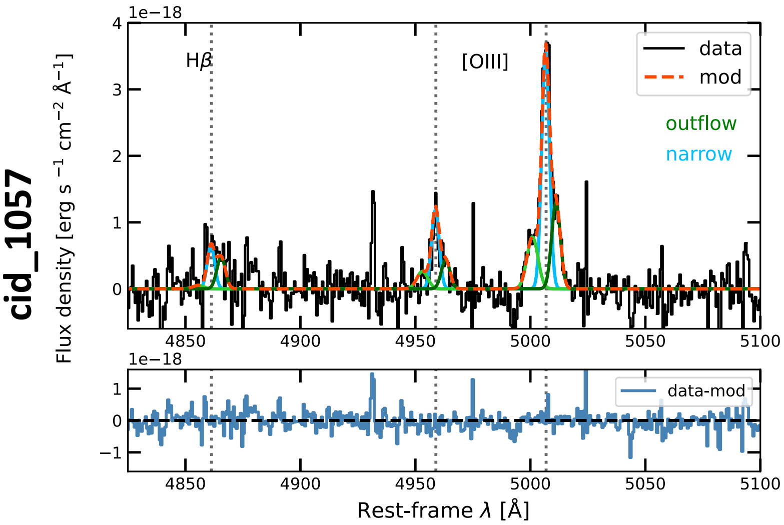

Fig. 6.3 *Integrated H-band spectrum of cid_1057, extracted from SINFONI data cube with a 0.25″-radius aperture, after subtracting a 1st-degree polynomial used to reproduce any residual faint continuum emission. Same as in Fig. 6.2. Three Gaussian component are used to properly model* [O III] *line profile: one to reproduce systemic, narrow line emission (lightblue), two for the blue and red wings detected in* [O III] *(different green colours).*

velocity. Also in XID614 and cid_2682, [O III] line profile apparently has a faint blue wing (see Figs. 6.1, 6.2), whereas it is hard to assess at first sight the presence of any possible blue [O III] wing in XID419 (see Fig. 6.1), due to bright residual sky emission (see Fig. 6.1). Therefore, we inspect kinematic maps of [O III] line emission in all galaxies (Figs. 6.4-6.6), either to confirm the outflow nature of broad, high-velocity line emission when clearly detected, or to search for kinematic evidence of ionised outflows in more ambiguous cases.

In Figs. 6.4–6.6, we show maps of [O III] line emission, describing spatial distribution and kinematics of ionised gas in all seven examined type-2 AGN, with S/N>3 cut. First-column maps display the [O III] intensity field computed as moment-0 of the total line profile (upper panel); and ratio values (f_{300}) of the flux in high-velocity channels ($|v| > 300$ km s^{-1}) to moment-0 flux (lower panel), being the first quantity a simplified but reasonable approximation of [O III] flux carried by outflows (Kakkad et al., 2020). For the seven examined type-2 AGN, we find the total (i.e. spatially integrated) flux at $|v| > 300$ km s^{-1} represents a significant fraction of the total moment-0 flux, ranging from 21% (in cid_1057) to 66% (in XID36).

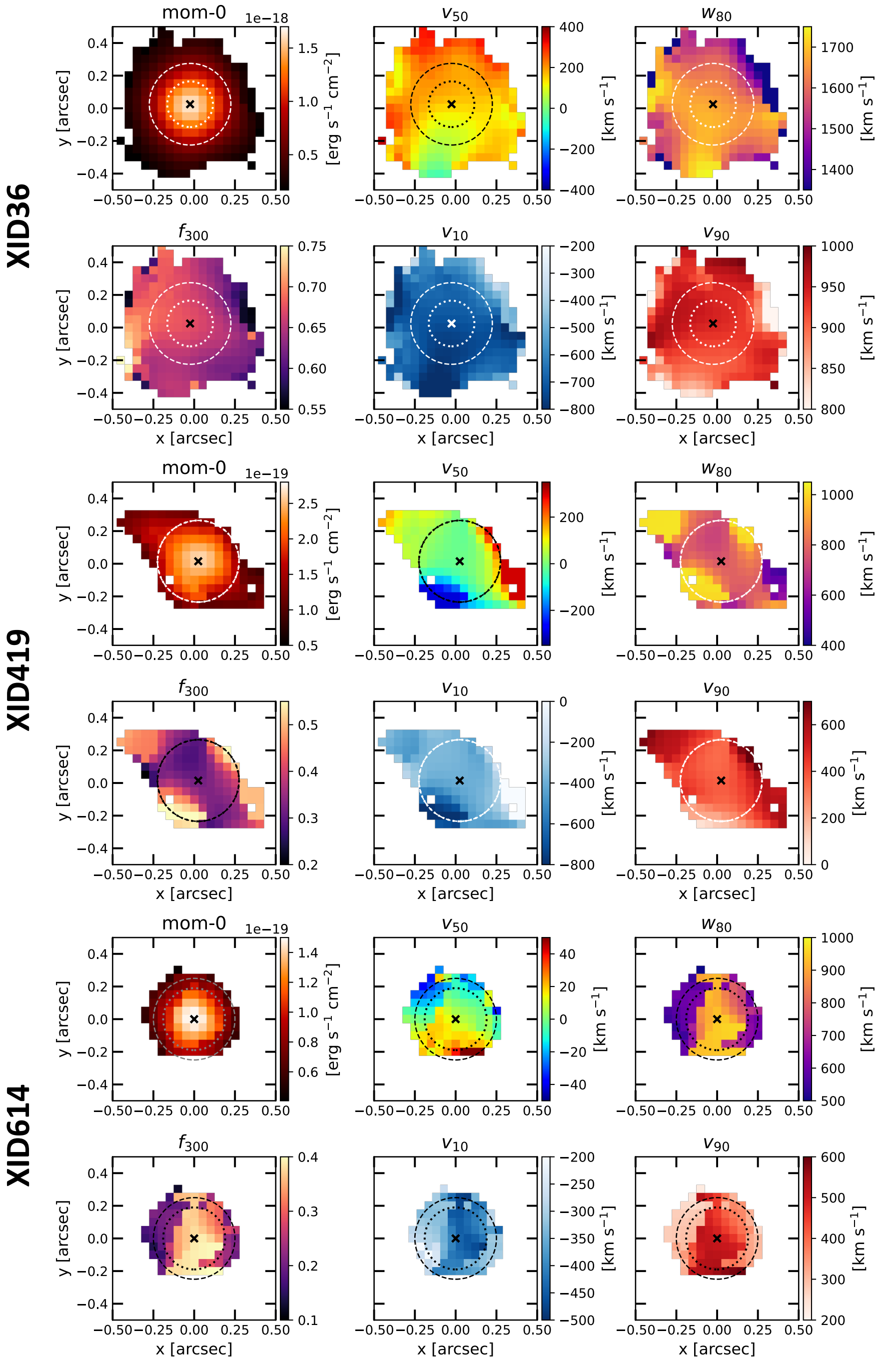

Fig. 6.4 *Morphology and kinematics of ionised gas in XID36, XID419 and XID614, as traced by total* [O III] *line emission. For each target, maps show: the intensity (moment-0) field; percentile velocities (v_{50}, v_{10}, v_{90}) and line width ($w_{80} = v_{90} - v_{10}$); and the ratio of the flux contained in* [O III] *wings (i.e. $|v| > 300$ km s^{-1}) over moment-0 flux (f_{300}). Dashed and dotted circumferences correspond to the 0.25″-radius aperture used to extract integrated spectra (Sects. 6.2.2 and 6.3.3.1), and to the mean H-band PSF (i.e. radius equal to $\langle\theta_{\rm PSF}\rangle/2$ in Table 6.2), respectively. In XID419 the two circumferences have the same 0.25″ radius. In all maps, we also mark the position of* [O III] *peak emission with a cross, and apply a S/N>3 cut.*

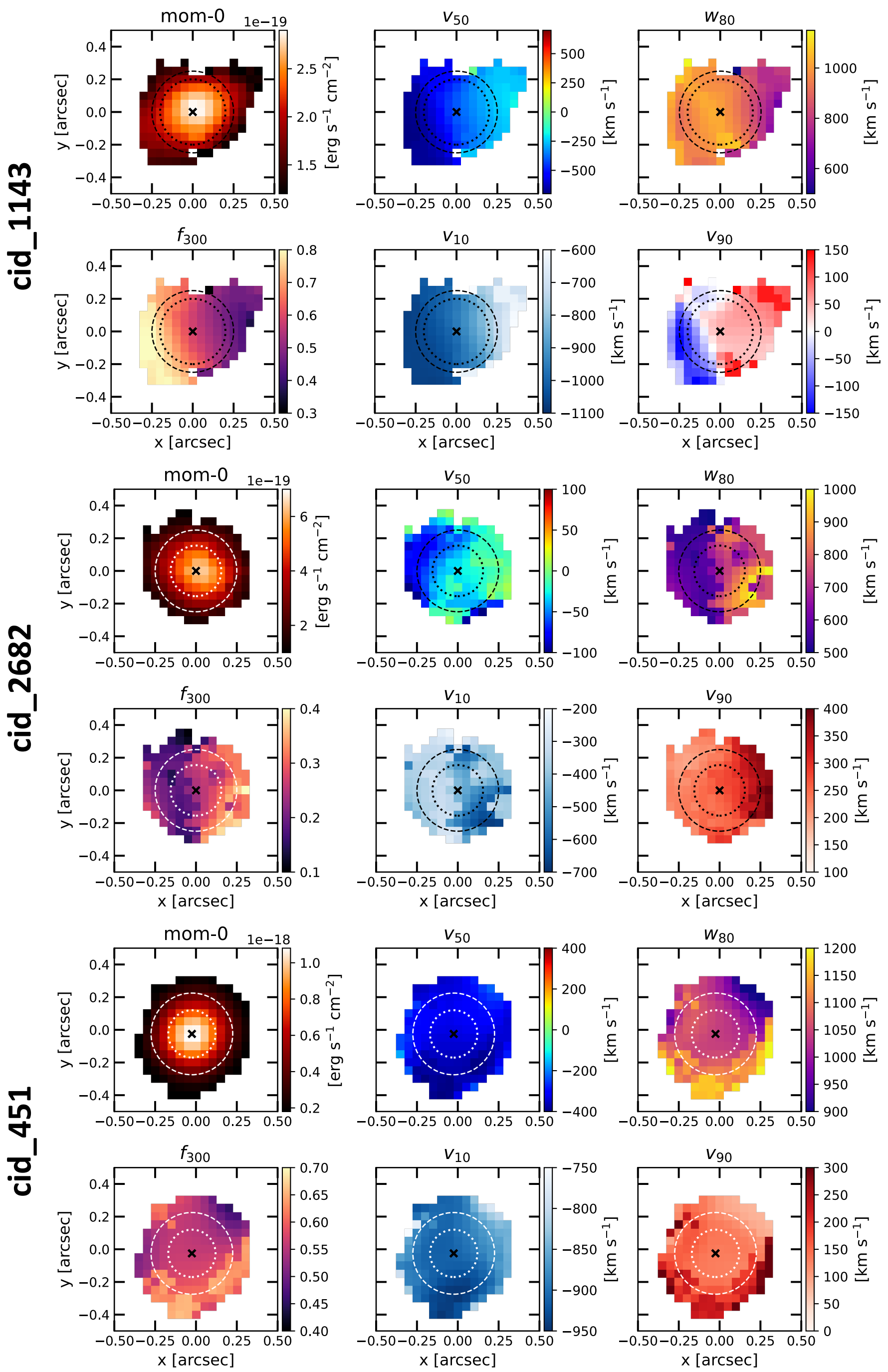

Fig. 6.5 *Morphology and kinematics of ionised gas in cid_1143, cid_2682 and cid_451, as traced by total* [O III] *line emission. Same as in Fig. 6.4.*

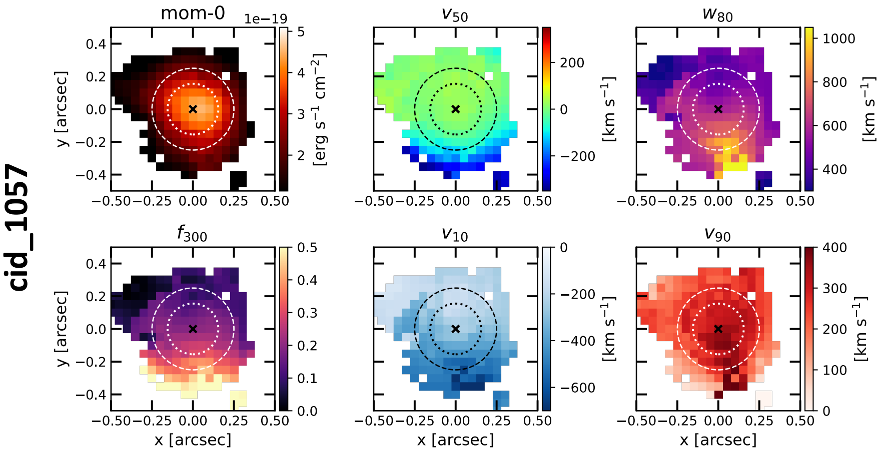

Fig. 6.6 *Morphology and kinematics of ionised gas in cid_1057, as traced by total* [O III] *line emission. Same as in Fig. 6.4.*

In addition, maps in the second and third columns of Figs. 6.4–6.6 show ionised gas kinematics described in terms of non-parametric percentile velocities[2]. Compared to parametric values, percentile velocities have the advantage of being independent on the adopted fitting function (e.g. the number of Gaussian components), which in turn may strongly depend on the S/N of the examined data (e.g. Harrison et al. 2014, Zakamska and Greene 2014). In particular, we adopt v_{50}, v_{10}, v_{90} velocities, and w_{80} line width (i.e. $w_{80} = v_{90} - v_{10}$), which is approximately equal to the FWHM of a Gaussian profile. Extreme v_{10} and v_{90} values are widely adopted as a reliable approximation of outflow velocity, for its approaching and receding components (e.g. Harrison et al. 2014, Carniani et al. 2015, Cresci et al. 2015a), respectively. Compared to moment-1 and moment-2 values (i.e. mean velocity and velocity dispersion, respectively), strongly affected by geometrical projection effects, v_{10} and v_{90} better avoid possible underestimates of the real outflow velocity, since we ignore its intrinsic geometry and inclination with respect to the line of sight. For all galaxies, v_{10} and v_{90} maps overall feature high velocities, with absolute values up to 800–1100 km s^{-1} in four targets (XID36, XID419, cid_1143, cid_451), and to 600–700 km s^{-1} in the remaining three (XID614, cid_1057, cid_2682). These large velocities are accompanied by w_{80} line widths larger than 800 km s^{-1} in most of the FoV of all targets, with maximum values of at least 1000 km s^{-1} (about 1700 km s^{-1} in XID36 and 1200 km s^{-1} in cid_451). Such large velocities and line widths point to ionised outflows as the most likely origin of such observed turbulent, high-velocity kinematics. Alternative phenomena can hardly explain such extreme kinematics. In fact, SF-driven outflows are typically characterised

---

[2] Percentile velocities v_{xx} used in the following are defined as the velocity containing xx% of the total [O III] line flux.

by low peak velocities (e.g. Arribas et al. 2014, Förster Schreiber et al. 2019); whereas galactic inflows are mostly observed in absorption with low bulk velocities and σ values (e.g. Bouché et al. 2013). From the relatively overall unperturbed morphology we can also exclude merging scenarios. Large line widths might also be due to turbulence in the galactic medium induced by the interaction of nuclear activity with the host environment, as observed in low-redshift type-2 active galaxies (e.g. Woo et al. 2016, Fischer et al. 2018, Venturi et al. 2021). Yet, such turbulence-induced effects are generally associated with relatively low centroid velocities (i.e. $|v| < 200-300$ km s^{-1}; Woo et al. 2016, Fischer et al. 2018), typical of gas at systemic or following rotation. This seems to be not the case of the broad Gaussian components used to reproduce [O III] line wings in SUPER type-2 systems, which mostly exhibit centroid velocities $|v| > 300$ km s^{-1} and appear not being associated with galaxy rotation. Finally, we point out that turbulence-induced effects have been traced in detail in observations of local Seyfert galaxies at high spatial resolution and sensitivity (see e.g. Fischer et al. 2018, Venturi et al. 2021). As a consequence, it might be hard to detect such effects in lower-quality data of $z \sim 2$ AGN, such as our SUPER observations with a spatial resolution of 2-4 kpc (see Table 6.2).

On the other side, v_{50} velocities are useful to describe the velocity field of the component dominating the overall kinematics of ionised gas. We find moderate v_{50} values in all galaxies ($|v_{50}|$ <400 km s^{-1}; even $|v_{50}|$ <100 km s^{-1} in XID614 and cid_2682), and blueshifted v_{50} values in most cases. This means that a significant fraction of total [O III] line emission is found in the blue wing of the line profile, further supporting the presence of fast ionised outflows in these galaxies. Similarly, v_{50} velocities in XID36 appear almost everywhere redshfted (reaching 400 km s^{-1}), as a consequence of the extended [O III] red wing dominating the overall [O III] kinematics in this object (see Fig. 6.1). Moreover, we detect a regular velocity gradient of v_{50} in a few galaxies: whereas in cid_1143 the v_{50} field is still outflow-dominated (i.e. totally blueshifted), with increasing absolute values from NW to SE (N is up, E to left), in XID419 and XID614 it seems to be consistent with galaxy disk rotation, with velocities going from negative to positive values passing through the galaxy centre.

In all maps, we draw two circumferences corresponding: to the 0.25$''$-radius aperture (dashed) used in Sect. 6.2.2 (also later in Sect. 6.3.3.1) to extract integrated SINFONI spectra; and to the mean H-band PSF (dotted), namely, with a radius equal to $\langle\theta_{\rm PSF}\rangle/2$ (see Table 6.2). In XID419 (Fig. 6.4) the two circumferences have the same radius. Compared to the corresponding H-band PSF, we see that in all galaxies except for XID614 the extent of S/N>3 [O III] line emission at $|v| > 300$ km s^{-1} is clearly larger than the instrumental PSF radius. This ensures us that high-velocity [O III] emission associated with outflows is spatially resolved in at least six objects of our sample. In XID614, S/N>3 [O III] maps and *H*-band PSF have approximately the same extent in all directions. (see Fig. 6.4). However, the fact that we see structures and variations in gas kinematics across the FoV of XID614 suggests that high-velocity [O III] line emission at large distance is at least marginally spatially resolved in our data.

6.3.2 Ionised outflow properties and energetics

Since Hβ is detected at low S/N in *H*-band type-2 data due to extinction effects[3] we derive ionised outflow properties from higher-S/N [O III] line emission. Some properties can be directly measured from SINFONI data, such as outflow velocity $v_{\rm out}$, radial extent $R_{\rm out}$, and [O III] luminosity $L_{\rm out}^{\rm [OIII]}$ associated with outflows. On the contrary, to estimate outflow mass rate $\dot{M}_{\rm out}$, we first need to make assumptions on quantities which cannot be measured from our data (i.e. electron density $n_{\rm e}$, and oxygen abundance [O/H]).

6.3.2.1 Directly measured outflow properties: velocity, radius and luminosity

Outflow properties we can directly measure are $v_{\rm out}$, $R_{\rm out}$ and $L_{\rm out}^{\rm [OIII]}$. As outflow velocity $v_{\rm out}$, we take for each target the maximum value of all observed v_{10} or v_{90} velocities (i.e. $v_{\rm out} = \max[v_{10}, v_{90}]$). This definition of outflow velocity is widely adopted in the literature (e.g. Cresci et al. 2015a, Carniani et al. 2015, Tozzi et al. 2021, Vayner et al. 2021a,b) and relies on the assumption that all observed lower velocities are consequence of projection effects. Other works use w_{80} as outflow velocity (e.g. Harrison et al. 2012, Kakkad et al. 2016, 2020). Yet, inferred w_{80} line widths strongly depend on the line profile, possibly determined by dust extinction. In fact, measuring outflow kinematics with w_{80} leads to higher velocities for symmetric lines compared to strongly asymmetric ones. Since here we are dealing with type-2 AGN, we expect significant dust extinction resulting in asymmetric, usually blueshifted line profiles, as a consequence of the redshifted outflow component being obscured by dust. Therefore, we measure $v_{\rm out}$ from v_{10} or v_{90} values, unlike what previously done in Kakkad et al. (2020), who employed w_{80} for the SUPER type-1 AGN sample. However, as mentioned in Sect. 6.3.1, all type-2 AGN show $w_{80} > 800$ km s^{-1} in most of the FoV and in correspondence of highest [O III] velocities, thus meeting the $w_{80} > 600$ km s^{-1} criterion used in Kakkad et al. (2020) to identify [O III] outflow emission (e.g. see also Harrison et al. 2016).

---

[3] Inferring ionised outflow properties from [O III] line emission requires more assumptions than using Hα or Hβ. However, as widely discussed throughout this chapter, hydrogen lines are overall detected at a lower S/N compared to [O III].

Using $v_{\rm out} = \max[|v_{10}|, |v_{90}|]$, we hence obtain wind velocities within $v_{\rm out}$ ~600–1100 km $\rm s^{-1}$, with a mean outflow velocity $\langle v_{\rm out}\rangle$ ~830 km $\rm s^{-1}$. For comparison, we also compute for each object the outflow velocity defined as $v_{\rm max} = v_{\rm bro} + 2\sigma_{\rm bro}$ (Rupke and Veilleux, 2013), where $v_{\rm bro}$ and $\sigma_{\rm bro}$ are velocity and velocity dispersion, respectively, of broad Gaussian components associated with outflows. This parametric definition of outflow velocity typically delivers values slightly larger compared to the $v_{\rm out}$ definition based v_{10} and v_{90} but, being adopted in several works (e.g. Brusa et al. 2015, Fiore et al. 2017, Leung et al. 2019), it is a useful quantity to compute for comparing our results with other from the literature (see Sect. 6.4). For XID419, we estimate $v_{\rm max}$ as twice the σ value of the single Gaussian employed, as done in Kakkad et al. (2020). The $v_{\rm out}$ values inferred for each galaxy are listed in Table 6.3, along with maximum observed values of $v_{\rm max}$ and w_{80} (as well as other outflow properties inferred in the following).

To estimate $R_{\rm out}$ instead, we first infer the observed (maximum) outflow radius $R_{\rm obs}$, measured from [O III] maps in Figs. 6.4-6.6 as the maximum extent from the centre of [O III] line emission at $|v|$ > 300 km $\rm s^{-1}$. We then correct $R_{\rm obs}$ for H-band PSF (i.e. $R_{\rm out} = \sqrt{R^2_{\rm obs} - (\theta_{\rm PSF}/2)^2}$; $\theta_{\rm PSF}$ values listed in Table 6.2), thus obtaining intrinsic radii of a few kpc for spatially resolved outflows ($R_{\rm out}$ ~2–4 kpc). For XID614, where the ionised outflow is marginally resolved, we consider the resulting measurement as an upper limit to $R_{\rm out}$ (i.e. $R_{\rm out} < 1.9$ kpc). All $R_{\rm out}$ estimates and upper limits are listed in Table 6.3).

To estimate the amount of [O III] flux associated with ionised winds, we follow same prescriptions adopted in Kakkad et al. (2020) for the SUPER type-1 AGN and sum over all S/N>3 spaxels the [O III] flux contained in high-velocity line channels (i.e. $|v|$ >300 km $\rm s^{-1}$). A non-parametric approach is more suitable for our data than a parametric one based on multi-Gaussian modelling, where the flux of broad, high-velocity is associated with outflows. In fact, the detection of a broad 'outflow' component depends on the S/N of data. Yet, as shown by the f_{300} ratio map in Fig. 6.4, a not negligible fraction (varying within 0.3–0.5) of [O III] flux is found in $|v|$ >300 km $\rm s^{-1}$ line channels, overall suggesting that this high-velocity gas is associated with outflows (discussed in Sect. 6.3.1). However, we point out that [O III] outflow fluxes obtained by summing spaxel-by-spaxel the flux of broad Gaussian components (for the six objects - all but XID419 - requiring a multi-Gaussian modelling of [O III]) are consistent with our non-parametric estimates within the uncertainty, differing on average by a factor of about 2 (same found in Kakkad et al. 2020 for type-1 AGN). Finally, all inferred (non-parametric) [O III] outflow fluxes are corrected for dust extinction using A_V values obtained in Sect. 6.2.2), and converted to intrinsic [O III] outflow luminosities $L^{\rm [OIII]}_{\rm out}$. All resulting dust-corrected $L^{\rm [OIII]}_{\rm out}$ values are reported in Table 6.3.

Table 6.3 *Main properties of ionised outflows in the seven SUPER type-2 AGN examined in this chapter. From left, columns list for each galaxy: (1) V-band extinction* A_V *(inferred in Sect. 6.2.2); (2) outflow radius* $R_{\rm out}$*; (3) outflow velocity* $v_{\rm out}$ *according to our adopted definition as* $v_{\rm out} = \max[|v_{10}|, |v_{90}|]$*; (4) dust-corrected* [O III] *outflow luminosity* $L_{\rm out}^{\rm [OIII]}$*, inferred from* $|v| > 300$ *km s*$^{-1}$ *line channels; (5) outflow mass rate* $\dot{M}_{\rm out}$*; maximum observed values of (6)* w_{80} *and (7)* $v_{\rm max}$ *(i.e.* $v_{\rm max} = v_{\rm bro} + 2\sigma_{\rm bro}$*; Rupke and Veilleux 2013).*

Target ID	A_V (1)	$R_{\rm out}$ kpc (2)	$v_{\rm out}$ km s^{-1} (3)	$L_{\rm out}^{\rm [OIII]}$ 10^{42} erg s^{-1} (4)	$\dot{M}_{\rm out}$ M$_\odot$ yr^{-1} (5)	w_{80} km s^{-1} (6)	$v_{\rm max}$ km s^{-1} (7)
XID36	1.3 ± 0.8	3.5	990 ± 50	14 ± 5	10 ± 6	1760 ± 120	1450 ± 80
XID419	> 0	3.6	790 ± 120	> 0.3	> 0.2	1020 ± 110	800 ± 40
XID614	2.8 ± 1.6	< 1.9	590 ± 60	2.2 ± 1.6	> 1.7	960 ± 140	910 ± 80
cid_1057	1.8 ± 1.0	3.1	720 ± 70	2.2 ± 1.0	1.3 ± 0.9	1130 ± 130	1420 ± 130
cid_1143	$1.2^{+1.8}_{-1.2}$	2.9	1070 ± 120	3^{+14}_{-2}	3^{+29}_{-2}	1320 ± 70	1370 ± 120
cid_2682	> 0.6	2.0	670 ± 80	> 0.9	> 0.8	1130 ± 90	1240 ± 130
cid_451	> 2.7	2.6	950 ± 40	> 30	> 27	1270 ± 70	1290 ± 40

6.3.2.2 Ionised outflow mass rate

The three quantities directly measured in previous subsection - namely, $v_{\rm out}$, $R_{\rm out}$ and $L_{\rm out}^{\rm [OIII]}$ - are fundamental ingredients to compute mass rate of ionised outflows. Following prescriptions adopted in Kakkad et al. (2020) for the SUPER type-1 AGN sample, we compute the mass of ionised outflows as follows (for an electron temperature of $T \sim 10^4$ K; e.g. Carniani et al. 2015, Kakkad et al. 2016):

$$M_{\rm out} = 0.8 \times 10^8 \left(\frac{L_{\rm out}^{\rm [OIII]}}{10^{44}\ {\rm erg\ s^{-1}}} \right) \left(\frac{n_{\rm e}}{500\ {\rm cm^{-3}}} \right)^{-1} \frac{{\rm M}_\odot}{10^{\rm [O/H]}}, \tag{6.1}$$

where all oxygen is assumed to be ionised to O^{2+}, $n_{\rm e}$ and [O/H] are electron density and oxygen abundance in solar units, respectively. For a uniformly filled (i.e. constant $n_{\rm e}$) outflow of bi-conical geometry, the mass rate $\dot{M}_{\rm out}$ at a certain radius $R_{\rm out}$ can be then calculated as (Fiore et al., 2017):

$$\dot{M}_{\rm out} = 3\ \frac{M_{\rm out} v_{\rm out}}{R_{\rm out}}, \tag{6.2}$$

which gives the instantaneous mass rate of ionised gas crossing a spherical sector at a distance $R_{\rm out}$ from the central AGN. Equation 6.1 requires values of [O/H] and $n_{\rm e}$ to compute ionised outflow mass, but none of them can be measured from our data. Hence, we assume a solar [O/H] abundance and $n_{\rm e} = 500 \pm 250$ cm^{-3} (i.e. 50% uncertainty) in agreement with previous studies (e.g. Storchi-Bergmann et al. 2010, Carniani et al. 2015, Riffel et al. 2015, Davies et al. 2020, Cresci et al. 2023) and consistently with prescriptions adopted in Kakkad et al. (2020) for SUPER type-1 AGN. In principle, $n_{\rm e}$ can be inferred from [S II]λ6716/[S II]λ6731 flux ratio (e.g. Osterbrock and Ferland 2006), but [S II] is undetected in SINFONI K-band data of type-2 AGN except for some faint [S II] emission in XID36 (see Fig. 6.1).

In Table 6.3, we summarise inferred properties of ionised outflows in the seven SUPER type-2 AGN, with corresponding uncertainties. We list also A_V estimates (or lower limits, derived in Sect. 6.2.2) used to obtain corresponding dust-corrected $L_{\rm out}^{\rm [OIII]}$ measurements (or lower limits). Errors on $v_{\rm out}$, w_{80} and $v_{\rm max}$ are 1σ-uncertainties resulting from kinematic analysis, while those on A_V, $L_{\rm out}^{\rm [OIII]}$ and $\dot{M}_{\rm out}$ are computed via error propagation. Due to the asymmetric uncertainty on A_V for cid_1143, errors on $L_{\rm out}^{\rm [OIII]}$ and $\dot{M}_{\rm out}$ for this object correspond to the minimum-maximum range of possible values, determined by the minimum/maximum values of the physical quantities they depend on. Despite being not obvious how to estimate them, we do not expect errors on $R_{\rm out}$ smaller than the SINFONI spatial pixel (i.e. 0.05″), which corresponds to about 0.4 kpc at $z \sim 2$. However, the uncertainty on our $\dot{M}_{\rm out}$ estimates is dominated by the large uncertainties on A_V (larger than 50%) and $n_{\rm e}$ (assumed equal to 50%). The inferred upper limit to $R_{\rm out}$ in XID614 leads to a corresponding lower limit to $\dot{M}_{\rm out}$ (i.e. $\dot{M}_{\rm out} > 1.7$ M$_\odot$ yr^{-1}).

Before SUPER observations, the galaxy cid_415 was observed with SINFONI in AO-mode, but with the largest 0.250″ pixel-scale and at lower spectral resolution with the HK filter (R ~1500). We notice that our inferred values of $R_{\rm out}$ and $v_{\rm out}$ ($R_{\rm out} \sim 2.6$ kpc and $v_{\rm out}$ ~950 km s^{-1}) are both smaller than those previously published ($R_{\rm out} \sim 5$ kpc and $v_{\rm out}$ ~1600 km s^{-1}; Perna et al. 2015b), based on these first SINFONI dataset. The smaller value of $R_{\rm out}$ is likely consequence of a surface brightness loss in our SINFONI data, due to the smaller pixel (0.100″) adopted in SUPER. Instead, the discrepancy in $v_{\rm out}$ is due to different definition of outflow velocity adopted in Perna et al. (2015b) (i.e. v_{02}), combined also with slightly different redshifts measured from [O III] peak in this work ($z = 2.444$) and in Perna et al. (2015b) ($z = 2.45$), leading to a systematic difference of about ~520 km s^{-1} in the adopted systemic galaxy velocity (with respect to velocities are computed). Accounting for these discrepancies, $v_{\rm out}$ values result to be consistent.

6.3.3 Comparison with SUPER type-1 AGN

In addition to presenting results on ionised outflows in SUPER type-2 AGN, we aim at unveiling any difference in outflow properties between type-1 and type-2 AGN, to shed light on the intrinsic nature of these two classes. To reach this goal, we make assumptions on type-1 wind properties ($v_{\rm out}$ and $R_{\rm out}$) consistently with those adopted for SUPER type-2 systems. These are slightly different from definitions originally employed in Kakkad et al. (2020), but necessary considering characteristics of [O III] outflow emission in SUPER type-2 AGN datasets. As discussed in Sect. 6.3.2.1, v_{10} and v_{90} indeed provide more suitable definitions of $v_{\rm out}$ in type-2 AGN, since its value is less sensitive to line profile shape, possibly driven by dust extinction, compared to w_{80}, originally adopted as outflow velocity in Kakkad et al. (2020). Moreover, being [O III] line emission unresolved in most of the SUPER type-1 AGN sample, Kakkad et al. (2020) computed outflow mass rates at a fixed radius of 2 kpc for all targets, which corresponds to about the maximum extent of observed unresolved emission. This is not the case for the overall type-2 AGN sample, where ionised outflows are clearly spatially resolved in six out of seven objects, with hints at [O III] outflow emission marginally resolved in the remaining one (i.e. XID614). Therefore, for the few type-1 AGN with clear detection of spatially resolved outflows, we take as outflow radius $R_{\rm out}$ the maximum distance of [O III] outflow emission (see Table 4 in Kakkad et al. 2020). For all other unresolved type-1 AGN, we use the maximum distance (or corresponding upper limit) from the AGN where is found the bulk of the ionised gas, as resulted from spectroastrometry analysis (Kakkad et al., 2020). With these values of $v_{\rm out}$ and $R_{\rm out}$, we re-compute $\dot{M}_{\rm out}$ for the type-1 subsample, consistently with type-2 AGN (see Sect. 6.3.2.2).

6.3.3.1 Faster outflows in type-2 AGN at the low-luminosity end of SUPER

Since the analysis of ionised outflows in SUPER type-2 AGN complements the results previously published for type-1 AGN (Kakkad et al., 2020), we here investigate wind properties as a function of fundamental host galaxy properties (i.e. bolometric luminosity $L_{\rm bol}$, stellar mass M_*, SFR), for the full SUPER sample. AGN and host galaxy properties of all SUPER galaxies were derived via SED fitting (Circosta et al., 2018), using the code CIGALE (Code Investigating GALaxy Emission; Noll et al. 2009). Regarding $L_{\rm bol}$, values inferred for SUPER targets ($L_{\rm bol} \sim 10^{45-48}$ erg s^{-1}) are in general too high to have a significant contribution from the host, therefore, they mainly reflect AGN luminosity.

We find the key result of our study by comparing wind kinematics as a function of $L_{\rm bol}$, while no clear trend of outflow properties (i.e. velocity and mass rate) with neither M_* nor SFR comes out. In Fig. 6.7, we show outflow velocity as a function of $L_{\rm bol}$ for SUPER type-2 (coloured thick crosses) and type-1 (grey squares) AGN. Left and middle panels show along the y-axis $v_{\rm out} = \max[|v_{10}|, |v_{90}|]$ and $v_{\rm max} = v_{\rm bro} + 2\sigma_{\rm bro}$ (see Table 6.3), respectively. For comparison, in the middle panel we also draw the well-known empirical $v_{\rm max} - L_{\rm bol}$ relation inferred in Fiore et al. (2017) (dotted line), and an updated version by Musiimenta

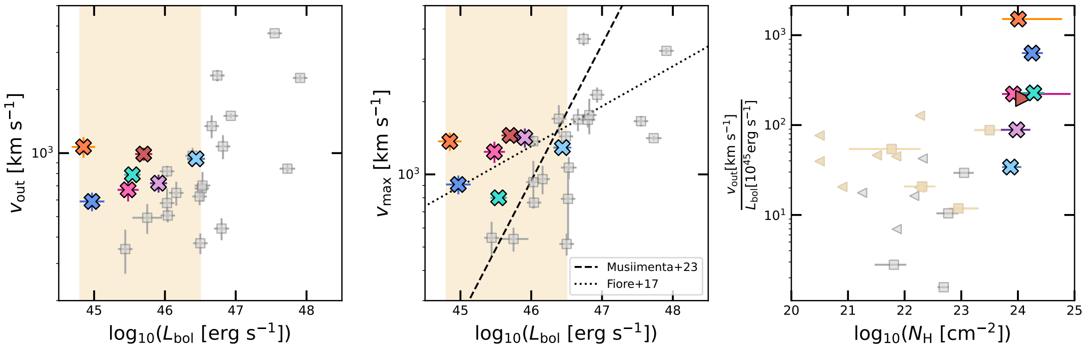

Fig. 6.7 *Outflow velocities* $v_{\rm out}$ *and* $v_{\rm max}$ *(left and middle panels; Table 6.3) as a function of* $L_{\rm bol}$*, and* $v_{\rm out}/L_{\rm bol}$ *ratios versus X-ray* $N_{\rm H}$ *measurements (right panel). Coloured thick crosses and grey squares represent SUPER type-2 and type-1 AGN (Kakkad et al., 2020); coloured/grey triangles in the right panel indicate upper/lower limits* $N_{\rm H}$*. In the middle panel, we also draw the well-known empirical relation by Fiore et al. (2017) (dotted line), along with a more recent version from Musiimenta et al. (2023) (dashed), including new measurements and only* $z > 0.5$ *objects. The overall distribution of measurements points to faster winds in type-2 obscured AGN than in type-1 systems, within the range of* $L_{\rm bol} = 10^{44.8-46.5}$ *erg s*$^{-1}$ *(orange shading in left/middle panels; orange shaded symbols for type-1 AGN in the right panel).*

et al. (2023), including recent results and considering $z > 0.5$ AGN only. Interestingly, SUPER type-2 AGN, residing all in the lower $L_{\rm bol}$ regime (i.e. $L_{\rm bol} \sim 10^{44.8-46.5}$; orange shading), host faster outflows than SUPER type-1 objects within the same $L_{\rm bol}$ range. Such a discrepancy appears in terms of both $v_{\rm out}$ and $v_{\rm max}$, with XID419 having the lowest $v_{\rm max}$ value among SUPER type-2 AGN, since it is computed as $v_{\rm max} = 2\sigma$, where $\sigma \sim 400$ km s^{-1} is the velocity dispersion of the only, nearly systemic Gaussian component employed (see Sect. 6.3.2.1).

To shed light on the nature of such a type-1/type-2 dichotomy observed in SUPER, we investigate the effect of different nuclear obscuring conditions on driving outflows in the right panel of Fig. 6.7. To remove any dependence of $v_{\rm out}$ on AGN luminosity (a well-known effect, discussed in Sect. 6.4), we normalise $v_{\rm out}$ to $L_{\rm bol}$ (in units of 10^{45} erg s^{-1}), and study how $v_{\rm out}/L_{\rm bol}$ ratios vary with hydrogen column density $N_{\rm H}$ (derived in Circosta et al. 2018 for the full SUPER sample), measured from X-ray data. Upper/lower limits on $N_{\rm H}$ are shown as triangles, and an orange shading is used to identify SUPER type-1 AGN lying in the low-$L_{\rm bol}$ regime (i.e. $L_{\rm bol} \sim 10^{44.8-46.5}$) highlighted in left and middle panels. In the right panel, we can see that SUPER type-1 and type-2 AGN occupy two distinct regions of the $(v_{\rm out}/L_{\rm bol}) - N_{\rm H}$ plane. The separation along the x-axis reflects the X-ray obscured/unobscured classification, which well agrees with the optical type-2/type-1 one, as already noticed in Circosta et al. (2018), with type-2 systems having X-ray column densities larger than about 10^{24} cm^{-2} ($N_{\rm H} < 10^{24}$ cm^{-2} for type-1 AGN in SUPER). Yet, it is more interesting the combined separation along the y-axis: the SUPER type-2 sample indeed features $v_{\rm out}/L_{\rm bol}$ values varying within ~30–1500 (with only cid_451 smaller than 80), with a mean value of ~400, while almost all type-1 AGN have ratios smaller than 50, with an overall mean value of ~40.

To confirm the presence of faster-ionised outflows in the SUPER type-2 population than in type-1 counterparts, as well as to rule out the possibility that it might be due to systematic differences in our [O III] line modelling compared to that performed in Kakkad et al. (2020), we separately stack [O III] spectra of type-2 and type-1 AGN in SUPER, to directly compare [O III] line profile of the two subsamples with $L_{\rm bol} \sim 10^{44.8-46.5}$: these are all type-2 systems, and eleven type-1 AGN (all points lying within the orange shading in Fig. 6.7). Selecting objects over this broad (about two orders of magnitude) range of luminosity ensures us to account for possible over/underestimates of $L_{\rm bol}$ from SED fitting in type-2 AGN (Circosta et al., 2018), due to fainter AGN emission hardly to constrain. Indeed, we find for type-2 AGN that $L_{\rm bol}$ values obtained from SED fitting differ from estimates based on dust-corrected [O III] luminosity (Lamastra et al., 2009) a mean factor of about 2 (computed for the four objects with A_V estimates, see Table 6.3), and from X-ray 2-10 keV luminosity (Duras et al., 2020) by a mean factor of 4, without obvious biases towards higher or lower $L_{\rm bol}$ from the SED fitting derivation. For each $L_{\rm bol}$-selected AGN, we extract an integrated, subtracted [O III]λ5007 spectrum[4], using an aperture of $0.25''$-radius. From the stack, we exclude spectra with a S/N<5 on [O III], which prevent us from an accurate comparison of line profiles, due to the high noise. We hence remain with six spectra of type-2 AGN (all but XID419), and six spectra of type-1 AGN (X_N_66_23, X_N_115_23, cid_467, S82X1905, S82X1940, S82X2058; Kakkad et al. 2020). In the stack, each integrated spectrum is weighed by its squared noise, and the final stacked type-2 and type-1 spectra (red and blue spectra in Fig. 6.8, respectively) are normalised to their resulting [O III] peak. We point out that results similar to those described below are obtained even by stacking unweighted spectra.

In Fig. 6.8, we show the resulting stacked spectra of [O III] emission line, obtained for type-2 (red) and type-1 (blue) AGN in SUPER, using a binning twice larger than SINFONI spectral channel to remove noisier channels. The type-2 [O III] line profile exhibits more prominent blue and red wings than type-1 spectrum. Yet, whereas all type-2 objects contribute to the [O III] blue wing, the red wing is dominated by XID36, as revealed by multiple stacks of type-2 integrated spectra, each time excluding one object.

---

[4] Subtracted [O III] spectra of type-2 AGN have been obtained after removing the best-fit 1st-degree polynomial used to model continuum emission (see Sect. 6.2.1), whereas for type-1 after removal of both continuum and BLR emission (Kakkad et al., 2020).

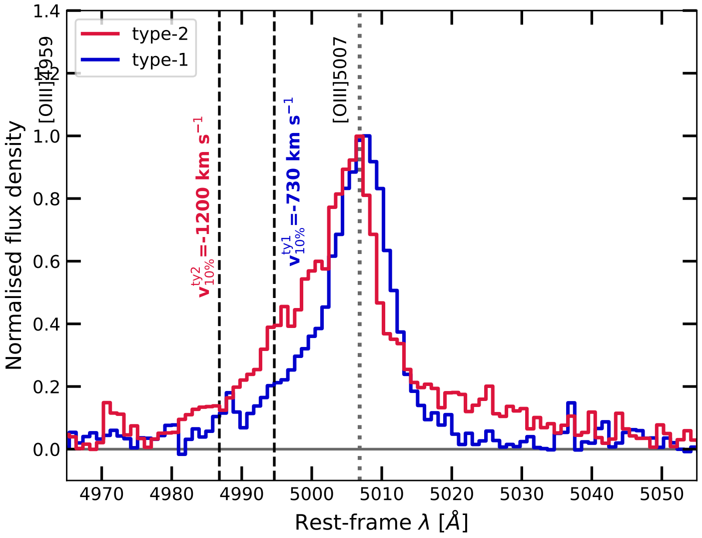

Fig. 6.8 *Stacked* [O III]λ5007 *spectra of type-2 (red) and type-1 (blue) AGN from SUPER with* $L_{\rm bol} \sim 10^{44.8-46.5}$ *(orange shading in Fig. 6.7), resulting from integrated (aperture of 0.25″-radius), subtracted* [O III] *spectra with S/N>5. Integrated spectra are averaged by squared noise, and then normalised to their* [O III] *peak. Comparing the two stacked spectra, we find a statistically significant (*$> 2\sigma$*) difference in* [O III] *blue wing, which is more prominent in type-2 spectrum of about 500 km s*$^{-1}$ *compared to the type-1 stack.*

To quantify the difference in [O III] blue wing profile, we measure v_{10} for both stacked spectra and run a boot-strapping of 400 stacks of six spectra, randomly selected according to a uniform distribution and allowing for repetitions, to calculate corresponding uncertainty as standard deviation of the 400 resulting v_{10} measurements. We thus obtain $v_{10}^{\rm ty2} = -1200 \pm 80$ km s^{-1} for the type-2 line profile, and $v_{10}^{\rm ty1} = -730 \pm 90$ km s^{-1} for the type-1 spectrum (see Fig. 6.8), pointing to a statistically significant ($> 2\sigma$) difference in [O III] blue wing from the two distinct AGN populations. The origin of such an observed difference, revealing faster ionised outflows in type-2 AGN, is discussed in Sect. 6.4.

6.3.3.2 Outflow mass rate as a function of bolometric luminosity

In Fig. 6.9, we study outflow mass rates as a function of $L_{\rm bol}$, for the full SUPER sample, to search for possible differences between distinct AGN populations. In the left panel, we plot $\dot{M}_{\rm out}$ values (same coloured markers as in Fig. 6.7), most of which are lower limits (coloured and grey triangles for type-2 and type-1 AGN, respectively). Lower limits are consequence of an upper limit to $R_{\rm out}$ and/or a lower limit to A_V (see Table 6.3). Similarly, the right panel shows $\dot{M}_{\rm max}$ values obtained by using in Eq. 6.2 $v_{\rm max}$ values (Rupke et al., 2005), so as to compare all measurements with $\dot{M}_{\rm max} - L_{\rm bol}$ scaling relations by Fiore et al.

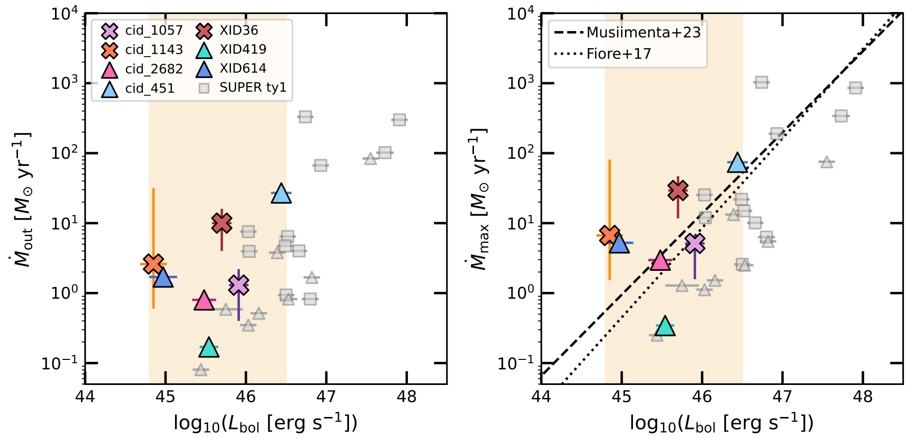

Fig. 6.9 *Outflow mass rates as a function of* $L_{\rm bol}$ *for the full SUPER sample. We show* $\dot{M}_{\rm out}$ *(based on prescriptions described in Sect. 6.3.2.2) and* $\dot{M}_{\rm max}$ *(using* $v_{\rm max}$ *in Eq. 6.2) in left and right panels, respectively. Upper/lower limits to mass rates are indicated with triangles. In right panel, scaling relations from Fiore et al. (2017) and Musiimenta et al. (2023) are shown as dotted and dashed lines, after being re-scaled to* $n_{\rm e} = 500$ *adopted for our targets, while values of* $\dot{M}_{\rm max}$ *have been multiplied by a factor of 2 to match definitions adopted in Fiore et al. (2017) and Musiimenta et al. (2023).*

(2017) (dotted line) and Musiimenta et al. (2023) (dashed), after being re-scaled to our adopted $n_{\rm e} \sim 500$ cm $^{-3}$. Moreover, since both scaling relations have been obtained by taking the flux of broad Gaussian components to calculate outflow mass rates, we correct all inferred mass rates (based on our non-parametric approach; see Sect. 6.3.2.1) by a factor of 2, corresponding to the approximated mean ratio of [O III] luminosity from broad Gaussian components to that from line channels at $|v| > 300$ km s^{-1} (same factor of ≈ 2 obtained for both type-2 and type-1 AGN, as calculated in Kakkad et al. 2020).

As opposed to Fig. 6.9, the large number of inferred lower limits to mass rates hampers any accurate comparison within the low-luminosity range previously selected ($L_{\rm bol} \sim 10^{44.8-46.5}$; orange shading). However, excluding lower limits, we find mean values of $\dot{M}_{\rm out} \sim 5$ M$_\odot$ yr^{-1} and $\dot{M}_{\rm max} \sim 7$ M$_\odot$ yr^{-1} for type-2 AGN, and $\dot{M}_{\rm out} \sim 5$ M$_\odot$ yr^{-1} and $\dot{M}_{\rm max} \sim 15$ M$_\odot$ yr^{-1} for low-$L_{\rm bol}$ selected type-1 AGN. Compared to Fig. 6.7, here it is harder to establish whether a separation between type-2 and type-1 AGN is actually present or not, due to the large uncertainty on outflow mass rates. Indeed, as explained in Sect. 6.3.2.2, mass rate estimates require several quantities to be assumed (e.g. $n_{\rm e}$, [O/H], ionisation), and strongly depend on the accuracy of the other measured parameters (e.g. A_V, $R_{\rm out}$). All this uncertainty contributes to increasing the scatter in the resulting mass rate values, which might hide any possible type-2/type-1 dichotomy, visible instead in terms of outflow kinematics.

6.3.4 Can ionised outflows escape galaxy gravitational potential?

To significantly affect their host galaxy, AGN-driven outflows must be energetic enough to sweep away a substantial amount of gas on large scales, up to escaping the gravitational potential of their galaxy. To establish whether ionised outflows may potentially reduce the gas reservoir of their host, we need to compare outflow velocities with the escape velocity $v_{\rm esc}$ of each galaxy. Following prescriptions from the literature (Marasco et al., 2023), we use the `python` package `galpy` (Bovy, 2015) to build a dynamical mass model consisting of a dark matter (DM) halo, a stellar disk, and a gaseous disk, to derive the total $v_{\rm esc}$ profile for SUPER targets with known M_*, derived from SED fitting (Circosta et al., 2018). All examined type-2 AGN galaxies have M_* estimates ranging within $M_* \sim 10^{10.7-11.2}$ M$_\odot$, while for only few type-1 systems M_* estimates are available ($M_* \sim 10^{10.1-11.2}$ M$_\odot$). In fact, the bright AGN component in type-1 systems typically overwhelms stellar emission, thus preventing us from constraining M_* in most cases (only six SUPER type-1; see Table A.2 in Circosta et al. 2018).

For the DM halo, we assume a Navarro-Frenk-White (NFW, Navarro et al. 1997) profile, with a virial mass M_{200} derived from M_* via the stellar-to-halo mass relation (Moster et al., 2013), and a concentration c determined from the $M_{200} - c$ relation (Dutton and Macciò, 2014); both relations are computed at the redshift of each target. We model the stellar disk with a double-exponential profile of scale-length $R_{\rm d}$ and scale-height $R_{\rm d}/5$, assuming $R_{\rm d}$ equal to the half-light radius R_{50} divided by 1.68 (correct for a pure exponential disk, Sérsic index $n = 1$). We determine R_{50} from the size-M_* relation for a disk galaxy ($n = 1$) at z$\sim$ 2.2 (Mowla et al., 2019). Since we have CO-based measurements of molecular gas mass $M_{\rm gas}$ for a few SUPER AGN (Circosta et al., 2021), we model a gaseous disk of $M_{\rm gas}$ equal to the mean value measured for SUPER targets (i.e. $M_{\rm gas} \sim 6 \times 10^9$ M$_\odot$), and same size as the stellar disk, since we expect the molecular gas to extend on scales comparable to those of stars. In doing so, we derive the $v_{\rm esc}$ profile of the total modelled mass distribution.

Since we are assuming that outflows move with constant speed, we compare $v_{\rm out}$ with the total $v_{\rm esc}$ at the maximum inferred outflow radius $R_{\rm out}$ (listed in Table 6.3) for type-2 (coloured symbols) and type-1 (grey) AGN in SUPER, with known M_* (Circosta et al., 2018). A dashed line indicates the locus of points with $v_{\rm out} = v_{\rm esc}$. Under the simplifying assumption that our dynamical modelling introduces no further uncertainty, we consider an error on $v_{\rm esc}$ due to the total uncertainty on M_*, given by both statistical (from SED fitting Circosta et al. 2018) and systematic (~0.1 dex; Pacifici et al. 2023) uncertainties. Triangles indicate lower limits to $v_{\rm esc}$, corresponding to upper limits to $R_{\rm out}$, since $v_{\rm esc}$ increases at decreasing $R_{\rm out}$.

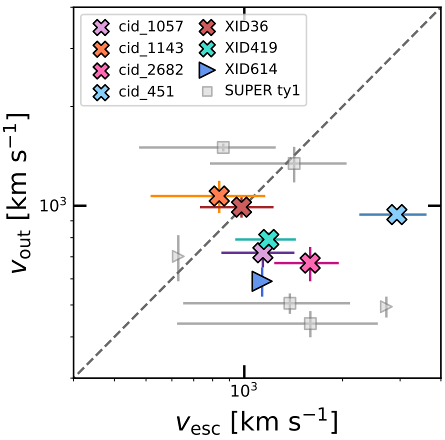

Fig. 6.10 *Outflow velocity* v_{out} *as a function of* v_{esc} *computed at* R_{out}*, as inferred from our galaxy mass modelling of type-2 (coloured symbols) and type-1 (grey) AGN in SUPER, with known* M_* *(Circosta et al., 2018). Triangles represent lower limits to* v_{esc} *(due to inferred upper limits to* R_{out}*), whereas dashed line indicates* $v_{out} = v_{esc}$ *values. Most AGN have* v_{esc} *larger than* v_{out}*, implying ionised outflows not fast enough to escape the gravitational galaxy potential.*

As shown in Fig. 6.10, eight galaxies (~62% of the total 13-AGN sample considered) have v_{esc} values (or lower limits) larger than v_{out}, whereas four (~31%) have v_{out} larger than or consistent with corresponding v_{esc}. There is also a type-1 AGN (cid_467) with an lower limit to v_{esc} lying just above the $v_{out} = v_{esc}$ line, but its real value is likely located in the $v_{out} < v_{esc}$ part of the plane. The overall picture seems to point to a minority of outflows fast enough to escape the gravitational potential of their galaxy. Moreover, our dynamical modelling necessarily relies on several simplified assumptions, such as outflows moving at constant velocity and uncertainty on v_{esc} only due to that M_*. Moreover, we are considering only gravity and no possible hydrodynamic effects: outflows could indeed get trapped in gaseous halos, eventually cool and re-accrete, even if they have initially high velocities. All these suggest that, despite the larger velocities in type-2 sources, only a small fraction of outflowing gas might escape the galaxy halo, thus questioning the ejective ability of outflows to expel the gas reservoir of their host as expected by several models (see Sect. 1.2.2).

6.4 Discussion

The main result of this chapter is that, in the lower L_{bol} regime ($L_{bol} \sim 10^{44.8-46.5}$), SUPER type-2 AGN host faster ionised outflows than their type-1 counterparts, as traced by higher [O III] velocities. At low redshift ($z < 0.8$), several studies have investigated ionised outflow

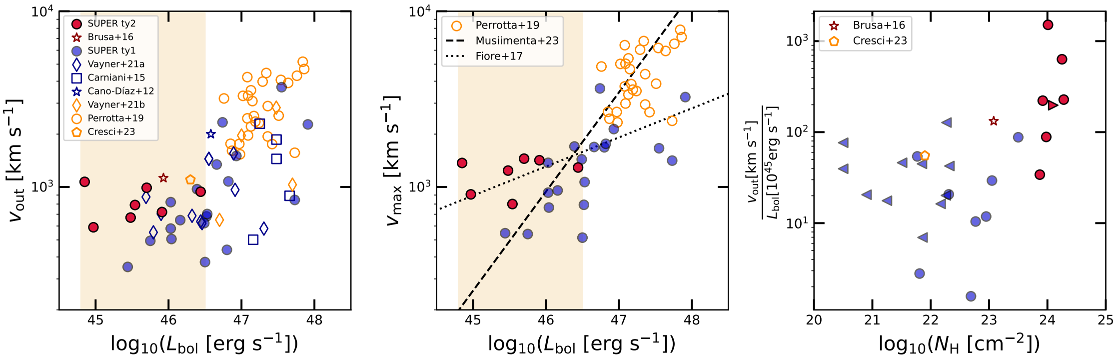

Fig. 6.11 *Same panels as in Fig. 6.7, showing SUPER type-2 (red filled circles) and type-1 (blue filled circles) measurements along with IFU-based results from the literature of other type-2 (red empty star; Brusa et al. 2016) and type-1 AGN (blue empty symbols; Cano-Díaz et al. 2012, Carniani et al. 2015, Vayner et al. 2021a) at z* $\sim 1-3$. *In orange, we highlight points relative to optically-classified type-1 AGN but red and obscured objects (Perrotta et al., 2019, Vayner et al., 2021b). Outflow velocities from Brusa et al. (2016) and Perrotta et al. (2019) have been corrected to account for discrepancies with* v_{out} *and* v_{max} *definitions here adopted (see Sect. 6.4). While 'standard' blue type-1 and red type-2 from the literature agree with values found in SUPER, the orange points, almost all at* $L_{bol} \gtrsim 10^{47}$ *erg s*$^{-1}$, *clearly show that higher outflow velocities are recovered if we select optical type-1 but dusty obscured objects.*

in large AGN samples, searching for differences between type-2 and type-1 systems. Most of them have found narrower and more symmetric [O III] line profiles in type-2 AGN pointing to the detection of both blueshifted and redshifted outflow components; on the contrary, type-1 AGN host almost exclusively blueshifted, with typically larger line widths and more negative velocities (e.g. Mullaney et al. 2013, Bae and Woo 2014, Rakshit and Woo 2018, Wang et al. 2018, Rojas et al. 2020). This is can be explained in terms of biconical outflow geometry in the context of standard unification models (e.g. Antonucci 1993, Urry and Padovani 1995; see Sect. 1.1.2.1), as a consequence of orientation effects along the line of sight combined with dust obscuration: assuming a nearly face-on orientation of type-1 AGN (i.e. with BLR emission well visible along the line of sight), the receding cone of the outflow remains hidden on the other side of the galaxy disk plane. However, most of low-redshift studies do not consider the well known dependence of outflow kinematics on AGN luminosity and accretion rate (e.g. Bae and Woo 2014, Woo et al. 2016, Rakshit and Woo 2018), and compare overall more luminous type-1 AGN with fainter type-2 samples, which may lead to an only apparent discrepancy. Moreover, as discussed in Sect. 1.1.2.3, nowadays increasing - such as the discovery of CL AGN (e.g. Shappee et al. 2014 and Tozzi et al. 2022 in Chapter 3; see Ricci and Trakhtenbrot 2022 for a recent review) - supports also other mechanisms at the origin of the type-1/type-2 AGN dichotomy, such as distinct phases within a common evolutionary sequence.

At high redshift ($z > 1$), where more complex processes take place - especially at crucial cosmic epochs of galaxy evolution such as ~ 2 - orientation effects might play a minor role compared to low redshift. Indeed, different AGN classes have been proposed as distinct evolutionary phases of galaxies' life cycle (Hopkins et al., 2006, Menci et al., 2008). In particular, X-ray bright but obscured ($L_{2-10\ \mathrm{keV}} > 10^{42}$ erg s^{-1}, $N_{\mathrm{H}} \gtrsim 10^{22}$ cm^{-2}) AGN at $z \sim 2$ have been proposed to be in the active 'blow-out' phase of AGN galaxies' evolution (e.g. Brusa et al. 2010, 2016, Zakamska et al. 2016, Perna et al. 2015a,b). In these obscured sources, dusty material favours the acceleration of outflows (e.g. Ishibashi and Fabian 2015, Costa et al. 2018), which efficiently clear out obscuring dust, and finally unveil the AGN. Radiation-pressure on dust has been indeed identified as the main mechanism responsible for the larger [O III] velocities and line widths observed in extremely red and luminous quasars (ERQs; $L_{\mathrm{bol}} > 10^{47}$ erg s^{-1}), compared to blue quasars at $z = 2-3$ (Perrotta et al., 2019). A similar discrepancy in [O III] velocities has been observed at lower redshift ($z < 0.4$) by DiPompeo et al. (2018), who selected obscured AGN, resembling the obscured high-redshift population, based on their optical-IR colours, and compared them with unobscured objects in matched luminosity bins.

Figure 6.11 displays same panels as in Fig. 6.7 and compares, as more homogeneously as possible, SUPER results of type-2 (red filled circles) and type-1 AGN (blue filled) along with IFU-based measurements from the literature for which homogenized quantities could be derived, obtained for other type-2 (red empty star; Brusa et al. 2016) and type-1 AGN (blue empty symbols; Cano-Díaz et al. 2012, Carniani et al. 2015, Vayner et al. 2021a) at $z = 1-3$. In orange, we highlight measurements relative to red and obscured AGN but showing BLR emission (hence, optical type-1 systems), which should be considered as an intermediate class of objects between standard blue type-1 and red type-2 AGN. These are: the obscured quasar XID2028 at $z \sim 1.6$ we studied in Cresci et al. 2023 (orange empty pentagon), the powerful obscured ERQs from Perrotta et al. (2019) (orange empty circles); and the sample of obscured quasars from Vayner et al. (2021b) (orange diamonds), among which all but one (the lowest-velocity orange diamond) are selected as ERQs.

The first panel compares v_{out} measurements from SUPER and the literature based on v_{10}/v_{90}, as obtained in Vayner et al. (2021a,b) (diamonds) and Cresci et al. (2023); whereas higher percentile outflow velocities were used in Brusa et al. (2016) and Perrotta et al. (2019) (i.e. v_{05} and v_{02}, respectively). Therefore, we correct outflow velocities inferred in Brusa et al. (2016) and Perrotta et al. (2019) by a factor of 0.86 and 0.77, respectively, corresponding to the mean ratio of $v_{10,90}$-to-$v_{05,95}$ and $v_{10,90}$-to-$v_{02,98}$ measured for SUPER type-2 AGN. We also add measurements from Cano-Díaz et al. (2012) and Carniani et al. (2015). Similarly, we re-scale v_{02} outflow velocities from Perrotta et al. (2019) by a factor of

1.2, as obtained from the mean $v_{\rm max}$-to-$v_{02,98}$ ratio for SUPER type-2 AGN, and plot them in the $v_{\rm max} - L_{\rm bol}$ plane (middle panel), along with $v_{\rm max}$ measurements for SUPER type-2 (derived in Sect. 6.3.2.1) and type-1 AGN (Kakkad et al., 2020).

As shown in Fig. 6.11, standard blue (unobscured) type-1 and red (obscured) type-2 AGN from the literature lie close to SUPER type-1 and type-2 points, respectively. However, within the optical type-1 AGN population, high outflow velocities appear if we select 'hybrid' obscured type-1 AGN, as shown by the distribution of orange points, consistently with the picture derived in this work.

The right-hand panel indeed shows that the hybrid type-1 AGN XID2028 from Cresci et al. (2023) (empty pentagon), which lies close to SUPER type-2 AGN (hence, with no difference in $v_{\rm out}$) in the left-hand panel, here clearly stands out from the type-2 population and locates at lower $N_{\rm H}$ along with the SUPER type-1 sample. On the contrary, the obscured type-2 AGN XID5395 (empty red star; Brusa et al. 2016) has a large $v_{\rm out}/L_{\rm bol}$ ratio (i.e. ~130) comparable with those of SUPER type-2 systems, and a slightly smaller column density ($N_H \sim 10^{23}$ cm^{-2}) but still placing in the nuclear high-obscured regime.

Therefore, radiation pressure of dust might be the dominant mechanism explaining the presence of faster-ionised outflows in type-2 AGN, also at lower bolometric with respect to that typical of ERQs ($L_{\rm bol} > 10^{47}$ erg s^{-1}) from Perrotta et al. (2019). Our analysis has furthermore revealed a clear type-1/type-2 dichotomy which fully reflects the X-ray unobscured/obscured classification based on obscuring material on nuclear scales. The SUPER type-2 AGN are all highly X-ray obscured with $N_{\rm H} \gtrsim 10^{24}$ cm^{-2}, which may explain the higher velocity of ionised outflows observed in type-2 AGN, compared type-1 counterparts within the same luminosity range. The novelty of our study is that, unlike previous works at $z \sim 2$ (Harrison et al., 2016, Perrotta et al., 2019), SUPER has provided evidence for the first time of a possible evolutionary origin of the type-2/type-1 AGN dichotomy at high redshift, where obscured type-2 systems evolve towards an unobscured type-1 phase, as radiation-pressure driven outflows blow out obscuring material, and make the central AGN and its BLR emission visible. The high-luminous ($L_{\rm bol} > 10^{47}$ erg s^{-1}) sample of $z = 2-3$ ERQs studied in Perrotta et al. (2019) indeed consists of type-1 AGN only. On another side, the published results from the KASHz survey (Harrison et al., 2016) relative to X-ray bright AGN ($L_{2-10\ {\rm keV}} > 10^{42}$ erg s^{-1}) at $z = 0.6-1.7$, shows no evidence for more extreme gas kinematics in obscured (type-2) objects than in unobscured (type-1) counterparts (see left panel of Fig. 6.7). We point out that this might be consequence of the lower S/N of KASHz data compared to SUPER, which leads to miss any extended [O III] line wing. This is indeed the case for cid_1143 and cid_451, among the few targets in common to both surveys (Scholtz et al., in prep.), where the shallower KMOS data completely miss the broad [O III] wing due to the outflow, thus underestimating its velocity.

6.5 Conclusion

This chapter has completed the analysis of SINFONI observations of the SUPER survey, by presenting new results on type-2 AGN. We analysed H-band data cubes (Sect. 6.2.1) and studied kinematics of ionised gas via [O III] line emission, finding evidence of ionised outflows in all seven examined type-2 AGN (Sect. 6.3.1). Detected ionised outflows are spatially resolved in five objects, while marginally resolved in the remaining two. In Sect. 6.3.2, we computed outflow properties, namely, velocity, radius and mass rate, with the latter corrected for dust extinction estimated from H- and K-band integrated spectra (Sect. 6.2.2). Interestingly, we find that, within the same luminosity range (i.e. $L_{\rm bol} = 10^{44.8-46.5}$ erg s^{-1}), SUPER type-2 AGN host faster winds than their type-1 counterparts (Fig. 6.7), as revealed by the statistically more prominent [O III] line wings (Fig. 6.8). We interpret this as a consequence of the larger amount of obscuring material ($N_{\rm H} \gtrsim 10^{24}$ cm^{-2} in all examined type-2 AGN), which favours the acceleration of winds via radiation-pressure on dust (e.g. Ishibashi and Fabian 2015, Costa et al. 2018). These results from the SUPER survey hint an evolutionary origin of the observed type-2/type-1 dichotomy at $z \sim 2$, in the context of galaxy evolution models (e.g. Hopkins et al. 2006, Menci et al. 2008). At $z \sim 2$, orientation effects might play a minor role in the type-1/type-2 classification, with type-2 being the blow-out phase (e.g. Hopkins et al. 2008), where fast winds are efficiently accelerated via radiation pressure. Such an interpretation had been already proposed for obscured AGN at $z \sim 2$ (e.g. Brusa et al. 2016, Zakamska et al. 2016, Perna et al. 2015b), but never clearly associated with the type-2 optical class, with some obscured AGN selected being actually type-1 systems (e.g. Perna et al. 2015a, Perrotta et al. 2019).

In spite of this type-2/type-1 dichotomy, ionised outflows detected in both classes of SUPER AGN seem to be not fast enough to successfully escape the gravitational potential of their galaxy (Fig. 6.10), thus questioning the ‘ejective’ ability of outflows to expel the host gas reservoir out of the galaxy.

To confirm this novel result found in SUPER, we will need in future larger samples of high-redshift type-1 and type-2 AGN. The new generation of IFU facilities, from both space (e.g NIRSpec on *JWST*) and the ground with AO (e.g. ERIS at VLT), will allow us to exploit as much as possible the power of spatially resolved observations, to take the next step to fully understand feedback mechanisms and AGN evolution at the Cosmic Noon.

Conclusions and future perspectives

This PhD thesis aims to investigate from the observational point of view three main aspects of AGN, providing a global overview of their rich phenomenology and crucial role in galaxy evolution:

- standard and novel optical emission-line diagnostics to select complete and unbiased samples of AGN galaxies (Chapter 2);
- the discovery of dramatic changes in the optical spectra of AGN (Chapter 3), pointing to type transitions known as changing-look (CL) events, which challenge the standard AGN unified model (e.g. Urry and Padovani 1995);
- large-scale AGN outflows from low redshift (Chapter 4) to $z \sim 2$, the so-called Cosmic Noon (Chapters 5 and 6), where both BH accretion and SF histories show the peak of their activity (e.g. Madau and Dickinson 2014). This represents the golden epoch of AGN feedback.

All these topics except for the study of the CL AGN in NGC 4156 (Chapter 3), based on multi-epoch integrated spectra, have been addressed by means of spatially resolved IFU observations obtained with ground-based facilities. In particular, Chapter 2 makes use of data from the local IFU MaNGA survey (Bundy et al., 2015), whereas Chapters 4-6 employs IFU observations of individual galaxies carried out with optical and near-IR spectrographs at the Very Large Telescope, MUSE and SINFONI/KMOS respectively.

More specifically, Chapter 2 has investigated the use of He IIλ4686 line emission (Shirazi and Brinchmann, 2012) as a tracer of AGN activity in MaNGA galaxies. Compared to standard optical BPT (e.g. Baldwin et al. 1981), the He II diagnostic has proven to be more successful at unveiling hidden AGN residing in star-forming galaxies, which miss the AGN classification according to BPT diagrams. With a view to exploring the high-redshift Universe at unprecedented spatial resolution and sensitivity with *JWST/NIRSpec* and other ground-based advanced spectrographs (e.g. ERIS and the upcoming MOONS at the VLT), the He II diagnostic is fundamental to discover AGN in typical high-redshift galaxies,

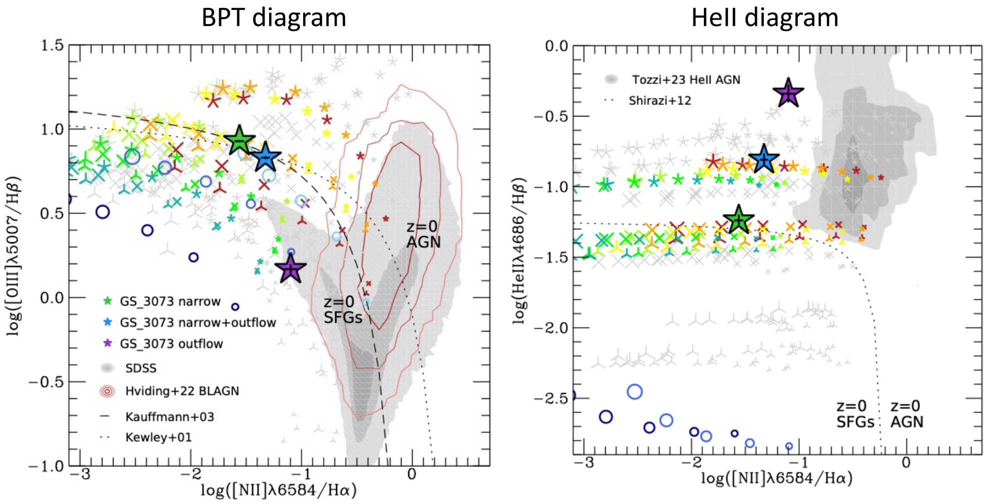

Fig. 6.12 *BPT (left) and* He II *(right; Shirazi and Brinchmann 2012, Tozzi et al. 2023) diagrams of a metal-poor galaxy at* $z \sim 5.5$*, observed with JWST/NIRSpec. Blue, purple and green stars refer to total (i.e. outflow + narrow), outflow and narrow line emission. Whereas the BPT diagram leads to an inconclusive classification of this galaxy, the* He II *unambiguously identifies AGN ionisation as the dominant mechanism in this galaxy, with measurements lying close to those we obtained locally in Tozzi et al. (2023) (Chapter 2).*

featured by an intense SF and metal-poor environments, where BPT are expected to fail (e.g. Nakajima and Maiolino 2022). First *JWST/NIRSpec* observations have been already demonstrating the key role played by He II line emission in the search for elusive AGN at high redshift ($z > 3$; Perna et al. 2023, Übler et al. 2023, Maiolino et al. 2023b), pointing to its higher diagnostic power compared to poorly reliable BPT diagnostics (see Fig. 6.12, adapted from Übler et al. 2023).

In Chapter 3, we report the discovery of the CL AGN in the local galaxy NGC 4156, as revealed by the appearance of BLR emission in 2019 in optical integrated spectra, totally absent in previous 2004 SDSS spectroscopy, which points to a transition from a type-2 toward a type-1. More recent 2022 spectroscopy furthermore suggests that now NGC 4156 is reverting back towards a type-2, consistently with the evolutionary picture proposed by Elitzur et al. (2014), where AGN transition through different optical spectral types as the central BH increases/decreases its accretion rate. The increasing number of newly discovered CL AGN (e.g. Ricci and Trakhtenbrot 2022) is now challenging the standard AGN unified model (e.g. Urry and Padovani 1995), where the type-2/type-1 dichotomy is explained in terms of different inclinations with respect to the line of sight. However, the mechanism driving such dramatic CL events is still uncertain, thus motivating further research and multi-epoch observations of already known CL AGN. Ongoing X-ray and optical monitoring of NGC 4156 with *Swift* and the Asiago telescope will help us constrain the typical time scales of these CL transitions and shed light on their physical origin.

The final three science chapters (Chapters 4-6) have focused on the spatially resolved study of AGN outflows via IFU spectroscopy, highlighting the importance of carrying out such a kind of research from low redshift, where the higher spatial resolution and sensitivity deliver a more detailed picture of outflows and their properties; to higher redshift, with a primary focus on the Cosmic Noon ($z \sim 2$; Madau and Dickinson 2014) - the golden epoch to catch AGN feedback in action. Chapter 4 has started this series of works on AGN outflows by presenting MUSE and KMOS observations offering an unprecedented optical and near-IR panoramic view of NGC 6240, an impressive local galaxy merger hosting a double AGN. With these sets of IFU observations, we traced spatial distribution and kinematics of ionised and warm molecular gas. We thus identified corresponding outflow components and used optical (e.g. Baldwin et al. 1981, Veilleux and Osterbrock 1987) and near-IR (e.g. Mouri 1994, Riffel et al. 2013) diagnostics to study the ionisation/excitation properties of gas in NGC 6240. In future, we will map the atomic neutral gas phase of outflows via optical Na ID absorption, and compare these three optical/near-IR components with the cold molecular phase of outflows traced via millimetric CO transitions (Saito et al., 2018).

Moving to $z \sim 2$, we have focused on the ionised phase of large-scale outflows, traced via rest-frame optical [O III]λ5007 line emission in near-IR SINFONI observations. In Chapter 5, we investigated the link of large-scale ionised outflows with nuclear X-ray ultra-fast outflows (UFOs) in two strongly lensed quasars, in the framework of wind feedback models (e.g. King and Pounds 2015). Taking advantage of the magnified view delivered by gravitational lensing, our results along with others from the literature support the major role played by nuclear UFOs in driving outflows on larger scales.

Finally, in Chapter 6 we completed this series of works on AGN outflows by presenting results on a sample of X-ray bright but optically obscured AGN from the SUPER survey (Circosta et al., 2018). The comparison between outflow and host galaxy properties in SUPER has provided observational evidence of a more efficient wind acceleration in obscured type-2 objects than in type-1 counterparts, likely favoured by the larger presence of dust (e.g. Costa et al. 2018). Our study has revealed such a type-1/type-2 dichotomy for the first time at $z \sim 2$, thus further supporting the 'blow-out' evolutionary scenario (e.g. Hopkins et al. 2006, Menci et al. 2008), where AGN evolve from a red obscured state to a blue unobscured one, as powerful winds efficiently sweep away obscuring material and dust.

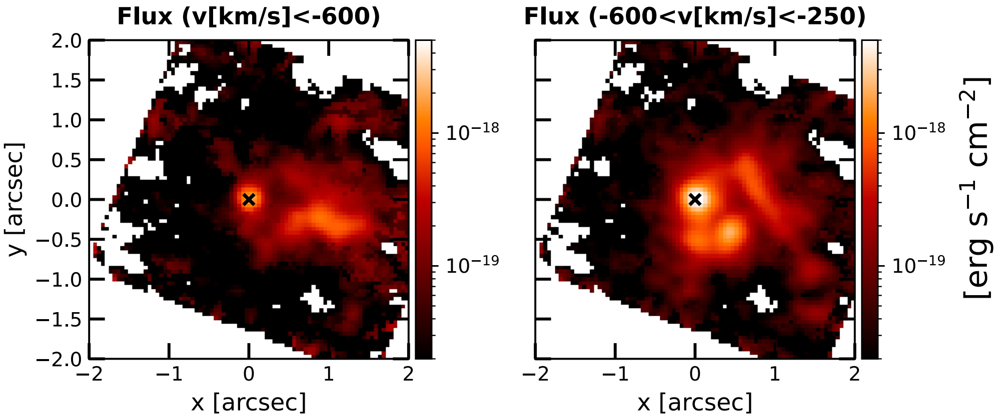

Fig. 6.13 *JWST/NIRSpec view of the obscured quasar XID2028 at* $z \sim 1.6$. *The two panels, adapted from Cresci et al. (2023), show* [O III] *channel maps in two different velocity bins: while the left-hand map at higher velocity traces outflow emission, known also from previous ground-based SINFONI observations (Cresci et al., 2015a), the right-hand panel reveals outflowing gas filaments at a lower velocity around an expanding bubble of hot gas. JWST/NIRSpec has delivered a novel view of the interplay between the outflow and its host in this galaxy at* $z \sim 1.6$.

New advanced IFU spectrographs - NIRSpec on *JWST* and ground-based AO-assisted facilities like ERIS at the VLT - are opening an unprecedented window at high spatial and spectral resolution on the $z > 2$ Universe. Our ERIS GTO (Guaranteed Time Observations) program HIPER (PI: G. Cresci) will expand our knowledge on AGN feedback at $z \sim 2$, by extending the results obtained so far with SUPER to higher spatial resolution. In particular, we will investigate the effects of AGN feedback on the host galaxy reservoir by targeting objects with available measurements of gas mass from ALMA observations. As shown by our successful study on XID2028 (Cresci et al. 2023; see also Veilleux et al. 2023), *JWST/NIRSpec* will complete the overall picture of AGN feedback at $z \sim 2$ with complementary observations at higher sensitivity, revealing a wealth of details hidden in previous ground-based IFU observations (see Fig. 6.13).

The new possibilities opened by this new generation of IFU instruments will thus allow us to take the next step to fully understand feedback mechanisms and AGN evolution at the Cosmic Noon.

Bibliography

Aalto, S., Garcia-Burillo, S., Muller, S., Winters, J. M., Gonzalez-Alfonso, E., van der Werf, P., Henkel, C., Costagliola, F., and Neri, R. (2015). High resolution observations of HCN and HCO^+ J = 3-2 in the disk and outflow of Mrk 231. Detection of vibrationally excited HCN in the warped nucleus. A&A, 574:A85.

Aalto, S., Garcia-Burillo, S., Muller, S., Winters, J. M., van der Werf, P., Henkel, C., Costagliola, F., and Neri, R. (2012). Detection of HCN, HCO^+, and HNC in the Mrk 231 molecular outflow. Dense molecular gas in the AGN wind. A&A, 537:A44.

Abazajian, K. N., Adelman-McCarthy, J. K., Agüeros, M. A., Allam, S. S., Allende Prieto, C., An, D., Anderson, K. S. J., Anderson, S. F., Annis, J., Bahcall, N. A., Bailer-Jones, C. A. L., Barentine, J. C., Bassett, B. A., Becker, A. C., Beers, T. C., Bell, E. F., Belokurov, V., Berlind, A. A., Berman, E. F., Bernardi, M., Bickerton, S. J., Bizyaev, D., Blakeslee, J. P., Blanton, M. R., Bochanski, J. J., Boroski, W. N., Brewington, H. J., Brinchmann, J., Brinkmann, J., Brunner, R. J., Budavári, T., Carey, L. N., Carliles, S., Carr, M. A., Castander, F. J., Cinabro, D., Connolly, A. J., Csabai, I., Cunha, C. E., Czarapata, P. C., Davenport, J. R. A., de Haas, E., Dilday, B., Doi, M., Eisenstein, D. J., Evans, M. L., Evans, N. W., Fan, X., Friedman, S. D., Frieman, J. A., Fukugita, M., Gänsicke, B. T., Gates, E., Gillespie, B., Gilmore, G., Gonzalez, B., Gonzalez, C. F., Grebel, E. K., Gunn, J. E., Györy, Z., Hall, P. B., Harding, P., Harris, F. H., Harvanek, M., Hawley, S. L., Hayes, J. J. E., Heckman, T. M., Hendry, J. S., Hennessy, G. S., Hindsley, R. B., Hoblitt, J., Hogan, C. J., Hogg, D. W., Holtzman, J. A., Hyde, J. B., Ichikawa, S.-i., Ichikawa, T., Im, M., Ivezić, Ž., Jester, S., Jiang, L., Johnson, J. A., Jorgensen, A. M., Jurić, M., Kent, S. M., Kessler, R., Kleinman, S. J., Knapp, G. R., Konishi, K., Kron, R. G., Krzesinski, J., Kuropatkin, N., Lampeitl, H., Lebedeva, S., Lee, M. G., Lee, Y. S., French Leger, R., Lépine, S., Li, N., Lima, M., Lin, H., Long, D. C., Loomis, C. P., Loveday, J., Lupton, R. H., Magnier, E., Malanushenko, O., Malanushenko, V., Mandelbaum, R., Margon, B., Marriner, J. P., Martínez-Delgado, D., Matsubara, T., McGehee, P. M., McKay, T. A., Meiksin, A., Morrison, H. L., Mullally, F., Munn, J. A., Murphy, T., Nash, T., Nebot, A., Neilsen, Eric H., J., Newberg, H. J., Newman, P. R., Nichol, R. C., Nicinski, T., Nieto-Santisteban, M., Nitta, A., Okamura, S., Oravetz, D. J., Ostriker, J. P., Owen, R., Padmanabhan, N., Pan, K., Park, C., Pauls, G., Peoples, John, J., Percival, W. J., Pier, J. R., Pope, A. C., Pourbaix, D., Price, P. A., Purger, N., Quinn, T., Raddick, M. J., Re Fiorentin, P., Richards, G. T., Richmond, M. W., Riess, A. G., Rix, H.-W., Rockosi, C. M., Sako, M., Schlegel, D. J., Schneider, D. P., Scholz, R.-D., Schreiber, M. R., Schwope, A. D., Seljak, U., Sesar, B., Sheldon, E., Shimasaku, K., Sibley, V. C., Simmons, A. E., Sivarani, T., Allyn Smith, J., Smith, M. C., Smolčić, V., Snedden, S. A., Stebbins, A., Steinmetz, M., Stoughton, C., Strauss, M. A., SubbaRao, M., Suto, Y., Szalay, A. S., Szapudi, I., Szkody, P., Tanaka, M., Tegmark, M., Teodoro, L. F. A., Thakar, A. R., Tremonti, C. A., Tucker, D. L., Uomoto, A., Vanden Berk, D. E., Vandenberg, J., Vidrih, S., Vogeley, M. S., Voges, W., Vogt, N. P., Wadadekar, Y., Watters, S., Weinberg, D. H., West, A. A., White, S. D. M., Wilhite, B. C., Wonders, A. C., Yanny, B., Yocum, D. R., York, D. G., Zehavi, I., Zibetti, S., and Zucker, D. B. (2009). The Seventh Data Release of the Sloan Digital Sky Survey. ApJS, 182(2):543–558.

Adelman-McCarthy, J. K., Agüeros, M. A., Allam, S. S., Allende Prieto, C., Anderson, K. S. J., Anderson, S. F., Annis, J., Bahcall, N. A., Bailer-Jones, C. A. L., Baldry, I. K., Barentine, J. C., Bassett, B. A., Becker, A. C., Beers, T. C., Bell, E. F., Berlind, A. A., Bernardi, M., Blanton, M. R., Bochanski, J. J., Boroski, W. N., Brinchmann, J., Brinkmann, J., Brunner, R. J., Budavári, T., Carliles, S., Carr, M. A., Castander, F. J., Cinabro, D., Cool, R. J., Covey, K. R., Csabai, I., Cunha, C. E., Davenport, J. R. A., Dilday, B., Doi, M., Eisenstein, D. J., Evans, M. L., Fan, X., Finkbeiner, D. P., Friedman, S. D., Frieman, J. A., Fukugita, M., Gänsicke, B. T., Gates, E., Gillespie, B., Glazebrook, K., Gray, J., Grebel, E. K., Gunn, J. E., Gurbani, V. K., Hall, P. B., Harding, P., Harvanek, M., Hawley, S. L., Hayes, J., Heckman, T. M., Hendry, J. S., Hindsley, R. B., Hirata, C. M., Hogan, C. J., Hogg, D. W., Hyde, J. B., Ichikawa, S.-i., Ivezić, Ž., Jester, S., Johnson, J. A., Jorgensen, A. M., Jurić, M., Kent, S. M., Kessler, R., Kleinman, S. J., Knapp, G. R., Kron, R. G., Krzesinski, J., Kuropatkin, N., Lamb, D. Q., Lampeitl, H., Lebedeva, S., Lee, Y. S., French Leger, R., Lépine, S., Lima, M., Lin, H., Long, D. C., Loomis, C. P., Loveday, J., Lupton, R. H., Malanushenko, O., Malanushenko, V., Mandelbaum, R., Margon, B., Marriner, J. P., Martínez-Delgado, D., Matsubara, T., McGehee, P. M., McKay, T. A., Meiksin, A., Morrison, H. L., Munn, J. A., Nakajima, R., Neilsen, Eric H., J., Newberg, H. J., Nichol, R. C., Nicinski, T., Nieto-Santisteban, M., Nitta, A., Okamura, S., Owen, R., Oyaizu, H., Padmanabhan, N., Pan, K., Park, C., Peoples, John, J., Pier, J. R., Pope, A. C., Purger, N., Raddick, M. J., Re Fiorentin, P., Richards, G. T., Richmond, M. W., Riess, A. G., Rix, H.-W., Rockosi, C. M., Sako, M., Schlegel, D. J., Schneider, D. P., Schreiber, M. R., Schwope, A. D., Seljak, U., Sesar, B., Sheldon, E., Shimasaku, K., Sivarani, T., Allyn Smith, J., Snedden, S. A., Steinmetz, M., Strauss, M. A., SubbaRao, M., Suto, Y., Szalay, A. S., Szapudi, I., Szkody, P., Tegmark, M., Thakar, A. R., Tremonti, C. A., Tucker, D. L., Uomoto, A., Vanden Berk, D. E., Vandenberg, J., Vidrih, S., Vogeley, M. S., Voges, W., Vogt, N. P., Wadadekar, Y., Weinberg, D. H., West, A. A., White, S. D. M., Wilhite, B. C., Yanny, B., Yocum, D. R., York, D. G., Zehavi, I., and Zucker, D. B. (2008). The Sixth Data Release of the Sloan Digital Sky Survey. ApJS, 175(2):297–313.

Aird, J., Coil, A. L., Georgakakis, A., Nandra, K., Barro, G., and Pérez-González, P. G. (2015). The evolution of the X-ray luminosity functions of unabsorbed and absorbed AGNs out to z∼ 5. MNRAS, 451(2):1892–1927.

Aird, J., Nandra, K., Laird, E. S., Georgakakis, A., Ashby, M. L. N., Barmby, P., Coil, A. L., Huang, J. S., Koekemoer, A. M., Steidel, C. C., and Willmer, C. N. A. (2010). The evolution of the hard X-ray luminosity function of AGN. MNRAS, 401(4):2531–2551.

Alam, S., Albareti, F. D., Allende Prieto, C., Anders, F., Anderson, S. F., Anderton, T., Andrews, B. H., Armengaud, E., Aubourg, É., Bailey, S., Basu, S., Bautista, J. E., Beaton, R. L., Beers, T. C., Bender, C. F., Berlind, A. A., Beutler, F., Bhardwaj, V., Bird, J. C., Bizyaev, D., Blake, C. H., Blanton, M. R., Blomqvist, M., Bochanski, J. J., Bolton, A. S., Bovy, J., Shelden Bradley, A., Brandt, W. N., Brauer, D. E., Brinkmann, J., Brown, P. J., Brownstein, J. R., Burden, A., Burtin, E., Busca, N. G., Cai, Z., Capozzi, D., Carnero Rosell, A., Carr, M. A., Carrera, R., Chambers, K. C., Chaplin, W. J., Chen, Y.-C., Chiappini, C., Chojnowski, S. D., Chuang, C.-H., Clerc, N., Comparat, J., Covey, K., Croft, R. A. C., Cuesta, A. J., Cunha, K., da Costa, L. N., Da Rio, N., Davenport, J. R. A., Dawson, K. S., De Lee, N., Delubac, T., Deshpande, R., Dhital, S., Dutra-Ferreira, L., Dwelly, T., Ealet, A., Ebelke, G. L., Edmondson, E. M., Eisenstein, D. J., Ellsworth, T., Elsworth, Y., Epstein, C. R., Eracleous, M., Escoffier, S., Esposito, M., Evans, M. L., Fan, X., Fernández-Alvar, E., Feuillet, D., Filiz Ak, N., Finley, H., Finoguenov, A., Flaherty, K., Fleming, S. W., Font-Ribera, A., Foster, J., Frinchaboy, P. M., Galbraith-Frew, J. G., García, R. A., García-Hernández, D. A., García Pérez, A. E., Gaulme, P., Ge, J., Génova-Santos, R., Georgakakis, A., Ghezzi, L., Gillespie, B. A., Girardi, L., Goddard, D., Gontcho, S. G. A., González Hernández, J. I., Grebel, E. K., Green, P. J., Grieb, J. N., Grieves, N., Gunn, J. E., Guo, H., Harding, P., Hasselquist, S., Hawley, S. L., Hayden, M., Hearty, F. R., Hekker, S., Ho, S., Hogg, D. W., Holley-Bockelmann, K., Holtzman, J. A., Honscheid, K., Huber, D., Huehnerhoff, J., Ivans, I. I., Jiang, L., Johnson, J. A., Kinemuchi, K., Kirkby, D., Kitaura, F., Klaene, M. A., Knapp, G. R., Kneib, J.-P., Koenig, X. P., Lam, C. R., Lan, T.-W., Lang, D., Laurent, P., Le Goff, J.-M., Leauthaud, A., Lee, K.-G., Lee, Y. S., Licquia, T. C., Liu, J., Long, D. C., López-Corredoira, M., Lorenzo-Oliveira, D., Lucatello, S., Lundgren, B., Lupton, R. H., Mack, Claude E., I., Mahadevan, S., Maia, M. A. G., Majewski, S. R., Malanushenko, E., Malanushenko, V., Manchado, A., Manera, M., Mao, Q., Maraston, C., Marchwinski, R. C., Margala, D., Martell, S. L., Martig, M., Masters, K. L., Mathur, S., McBride, C. K., McGehee, P. M., McGreer, I. D., McMahon, R. G., Ménard, B., Menzel, M.-L., Merloni, A., Mészáros, S., Miller, A. A., Miralda-Escudé, J., Miyatake, H., Montero-Dorta, A. D., More, S., Morganson, E., Morice-Atkinson, X., Morrison, H. L., Mosser, B., Muna, D., Myers, A. D., Nandra, K., Newman, J. A., Neyrinck, M., Nguyen, D. C., Nichol, R. C., Nidever, D. L., Noterdaeme, P., Nuza, S. E., O'Connell, J. E., O'Connell, R. W., O'Connell, R., Ogando, R. L. C., Olmstead, M. D., Oravetz, A. E., Oravetz, D. J., Osumi, K., Owen, R., Padgett, D. L., Padmanabhan, N., Paegert, M., Palanque-Delabrouille, N., Pan, K., Parejko, J. K., Pâris, I., Park, C., Pattarakijwanich, P., Pellejero-Ibanez, M., Pepper, J., Percival, W. J., Pérez-Fournon, I., Pérez-Ràfols, I., Petitjean, P., Pieri, M. M., Pinsonneault, M. H., Porto de Mello, G. F., Prada, F., Prakash, A., Price-Whelan, A. M., Protopapas, P., Raddick, M. J., Rahman, M., Reid, B. A., Rich, J., Rix, H.-W., Robin, A. C., Rockosi, C. M., Rodrigues, T. S., Rodríguez-Torres, S., Roe, N. A., Ross, A. J., Ross, N. P., Rossi, G., Ruan, J. J., Rubiño-Martín, J. A., Rykoff, E. S., Salazar-Albornoz, S., Salvato, M., Samushia, L., Sánchez, A. G., Santiago, B., Sayres, C., Schiavon, R. P., Schlegel, D. J., Schmidt, S. J., Schneider, D. P., Schultheis, M., Schwope, A. D., Scóccola, C. G., Scott, C., Sellgren, K., Seo, H.-J., Serenelli, A., Shane, N., Shen, Y., Shetrone, M., Shu, Y., Silva Aguirre, V., Sivarani, T., Skrutskie, M. F., Slosar, A., Smith, V. V., Sobreira, F., Souto, D., Stassun, K. G., Steinmetz, M., Stello, D., Strauss, M. A., Streblyanska, A., Suzuki, N., Swanson, M. E. C., Tan, J. C., Tayar, J., Terrien, R. C., Thakar, A. R., Thomas, D., Thomas, N., Thompson, B. A., Tinker, J. L., Tojeiro, R., Troup, N. W., Vargas-Magaña, M., Vazquez, J. A., Verde, L., Viel, M., Vogt, N. P., Wake, D. A., Wang, J., Weaver, B. A., Weinberg, D. H., Weiner, B. J., White, M., Wilson, J. C., Wisniewski, J. P., Wood-Vasey, W. M., Ye'che, C., York, D. G., Zakamska, N. L., Zamora, O., Zasowski, G., Zehavi, I., Zhao, G.-B., Zheng, Z., Zhou, X., Zhou, Z., Zou, H., and Zhu, G. (2015). The Eleventh and Twelfth Data Releases of the Sloan Digital Sky Survey: Final Data from SDSS-III. ApJS, 219(1):12.

Alexander, D. M. and Hickox, R. C. (2012). What drives the growth of black holes? New A Rev., 56(4):93–121.

Allington-Smith, J. and Content, R. (1998). Sampling and Background Subtraction in

Fiber-Lenslet Integral Field Spectrographs. PASP, 110(752):1216–1234.

Alloin, D., Pelat, D., Phillips, M. M., Fosbury, R. A. E., and Freeman, K. (1986). Recurrent Outbursts in the Broad-Line Region of NGC 1566. ApJ, 308:23.

Antonucci, R. (1993). Unified models for active galactic nuclei and quasars. ARA&A, 31:473–521.

Antonucci, R. (2012). A panchromatic review of thermal and nonthermal active galactic nuclei. *Astronomical and Astrophysical Transactions*, 27(4):557–602.

Aretxaga, I., Joguet, B., Kunth, D., Melnick, J., and Terlevich, R. J. (1999). Seyfert 1 Mutation of the Classical Seyfert 2 Nucleus NGC 7582. ApJ, 519(2):L123–L126.

Armus, L., Bernard-Salas, J., Spoon, H. W. W., Marshall, J. A., Charmandaris, V., Higdon, S. J. U., Desai, V., Hao, L., Teplitz, H. I., Devost, D., Brandl, B. R., Soifer, B. T., and Houck, J. R. (2006). Detection of the Buried Active Galactic Nucleus in NGC 6240 with the Infrared Spectrograph on the Spitzer Space Telescope. ApJ, 640(1):204–210.

Arribas, S., Colina, L., Bellocchi, E., Maiolino, R., and Villar-Martín, M. (2014). Ionized gas outflows and global kinematics of low-z luminous star-forming galaxies. A&A, 568:A14.

Assef, R. J., Denney, K. D., Kochanek, C. S., Peterson, B. M., Kozłowski, S., Ageorges, N., Barrows, R. S., Buschkamp, P., Dietrich, M., Falco, E., Feiz, C., Gemperlein, H., Germeroth, A., Grier, C. J., Hofmann, R., Juette, M., Khan, R., Kilic, M., Knierim, V., Laun, W., Lederer, R., Lehmitz, M., Lenzen, R., Mall, U., Madsen, K. K., Mandel, H., Martini, P., Mathur, S., Mogren, K., Mueller, P., Naranjo, V., Pasquali, A., Polsterer, K., Pogge, R. W., Quirrenbach, A., Seifert, W., Stern, D., Shappee, B., Storz, C., Van Saders, J., Weiser, P., and Zhang, D. (2011). Black Hole Mass Estimates Based on C IV are Consistent with Those Based on the Balmer Lines. ApJ, 742(2):93.

Bañados, E., Mazzucchelli, C., Momjian, E., Eilers, A.-C., Wang, F., Schindler, J.-T., Connor, T., Andika, I. T., Barth, A. J., Carilli, C., Davies, F. B., Decarli, R., Fan, X., Farina, E. P., Hennawi, J. F., Pensabene, A., Stern, D., Venemans, B. P., Wenzl, L., and Yang, J. (2021). The Discovery of a Highly Accreting, Radio-loud Quasar at z = 6.82. ApJ, 909(1):80.

Bacon, R., Accardo, M., Adjali, L., Anwand, H., Bauer, S., Biswas, I., Blaizot, J., Boudon, D., Brau-Nogue, S., Brinchmann, J., Caillier, P., Capoani, L., Carollo, C. M., Contini, T., Couderc, P., Daguisé, E., Deiries, S., Delabre, B., Dreizler, S., Dubois, J., Dupieux, M., Dupuy, C., Emsellem, E., Fechner, T., Fleischmann, A., François, M., Gallou, G., Gharsa, T., Glindemann, A., Gojak, D., Guiderdoni, B., Hansali, G., Hahn, T., Jarno, A., Kelz, A., Koehler, C., Kosmalski, J., Laurent, F., Le Floch, M., Lilly, S. J., Lizon, J. L., Loupias, M., Manescau, A., Monstein, C., Nicklas, H., Olaya, J. C., Pares, L., Pasquini, L., Pécontal-Rousset, A., Pelló, R., Petit, C., Popow, E., Reiss, R., Remillieux, A., Renault, E., Roth, M., Rupprecht, G., Serre, D., Schaye, J., Soucail, G., Steinmetz, M., Streicher, O., Stuik, R., Valentin, H., Vernet, J., Weilbacher, P., Wisotzki, L., and Yerle, N. (2010). The MUSE second-generation VLT instrument. In McLean, I. S., Ramsay, S. K., and Takami, H., editors, *Ground-based and Airborne Instrumentation for Astronomy III*, volume 7735 of *Society of Photo-Optical Instrumentation Engineers (SPIE) Conference Series*, page 773508.

Bae, H.-J. and Woo, J.-H. (2014). A Census of Gas Outflows in Type 2 Active Galactic Nuclei. ApJ, 795(1):30.

Bae, H.-J. and Woo, J.-H. (2018). The Independence of Neutral and Ionized Gas Outflows in Low-z Galaxies. ApJ, 853(2):185.

Baldry, I. K., Balogh, M. L., Bower, R. G., Glazebrook, K., Nichol, R. C., Bamford, S. P., and Budavari, T. (2006). Galaxy bimodality versus stellar mass and environment. MNRAS, 373(2):469–483.

Baldry, I. K., Glazebrook, K., Brinkmann, J., Ivezić, Ž., Lupton, R. H., Nichol, R. C., and Szalay, A. S. (2004). Quantifying the Bimodal Color-Magnitude Distribution of Galaxies. ApJ, 600(2):681–694.

Baldwin, C., McDermid, R. M., Kuntschner, H., Maraston, C., and Conroy, C. (2018). Comparison of stellar population model predictions using optical and infrared spectroscopy. MNRAS, 473(4):4698–4721.

Baldwin, J. A., Phillips, M. M., and Terlevich, R. (1981). Classification parameters for the emission-line spectra of extragalactic objects. PASP, 93:5–19.

Balmaverde, B., Marconi, A., Brusa, M., Carniani, S., Cresci, G., Lusso, E., Maiolino, R., Mannucci, F., and Nagao, T. (2016). Is there any evidence that ionized outflows quench star formation in type 1 quasars at $z < 1$? A&A, 585:A148.

Bär, R. E., Weigel, A. K., Sartori, L. F., Oh, K., Koss, M., and Schawinski, K. (2017). Active galactic nuclei from He II: a more complete census of AGN in SDSS galaxies yields a new population of low-luminosity AGN in highly star-forming galaxies. MNRAS, 466(3):2879–2887.

Barnes, J. E. and Hernquist, L. (1996). Transformations of Galaxies. II. Gasdynamics in Merging Disk Galaxies. ApJ, 471:115.

Barnes, J. E. and Hernquist, L. E. (1991). Fueling Starburst Galaxies with Gas-rich Mergers. ApJ, 370:L65.

Bautista, M. A. and Kallman, T. R. (2001). The XSTAR Atomic Database. ApJS, 134(1):139–149.

Bayliss, M. B., Sharon, K., Acharyya, A., Gladders, M. D., Rigby, J. R., Bian, F., Bordoloi, R., Runnoe, J., Dahle, H., Kewley, L., Florian, M., Johnson, T., and Paterno-Mahler, R. (2017). Spatially Resolved Patchy Lyα Emission within the Central Kiloparsec of a Strongly Lensed Quasar Host Galaxy at $z = 2.8$. ApJ, 845(2):L14.

Becker, R. H., White, R. L., and Helfand, D. J. (1995). The FIRST Survey: Faint Images of the Radio Sky at Twenty Centimeters. ApJ, 450:559.

Beckers, J. M. (1993). Adaptive Optics for Astronomy: Principles, Performance, and Applications. ARA&A, 31:13–62.

Belfiore, F., Westfall, K. B., Schaefer, A., Cappellari, M., Ji, X., Bershady, M. A., Tremonti, C., Law, D. R., Yan, R., Bundy, K., Shetty, S., Drory, N., Thomas, D., Emsellem, E., and Sánchez, S. F. (2019). The Data Analysis Pipeline for the SDSS-IV MaNGA IFU Galaxy Survey: Emission-line Modeling. AJ, 158(4):160.

Bell, E. F., McIntosh, D. H., Katz, N., and Weinberg, M. D. (2003). The Optical and Near-Infrared Properties of Galaxies. I. Luminosity and Stellar Mass Functions. ApJS, 149(2):289–312.

Belladitta, S., Moretti, A., Caccianiga, A., Spingola, C., Severgnini, P., Della Ceca, R., Ghisellini, G., Dallacasa, D., Sbarrato, T., Cicone, C., Cassarà, L. P., and Pedani, M. (2020). The first blazar observed at z > 6. A&A, 635:L7.

Bennert, N., Falcke, H., Schulz, H., Wilson, A. S., and Wills, B. J. (2002). Size and Structure of the Narrow-Line Region of Quasars. ApJ, 574(2):L105–L109.

Bentz, M. C., Denney, K. D., Grier, C. J., Barth, A. J., Peterson, B. M., Vestergaard, M., Bennert, V. N., Canalizo, G., De Rosa, G., Filippenko, A. V., Gates, E. L., Greene, J. E., Li, W., Malkan, M. A., Pogge, R. W., Stern, D., Treu, T., and Woo, J.-H. (2013). The Low-luminosity End of the Radius-Luminosity Relationship for Active Galactic Nuclei. ApJ, 767(2):149.

Berney, S., Koss, M., Trakhtenbrot, B., Ricci, C., Lamperti, I., Schawinski, K., Baloković, M., Crenshaw, D. M., Fischer, T., Gehrels, N., Harrison, F., Hashimoto, Y., Ichikawa, K., Mushotzky, R., Oh, K., Stern, D., Treister, E., Ueda, Y., Veilleux, S., and Winter, L. (2015). BAT AGN spectroscopic survey-II. X-ray emission and high-ionization optical emission lines. MNRAS, 454(4):3622–3634.

Best, P. N., Kauffmann, G., Heckman, T. M., Brinchmann, J., Charlot, S., Ivezić, Ž., and White, S. D. M. (2005). The host galaxies of radio-loud active galactic nuclei: mass dependences, gas cooling and active galactic nuclei feedback. MNRAS, 362(1):25–40.

Beswick, R. J., Pedlar, A., Mundell, C. G., and Gallimore, J. F. (2001). A MERLIN neutral hydrogen absorption study of the luminous infrared merger NGC 6240. MNRAS, 325(1):151–158.

Beuchert, T., Markowitz, A. G., Krauß, F., Miniutti, G., Longinotti, A. L., Guainazzi, M., de La Calle Pérez, I., Malkan, M., Elvis, M., Miyaji, T., Hiriart, D., López, J. M., Agudo, I., Dauser, T., Garcia, J., Kreikenbohm, A., Kadler, M., and Wilms, J. (2015). A variable-density absorption event in NGC 3227 mapped with Suzaku and Swift. A&A, 584:A82.

Bischetti, M., Maiolino, R., Carniani, S., Fiore, F., Piconcelli, E., and Fluetsch, A. (2019). Widespread QSO-driven outflows in the early Universe. A&A, 630:A59.

Black, J. H. and van Dishoeck, E. F. (1987). Fluorescent Excitation of Interstellar H 2. ApJ, 322:412.

Blanton, M. R., Bershady, M. A., Abolfathi, B., Albareti, F. D., Allende Prieto, C., Almeida, A., Alonso-García, J., Anders, F., Anderson, S. F., Andrews, B., Aquino-Ortíz, E., Aragón-Salamanca, A., Argudo-Fernández, M., Armengaud, E., Aubourg, E., Avila-Reese, V., Badenes, C., Bailey, S., Barger, K. A., Barrera-Ballesteros, J., Bartosz, C., Bates, D., Baumgarten, F., Bautista, J., Beaton, R., Beers, T. C., Belfiore, F., Bender, C. F., Berlind, A. A., Bernardi, M., Beutler, F., Bird, J. C., Bizyaev, D., Blanc, G. A., Blomqvist, M., Bolton, A. S., Boquien, M., Borissova, J., van den Bosch, R., Bovy, J., Brandt, W. N., Brinkmann, J., Brownstein, J. R., Bundy, K., Burgasser, A. J., Burtin, E., Busca, N. G., Cappellari, M., Delgado Carigi, M. L., Carlberg, J. K., Carnero Rosell, A., Carrera, R., Chanover, N. J., Cherinka, B., Cheung, E., Gómez Maqueo Chew, Y., Chiappini, C., Choi, P. D., Chojnowski, D., Chuang, C.-H., Chung, H., Cirolini, R. F., Clerc, N., Cohen, R. E., Comparat, J., da Costa, L., Cousinou, M.-C., Covey, K., Crane, J. D., Croft, R. A. C., Cruz-Gonzalez, I., Garrido Cuadra, D., Cunha, K., Damke, G. J., Darling, J., Davies, R., Dawson, K., de la Macorra, A., Dell'Agli, F., De Lee, N., Delubac, T., Di Mille, F., Diamond-Stanic, A., Cano-Díaz, M., Donor, J., Downes, J. J., Drory, N., du Mas des Bourboux, H., Duckworth, C. J., Dwelly, T., Dyer, J., Ebelke, G., Eigenbrot, A. D., Eisenstein, D. J., Emsellem, E., Eracleous, M., Escoffier, S., Evans, M. L., Fan, X., Fernández-Alvar, E., Fernandez-Trincado, J. G., Feuillet, D. K., Finoguenov, A., Fleming, S. W., Font-Ribera, A., Fredrickson, A., Freischlad, G., Frinchaboy, P. M., Fuentes, C. E., Galbany, L., Garcia-Dias, R., García-Hernández, D. A., Gaulme, P., Geisler, D., Gelfand, J. D., Gil-Marín, H., Gillespie, B. A., Goddard, D., Gonzalez-Perez, V., Grabowski, K., Green, P. J., Grier, C. J., Gunn, J. E., Guo, H., Guy, J., Hagen, A., Hahn, C., Hall, M., Harding, P., Hasselquist, S., Hawley, S. L., Hearty, F., Gonzalez Hernández, J. I., Ho, S., Hogg, D. W., Holley-Bockelmann, K., Holtzman, J. A., Holzer, P. H., Huehnerhoff, J., Hutchinson, T. A., Hwang, H. S., Ibarra-Medel, H. J., da Silva Ilha, G., Ivans, I. I., Ivory, K., Jackson, K., Jensen, T. W., Johnson, J. A., Jones, A., Jönsson, H., Jullo, E., Kamble, V., Kinemuchi, K., Kirkby, D., Kitaura, F.-S., Klaene, M., Knapp, G. R., Kneib, J.-P., Kollmeier, J. A., Lacerna, I., Lane, R. R., Lang, D., Law, D. R., Lazarz, D., Lee, Y., Le Goff, J.-M., Liang, F.-H., Li, C., Li, H., Lian, J., Lima, M., Lin, L., Lin, Y.-T., Bertran de Lis, S., Liu, C., de Icaza Lizaola, M. A. C., Long, D., Lucatello, S., Lundgren, B., MacDonald, N. K., Deconto Machado, A., MacLeod, C. L., Mahadevan, S., Geimba Maia, M. A., Maiolino, R., Majewski, S. R., Malanushenko, E., Malanushenko, V., Manchado, A., Mao, S., Maraston, C., Marques-Chaves, R., Masseron, T., Masters, K. L., McBride, C. K., McDermid, R. M., McGrath, B., McGreer, I. D., Medina Peña, N., Melendez, M., Merloni, A., Merrifield, M. R., Meszaros, S., Meza, A., Minchev, I., Minniti, D., Miyaji, T., More, S., Mulchaey, J., Müller-Sánchez, F., Muna, D., Munoz, R. R., Myers, A. D., Nair, P., Nandra, K., Correa do Nascimento, J., Negrete, A., Ness, M., Newman, J. A., Nichol, R. C., Nidever, D. L., Nitschelm, C., Ntelis, P., O'Connell, J. E., Oelkers, R. J., Oravetz, A., Oravetz, D., Pace, Z., Padilla, N., Palanque-Delabrouille, N., Alonso Palicio, P., Pan, K., Parejko, J. K., Parikh, T., Pâris, I., Park, C., Patten, A. Y., Peirani, S., Pellejero-Ibanez, M., Penny, S., Percival, W. J., Perez-Fournon, I., Petitjean, P., Pieri, M. M., Pinsonneault, M., Pisani, A., Poleski, R., Prada, F., Prakash, A., Queiroz, A. B. d. A., Raddick, M. J., Raichoor, A., Barboza Rembold, S., Richstein, H., Riffel, R. A., Riffel, R., Rix, H.-W., Robin, A. C., Rockosi, C. M., Rodríguez-Torres, S., Roman-Lopes, A., Román-Zúñiga, C., Rosado, M., Ross, A. J., Rossi, G., Ruan, J., Ruggeri, R., Rykoff, E. S., Salazar-Albornoz, S., Salvato, M., Sánchez, A. G., Aguado, D. S., Sánchez-Gallego, J. R., Santana, F. A., Santiago, B. X., Sayres, C., Schiavon, R. P., da Silva Schimoia, J., Schlafly, E. F., Schlegel, D. J., Schneider, D. P., Schultheis, M., Schuster, W. J., Schwope, A., Seo, H.-J., Shao, Z., Shen, S., Shetrone, M., Shull, M., Simon, J. D., Skinner, D., Skrutskie, M. F., Slosar, A., Smith, V. V., Sobeck, J. S., Sobreira, F., Somers, G., Souto, D., Stark, D. V., Stassun, K., Stauffer, F., Steinmetz, M., Storchi-Bergmann, T., Streblyanska, A., Stringfellow, G. S., Suárez, G., Sun, J., Suzuki, N., Szigeti, L., Taghizadeh-Popp, M., Tang, B., Tao, C., Tayar, J., Tembe, M., Teske, J., Thakar, A. R., Thomas, D., Thompson, B. A., Tinker, J. L., Tissera, P., Tojeiro, R., Hernandez Toledo, H., de la Torre, S., Tremonti, C., Troup, N. W., Valenzuela, O., Martinez Valpuesta, I., Vargas-González, J., Vargas-Magaña, M., Vazquez, J. A., Villanova, S., Vivek, M., Vogt, N., Wake, D., Walterbos, R., Wang, Y., Weaver, B. A., Weijmans, A.-M., Weinberg, D. H., Westfall, K. B., Whelan, D. G., Wild, V., Wilson, J., Wood-Vasey, W. M., Wylezalek, D., Xiao, T., Yan, R., Yang, M., Ybarra, J. E., Yèche, C., Zakamska, N., Zamora, O., Zarrouk, P., Zasowski, G., Zhang, K., Zhao, G.-B., Zheng, Z., Zheng, Z., Zhou, X., Zhou, Z.-M., Zhu, G. B., Zoccali, M., and Zou, H. (2017). Sloan Digital Sky Survey IV: Mapping the Milky Way, Nearby Galaxies, and the Distant Universe. AJ, 154(1):28.

Bluck, A. F. L., Maiolino, R., Piotrowska, J. M., Trussler, J., Ellison, S. L., Sánchez, S. F., Thorp, M. D., Teimoorinia, H., Moreno, J., and Conselice, C. J. (2020). How do central and satellite galaxies quench? - Insights from spatially resolved spectroscopy in the MaNGA survey. MNRAS, 499(1):230–268.

Bock, D. C. J., Large, M. I., and Sadler, E. M. (1999). SUMSS: A Wide-Field Radio Imaging Survey of the Southern Sky. I. Science Goals, Survey Design, and Instrumentation. AJ, 117(3):1578–1593.

Bogdanović, T., Ge, J., Max, C. E., and Raschke, L. M. (2003). Circumnuclear Shock and Starburst in NGC 6240: Near-Infrared Imaging and Spectroscopy with Adaptive Optics. AJ, 126(5):2299–2306.

Bolatto, A. D., Wolfire, M., and Leroy, A. K. (2013). The CO-to-H_2 Conversion Factor. ARA&A, 51(1):207–268.

Bordoloi, R., Lilly, S. J., Hardmeier, E., Contini, T., Kneib, J. P., Le Fevre, O., Mainieri, V., Renzini, A., Scodeggio, M., Zamorani, G., Bardelli, S., Bolzonella, M., Bongiorno, A., Caputi, K., Carollo, C. M., Cucciati, O., de la Torre, S., de Ravel, L., Garilli, B., Iovino, A., Kampczyk, P., Kovač, K., Knobel, C., Lamareille, F., Le Borgne, J. F., Le Brun, V., Maier, C., Mignoli, M., Oesch, P., Pello, R., Peng, Y., Perez Montero, E., Presotto, V., Silverman, J., Tanaka, M., Tasca, L., Tresse, L., Vergani, D., Zucca, E., Cappi, A., Cimatti, A., Coppa, G., Franzetti, P., Koekemoer, A., Moresco, M., Nair, P., and Pozzetti, L. (2014). The Dependence of Galactic Outflows on the Properties and Orientation of zCOSMOS Galaxies at z ~1. ApJ, 794(2):130.

Boroson, T. (2005). Blueshifted [O III] Emission: Indications of a Dynamic Narrow-Line Region. AJ, 130(2):381–386.

Boroson, T. A. and Green, R. F. (1992). The Emission-Line Properties of Low-Redshift Quasi-stellar Objects. ApJS, 80:109.

Böttcher, M. and Dermer, C. D. (2010). Timing Signatures of the Internal-Shock Model for Blazars. ApJ, 711(1):445–460.

Bouché, N., Murphy, M. T., Kacprzak, G. G., Péroux, C., Contini, T., Martin, C. L., and Dessauges-Zavadsky, M. (2013). Signatures of Cool Gas Fueling a Star-Forming Galaxy at Redshift 2.3. *Science*, 341(6141):50–53.

Bovy, J. (2015). galpy: A python Library for Galactic Dynamics. ApJS, 216(2):29.

Bower, R. G., Benson, A. J., Malbon, R., Helly, J. C., Frenk, C. S., Baugh, C. M., Cole, S., and Lacey, C. G. (2006). Breaking the hierarchy of galaxy formation. MNRAS, 370(2):645–655.

Boyle, B. J., Fong, R., Shanks, T., and Peterson, B. A. (1990). A catalogue of faint, UV-excess objects. MNRAS, 243:1–56.

Brand, P. W. J. L., Toner, M. P., Geballe, T. R., Webster, A. S., Williams, P. M., and Burton, M. G. (1989). The constancy of the ratio of the molecular hydrogen lines at 3.8 mu.m in Orion. MNRAS, 236:929–934.

Brinchmann, J., Kunth, D., and Durret, F. (2008). Galaxies with Wolf-Rayet signatures in the low-redshift Universe. A survey using the Sloan Digital Sky Survey. A&A, 485(3):657–677.

Brusa, M., Bongiorno, A., Cresci, G., Perna, M., Marconi, A., Mainieri, V., Maiolino, R., Salvato, M., Lusso, E., Santini, P., Comastri, A., Fiore, F., Gilli, R., La Franca, F., Lanzuisi, G., Lutz, D., Merloni, A., Mignoli, M., Onori, F., Piconcelli, E., Rosario, D., Vignali, C., and Zamorani, G. (2015). X-shooter reveals powerful outflows in z ~ 1.5 X-ray selected obscured quasi-stellar objects. MNRAS, 446(3):2394–2417.

Brusa, M., Civano, F., Comastri, A., Miyaji, T., Salvato, M., Zamorani, G., Cappelluti, N., Fiore, F., Hasinger, G., Mainieri, V., Merloni, A., Bongiorno, A., Capak, P., Elvis, M., Gilli, R., Hao, H., Jahnke, K., Koekemoer, A. M., Ilbert, O., Le Floc'h, E., Lusso, E., Mignoli, M., Schinnerer, E., Silverman, J. D., Treister, E., Trump, J. D., Vignali, C., Zamojski, M., Aldcroft, T., Aussel, H., Bardelli, S., Bolzonella, M., Cappi, A., Caputi, K., Contini, T., Finoguenov, A., Fruscione, A., Garilli, B., Impey, C. D., Iovino, A., Iwasawa, K., Kampczyk, P., Kartaltepe, J., Kneib, J. P., Knobel, C., Kovac, K., Lamareille, F., Leborgne, J. F., Le Brun, V., Le Fevre, O., Lilly, S. J., Maier, C., McCracken, H. J., Pello, R., Peng, Y. J., Perez-Montero, E., de Ravel, L., Sanders, D., Scodeggio, M., Scoville, N. Z., Tanaka, M., Taniguchi, Y., Tasca, L., de la Torre, S., Tresse, L., Vergani, D., and Zucca, E. (2010). The XMM-Newton Wide-field Survey in the Cosmos Field (XMM-COSMOS): Demography and Multiwavelength Properties of Obscured and Unobscured Luminous Active Galactic Nuclei. ApJ, 716(1):348–369.

Brusa, M., Cresci, G., Daddi, E., Paladino, R., Perna, M., Bongiorno, A., Lusso, E., Sargent, M. T., Casasola, V., Feruglio, C., Fraternali, F., Georgiev, I., Mainieri, V., Carniani, S., Comastri, A., Duras, F., Fiore, F., Mannucci, F., Marconi, A., Piconcelli, E., Zamorani, G., Gilli, R., La Franca, F., Lanzuisi, G., Lutz, D., Santini, P., Scoville, N. Z., Vignali, C., Vito, F., Rabien, S., Busoni, L., and Bonaglia, M. (2018). Molecular outflow and feedback in the obscured quasar XID2028 revealed by ALMA. A&A, 612:A29.

Brusa, M., Perna, M., Cresci, G., Schramm, M., Delvecchio, I., Lanzuisi, G., Mainieri, V., Mignoli, M., Zamorani, G., Berta, S., Bongiorno, A., Comastri, A., Fiore, F., Kakkad, D., Marconi, A., Rosario, D., Contini, T., and Lamareille, F. (2016). A fast ionised wind in a star-forming quasar system at z ~1.5 resolved through adaptive optics assisted near-infrared data. A&A, 588:A58.

Bundy, K., Bershady, M. A., Law, D. R., Yan, R., Drory, N., MacDonald, N., Wake, D. A., Cherinka, B., Sánchez-Gallego, J. R., Weijmans, A.-M., Thomas, D., Tremonti, C., Masters, K., Coccato, L., Diamond-Stanic, A. M., Aragón-Salamanca, A., Avila-Reese, V., Badenes, C., Falcón-Barroso, J., Belfiore, F., Bizyaev, D., Blanc, G. A., Bland-Hawthorn, J., Blanton,

M. R., Brownstein, J. R., Byler, N., Cappellari, M., Conroy, C., Dutton, A. A., Emsellem, E., Etherington, J., Frinchaboy, P. M., Fu, H., Gunn, J. E., Harding, P., Johnston, E. J., Kauffmann, G., Kinemuchi, K., Klaene, M. A., Knapen, J. H., Leauthaud, A., Li, C., Lin, L., Maiolino, R., Malanushenko, V., Malanushenko, E., Mao, S., Maraston, C., McDermid, R. M., Merrifield, M. R., Nichol, R. C., Oravetz, D., Pan, K., Parejko, J. K., Sanchez, S. F., Schlegel, D., Simmons, A., Steele, O., Steinmetz, M., Thanjavur, K., Thompson, B. A., Tinker, J. L., van den Bosch, R. C. E., Westfall, K. B., Wilkinson, D., Wright, S., Xiao, T., and Zhang, K. (2015). Overview of the SDSS-IV MaNGA Survey: Mapping nearby Galaxies at Apache Point Observatory. ApJ, 798(1):7.

Calderone, G., Nicastro, L., Ghisellini, G., Dotti, M., Sbarrato, T., Shankar, F., and Colpi, M. (2017). QSFIT: automatic analysis of optical AGN spectra. MNRAS, 472(4):4051–4080.

Calzetti, D., Armus, L., Bohlin, R. C., Kinney, A. L., Koornneef, J., and Storchi-Bergmann, T. (2000). The Dust Content and Opacity of Actively Star-forming Galaxies. ApJ, 533(2):682–695.

Canalizo, G. and Stockton, A. (2001). Quasi-Stellar Objects, Ultraluminous Infrared Galaxies, and Mergers. ApJ, 555(2):719–743.

Cano-Díaz, M., Maiolino, R., Marconi, A., Netzer, H., Shemmer, O., and Cresci, G. (2012). Observational evidence of quasar feedback quenching star formation at high redshift. A&A, 537:L8.

Cappellari, M. (2017). Improving the full spectrum fitting method: accurate convolution with Gauss-Hermite functions. MNRAS, 466(1):798–811.

Cappellari, M. and Copin, Y. (2003). Adaptive spatial binning of integral-field spectroscopic data using Voronoi tessellations. MNRAS, 342(2):345–354.

Cappellari, M. and Emsellem, E. (2004). Parametric Recovery of Line-of-Sight Velocity Distributions from Absorption-Line Spectra of Galaxies via Penalized Likelihood. PASP, 116(816):138–147.

Cappi, M., Tombesi, F., Bianchi, S., Dadina, M., Giustini, M., Malaguti, G., Maraschi, L., Palumbo, G. G. C., Petrucci, P. O., Ponti, G., Vignali, C., and Yaqoob, T. (2009). X-ray evidence for a mildly relativistic and variable outflow in the luminous Seyfert 1 galaxy Mrk 509. A&A, 504(2):401–407.

Carilli, C. L. and Walter, F. (2013). Cool Gas in High-Redshift Galaxies. ARA&A, 51(1):105–161.

Carniani, S., Marconi, A., Maiolino, R., Balmaverde, B., Brusa, M., Cano-Díaz, M., Cicone, C., Comastri, A., Cresci, G., Fiore, F., Feruglio, C., La Franca, F., Mainieri, V., Mannucci, F., Nagao, T., Netzer, H., Piconcelli, E., Risaliti, G., Schneider, R., and Shemmer, O. (2015). Ionised outflows in z ~2.4 quasar host galaxies. A&A, 580:A102.

Carniani, S., Marconi, A., Maiolino, R., Balmaverde, B., Brusa, M., Cano-Díaz, M., Cicone, C., Comastri, A., Cresci, G., Fiore, F., Feruglio, C., La Franca, F., Mainieri, V., Mannucci, F., Nagao, T., Netzer, H., Piconcelli, E., Risaliti, G., Schneider, R., and Shemmer, O. (2016). Fast outflows and star formation quenching in quasar host galaxies. A&A, 591:A28.

Carniani, S., Venturi, G., Parlanti, E., de Graaff, A., Maiolino, R., Arribas, S., Bonaventura, N., Boyett, K., Bunker, A. J., Cameron, A. J., Charlot, S., Chevallard, J., Curti, M., Curtis-Lake, E., Eisenstein, D. J., Giardino, G., Hausen, R., Kumari, N., Maseda, M. V., Nelson, E., Perna, M., Rix, H.-W., Robertson, B., Rodríguez Del Pino, B., Sandles, L., Scholtz, J., Simmonds, C., Smit, R., Tacchella, S., Übler, H., Williams, C. C., Willott, C., and Witstok, J. (2023). JADES: The incidence rate and properties of galactic outflows in low-mass galaxies across $3 < z < 9$. *arXiv e-prints*, page arXiv:2306.11801.

Cazzoli, S., Arribas, S., Maiolino, R., and Colina, L. (2016). Neutral gas outflows in nearby [U]LIRGs via optical NaD feature. A&A, 590:A125.

Chartas, G., Brandt, W. N., and Gallagher, S. C. (2003). XMM-Newton Reveals the Quasar Outflow in PG 1115+080. ApJ, 595(1):85–93.

Chartas, G., Cappi, M., Hamann, F., Eracleous, M., Strickland, S., Giustini, M., and Misawa, T. (2016). The Wide-angle Outflow of the Lensed $z = 1.51$ AGN HS 0810+2554. ApJ, 824(1):53.

Chartas, G., Cappi, M., Vignali, C., Dadina, M., James, V., Lanzuisi, G., Giustini, M., Gaspari, M., Strickland, S., and Bertola, E. (2021). Multiphase Powerful Outflows Detected in High-z Quasars. ApJ, 920(1):24.

Chartas, G., Charlton, J., Eracleous, M., Giustini, M., Hidalgo, P. R., Ganguly, R., Hamann, F., Misawa, T., and Tytler, D. (2009a). High velocity outflows in narrow absorption line quasars. New A Rev., 53(7-10):128–132.

Chartas, G., Davidson, E., Brusa, M., Vignali, C., Cappi, M., Dadina, M., Cresci, G., Paladino, R., Lanzuisi, G., and Comastri, A. (2020). Linking the small-scale relativistic winds and the large-scale molecular outflows in the $z = 1.51$ lensed quasar HS 0810+2554. MNRAS, 496(1):598–611.

Chartas, G., Eracleous, M., Dai, X., Agol, E., and Gallagher, S. (2007). Discovery of Probable Relativistic Fe Emission and Absorption in the Cloverleaf Quasar H 1413+117. ApJ, 661(2):678–692.

Chartas, G., Hamann, F., Eracleous, M., Misawa, T., Cappi, M., Giustini, M., Charlton, J. C., and Marvin, M. (2014). Magnified Views of the Ultrafast Outflow of the $z = 1.51$ Active Galactic Nucleus HS 0810+2554. ApJ, 783(1):57.

Chartas, G., Saez, C., Brandt, W. N., Giustini, M., and Garmire, G. P. (2009b). Confirmation of and Variable Energy Injection by a Near-Relativistic Outflow in APM 08279+5255. ApJ, 706(1):644–656.

Cherinka, B., Andrews, B. H., Sánchez-Gallego, J., Brownstein, J., Argudo-Fernández, M., Blanton, M., Bundy, K., Jones, A., Masters, K., Law, D. R., Rowlands, K., Weijmans, A.-M., Westfall, K., and Yan, R. (2019). Marvin: A Tool Kit for Streamlined Access and Visualization of the SDSS-IV MaNGA Data Set. AJ, 158(2):74.

Cicone, C., Brusa, M., Ramos Almeida, C., Cresci, G., Husemann, B., and Mainieri, V. (2018). The largely unconstrained multiphase nature of outflows in AGN host galaxies. *Nature Astronomy*, 2:176–178.

Cicone, C., Feruglio, C., Maiolino, R., Fiore, F., Piconcelli, E., Menci, N., Aussel, H., and Sturm, E. (2012). The physics and the structure of the quasar-driven outflow in Mrk 231. A&A, 543:A99.

Cicone, C., Maiolino, R., Aalto, S., Muller, S., and Feruglio, C. (2020). Enhanced UV radiation and dense clumps in the molecular outflow of Mrk 231. A&A, 633:A163.

Cicone, C., Maiolino, R., Gallerani, S., Neri, R., Ferrara, A., Sturm, E., Fiore, F., Piconcelli, E., and Feruglio, C. (2015). Very extended cold gas, star formation and outflows in the halo of a bright quasar at $z > 6$. A&A, 574:A14.

Cicone, C., Maiolino, R., Sturm, E., Graciá-Carpio, J., Feruglio, C., Neri, R., Aalto, S., Davies, R., Fiore, F., Fischer, J., García-Burillo, S., González-Alfonso, E., Hailey-Dunsheath, S., Piconcelli, E., and Veilleux, S. (2014). Massive molecular outflows and evidence for AGN feedback from CO observations. A&A, 562:A21.

Cid Fernandes, R., Stasińska, G., Mateus, A., and Vale Asari, N. (2011). A comprehensive classification of galaxies in the Sloan Digital Sky Survey: how to tell true from fake AGN? MNRAS, 413(3):1687–1699.

Ciotti, L., Ostriker, J. P., and Proga, D. (2010). Feedback from Central Black Holes in Elliptical Galaxies. III. Models with Both Radiative and Mechanical Feedback. ApJ, 717(2):708–723.

Circosta, C., Mainieri, V., Lamperti, I., Padovani, P., Bischetti, M., Harrison, C. M., Kakkad, D., Zanella, A., Vietri, G., Lanzuisi, G., Salvato, M., Brusa, M., Carniani, S., Cicone, C., Cresci, G., Feruglio, C., Husemann, B., Mannucci, F., Marconi, A., Perna, M., Piconcelli, E., Puglisi, A., Saintonge, A., Schramm, M., Vignali, C., and Zappacosta, L. (2021). SUPER. IV. CO($J = 3$-2) properties of active galactic nucleus hosts at cosmic noon revealed by ALMA. A&A, 646:A96.

Circosta, C., Mainieri, V., Padovani, P., Lanzuisi, G., Salvato, M., Harrison, C. M., Kakkad, D., Puglisi, A., Vietri, G., Zamorani, G., Cicone, C., Husemann, B., Vignali, C., Balmaverde, B., Bischetti, M., Bongiorno, A., Brusa, M., Carniani, S., Civano, F., Comastri, A., Cresci, G., Feruglio, C., Fiore, F., Fotopoulou, S., Karim, A., Lamastra, A., Magnelli, B., Mannucci, F., Marconi, A., Merloni, A., Netzer, H., Perna, M., Piconcelli, E., Rodighiero, G., Schinnerer, E., Schramm, M., Schulze, A., Silverman, J., and Zappacosta, L. (2018). SUPER. I. Toward an unbiased study of ionized outflows in $z \sim 2$ active galactic nuclei: survey overview and sample characterization. A&A, 620:A82.

Civano, F., Marchesi, S., Comastri, A., Urry, M. C., Elvis, M., Cappelluti, N., Puccetti, S., Brusa, M., Zamorani, G., Hasinger, G., Aldcroft, T., Alexander, D. M., Allevato, V., Brunner, H., Capak, P., Finoguenov, A., Fiore, F., Fruscione, A., Gilli, R., Glotfelty, K., Griffiths, R. E., Hao, H., Harrison, F. A., Jahnke, K., Kartaltepe, J., Karim, A., LaMassa, S. M., Lanzuisi, G., Miyaji, T., Ranalli, P., Salvato, M., Sargent, M., Scoville, N. J., Schawinski, K., Schinnerer, E., Silverman, J., Smolcic, V., Stern, D., Toft, S., Trakhtenbrot, B., Treister, E., and Vignali, C. (2016). The Chandra Cosmos Legacy Survey: Overview and Point Source Catalog. ApJ, 819(1):62.

Coatman, L., Hewett, P. C., Banerji, M., Richards, G. T., Hennawi, J. F., and Prochaska, J. X. (2017). Correcting C IV-based virial black hole masses. MNRAS, 465(2):2120–2142.

Cohen, R. D., Rudy, R. J., Puetter, R. C., Ake, T. B., and Foltz, C. B. (1986). Variability of Markarian 1018: Seyfert 1.9 to Seyfert 1. ApJ, 311:135.

Colina, L., Piqueras López, J., Arribas, S., Riffel, R., Riffel, R. A., Rodriguez-Ardila, A., Pastoriza, M., Storchi-Bergmann, T., Alonso-Herrero, A., and Sales, D. (2015). Understanding the two-dimensional ionization structure in luminous infrared galaxies. A near-IR integral field spectroscopy perspective. A&A, 578:A48.

Comerford, J. M., Gerke, B. F., Stern, D., Cooper, M. C., Weiner, B. J., Newman, J. A., Madsen, K., and Barrows, R. S. (2012). Kiloparsec-scale Spatial Offsets in Double-peaked Narrow-line Active Galactic Nuclei. I. Markers for Selection of Compelling Dual Active Galactic Nucleus Candidates. ApJ, 753(1):42.

Comerford, J. M. and Greene, J. E. (2014). Offset Active Galactic Nuclei as Tracers of Galaxy Mergers and Supermassive Black Hole Growth. ApJ, 789(2):112.

Comerford, J. M., Negus, J., Müller-Sánchez, F., Eracleous, M., Wylezalek, D., Storchi-Bergmann, T., Greene, J. E., Barrows, R. S., Nevin, R., Roy, N., and Stemo, A. (2020). A Catalog of 406 AGNs in MaNGA: A Connection between Radio-mode AGNs and Star Formation Quenching. ApJ, 901(2):159.

Concas, A., Popesso, P., Brusa, M., Mainieri, V., and Thomas, D. (2019). Two-face(s): ionized and neutral gas winds in the local Universe. A&A, 622:A188.

Condon, J. J., Cotton, W. D., Greisen, E. W., Yin, Q. F., Perley, R. A., Taylor, G. B., and Broderick, J. J. (1998). The NRAO VLA Sky Survey. AJ, 115(5):1693–1716.

Costa, T., Rosdahl, J., Sijacki, D., and Haehnelt, M. G. (2018). Quenching star formation with quasar outflows launched by trapped IR radiation. MNRAS, 479(2):2079–2111.

Crenshaw, D. M., Fischer, T. C., Kraemer, S. B., and Schmitt, H. R. (2015). Feedback from Mass Outflows in Nearby Active Galactic Nuclei. II. Outflows in the Narrow-line Region of NGC 4151. ApJ, 799(1):83.

Crenshaw, D. M., Kraemer, S. B., and George, I. M. (2003). Mass Loss from the Nuclei of Active Galaxies. ARA&A, 41:117–167.

Cresci, G., Hicks, E. K. S., Genzel, R., Förster Schreiber, N. M., Davies, R., Bouché, N., Buschkamp, P., Genel, S., Shapiro, K., Tacconi, L., Sommer-Larsen, J., Burkert, A., Eisenhauer, F., Gerhard, O., Lutz, D., Naab, T., Sternberg, A., Cimatti, A., Daddi, E., Erb, D. K., Kurk, J., Lilly, S. L., Renzini, A., Shapley, A., Steidel, C. C., and Caputi, K. (2009). The SINS Survey: Modeling the Dynamics of z ~2 Galaxies and the High-z Tully-Fisher Relation. ApJ, 697(1):115–132.

Cresci, G., Mainieri, V., Brusa, M., Marconi, A., Perna, M., Mannucci, F., Piconcelli, E., Maiolino, R., Feruglio, C., Fiore, F., Bongiorno, A., Lanzuisi, G., Merloni, A., Schramm, M., Silverman, J. D., and Civano, F. (2015a). Blowin' in the Wind: Both "Negative" and "Positive" Feedback in an Obscured High-z Quasar. ApJ, 799(1):82.

Cresci, G. and Maiolino, R. (2018). Observing positive and negative AGN feedback. *Nature Astronomy*, 2:179–180.

Cresci, G., Mannucci, F., Maiolino, R., Marconi, A., Gnerucci, A., and Magrini, L. (2010). Gas accretion as the origin of chemical abundance gradients in distant galaxies. Nature, 467(7317):811–813.

Cresci, G., Marconi, A., Zibetti, S., Risaliti, G., Carniani, S., Mannucci, F., Gallazzi, A., Maiolino, R., Balmaverde, B., Brusa, M., Capetti, A., Cicone, C., Feruglio, C., Bland-Hawthorn, J., Nagao, T., Oliva, E., Salvato, M., Sani, E., Tozzi, P., Urrutia, T., and Venturi, G. (2015b). The MAGNUM survey: positive feedback in the nuclear region of NGC 5643 suggested by MUSE. A&A, 582:A63.

Cresci, G., Tozzi, G., Perna, M., Brusa, M., Marconcini, C., Marconi, A., Carniani, S., Brienza, M., Giroletti, M., Belfiore, F., Ginolfi, M., Mannucci, F., Ulivi, L., Scholtz, J., Venturi, G., Arribas, S., Übler, H., D'Eugenio, F., Mingozzi, M., Balmaverde, B., Capetti, A., Parlanti, E., and Zana, T. (2023). Bubbles and outflows: The novel JWST/NIRSpec view of the z = 1.59 obscured quasar XID2028. A&A, 672:A128.

Croton, D. J., Springel, V., White, S. D. M., De Lucia, G., Frenk, C. S., Gao, L., Jenkins, A., Kauffmann, G., Navarro, J. F., and Yoshida, N. (2006). The many lives of active galactic nuclei: cooling flows, black holes and the luminosities and colours of galaxies. MNRAS, 365(1):11–28.

da Silva, P., Steiner, J. E., and Menezes, R. B. (2017). NGC 1566: analysis of the nuclear region from optical and near-infrared Integral Field Unit spectroscopy. MNRAS, 470(4):3850–3876.

Daddi, E., Alexander, D. M., Dickinson, M., Gilli, R., Renzini, A., Elbaz, D., Cimatti, A., Chary, R., Frayer, D., Bauer, F. E., Brandt, W. N., Giavalisco, M., Grogin, N. A., Huynh, M., Kurk, J., Mignoli, M., Morrison, G., Pope, A., and Ravindranath, S. (2007). Multiwavelength Study of Massive Galaxies at z~2. II. Widespread Compton-thick Active Galactic Nuclei and the Concurrent Growth of Black Holes and Bulges. ApJ, 670(1):173–189.

Dadina, M., Guainazzi, M., Cappi, M., Bianchi, S., Vignali, C., Malaguti, G., and Comastri, A. (2010). X-ray imaging of the ionisation cones in NGC 5252. A&A, 516:A9.

Dadina, M., Vignali, C., Cappi, M., Lanzuisi, G., Ponti, G., Torresi, E., De Marco, B., Chartas, G., and Giustini, M. (2018). Yet another UFO in the X-ray spectrum of a high-z lensed QSO. A&A, 610:L13.

Dasyra, K. M. and Combes, F. (2011). Turbulent and fast motions of H_2 gas in active galactic nuclei. A&A, 533:L10.

Dasyra, K. M. and Combes, F. (2012). Cold and warm molecular gas in the outflow of 4C 12.50. A&A, 541:L7.

Dasyra, K. M., Combes, F., Oosterloo, T., Oonk, J. B. R., Morganti, R., Salomé, P., and Vlahakis, N. (2016). ALMA reveals optically thin, highly excited CO gas in the jet-driven winds of the galaxy IC 5063. A&A, 595:L7.

Davé, R., Anglés-Alcázar, D., Narayanan, D., Li, Q., Rafieferantsoa, M. H., and Appleby, S. (2019). SIMBA: Cosmological simulations with black hole growth and feedback. MNRAS, 486(2):2827–2849.

Davies, R., Baron, D., Shimizu, T., Netzer, H., Burtscher, L., de Zeeuw, P. T., Genzel, R., Hicks, E. K. S., Koss, M., Lin, M. Y., Lutz, D., Maciejewski, W., Müller-Sánchez, F., Orban de Xivry, G., Ricci, C., Riffel, R., Riffel, R. A., Rosario, D., Schartmann, M., Schnorr-Müller, A., Shangguan, J., Sternberg, A., Sturm, E., Storchi-Bergmann, T., Tacconi, L., and Veilleux, S. (2020). Ionized outflows in local luminous AGN: what are the real densities and outflow rates? MNRAS, 498(3):4150–4177.

Davies, R. I. (2007). A method to remove residual OH emission from near-infrared spectra. MNRAS, 375(3):1099–1105.

Davies, R. I., Maciejewski, W., Hicks, E. K. S., Emsellem, E., Erwin, P., Burtscher, L., Dumas, G., Lin, M., Malkan, M. A., Müller-Sánchez, F., Orban de Xivry, G., Rosario, D. J., Schnorr-Müller, A., and Tran, A. (2014). Fueling Active Galactic Nuclei. II. Spatially Resolved Molecular Inflows and Outflows. ApJ, 792(2):101.

Davies, R. L., Schirmer, M., and Turner, J. E. H. (2015). The 'Green Bean' Galaxy SDSS J224024.1-092748: unravelling the emission signature of a quasar ionization echo. MNRAS, 449(2):1731–1752.

Dekel, A. and Silk, J. (1986). The Origin of Dwarf Galaxies, Cold Dark Matter, and Biased Galaxy Formation. ApJ, 303:39.

Del Moro, A., Alexander, D. M., Mullaney, J. R., Daddi, E., Pannella, M., Bauer, F. E., Pope, A., Dickinson, M., Elbaz, D., Barthel, P. D., Garrett, M. A., Brandt, W. N., Charmandaris, V., Chary, R. R., Dasyra, K., Gilli, R., Hickox, R. C., Hwang, H. S., Ivison, R. J., Juneau, S., Le Floc'h, E., Luo, B., Morrison, G. E., Rovilos, E., Sargent, M. T., and Xue, Y. Q. (2013). GOODS-Herschel: radio-excess signature of hidden AGN activity in distant star-forming galaxies. A&A, 549:A59.

Denney, K. D., De Rosa, G., Croxall, K., Gupta, A., Bentz, M. C., Fausnaugh, M. M., Grier, C. J., Martini, P., Mathur, S., Peterson, B. M., Pogge, R. W., and Shappee, B. J. (2014). The Typecasting of Active Galactic Nuclei: Mrk 590 no Longer Fits the Role. ApJ, 796(2):134.

Di Matteo, T., Springel, V., and Hernquist, L. (2005). Energy input from quasars regulates the growth and activity of black holes and their host galaxies. Nature, 433(7026):604–607.

Díaz, A. I., Castellanos, M., Terlevich, E., and Luisa García-Vargas, M. (2000). Chemical abundances and ionizing clusters of Hii regions in the LINER galaxy NGC 4258. MNRAS, 318(2):462–474.

Dicken, D., Tadhunter, C., Morganti, R., Buchanan, C., Oosterloo, T., and Axon, D. (2008). The Origin of the Infrared Emission in Radio Galaxies. I. New Mid- to Far-Infrared and Radio Observations of the 2 Jy Sample. ApJ, 678(2):712–728.

DiPompeo, M. A., Hickox, R. C., Carroll, C. M., Runnoe, J. C., Mullaney, J. R., and Fischer, T. C. (2018). The [O III] Profiles of Infrared-selected Active Galactic Nuclei: More Powerful Outflows in the Obscured Population. ApJ, 856(1):76.

Donley, J. L., Koekemoer, A. M., Brusa, M., Capak, P., Cardamone, C. N., Civano, F., Ilbert, O., Impey, C. D., Kartaltepe, J. S., Miyaji, T., Salvato, M., Sanders, D. B., Trump, J. R., and Zamorani, G. (2012). Identifying Luminous Active Galactic Nuclei in Deep Surveys: Revised IRAC Selection Criteria. ApJ, 748(2):142.

Donley, J. L., Rieke, G. H., Pérez-González, P. G., and Barro, G. (2008). Spitzer's Contribution to the AGN Population. ApJ, 687(1):111–132.

Downes, D. and Solomon, P. M. (1998). Rotating Nuclear Rings and Extreme Starbursts in Ultraluminous Galaxies. ApJ, 507(2):615–654.

Downes, D., Solomon, P. M., and Radford, S. J. E. (1993). Molecular Gas Mass and Far-Infrared Emission from Distant Luminous Galaxies. ApJ, 414:L13.

Draine, B. T. and Woods, D. T. (1990). On the H 2 Line Emission from NGC 6240 and Other Starburst Galaxies. ApJ, 363:464.

Drory, N., MacDonald, N., Bershady, M. A., Bundy, K., Gunn, J., Law, D. R., Smith, M., Stoll, R., Tremonti, C. A., Wake, D. A., Yan, R., Weijmans, A. M., Byler, N., Cherinka, B., Cope, F., Eigenbrot, A., Harding, P., Holder, D., Huehnerhoff, J., Jaehnig, K., Jansen, T. C., Klaene, M., Paat, A. M., Percival, J., and Sayres, C. (2015). The MaNGA Integral Field Unit Fiber Feed System for the Sloan 2.5 m Telescope. AJ, 149(2):77.

Duras, F., Bongiorno, A., Ricci, F., Piconcelli, E., Shankar, F., Lusso, E., Bianchi, S., Fiore, F., Maiolino, R., Marconi, A., Onori, F., Sani, E., Schneider, R., Vignali, C., and La Franca, F. (2020). Universal bolometric corrections for active galactic nuclei over seven luminosity decades. A&A, 636:A73.

Dutton, A. A. and Macciò, A. V. (2014). Cold dark matter haloes in the Planck era: evolution of structural parameters for Einasto and NFW profiles. MNRAS, 441(4):3359–3374.

Eisenhauer, F., Abuter, R., Bickert, K., Biancat-Marchet, F., Bonnet, H., Brynnel, J., Conzelmann, R. D., Delabre, B., Donaldson, R., Farinato, J., Fedrigo, E., Genzel, R., Hubin, N. N., Iserlohe, C., Kasper, M. E., Kissler-Patig, M., Monnet, G. J., Roehrle, C., Schreiber, J., Stroebele, S., Tecza, M., Thatte, N. A., and Weisz, H. (2003). SINFONI - Integral field spectroscopy at 50 milli-arcsecond resolution with the ESO VLT. In Iye, M. and Moorwood, A. F. M., editors, *Instrument Design and Performance for Optical/Infrared Ground-based Telescopes*, volume 4841 of *Society of Photo-Optical Instrumentation Engineers (SPIE) Conference Series*, pages 1548–1561.

Elbaz, D., Dickinson, M., Hwang, H. S., Díaz-Santos, T., Magdis, G., Magnelli, B., Le Borgne, D., Galliano, F., Pannella, M., Chanial, P., Armus, L., Charmandaris, V., Daddi, E., Aussel, H., Popesso, P., Kartaltepe, J., Altieri, B., Valtchanov, I., Coia, D., Dannerbauer, H., Dasyra, K., Leiton, R., Mazzarella, J., Alexander, D. M., Buat, V., Burgarella, D., Chary, R. R., Gilli, R., Ivison, R. J., Juneau, S., Le Floc'h, E., Lutz, D., Morrison, G. E., Mullaney, J. R., Murphy, E., Pope, A., Scott, D., Brodwin, M., Calzetti, D., Cesarsky, C., Charlot, S., Dole, H., Eisenhardt, P., Ferguson, H. C., Förster Schreiber, N., Frayer, D., Giavalisco, M., Huynh, M., Koekemoer, A. M., Papovich, C., Reddy, N., Surace, C., Teplitz, H., Yun, M. S., and Wilson, G. (2011). GOODS-Herschel: an infrared main sequence for star-forming galaxies. A&A, 533:A119.

Elitzur, M., Ho, L. C., and Trump, J. R. (2014). Evolution of broad-line emission from active galactic nuclei. MNRAS, 438(4):3340–3351.

Elvis, M., Maccacaro, T., Wilson, A. S., Ward, M. J., Penston, M. V., Fosbury, R. A. E., and Perola, G. C. (1978). Seyfert galaxies as X-ray sources. MNRAS, 183:129–157.

Elvis, M., Risaliti, G., Nicastro, F., Miller, J. M., Fiore, F., and Puccetti, S. (2004). An Unveiling Event in the Type 2 Active Galactic Nucleus NGC 4388:A Challenge for a Parsec-Scale Absorber. ApJ, 615(1):L25–L28.

Elvis, M., Schreier, E. J., Tonry, J., Davis, M., and Huchra, J. P. (1981). Two optically dull galaxies with strong nuclear X-ray sources. ApJ, 246:20–27.

Elvis, M., Wilkes, B. J., McDowell, J. C., Green, R. F., Bechtold, J., Willner, S. P., Oey, M. S., Polomski, E., and Cutri, R. (1994). Atlas of Quasar Energy Distributions. ApJS, 95:1.

Emonts, B. H. C., Colina, L., Piqueras-López, J., Garcia-Burillo, S., Pereira-Santaella, M., Arribas, S., Labiano, A., and Alonso-Herrero, A. (2017). Outflows of hot molecular gas in ultra-luminous infrared galaxies mapped with VLT-SINFONI. A&A, 607:A116.

Engel, H., Davies, R. I., Genzel, R., Tacconi, L. J., Hicks, E. K. S., Sturm, E., Naab, T., Johansson, P. H., Karl, S. J., Max, C. E., Medling, A., and van der Werf, P. P. (2010). NGC 6240: merger-induced star formation and gas dynamics. A&A, 524:A56.

Eracleous, M. and Halpern, J. P. (2001). NGC 3065: A Certified LINER with Broad, Variable Balmer Lines. ApJ, 554(1):240–244.

Fabbiano, G., Paggi, A., Karovska, M., Elvis, M., Nardini, E., and Wang, J. (2020). Revisiting the Complex Nuclear Region of NGC 6240 with Chandra. ApJ, 902(1):49.

Faber, S. M. and Jackson, R. E. (1976). Velocity dispersions and mass-to-light ratios for elliptical galaxies. ApJ, 204:668–683.

Fabian, A. C. (1999). The obscured growth of massive black holes. MNRAS, 308(4):L39–L43.

Fabian, A. C. (2012). Observational Evidence of Active Galactic Nuclei Feedback. ARA&A, 50:455–489.

Fabian, A. C., Vasudevan, R. V., and Gandhi, P. (2008). The effect of radiation pressure on dusty absorbing gas around active galactic nuclei. MNRAS, 385(1):L43–L47.

Faucher-Giguère, C.-A. and Quataert, E. (2012). The physics of galactic winds driven by active galactic nuclei. MNRAS, 425(1):605–622.

Fawcett, V. A., Alexander, D. M., Brodzeller, A., Edge, A. C., Rosario, D. J., Myers, A. D., Aguilar, J., Ahlen, S., Alfarsy, R., Brooks, D., Canning, R., Circosta, C., Dawson, K., de la Macorra, A., Doel, P., Fanning, K., Font-Ribera, A., Forero-Romero, J. E., Gontcho, S. G. A., Guy, J., Harrison, C. M., Honscheid, K., Juneau, S., Kehoe, R., Kisner, T., Kremin, A., Landriau, M., Manera, M., Meisner, A. M., Miquel, R., Moustakas, J., Nie, J., Percival, W. J., Poppett, C., Pucha, R., Rossi, G., Schlegel, D., Siudek, M., Tarlé, G., Weaver, B. A., Zhou, Z., and Zou, H. (2023). A striking relationship between dust extinction and radio detection in DESI QSOs: evidence for a dusty blow-out phase in red QSOs. MNRAS.

Feltre, A., Charlot, S., and Gutkin, J. (2016). Nuclear activity versus star formation: emission-line diagnostics at ultraviolet and optical wavelengths. MNRAS, 456(3):3354–3374.

Feltre, A., Gruppioni, C., Marchetti, L., Mahoro, A., Salvestrini, F., Mignoli, M., Bisigello, L., Calura, F., Charlot, S., Chevallard, J., Romero-Colmenero, E., Curtis-Lake, E., Delvecchio, I., Dors, O. L., Hirschmann, M., Jarrett, T., Marchesi, S., Moloko, M. E., Plat, A., Pozzi, F., Sefako, R., Traina, A., Vaccari, M., Väisänen, P., Vallini, L., Vidal-García, A., and Vignali, C. (2023). Optical and mid-infrared line emission in nearby Seyfert galaxies. A&A, 675:A74.

Ferland, G. J., Hu, C., Wang, J.-M., Baldwin, J. A., Porter, R. L., van Hoof, P. A. M., and Williams, R. J. R. (2009). Implications of Infalling Fe II-Emitting Clouds in Active Galactic Nuclei: Anisotropic Properties. ApJ, 707(1):L82–L86.

Fernández-Ontiveros, J. A., Armus, L., Baes, M., Bernard-Salas, J., Bolatto, A. D., Braine, J., Ciesla, L., De Looze, I., Egami, E., Fischer, J., Giard, M., González-Alfonso, E., Granato, G. L., Gruppioni, C., Imanishi, M., Ishihara, D., Kaneda, H., Madden, S., Malkan, M., Matsuhara, H., Matsuura, M., Nagao, T., Najarro, F., Nakagawa, T., Onaka, T., Oyabu, S., Pereira-Santaella, M., Pérez Fournon, I., Roelfsema, P., Santini, P., Silva, L., Smith, J. D. T., Spinoglio, L., van der Tak, F., Wada, T., and Wu, R. (2017). SPICA and the Chemical Evolution of Galaxies: The Rise of Metals and Dust. PASA, 34:e053.

Fernández-Ontiveros, J. A., Spinoglio, L., Pereira-Santaella, M., Malkan, M. A., Andreani, P., and Dasyra, K. M. (2016). Far-infrared Line Spectra of Active Galaxies from the Herschel/PACS Spectrometer: The Complete Database. ApJS, 226(2):19.

Ferrarese, L. and Ford, H. (2005). Supermassive Black Holes in Galactic Nuclei: Past, Present and Future Research. Space Sci. Rev., 116(3-4):523–624.

Ferrarese, L. and Merritt, D. (2000). A Fundamental Relation between Supermassive Black Holes and Their Host Galaxies. ApJ, 539(1):L9–L12.

Feruglio, C., Ferrara, A., Bischetti, M., Downes, D., Neri, R., Ceccarelli, C., Cicone, C., Fiore, F., Gallerani, S., Maiolino, R., Menci, N., Piconcelli, E., Vietri, G., Vignali, C., and Zappacosta, L. (2017). On the discovery of fast molecular gas in the UFO/BAL quasar APM 08279+5255 at z = 3.912. A&A, 608:A30.

Feruglio, C., Fiore, F., Carniani, S., Piconcelli, E., Zappacosta, L., Bongiorno, A., Cicone, C., Maiolino, R., Marconi, A., Menci, N., Puccetti, S., and Veilleux, S. (2015). The multi-phase winds of Markarian 231: from the hot, nuclear, ultra-fast wind to the galaxy-scale, molecular outflow. A&A, 583:A99.

Feruglio, C., Fiore, F., Piconcelli, E., Cicone, C., Maiolino, R., Davies, R., and Sturm, E. (2013). High resolution mapping of CO(1-0) in NGC 6240. A&A, 558:A87.

Feruglio, C., Maiolino, R., Piconcelli, E., Menci, N., Aussel, H., Lamastra, A., and Fiore, F. (2010). Quasar feedback revealed by giant molecular outflows. A&A, 518:L155.

Fiore, F., Feruglio, C., Shankar, F., Bischetti, M., Bongiorno, A., Brusa, M., Carniani, S., Cicone, C., Duras, F., Lamastra, A., Mainieri, V., Marconi, A., Menci, N., Maiolino, R., Piconcelli, E., Vietri, G., and Zappacosta, L. (2017). AGN wind scaling relations and the co-evolution of black holes and galaxies. A&A, 601:A143.

Fischer, J., Sturm, E., González-Alfonso, E., Graciá-Carpio, J., Hailey-Dunsheath, S., Poglitsch, A., Contursi, A., Lutz, D., Genzel, R., Sternberg, A., Verma, A., and Tacconi, L. (2010). Herschel-PACS spectroscopic diagnostics of local ULIRGs: Conditions and kinematics in Markarian 231. A&A, 518:L41.

Fischer, T. C., Crenshaw, D. M., Kraemer, S. B., and Schmitt, H. R. (2013). Determining Inclinations of Active Galactic Nuclei via their Narrow-line Region Kinematics. I. Observational Results. ApJS, 209(1):1.

Fischer, T. C., Kraemer, S. B., Schmitt, H. R., Longo Micchi, L. F., Crenshaw, D. M., Revalski, M., Vestergaard, M., Elvis, M., Gaskell, C. M., Hamann, F., Ho, L. C., Hutchings, J., Mushotzky, R., Netzer, H., Storchi-Bergmann, T., Straughn, A., Turner, T. J., and Ward, M. J. (2018). Hubble Space Telescope Observations of Extended [O III]λ 5007 Emission in Nearby QSO2s: New Constraints on AGN Host Galaxy Interaction. ApJ, 856(2):102.

Fischer, T. C., Machuca, C., Diniz, M. R., Crenshaw, D. M., Kraemer, S. B., Riffel, R. A., Schmitt, H. R., Baron, F., Storchi-Bergmann, T., Straughn, A. N., Revalski, M., and Pope, C. L. (2017). Gemini Near Infrared Field Spectrograph Observations of the Seyfert 2 Galaxy Mrk 573: In Situ Acceleration of Ionized and Molecular Gas off Fueling Flows. ApJ, 834(1):30.

Fluetsch, A., Maiolino, R., Carniani, S., Arribas, S., Belfiore, F., Bellocchi, E., Cazzoli, S., Cicone, C., Cresci, G., Fabian, A. C., Gallagher, R., Ishibashi, W., Mannucci, F., Marconi, A., Perna, M., Sturm, E., and Venturi, G. (2021). Properties of the multiphase outflows in local (ultra)luminous infrared galaxies. MNRAS, 505(4):5753–5783.

Fluetsch, A., Maiolino, R., Carniani, S., Marconi, A., Cicone, C., Bourne, M. A., Costa, T., Fabian, A. C., Ishibashi, W., and Venturi, G. (2019). Cold molecular outflows in the local Universe and their feedback effect on galaxies. MNRAS, 483(4):4586–4614.

Förster Schreiber, N. M., Genzel, R., Newman, S. F., Kurk, J. D., Lutz, D., Tacconi, L. J., Wuyts, S., Bandara, K., Burkert, A., Buschkamp, P., Carollo, C. M., Cresci, G., Daddi, E., Davies, R., Eisenhauer, F., Hicks, E. K. S., Lang, P., Lilly, S. J., Mainieri, V., Mancini, C., Naab, T., Peng, Y., Renzini, A., Rosario, D., Shapiro Griffin, K., Shapley, A. E., Sternberg, A., Tacchella, S., Vergani, D., Wisnioski, E., Wuyts, E., and Zamorani, G. (2014). The Sins/zC-Sinf Survey of z $\sim$2 Galaxy Kinematics: Evidence for Powerful Active Galactic Nucleus-Driven Nuclear Outflows in Massive Star-Forming Galaxies. ApJ, 787(1):38.

Förster Schreiber, N. M., Übler, H., Davies, R. L., Genzel, R., Wisnioski, E., Belli, S., Shimizu, T., Lutz, D., Fossati, M., Herrera-Camus, R., Mendel, J. T., Tacconi, L. J., Wilman, D., Beifiori, A., Brammer, G. B., Burkert, A., Carollo, C. M., Davies, R. I., Eisenhauer, F., Fabricius, M., Lilly, S. J., Momcheva, I., Naab, T., Nelson, E. J., Price, S. H., Renzini, A., Saglia, R., Sternberg, A., van Dokkum, P., and Wuyts, S. (2019). The KMOS^{3D} Survey: Demographics and Properties of Galactic Outflows at z = 0.6-2.7. ApJ, 875(1):21.

Fosbury, R. A. E. and Wall, J. V. (1979). The unusual radio galaxy NGC 6240. MNRAS, 189:79–88.

Fruchter, A. S. and Hook, R. N. (2019). *Drizzle: A Method for the Linear Reconstruction of Undersampled Images.* PASP.

Fu, H. and Stockton, A. (2009). Extended Emission-Line Regions: Remnants of Quasar Superwinds? ApJ, 690(1):953–973.

Fyhrie, A., Glenn, J., Rangwala, N., Wheeler, J., Beck, S., and Bally, J. (2021). Molecular Gas in the Nuclear Region of NGC 6240. ApJ, 922(2):208.

Gagne, J. P., Crenshaw, D. M., Kraemer, S. B., Schmitt, H. R., Keel, W. C., Rafter, S., Fischer, T. C., Bennert, V. N., and Schawinski, K. (2014). Spatially Resolved Spectra of the "Teacup" Active Galactic Nucleus: Tracing the History of a Dying Quasar. ApJ, 792(1):72.

Gallagher, R., Maiolino, R., Belfiore, F., Drory, N., Riffel, R., and Riffel, R. A. (2019). Widespread star formation inside galactic outflows. MNRAS, 485(3):3409–3429.

Gallimore, J. F. and Beswick, R. (2004). Parsec-Scale Radio Structure of the Double Active Nucleus of NGC 6240. AJ, 127(1):239–251.

Ganguly, R., Brotherton, M. S., Cales, S., Scoggins, B., Shang, Z., and Vestergaard, M. (2007). Outflows and the Physical Properties of Quasars. ApJ, 665(2):990–1003.

Garnett, D. R., Kennicutt, Robert C., J., Chu, Y.-H., and Skillman, E. D. (1991). He II Emission in Extragalactic H II Regions. ApJ, 373:458.

Gebhardt, K., Bender, R., Bower, G., Dressler, A., Faber, S. M., Filippenko, A. V., Green, R., Grillmair, C., Ho, L. C., Kormendy, J., Lauer, T. R., Magorrian, J., Pinkney, J., Richstone, D., and Tremaine, S. (2000). A Relationship between Nuclear Black Hole Mass and Galaxy Velocity Dispersion. ApJ, 539(1):L13–L16.

Gelbord, J. M., Mullaney, J. R., and Ward, M. J. (2009). AGN with strong forbidden high-ionization lines selected from the Sloan Digital Sky Survey. MNRAS, 397(1):172–189.

Genzel, R. and Cesarsky, C. J. (2000). Extragalactic Results from the Infrared Space Observatory. ARA&A, 38:761–814.

Genzel, R., Lutz, D., Sturm, E., Egami, E., Kunze, D., Moorwood, A. F. M., Rigopoulou, D., Spoon, H. W. W., Sternberg, A., Tacconi-Garman, L. E., Tacconi, L., and Thatte, N. (1998). What Powers Ultraluminous IRAS Galaxies? ApJ, 498(2):579–605.

Genzel, R., Schödel, R., Ott, T., Eckart, A., Alexander, T., Lacombe, F., Rouan, D., and Aschenbach, B. (2003). Near-infrared flares from accreting gas around the supermassive black hole at the Galactic Centre. Nature, 425(6961):934–937.

George, I. M. and Fabian, A. C. (1991). X-ray reflection from cold matter in Active Galactic Nuclei and X-ray binaries. MNRAS, 249:352.

Gerssen, J., van der Marel, R. P., Axon, D., Mihos, J. C., Hernquist, L., and Barnes, J. E. (2004). Hubble Space Telescope Observations of NGC 6240: A Case Study of an Ultraluminous Infrared Galaxy with Obscured Activity. AJ, 127(1):75–89.

Ghez, A. M., Klein, B. L., Morris, M., and Becklin, E. E. (1998). High Proper-Motion Stars in the Vicinity of Sagittarius A*: Evidence for a Supermassive Black Hole at the Center of Our Galaxy. ApJ, 509(2):678–686.

Gillessen, S., Eisenhauer, F., Fritz, T. K., Bartko, H., Dodds-Eden, K., Pfuhl, O., Ott, T., and Genzel, R. (2009). The Orbit of the Star S2 Around SGR A* from Very Large Telescope and Keck Data. ApJ, 707(2):L114–L117.

Gilli, R., Maiolino, R., Marconi, A., Risaliti, G., Dadina, M., Weaver, K. A., and Colbert, E. J. M. (2000). The variability of the Seyfert galaxy NGC 2992: the case for a revived AGN. A&A, 355:485–498.

Gnilka, C. L., Crenshaw, D. M., Fischer, T. C., Revalski, M., Meena, B., Martinez, F., Polack, G. E., Machuca, C., Dashtamirova, D., Kraemer, S. B., Schmitt, H. R., Riffel, R. A., and Storchi-Bergmann, T. (2020). Gemini Near-Infrared Field Spectrograph Observations of the Seyfert 2 Galaxy Mrk 3: Feeding and Feedback on Galactic and Nuclear Scales. ApJ, 893(1):80.

Gofford, J., Reeves, J. N., Tombesi, F., Braito, V., Turner, T. J., Miller, L., and Cappi, M. (2013). The Suzaku view of highly ionized outflows in AGN - I. Statistical detection and global absorber properties. MNRAS, 430(1):60–80.

Gonzaga, S., Hack, W., Fruchter, A., and Mack, J. (2019). *The DrizzlePac Handbook*. Baltimore, STScI.

Goodrich, R. W. (1989). Spectropolarimetry and Variability of Seyfert 1.8 and 1.9 Galaxies. ApJ, 340:190.

Goulding, A. D. and Alexander, D. M. (2009). Towards a complete census of AGN in nearby Galaxies: a large population of optically unidentified AGN. MNRAS, 398(3):1165–1193.

Graham, A. W. (2007). The black hole mass - spheroid luminosity relation. MNRAS, 379(2):711–722.

Graham, A. W. (2008). Fundamental Planes and the Barless M_{BH}-σ Relation for Supermassive Black Holes. ApJ, 680(1):143–153.

Graham, A. W., Onken, C. A., Athanassoula, E., and Combes, F. (2011). An expanded M_{bh}-σ diagram, and a new calibration of active galactic nuclei masses. MNRAS, 412(4):2211–2228.

Graham, A. W. and Scott, N. (2013). The M $_{BH}$-L $_{spheroid}$ Relation at High and Low Masses, the Quadratic Growth of Black Holes, and Intermediate-mass Black Hole Candidates. ApJ, 764(2):151.

Graham, M. J., Ross, N. P., Stern, D., Drake, A. J., McKernan, B., Ford, K. E. S., Djorgovski, S. G., Mahabal, A. A., Glikman, E., Larson, S., and Christensen, E. (2020). Understanding extreme quasar optical variability with CRTS - II. Changing-state quasars. MNRAS, 491(4):4925–4948.

Granato, G. L., De Zotti, G., Silva, L., Bressan, A., and Danese, L. (2004). A Physical Model for the Coevolution of QSOs and Their Spheroidal Hosts. ApJ, 600(2):580–594.

GRAVITY Collaboration, Amorim, A., Bauböck, M., Brandner, W., Clénet, Y., Davies, R., de Zeeuw, P. T., Dexter, J., Eckart, A., Eisenhauer, F., Förster Schreiber, N. M., Gao, F., Garcia, P. J. V., Genzel, R., Gillessen, S., Gratadour, D., Hönig, S., Kishimoto, M., Lacour, S., Lutz, D., Millour, F., Netzer, H., Ott, T., Paumard, T., Perraut, K., Perrin, G., Peterson, B. M., Petrucci, P. O., Pfuhl, O., Prieto, M. A., Rouan, D., Shangguan, J., Shimizu, T., Schartmann, M., Stadler, J., Sternberg, A., Straub, O., Straubmeier, C., Sturm, E., Tacconi, L. J., Tristram, K. R. W., Vermot, P., von Fellenberg, S., Waisberg, I., Widmann, F., and Woillez, J. (2020). The spatially resolved broad line region of IRAS 09149-6206. A&A, 643:A154.

GRAVITY Collaboration, Sturm, E., Dexter, J., Pfuhl, O., Stock, M. R., Davies, R. I., Lutz, D., Clénet, Y., Eckart, A., Eisenhauer, F., Genzel, R., Gratadour, D., Hönig, S. F., Kishimoto, M., Lacour, S., Millour, F., Netzer, H., Perrin, G., Peterson, B. M., Petrucci, P. O., Rouan, D., Waisberg, I., Woillez, J., Amorim, A., Brandner, W., Förster Schreiber, N. M., Garcia, P. J. V., Gillessen, S., Ott, T., Paumard, T., Perraut, K., Scheithauer, S., Straubmeier, C., Tacconi, L. J., and Widmann, F. (2018). Spatially resolved rotation of the broad-line region of a quasar at sub-parsec scale. Nature, 563(7733):657–660.

Greene, J. E. and Ho, L. C. (2005). Estimating Black Hole Masses in Active Galaxies Using the Hα Emission Line. ApJ, 630(1):122–129.

Greene, J. E., Peng, C. Y., Kim, M., Kuo, C.-Y., Braatz, J. A., Impellizzeri, C. M. V., Condon, J. J., Lo, K. Y., Henkel, C., and Reid, M. J. (2010). Precise Black Hole Masses from Megamaser Disks: Black Hole-Bulge Relations at Low Mass. ApJ, 721(1):26–45.

Greene, J. E., Zakamska, N. L., Ho, L. C., and Barth, A. J. (2011). Feedback in Luminous Obscured Quasars. ApJ, 732(1):9.

Gregory, S. A., Tifft, W. G., and Cocke, W. J. (1991). Variability of the Broad Line Spectrum of Markarian 372. AJ, 102:1977.

Guainazzi, M., Matt, G., and Perola, G. C. (2005). X-ray obscuration and obscured AGN in the local universe. A&A, 444(1):119–132.

Guainazzi, M., Nicastro, F., Fiore, F., Matt, G., McHardy, I., Orr, A., Barr, P., Fruscione, A., Papadakis, I., Parmar, A. N., Uttley, P., Perola, G. C., and Piro, L. (1998). A swan song: the disappearance of the nucleus of NGC 4051 and the echo of its past glory. MNRAS, 301(1):L1–L4.

Gültekin, K., Richstone, D. O., Gebhardt, K., Lauer, T. R., Tremaine, S., Aller, M. C., Bender, R., Dressler, A., Faber, S. M., Filippenko, A. V., Green, R., Ho, L. C., Kormendy, J., Magorrian, J., Pinkney, J., and Siopis, C. (2009). The M-σ and M-L Relations in Galactic Bulges, and Determinations of Their Intrinsic Scatter. ApJ, 698(1):198–221.

Gunn, J. E., Siegmund, W. A., Mannery, E. J., Owen, R. E., Hull, C. L., Leger, R. F., Carey, L. N., Knapp, G. R., York, D. G., Boroski, W. N., Kent, S. M., Lupton, R. H., Rockosi, C. M., Evans, M. L., Waddell, P., Anderson, J. E., Annis, J., Barentine, J. C., Bartoszek, L. M., Bastian, S., Bracker, S. B., Brewington, H. J., Briegel, C. I., Brinkmann, J., Brown, Y. J., Carr, M. A., Czarapata, P. C., Drennan, C. C., Dombeck, T., Federwitz, G. R., Gillespie, B. A., Gonzales, C., Hansen, S. U., Harvanek, M., Hayes, J., Jordan, W., Kinney, E., Klaene, M., Kleinman, S. J., Kron, R. G., Kresinski, J., Lee, G., Limmongkol, S., Lindenmeyer,

C. W., Long, D. C., Loomis, C. L., McGehee, P. M., Mantsch, P. M., Neilsen, Eric H., J., Neswold, R. M., Newman, P. R., Nitta, A., Peoples, John, J., Pier, J. R., Prieto, P. S., Prosapio, A., Rivetta, C., Schneider, D. P., Snedden, S., and Wang, S.-i. (2006). The 2.5 m Telescope of the Sloan Digital Sky Survey. AJ, 131(4):2332–2359.

Guolo, M., Ruschel-Dutra, D., Grupe, D., Peterson, B. M., Storchi-Bergmann, T., Schimoia, J., Nemmen, R., and Robinson, A. (2021). The Eddington ratio-dependent 'changing look' events in NGC 2992. MNRAS, 508(1):144–156.

Haehnelt, M. G. and Kauffmann, G. (2000). The correlation between black hole mass and bulge velocity dispersion in hierarchical galaxy formation models. MNRAS, 318(3):L35–L38.

Hainline, K. N., Hickox, R. C., Chen, C.-T., Carroll, C. M., Jones, M. L., Zervos, A. S., and Goulding, A. D. (2016). A Tale of Two Narrow-line Regions: Ionization, Kinematics, and Spectral Energy Distributions for a Local Pair of Merging Obscured Active Galaxies. ApJ, 823(1):42.

Häring, N. and Rix, H.-W. (2004). On the Black Hole Mass-Bulge Mass Relation. ApJ, 604(2):L89–L92.

Harrison, C. M., Alexander, D. M., Mullaney, J. R., Stott, J. P., Swinbank, A. M., Arumugam, V., Bauer, F. E., Bower, R. G., Bunker, A. J., and Sharples, R. M. (2016). The KMOS AGN Survey at High redshift (KASHz): the prevalence and drivers of ionized outflows in the host galaxies of X-ray AGN. MNRAS, 456(2):1195–1220.

Harrison, C. M., Alexander, D. M., Mullaney, J. R., and Swinbank, A. M. (2014). Kiloparsec-scale outflows are prevalent among luminous AGN: outflows and feedback in the context of the overall AGN population. MNRAS, 441(4):3306–3347.

Harrison, C. M., Alexander, D. M., Swinbank, A. M., Smail, I., Alaghband-Zadeh, S., Bauer, F. E., Chapman, S. C., Del Moro, A., Hickox, R. C., Ivison, R. J., Menéndez-Delmestre, K., Mullaney, J. R., and Nesvadba, N. P. H. (2012). Energetic galaxy-wide outflows in high-redshift ultraluminous infrared galaxies hosting AGN activity. MNRAS, 426(2):1073–1096.

Harrison, C. M., Costa, T., Tadhunter, C. N., Flütsch, A., Kakkad, D., Perna, M., and Vietri, G. (2018). AGN outflows and feedback twenty years on. *Nature Astronomy*, 2:198–205.

Hasinger, G., Schartel, N., and Komossa, S. (2002). Discovery of an Ionized Fe K Edge in the z=3.91 Broad Absorption Line Quasar APM 08279+5255 with XMM-Newton. ApJ, 573(2):L77–L80.

Heckman, T. M. and Best, P. N. (2014). The Coevolution of Galaxies and Supermassive Black Holes: Insights from Surveys of the Contemporary Universe. ARA&A, 52:589–660.

Heckman, T. M., Miley, G. K., and Green, R. F. (1984). The kinematics of the narrow-line region in active galaxies and quasars. III. Correlations with the broad-line region and radio emission. ApJ, 281:525–534.

Hinshaw, G., Larson, D., Komatsu, E., Spergel, D. N., Bennett, C. L., Dunkley, J., Nolta, M. R., Halpern, M., Hill, R. S., Odegard, N., Page, L., Smith, K. M., Weiland, J. L., Gold, B., Jarosik, N., Kogut, A., Limon, M., Meyer, S. S., Tucker, G. S., Wollack, E., and Wright, E. L. (2013). Nine-year Wilkinson Microwave Anisotropy Probe (WMAP) Observations: Cosmological Parameter Results. ApJS, 208(2):19.

Ho, L. (1999). Supermassive Black Holes in Galactic Nuclei: Observational Evidence and Astrophysical Consequences. In Chakrabarti, S. K., editor, *Observational Evidence for the Black Holes in the Universe*, volume 234 of *Astrophysics and Space Science Library*, page 157.

Hönig, S. F., Beckert, T., Ohnaka, K., and Weigelt, G. (2006). Radiative transfer modeling of three-dimensional clumpy AGN tori and its application to NGC 1068. A&A, 452(2):459–471.

Hopkins, P. F. and Elvis, M. (2010). Quasar feedback: more bang for your buck. MNRAS, 401(1):7–14.

Hopkins, P. F., Hernquist, L., Cox, T. J., Di Matteo, T., Robertson, B., and Springel, V. (2006). A Unified, Merger-driven Model of the Origin of Starbursts, Quasars, the Cosmic X-Ray Background, Supermassive Black Holes, and Galaxy Spheroids. ApJS, 163(1):1–49.

Hopkins, P. F., Hernquist, L., Cox, T. J., and Kereš, D. (2008). A Cosmological Framework for the Co-Evolution of Quasars, Supermassive Black Holes, and Elliptical Galaxies. I. Galaxy Mergers and Quasar Activity. ApJS, 175(2):356–389.

Hopkins, P. F., Wetzel, A., Kereš, D., Faucher-Giguère, C.-A., Quataert, E., Boylan-Kolchin, M., Murray, N., Hayward, C. C., Garrison-Kimmel, S., Hummels, C., Feldmann, R., Torrey, P., Ma, X., Anglés-Alcázar, D., Su, K.-Y., Orr, M., Schmitz, D., Escala, I., Sanderson, R., Grudić, M. Y., Hafen, Z., Kim, J.-H., Fitts, A., Bullock, J. S., Wheeler, C., Chan, T. K., Elbert, O. D., and Narayanan, D. (2018). FIRE-2 simulations: physics versus numerics in galaxy formation. MNRAS, 480(1):800–863.

Howell, J. H., Armus, L., Mazzarella, J. M., Evans, A. S., Surace, J. A., Sanders, D. B., Petric, A., Appleton, P., Bothun, G., Bridge, C., Chan, B. H. P., Charmandaris, V., Frayer, D. T., Haan, S., Inami, H., Kim, D.-C., Lord, S., Madore, B. F., Melbourne, J., Schulz, B., U, V., Vavilkin, T., Veilleux, S., and Xu, K. (2010). The Great Observatories All-sky LIRG Survey: Comparison of Ultraviolet and Far-infrared Properties. ApJ, 715(1):572–588.

Hsieh, B. C., Lin, L., Lin, J. H., Pan, H. A., Hsu, C. H., Sánchez, S. F., Cano-Díaz, M., Zhang, K., Yan, R., Barrera-Ballesteros, J. K., Boquien, M., Riffel, R., Brownstein, J., Cruz-González, I., Hagen, A., Ibarra, H., Pan, K., Bizyaev, D., Oravetz, D., and Simmons, A. (2017). SDSS-IV MaNGA: Spatially Resolved Star Formation Main Sequence and LI(N)ER Sequence. ApJ, 851(2):L24.

Huang, Y.-K., Hu, C., Zhao, Y.-L., Zhang, Z.-X., Lu, K.-X., Wang, K., Zhang, Y., Du, P., Li, Y.-R., Bai, J.-M., Ho, L. C., Bian, W.-H., Yuan, Y.-F., and Wang, J.-M. (2019). Reverberation Mapping of the Narrow-line Seyfert 1 Galaxy I Zwicky 1: Black Hole Mass. ApJ, 876(2):102.

Husemann, B., Urrutia, T., Tremblay, G. R., Krumpe, M., Dexter, J., Busch, G., Combes, F., Croom, S. M., Davis, T. A., Eckart, A., McElroy, R. E., Perez-Torres, M., Powell, M., and Scharwächter, J. (2016). The Close AGN Reference Survey (CARS). What is causing Mrk 1018's return to the shadows after 30 years? A&A, 593:L9.

Hutsemékers, D., Agís González, B., Marin, F., Sluse, D., Ramos Almeida, C., and Acosta Pulido, J. A. (2019). Polarization of changing-look quasars. A&A, 625:A54.

Ilha, G. d. S., Bianchin, M., and Riffel, R. A. (2016). The origin of the near-IR line emission from molecular, low and high ionization gas in the inner kiloparsec of NGC 6240. Ap&SS, 361(6):178.

Ilić, D., Oknyansky, V., Popović, L. Č., Tsygankov, S. S., Belinski, A. A., Tatarnikov, A. M., Dodin, A. V., Shatsky, N. I., Ikonnikova, N. P., Rakić, N., Kovačević, A., Marčeta-Mandić, S., Burlak, M. A., Mishin, E. O., Metlova, N. V., Potanin, S. A., and Zheltoukhov, S. G. (2020). A flare in the optical spotted in the changing-look Seyfert NGC 3516. A&A, 638:A13.

Inada, N., Oguri, M., Becker, R. H., White, R. L., Gregg, M. D., Schechter, P. L., Kawano, Y., Kochanek, C. S., Richards, G. T., Schneider, D. P., Barentine, J. C., Brewington, H. J., Brinkmann, J., Harvanek, M., Kleinman, S. J., Krzesinski, J., Long, D., Neilsen, Eric H., J., Nitta, A., Snedden, S. A., and York, D. G. (2006). SDSS J0806+2006 and SDSS J1353+1138: Two New Gravitationally Lensed Quasars from the Sloan Digital Sky Survey. AJ, 131(4):1934–1941.

Ishibashi, W. and Fabian, A. C. (2012). Active galactic nucleus feedback and triggering of star formation in galaxies. MNRAS, 427(4):2998–3005.

Ishibashi, W. and Fabian, A. C. (2014). How the central black hole may shape its host galaxy through AGN feedback. MNRAS, 441(2):1474–1478.

Ishibashi, W. and Fabian, A. C. (2015). AGN feedback: galactic-scale outflows driven by radiation pressure on dust. MNRAS, 451(1):93–102.

Ishibashi, W. and Fabian, A. C. (2018). Variations on a theme of AGN-driven outflows: luminosity evolution and ambient density distribution. MNRAS, 481(4):4522–4531.

Ishibashi, W., Fabian, A. C., and Arakawa, N. (2021). AGN-driven galactic outflows: comparing models to observations. MNRAS, 502(3):3638–3645.

Ishibashi, W., Fabian, A. C., and Canning, R. E. A. (2013). Can AGN feedback-driven star formation explain the size evolution of massive galaxies? MNRAS, 431(3):2350–2355.

Iyomoto, N., Makishima, K., Fukazawa, Y., Tashiro, M., and Ishisaki, Y. (1997). Detection of Strong Fe-K Lines from the Spiral Galaxies NGC 1365 and NGC 1386. PASJ, 49:425–434.

Jackson, N., Tagore, A. S., Roberts, C., Sluse, D., Stacey, H., Vives-Arias, H., Wucknitz, O., and Volino, F. (2015). Observations of radio-quiet quasars at 10-mas resolution by use of gravitational lensing. MNRAS, 454(1):287–298.

Jana, A., Kumari, N., Nandi, P., Naik, S., Chatterjee, A., Jaisawal, G. K., Hayasaki, K., and Ricci, C. (2021). Broad-band X-ray observations of the 2018 outburst of the changing-look active galactic nucleus NGC 1566. MNRAS, 507(1):687–703.

Janssen, A. W., Christopher, N., Sturm, E., Veilleux, S., Contursi, A., González-Alfonso, E., Fischer, J., Davies, R., Verma, A., Graciá-Carpio, J., Genzel, R., Lutz, D., Sternberg, A., Tacconi, L., Burtscher, L., and Poglitsch, A. (2016). Broad [C II] Line Wings as Tracer of Molecular and Multi-phase Outflows in Infrared Bright Galaxies. ApJ, 822(1):43.

Joseph, R. D., Wade, R., and Wright, G. S. (1984). Detection of molecular hydrogen in two merging galaxies. Nature, 311(5982):132–133.

Kaastra, J. S., Kriss, G. A., Cappi, M., Mehdipour, M., Petrucci, P. O., Steenbrugge, K. C., Arav, N., Behar, E., Bianchi, S., Boissay, R., Branduardi-Raymont, G., Chamberlain, C., Costantini, E., Ely, J. C., Ebrero, J., Di Gesu, L., Harrison, F. A., Kaspi, S., Malzac, J., De Marco, B., Matt, G., Nandra, K., Paltani, S., Person, R., Peterson, B. M., Pinto, C., Ponti, G., Pozo Nuñez, F., De Rosa, A., Seta, H., Ursini, F., de Vries, C. P., Walton, D. J., and Whewell, M. (2014). A fast and long-lived outflow from the supermassive black hole in NGC 5548. *Science*, 345(6192):64–68.

Kakkad, D., Mainieri, V., Padovani, P., Cresci, G., Husemann, B., Carniani, S., Brusa, M., Lamastra, A., Lanzuisi, G., Piconcelli, E., and Schramm, M. (2016). Tracing outflows in the AGN forbidden region with SINFONI. A&A, 592:A148.

Kakkad, D., Mainieri, V., Vietri, G., Carniani, S., Harrison, C. M., Perna, M., Scholtz, J., Circosta, C., Cresci, G., Husemann, B., Bischetti, M., Feruglio, C., Fiore, F., Marconi, A., Padovani, P., Brusa, M., Cicone, C., Comastri, A., Lanzuisi, G., Mannucci, F., Menci, N., Netzer, H., Piconcelli, E., Puglisi, A., Salvato, M., Schramm, M., Silverman, J., Vignali, C., Zamorani, G., and Zappacosta, L. (2020). SUPER. II. Spatially resolved ionised gas kinematics and scaling relations in $z \sim 2$ AGN host galaxies. A&A, 642:A147.

Kara, E., Mehdipour, M., Kriss, G. A., Cackett, E. M., Arav, N., Barth, A. J., Byun, D., Brotherton, M. S., De Rosa, G., Gelbord, J., Hernández Santisteban, J. V., Hu, C., Kaastra, J., Landt, H., Li, Y.-R., Miller, J. A., Montano, J., Partington, E., Aceituno, J., Bai, J.-M., Bao, D., Bentz, M. C., Brink, T. G., Chelouche, D., Chen, Y.-J., Colmenero, E. R., Dalla Bontà, E., Dehghanian, M., Du, P., Edelson, R., Ferland, G. J., Ferrarese, L., Fian, C., Filippenko, A. V., Fischer, T., Goad, M. R., González Buitrago, D. H., Gorjian, V., Grier, C. J., Guo, W.-J., Hall, P. B., Ho, L. C., Homayouni, Y., Horne, K., Ilić, D., Jiang, B.-W., Joner, M. D., Kaspi, S., Kochanek, C. S., Korista, K. T., Kynoch, D., Li, S.-S., Liu, J.-R., McHardy, I. M., McLane, J. N., Mitchell, J. A. J., Netzer, H., Olson, K. A., Pogge, R. W., Popović, L. Č., Proga, D., Storchi-Bergmann, T., Strasburger, E., Treu, T., Vestergaard, M., Wang, J.-M., Ward, M. J., Waters, T., Williams, P. R., Yang, S., Yao, Z.-H., Zastrocky, T. E., Zhai, S., and Zu, Y. (2021). AGN STORM 2. I. First results: A Change in the Weather of Mrk 817. ApJ, 922(2):151.

Kaspi, S., Smith, P. S., Netzer, H., Maoz, D., Jannuzi, B. T., and Giveon, U. (2000). Reverberation Measurements for 17 Quasars and the Size-Mass-Luminosity Relations in Active Galactic Nuclei. ApJ, 533(2):631–649.

Kauffmann, G. and Haehnelt, M. (2000). A unified model for the evolution of galaxies and quasars. MNRAS, 311(3):576–588.

Kauffmann, G., Heckman, T. M., Tremonti, C., Brinchmann, J., Charlot, S., White, S. D. M., Ridgway, S. E., Brinkmann, J., Fukugita, M., Hall, P. B., Ivezić, Ž., Richards, G. T., and Schneider, D. P. (2003). The host galaxies of active galactic nuclei. MNRAS, 346(4):1055–1077.

Keel, W. C., Chojnowski, S. D., Bennert, V. N., Schawinski, K., Lintott, C. J., Lynn, S., Pancoast, A., Harris, C., Nierenberg, A. M., Sonnenfeld, A., and Proctor, R. (2012). The Galaxy Zoo survey for giant AGN-ionized clouds: past and present black hole accretion events. MNRAS, 420(1):878–900.

Keel, W. C., Maksym, W. P., Bennert, V. N., Lintott, C. J., Chojnowski, S. D., Moiseev, A., Smirnova, A., Schawinski, K., Urry, C. M., Evans, D. A., Pancoast, A., Scott, B., Showley, C., and Flatland, K. (2015). HST Imaging of Fading AGN Candidates. I. Host-galaxy Properties and Origin of the Extended Gas. AJ, 149(5):155.

Kellermann, K. I., Sramek, R., Schmidt, M., Shaffer, D. B., and Green, R. (1989). VLA Observations of Objects in the Palomar Bright Quasar Survey. AJ, 98:1195.

Kennicutt, R. C., J. and Keel, W. C. (1984). Induced nuclear emission-line activity in interacting spiral galaxies. ApJ, 279:L5–L9.

Kennicutt, Robert C., J. (1992). The Integrated Spectra of Nearby Galaxies: General Properties and Emission-Line Spectra. ApJ, 388:310.

Kerr, R. P. (1963). Gravitational Field of a Spinning Mass as an Example of Algebraically Special Metrics. Phys. Rev. Lett., 11(5):237–238.

Kewley, L. J., Dopita, M. A., Sutherland, R. S., Heisler, C. A., and Trevena, J. (2001). Theoretical Modeling of Starburst Galaxies. ApJ, 556(1):121–140.

Kewley, L. J., Groves, B., Kauffmann, G., and Heckman, T. (2006). The host galaxies and classification of active galactic nuclei. MNRAS, 372(3):961–976.

King, A. and Pounds, K. (2015). Powerful Outflows and Feedback from Active Galactic Nuclei. ARA&A, 53:115–154.

King, A. R. (2010). Black hole outflows. MNRAS, 402(3):1516–1522.

Klindt, L., Alexander, D. M., Rosario, D. J., Lusso, E., and Fotopoulou, S. (2019). Fundamental differences in the radio properties of red and blue quasars: evolution strongly favoured over orientation. MNRAS, 488(3):3109–3128.

Kocevski, D. D., Brightman, M., Nandra, K., Koekemoer, A. M., Salvato, M., Aird, J., Bell, E. F., Hsu, L.-T., Kartaltepe, J. S., Koo, D. C., Lotz, J. M., McIntosh, D. H., Mozena, M., Rosario, D., and Trump, J. R. (2015). Are Compton-thick AGNs the Missing Link between Mergers and Black Hole Growth? ApJ, 814(2):104.

Kollatschny, W., Weilbacher, P. M., Ochmann, M. W., Chelouche, D., Monreal-Ibero, A., Bacon, R., and Contini, T. (2020). NGC 6240: A triple nucleus system in the advanced or final state of merging. A&A, 633:A79.

Komossa, S., Burwitz, V., Hasinger, G., Predehl, P., Kaastra, J. S., and Ikebe, Y. (2003). Discovery of a Binary Active Galactic Nucleus in the Ultraluminous Infrared Galaxy NGC 6240 Using Chandra. ApJ, 582(1):L15–L19.

Komossa, S., Xu, D., Zhou, H., Storchi-Bergmann, T., and Binette, L. (2008). On the Nature of Seyfert Galaxies with High [O III] λ5007 Blueshifts. ApJ, 680(2):926–938.

Kormendy, J. (1993). Kinematics of extragalactic bulges: evidence that some bulges are really disks. In Dejonghe, H. and Habing, H. J., editors, *Galactic Bulges*, volume 153, page 209.

Kormendy, J. and Bender, R. (2009). Correlations between Supermassive Black Holes, Velocity Dispersions, and Mass Deficits in Elliptical Galaxies with Cores. ApJ, 691(2):L142–L146.

Kormendy, J. and Bender, R. (2011). Supermassive black holes do not correlate with dark matter haloes of galaxies. Nature, 469(7330):377–380.

Kormendy, J. and Gebhardt, K. (2001). Supermassive black holes in galactic nuclei. In Wheeler, J. C. and Martel, H., editors, *20th Texas Symposium on relativistic astrophysics*, volume 586 of *American Institute of Physics Conference Series*, pages 363–381.

Kormendy, J. and Ho, L. C. (2013). Coevolution (Or Not) of Supermassive Black Holes and Host Galaxies. ARA&A, 51(1):511–653.

Koss, M. J., Blecha, L., Bernhard, P., Hung, C.-L., Lu, J. R., Trakhtenbrot, B., Treister, E., Weigel, A., Sartori, L. F., Mushotzky, R., Schawinski, K., Ricci, C., Veilleux, S., and Sanders, D. B. (2018). A population of luminous accreting black holes with hidden mergers. Nature, 563(7730):214–216.

Kovačević, J., Popović, L. Č., and Dimitrijević, M. S. (2010). Analysis of Optical Fe II Emission in a Sample of Active Galactic Nucleus Spectra. ApJS, 189(1):15–36.

Krumpe, M., Husemann, B., Tremblay, G. R., Urrutia, T., Powell, M., Davis, T. A., Scharwächter, J., Dexter, J., Busch, G., Combes, F., Croom, S. M., Eckart, A., McElroy, R. E., Perez-Torres, M., and Leung, G. (2017). The Close AGN Reference Survey (CARS). Mrk 1018 halts dimming and experiences strong short-term variability. A&A, 607:L9.

Laing, R. A., Riley, J. M., and Longair, M. S. (1983). Bright radio sources at 178 MHz : flux densities, optical identifications and the cosmological evolution of powerful radio galaxies. MNRAS, 204:151–187.

LaMassa, S. M., Cales, S., Moran, E. C., Myers, A. D., Richards, G. T., Eracleous, M., Heckman, T. M., Gallo, L., and Urry, C. M. (2015). The Discovery of the First "Changing Look" Quasar: New Insights Into the Physics and Phenomenology of Active Galactic Nucleus. ApJ, 800(2):144.

Lamastra, A., Bianchi, S., Matt, G., Perola, G. C., Barcons, X., and Carrera, F. J. (2009). The bolometric luminosity of type 2 AGN from extinction-corrected [OIII]. No evidence of Eddington-limited sources. A&A, 504(1):73–79.

Lanzuisi, G., Giustini, M., Cappi, M., Dadina, M., Malaguti, G., Vignali, C., and Chartas, G. (2012). HS 1700+6416: the first high-redshift unlensed narrow absorption line-QSO showing variable high-velocity outflows. A&A, 544:A2.

Laor, A. (2001). On the Linearity of the Black Hole-Bulge Mass Relation in Active and in Nearby Galaxies. ApJ, 553(2):677–682.

Laor, A. and Behar, E. (2008). On the origin of radio emission in radio-quiet quasars. MNRAS, 390(2):847–862.

Larkin, J. E., Armus, L., Knop, R. A., Soifer, B. T., and Matthews, K. (1998). A Near-Infrared Spectroscopic Survey of LINER Galaxies. ApJS, 114(1):59–72.

Law, D. R., Cherinka, B., Yan, R., Andrews, B. H., Bershady, M. A., Bizyaev, D., Blanc, G. A., Blanton, M. R., Bolton, A. S., Brownstein, J. R., Bundy, K., Chen, Y., Drory, N., D'Souza, R., Fu, H., Jones, A., Kauffmann, G., MacDonald, N., Masters, K. L., Newman, J. A., Parejko, J. K., Sánchez-Gallego, J. R., Sánchez, S. F., Schlegel, D. J., Thomas, D., Wake, D. A., Weijmans, A.-M., Westfall, K. B., and Zhang, K. (2016). The Data Reduction Pipeline for the SDSS-IV MaNGA IFU Galaxy Survey. AJ, 152(4):83.

Law, D. R., Steidel, C. C., Erb, D. K., Larkin, J. E., Pettini, M., Shapley, A. E., and Wright, S. A. (2009). The Kiloparsec-scale Kinematics of High-redshift Star-forming Galaxies. ApJ, 697(2):2057–2082.

Law, D. R., Yan, R., Bershady, M. A., Bundy, K., Cherinka, B., Drory, N., MacDonald, N., Sánchez-Gallego, J. R., Wake, D. A., Weijmans, A.-M., Blanton, M. R., Klaene, M. A., Moran, S. M., Sanchez, S. F., and Zhang, K. (2015). Observing Strategy for the SDSS-IV/MaNGA IFU Galaxy Survey. AJ, 150(1):19.

Lawrence, A., Bruce, A. G., MacLeod, C., Gezari, S., Elvis, M., Ward, M., Smartt, S. J., Smith, K. W., Wright, D., Fraser, M., Marshall, P., Kaiser, N., Burgett, W., Magnier, E., Tonry, J., Chambers, K., Wainscoat, R., Waters, C., Price, P., Metcalfe, N., Valenti, S., Kotak, R., Mead, A., Inserra, C., Chen, T. W., and Soderberg, A. (2016). Slow-blue nuclear hypervariables in PanSTARRS-1. MNRAS, 463(1):296–331.

Lee, N., Sanders, D. B., Casey, C. M., Toft, S., Scoville, N. Z., Hung, C.-L., Le Floc'h, E., Ilbert, O., Zahid, H. J., Aussel, H., Capak, P., Kartaltepe, J. S., Kewley, L. J., Li, Y., Schawinski, K., Sheth, K., and Xiao, Q. (2015). A Turnover in the Galaxy Main Sequence of Star Formation at $M_* \sim 10^{10} M_\odot$ for Redshifts $z < 1.3$. ApJ, 801(2):80.

Lehmer, B. D., Alexander, D. M., Bauer, F. E., Brandt, W. N., Goulding, A. D., Jenkins, L. P., Ptak, A., and Roberts, T. P. (2010). A Chandra Perspective on Galaxy-wide X-ray Binary Emission and its Correlation with Star Formation Rate and Stellar Mass: New Results from Luminous Infrared Galaxies. ApJ, 724(1):559–571.

Leighly, K. M. (1999). A Comprehensive Spectral and Variability Study of Narrow-Line Seyfert 1 Galaxies Observed by ASCA. II. Spectral Analysis and Correlations. ApJS, 125(2):317–348.

Lepp, S. and McCray, R. (1983). X-ray sources in molecular clouds. ApJ, 269:560–567.

Leung, G. C. K., Coil, A. L., Aird, J., Azadi, M., Kriek, M., Mobasher, B., Reddy, N., Shapley, A., Siana, B., Fetherolf, T., Fornasini, F. M., Freeman, W. R., Price, S. H., Sanders, R. L., Shivaei, I., and Zick, T. (2019). The MOSDEF Survey: A Census of AGN-driven Ionized Outflows at z = 1.4-3.8. ApJ, 886(1):11.

Liang, F.-H., Li, C., Li, N., Yan, R., Mo, H., Zhang, W., Machuca, C., and Roman-Lopes, A. (2020). Wolf-Rayet Galaxies in SDSS-IV MaNGA. I. Catalog Construction and Sample Properties. ApJ, 896(2):121.

Lilly, S. J., Eales, S. A., Gear, W. K. P., Hammer, F., Le Fèvre, O., Crampton, D., Bond, J. R., and Dunne, L. (1999). The Canada-United Kingdom Deep Submillimeter Survey. II. First Identifications, Redshifts, and Implications for Galaxy Evolution. ApJ, 518(2):641–655.

Longinotti, A. L., Krongold, Y., Guainazzi, M., Giroletti, M., Panessa, F., Costantini, E., Santos-Lleo, M., and Rodriguez-Pascual, P. (2015). X-Ray High-resolution Spectroscopy Reveals Feedback in a Seyfert Galaxy from an Ultra-fast Wind with Complex Ionization and Velocity Structure. ApJ, 813(2):L39.

Ludwig, R. R., Wills, B., Greene, J. E., and Robinson, E. L. (2009). Strong [O III] Objects Among SDSS Broad-line Active Galaxies. ApJ, 706(2):995–1007.

Luo, B., Brandt, W. N., Xue, Y. Q., Lehmer, B., Alexander, D. M., Bauer, F. E., Vito, F., Yang, G., Basu-Zych, A. R., Comastri, A., Gilli, R., Gu, Q. S., Hornschemeier, A. E., Koekemoer, A., Liu, T., Mainieri, V., Paolillo, M., Ranalli, P., Rosati, P., Schneider, D. P., Shemmer, O., Smail, I., Sun, M., Tozzi, P., Vignali, C., and Wang, J. X. (2017). The Chandra Deep Field-South Survey: 7 Ms Source Catalogs. ApJS, 228(1):2.

Lusso, E., Casetti, L., Pancrazzi, M., and Romoli, M. (2022). Hands-on learning at a world-class telescope. *arXiv e-prints*, page arXiv:2210.13360.

Lusso, E., Comastri, A., Simmons, B. D., Mignoli, M., Zamorani, G., Vignali, C., Brusa, M., Shankar, F., Lutz, D., Trump, J. R., Maiolino, R., Gilli, R., Bolzonella, M., Puccetti, S., Salvato, M., Impey, C. D., Civano, F., Elvis, M., Mainieri, V., Silverman, J. D., Koekemoer, A. M., Bongiorno, A., Merloni, A., Berta, S., Le Floc'h, E., Magnelli, B., Pozzi, F., and Riguccini, L. (2012). Bolometric luminosities and Eddington ratios of X-ray selected active galactic nuclei in the XMM-COSMOS survey. MNRAS, 425(1):623–640.

Lutz, D., Sturm, E., Genzel, R., Spoon, H. W. W., Moorwood, A. F. M., Netzer, H., and Sternberg, A. (2003). ISO spectroscopy of star formation and active nuclei in the luminous infrared galaxy <ASTROBJ>NGC 6240</ASTROBJ>. A&A, 409:867–878.

MacLeod, C. L., Ross, N. P., Lawrence, A., Goad, M., Horne, K., Burgett, W., Chambers, K. C., Flewelling, H., Hodapp, K., Kaiser, N., Magnier, E., Wainscoat, R., and Waters, C. (2016). A systematic search for changing-look quasars in SDSS. MNRAS, 457(1):389–404.

Madau, P. and Dickinson, M. (2014). Cosmic Star-Formation History. ARA&A, 52:415–486.

Madau, P., Ferguson, H. C., Dickinson, M. E., Giavalisco, M., Steidel, C. C., and Fruchter, A. (1996). High-redshift galaxies in the Hubble Deep Field: colour selection and star formation history to z~4. MNRAS, 283(4):1388–1404.

Magorrian, J., Tremaine, S., Richstone, D., Bender, R., Bower, G., Dressler, A., Faber, S. M., Gebhardt, K., Green, R., Grillmair, C., Kormendy, J., and Lauer, T. (1998). The Demography of Massive Dark Objects in Galaxy Centers. AJ, 115(6):2285–2305.

Maiolino, R., Gallerani, S., Neri, R., Cicone, C., Ferrara, A., Genzel, R., Lutz, D., Sturm, E., Tacconi, L. J., Walter, F., Feruglio, C., Fiore, F., and Piconcelli, E. (2012). Evidence of strong quasar feedback in the early Universe. MNRAS, 425(1):L66–L70.

Maiolino, R., Russell, H. R., Fabian, A. C., Carniani, S., Gallagher, R., Cazzoli, S., Arribas, S., Belfiore, F., Bellocchi, E., Colina, L., Cresci, G., Ishibashi, W., Marconi, A., Mannucci, F., Oliva, E., and Sturm, E. (2017). Star formation inside a galactic outflow. Nature, 544(7649):202–206.

Maiolino, R., Scholtz, J., Witstok, J., Carniani, S., D'Eugenio, F., de Graaff, A., Uebler, H., Tacchella, S., Curtis-Lake, E., Arribas, S., Bunker, A., Charlot, S., Chevallard, J., Curti, M., Looser, T. J., Maseda, M. V., Rawle, T., Rodriguez Del Pino, B., Willott, C. J., Egami, E., Eisenstein, D., Hainline, K., Robertson, B., Williams, C. C., Willmer, C. N. A., Baker, W. M., Boyett, K., DeCoursey, C., Fabian, A. C., Helton, J. M., Ji, Z., Jones, G. C., Kumari, N., Laporte, N., Nelson, E., Perna, M., Sandles, L., Shivaei, I., and Sun, F. (2023a). A small and vigorous black hole in the early Universe. *arXiv e-prints*, page arXiv:2305.12492.

Maiolino, R., Uebler, H., Perna, M., Scholtz, J., D'Eugenio, F., Witten, C., Laporte, N., Witstok, J., Carniani, S., Tacchella, S., Baker, W., Arribas, S., Nakajima, K., Eisenstein, D., Bunker, A., Charlot, S., Cresci, G., Curti, M., Curtis-Lake, E., de Graaff, A., Ji, Z., Johnson, B. D., Kumari, N., Looser, T. J., Maseda, M., Robertson, B., Rodriguez Del Pino, B., Sandles, L., Simmonds, C., Smit, R., Sun, F., Venturi, G., Williams, C., and Willmer, C. (2023b). JWST-JADES. Possible Population III signatures at z=10.6 in the halo of GN-z11. *arXiv e-prints*, page arXiv:2306.00953.

Mannucci, F., Pancino, E., Belfiore, F., Cicone, C., Ciurlo, A., Cresci, G., Lusso, E., Marasco, A., Marconi, A., Nardini, E., Pinna, E., Severgnini, P., Saracco, P., Tozzi, G., and Yeh, S. (2022). Unveiling the population of dual and lensed active galactic nuclei at sub-arcsec separations. *Nature Astronomy*, 6:1185–1192.

Marasco, A., Belfiore, F., Cresci, G., Lelli, F., Venturi, G., Hunt, L. K., Concas, A., Marconi, A., Mannucci, F., Mingozzi, M., McLeod, A. F., Kumari, N., Carniani, S., Vanzi, L., and Ginolfi, M. (2023). Shaken, but not expelled: Gentle baryonic feedback from nearby starburst dwarf galaxies. A&A, 670:A92.

Marasco, A., Cresci, G., Nardini, E., Mannucci, F., Marconi, A., Tozzi, P., Tozzi, G., Amiri, A., Venturi, G., Piconcelli, E., Lanzuisi, G., Tombesi, F., Mingozzi, M., Perna, M., Carniani, S., Brusa, M., and di Serego Alighieri, S. (2020). Galaxy-scale ionised winds driven by ultra-fast outflows in two nearby quasars. A&A, 644:A15.

Maraston, C. and Strömbäck, G. (2011). Stellar population models at high spectral resolution. MNRAS, 418(4):2785–2811.

Marconcini, C., Marconi, A., Cresci, G., Venturi, G., Ulivi, L., Mannucci, F., Belfiore, F., Tozzi, G., Ginolfi, M., Marasco, A., Carniani, S., Amiri, A., Di Teodoro, E., Scialpi, M., Tomicic, N., Mingozzi, M., Brazzini, M., and Moreschini, B. (2023). MOKA^{3D}: An innovative approach to 3D gas kinematic modelling. I. Application to AGN ionised outflows. A&A, 677:A58.

Marconi, A. and Hunt, L. K. (2003). The Relation between Black Hole Mass, Bulge Mass, and Near-Infrared Luminosity. ApJ, 589(1):L21–L24.

Marconi, A., Risaliti, G., Gilli, R., Hunt, L. K., Maiolino, R., and Salvati, M. (2004). Local supermassive black holes, relics of active galactic nuclei and the X-ray background. MNRAS, 351(1):169–185.

Marin, F. and Hutsemékers, D. (2020). Tracking the state transitions in changing-look active galactic nuclei through their polarized-light echoes. A&A, 636:A23.

Marinacci, F., Vogelsberger, M., Pakmor, R., Torrey, P., Springel, V., Hernquist, L., Nelson, D., Weinberger, R., Pillepich, A., Naiman, J., and Genel, S. (2018). First results from the IllustrisTNG simulations: radio haloes and magnetic fields. MNRAS, 480(4):5113–5139.

Marscher, A. P. and Gear, W. K. (1985). Models for high-frequency radio outbursts in extragalactic sources, with application to the early 1983 millimeter-to-infrared flare of 3C 273. ApJ, 298:114–127.

Marshall, M. A., Perna, M., Willott, C. J., Maiolino, R., Scholtz, J., Übler, H., Carniani, S., Arribas, S., Lützgendorf, N., Bunker, A. J., Charlot, S., Ferruit, P., Jakobsen, P., Rix, H.-W., Rodríguez Del Pino, B., Böker, T., Cameron, A. J., Cresci, G., Curtis-Lake, E., Jones, G. C., Kumari, N., Pérez-González, P. G., and Reed, S. L. (2023). GA-NIFS: Black hole and host galaxy properties of two z≃6.8 quasars from the NIRSpec IFU. *arXiv e-prints*, page arXiv:2302.04795.

Matthews, T. A. and Sandage, A. R. (1963). Optical Identification of 3C 48, 3C 196, and 3C 286 with Stellar Objects. ApJ, 138:30.

Matzeu, G. A., Brusa, M., Lanzuisi, G., Dadina, M., Bianchi, S., Kriss, G., Mehdipour, M., Nardini, E., Chartas, G., Middei, R., Piconcelli, E., Gianolli, V., Comastri, A., Longinotti, A. L., Krongold, Y., Ricci, F., Petrucci, P. O., Tombesi, F., Luminari, A., Zappacosta, L., Miniutti, G., Gaspari, M., Behar, E., Bischetti, M., Mathur, S., Perna, M., Giustini, M., Grandi, P., Torresi, E., Vignali, C., Bruni, G., Cappi, M., Costantini, E., Cresci, G., De Marco, B., De Rosa, A., Gilli, R., Guainazzi, M., Kaastra, J., Kraemer, S., La Franca, F., Marconi, A., Panessa, F., Ponti, G., Proga, D., Ursini, F., Baldini, P., Fiore, F., King, A. R., Maiolino, R., Matt, G., and Merloni, A. (2023). Supermassive Black Hole Winds in X-rays: SUBWAYS. I. Ultra-fast outflows in quasars beyond the local Universe. A&A, 670:A182.

Max, C. E., Canalizo, G., and de Vries, W. H. (2007). Locating the Two Black Holes in NGC 6240. *Science*, 316(5833):1877.

Max, C. E., Canalizo, G., Macintosh, B. A., Raschke, L., Whysong, D., Antonucci, R., and Schneider, G. (2005). The Core of NGC 6240 from Keck Adaptive Optics and Hubble Space Telescope NICMOS Observations. ApJ, 621(2):738–749.

Max-Moerbeck, W., Hovatta, T., Richards, J. L., King, O. G., Pearson, T. J., Readhead, A. C. S., Reeves, R., Shepherd, M. C., Stevenson, M. A., Angelakis, E., Fuhrmann, L., Grainge, K. J. B., Pavlidou, V., Romani, R. W., and Zensus, J. A. (2014). Time correlation between the radio and gamma-ray activity in blazars and the production site of the gamma-ray emission. MNRAS, 445(1):428–436.

Mazzalay, X., Saglia, R. P., Erwin, P., Fabricius, M. H., Rusli, S. P., Thomas, J., Bender, R., Opitsch, M., Nowak, N., and Williams, M. J. (2013). Molecular gas in the centre of nearby galaxies from VLT/SINFONI integral field spectroscopy - I. Morphology and mass inventory. MNRAS, 428(3):2389–2406.

McConnell, N. J. and Ma, C.-P. (2013). Revisiting the Scaling Relations of Black Hole Masses and Host Galaxy Properties. ApJ, 764(2):184.

McElroy, R. E., Husemann, B., Croom, S. M., Davis, T. A., Bennert, V. N., Busch, G., Combes, F., Eckart, A., Perez-Torres, M., Powell, M., Scharwächter, J., Tremblay, G. R., and Urrutia, T. (2016). The Close AGN Reference Survey (CARS). Mrk 1018 returns to the shadows after 30 years as a Seyfert 1. A&A, 593:L8.

McGreer, I. D., Becker, R. H., Helfand, D. J., and White, R. L. (2006). Discovery of a z = 6.1 Radio-Loud Quasar in the NOAO Deep Wide Field Survey. ApJ, 652(1):157–162.

McLure, R. J. and Dunlop, J. S. (2002). On the black hole-bulge mass relation in active and inactive galaxies. MNRAS, 331(3):795–804.

Medling, A. M., Ammons, S. M., Max, C. E., Davies, R. I., Engel, H., and Canalizo, G. (2011). Mass of the Southern Black Hole in NGC 6240 from Laser Guide Star Adaptive Optics. ApJ, 743(1):32.

Medling, A. M., Kewley, L. J., Calzetti, D., Privon, G. C., Larson, K., Rich, J. A., Armus, L., Allen, M. G., Bicknell, G. V., Díaz-Santos, T., Heckman, T. M., Leitherer, C., Max, C. E., Rupke, D. S. N., Treister, E., Messias, H., and Wagner, A. Y. (2021). Tracing the Ionization Structure of the Shocked Filaments of NGC 6240. ApJ, 923(2):160.

Medling, A. M., U, V., Guedes, J., Max, C. E., Mayer, L., Armus, L., Holden, B., Roškar, R., and Sanders, D. (2014). Stellar and Gaseous Nuclear Disks Observed in Nearby (U)LIRGs. ApJ, 784(1):70.

Mehdipour, M., Kaastra, J. S., Kriss, G. A., Arav, N., Behar, E., Bianchi, S., Branduardi-Raymont, G., Cappi, M., Costantini, E., Ebrero, J., Di Gesu, L., Kaspi, S., Mao, J., De Marco, B., Matt, G., Paltani, S., Peretz, U., Peterson, B. M., Petrucci, P. O., Pinto, C., Ponti, G., Ursini, F., de Vries, C. P., and Walton, D. J. (2017). Chasing obscuration in type-I AGN: discovery of an eclipsing clumpy wind at the outer broad-line region of NGC 3783. A&A, 607:A28.

Mehdipour, M., Kriss, G. A., Brusa, M., Matzeu, G. A., Gaspari, M., Kraemer, S. B., Mathur, S., Behar, E., Bianchi, S., Cappi, M., Chartas, G., Costantini, E., Cresci, G., Dadina, M., De Marco, B., De Rosa, A., Dunn, J. P., Gianolli, V. E., Giustini, M., Kaastra, J. S., King, A. R., Krongold, Y., La Franca, F., Lanzuisi, G., Longinotti, A. L., Luminari, A., Middei, R., Miniutti, G., Nardini, E., Perna, M., Petrucci, P. O., Piconcelli, E., Ponti, G., Ricci, F., Tombesi, F., Ursini, F., Vignali, C., and Zappacosta, L. (2023). Supermassive Black Hole Winds in X-rays: SUBWAYS. II. HST UV spectroscopy of winds at intermediate redshifts. A&A, 670:A183.

Menci, N., Fiore, F., Puccetti, S., and Cavaliere, A. (2008). The Blast Wave Model for AGN Feedback: Effects on AGN Obscuration. ApJ, 686(1):219–229.

Mereghetti, S., Balman, S., Caballero-Garcia, M., Del Santo, M., Doroshenko, V., Erkut, M. H., Hanlon, L., Hoeflich, P., Markowitz, A., Osborne, J. P., Pian, E., Rivera Sandoval, L., Webb, N., Amati, L., Ambrosi, E., Beardmore, A. P., Blain, A., Bozzo, E., Burderi, L., Campana, S., Casella, P., D'Aí, A., D'Ammando, F., De Colle, F., Della Valle, M., De Martino, D., Di Salvo, T., Doyle, M., Esposito, P., Frontera, F., Gandhi, P., Ghisellini, G., Gotz, D., Grinberg, V., Guidorzi, C., Hudec, R., Iaria, R., Izzo, L., Jaisawal, G. K., Jonker, P. G., Kong, A. K. H., Krumpe, M., Kumar, P., Manousakis, A., Marino, A., Martin-Carrillo, A., Mignani, R., Miniutti, G., Mundell, C. G., Mukai, K., Nucita, A. A., O'Brien, P. T., Orlandini, M., Orio, M., Palazzi, E., Papitto, A., Pintore, F., Piranomonte, S., Porquet, D., Ricci, C., Riggio, A., Rigoselli, M., Rodriguez, J., Saha, T., Sanna, A., Santangelo, A., Saxton, R., Sidoli, L., Stiele, H., Tagliaferri, G., Tavecchio, F., Tiengo, A., Tsygankov, S., Turriziani, S., Wijnands, R., Zane, S., and Zhang, B. (2021). Time domain astronomy with the THESEUS satellite. *Experimental Astronomy*, 52(3):309–406.

Merritt, D. and Ferrarese, L. (2001). Black hole demographics from the M_L-σ relation. MNRAS, 320(3):L30–L34.

Mezcua, M., Civano, F., Fabbiano, G., Miyaji, T., and Marchesi, S. (2016). A Population of Intermediate-mass Black Holes in Dwarf Starburst Galaxies Up to Redshift=1.5. ApJ, 817(1):20.

Mezcua, M. and Domínguez Sánchez, H. (2020). Hidden AGNs in Dwarf Galaxies Revealed by MaNGA: Light Echoes, Off-nuclear Wanderers, and a New Broad-line AGN. ApJ, 898(2):L30.

Mignoli, M., Feltre, A., Bongiorno, A., Calura, F., Gilli, R., Vignali, C., Zamorani, G., Lilly, S. J., Le Fèvre, O., Bardelli, S., Bolzonella, M., Bordoloi, R., Le Brun, V., Caputi, K. I., Cimatti, A., Diener, C., Garilli, B., Koekemoer, A. M., Maier, C., Mainieri, V., Peng, Y., Pérez Montero, E., Silverman, J. D., and Zucca, E. (2019). Obscured AGN at $1.5 < z < 3.0$ from the zCOSMOS-deep Survey . I. Properties of the emitting gas in the narrow-line region. A&A, 626:A9.

Mignoli, M., Vignali, C., Gilli, R., Comastri, A., Zamorani, G., Bolzonella, M., Bongiorno, A., Lamareille, F., Nair, P., Pozzetti, L., Lilly, S. J., Carollo, C. M., Contini, T., Kneib, J. P., Le Fèvre, O., Mainieri, V., Renzini, A., Scodeggio, M., Bardelli, S., Caputi, K., Cucciati, O., de la Torre, S., de Ravel, L., Franzetti, P., Garilli, B., Iovino, A., Kampczyk, P., Knobel, C., Kovač, K., Le Borgne, J. F., Le Brun, V., Maier, C., Pellò, R., Peng, Y., Perez Montero, E., Presotto, V., Silverman, J. D., Tanaka, M., Tasca, L., Tresse, L., Vergani, D., Zucca, E., Bordoloi, R., Cappi, A., Cimatti, A., Koekemoer, A. M., McCracken, H. J., Moresco, M., and Welikala, N. (2013). Obscured AGN at $z \sim 1$ from the zCOSMOS-Bright Survey. I. Selection and optical properties of a [Ne v]-selected sample. A&A, 556:A29.

Mingozzi, M., Cresci, G., Venturi, G., Marconi, A., Mannucci, F., Perna, M., Belfiore, F., Carniani, S., Balmaverde, B., Brusa, M., Cicone, C., Feruglio, C., Gallazzi, A., Mainieri, V., Maiolino, R., Nagao, T., Nardini, E., Sani, E., Tozzi, P., and Zibetti, S. (2019). The MAGNUM survey: different gas properties in the outflowing and disc components in nearby active galaxies with MUSE. A&A, 622:A146.

Mingozzi, M., James, B. L., Berg, D., Arellano-Córdova, K. Z., Plat, A., Scarlata, C., Aloisi, A., Amorín, R. O., Brinchmann, J., Charlot, S., Chisholm, J., Feltre, A., Gazagnes, S., Hayes, M., Heckman, T., Hernandez, S., Kewley, L. J., Kumari, N., Leitherer, C., Martin, C. L., Maseda, M., Nanayakkara, T., Ravindranath, S., Rigby, J. R., Senchyna, P., Skillman, E. D., Sugahara, Y., Wilkins, S. M., Wofford, A., and Xu, X. (2023). CLASSY VIII: Exploring the Source of Ionization with UV ISM diagnostics in local High-z Analogs. *arXiv e-prints*, page arXiv:2306.15062.

Mizumoto, M., Izumi, T., and Kohno, K. (2019). Kinetic Energy Transfer from X-Ray Ultrafast Outflows to Millimeter/Submillimeter Cold Molecular Outflows in Seyfert Galaxies. ApJ, 871(2):156.

Molina, M., Reines, A. E., Latimer, L. J., Baldassare, V., and Salehirad, S. (2021). A Sample of Massive Black Holes in Dwarf Galaxies Detected via [Fe X] Coronal Line Emission: Active Galactic Nuclei and/or Tidal Disruption Events. ApJ, 922(2):155.

Morganti, R., Oosterloo, T., Oonk, J. B. R., Frieswijk, W., and Tadhunter, C. (2015). The fast molecular outflow in the Seyfert galaxy IC 5063 as seen by ALMA. A&A, 580:A1.

Morganti, R., Oosterloo, T. A., Tadhunter, C. N., van Moorsel, G., and Emonts, B. (2005a). The location of the broad H i absorption in 3C 305: clear evidence for a jet-accelerated neutral outflow. A&A, 439(2):521–526.

Morganti, R., Tadhunter, C. N., and Oosterloo, T. A. (2005b). Fast neutral outflows in powerful radio galaxies: a major source of feedback in massive galaxies. A&A, 444(1):L9–L13.

Morganti, R., Veilleux, S., Oosterloo, T., Teng, S. H., and Rupke, D. (2016). Another piece of the puzzle: The fast H I outflow in Mrk 231. A&A, 593:A30.

Mosquera, A. M. and Kochanek, C. S. (2011). The Microlensing Properties of a Sample of 87 Lensed Quasars. ApJ, 738(1):96.

Moster, B. P., Naab, T., and White, S. D. M. (2013). Galactic star formation and accretion histories from matching galaxies to dark matter haloes. MNRAS, 428(4):3121–3138.

Mouri, H. (1994). Molecular Hydrogen Emission in Galaxies: Determination of Excitation Mechanism. ApJ, 427:777.

Mowla, L., van der Wel, A., van Dokkum, P., and Miller, T. B. (2019). A Mass-dependent Slope of the Galaxy Size-Mass Relation out to z ∼ 3: Further Evidence for a Direct Relation between Median Galaxy Size and Median Halo Mass. ApJ, 872(1):L13.

Mullaney, J. R., Alexander, D. M., Fine, S., Goulding, A. D., Harrison, C. M., and Hickox, R. C. (2013). Narrow-line region gas kinematics of 24 264 optically selected AGN: the radio connection. MNRAS, 433(1):622–638.

Mullaney, J. R., Alexander, D. M., Goulding, A. D., and Hickox, R. C. (2011). Defining the intrinsic AGN infrared spectral energy distribution and measuring its contribution to the infrared output of composite galaxies. MNRAS, 414(2):1082–1110.

Müller-Sánchez, F., Nevin, R., Comerford, J. M., Davies, R. I., Privon, G. C., and Treister, E. (2018). Two separate outflows in the dual supermassive black hole system NGC 6240. Nature, 556(7701):345–348.

Musiimenta, B., Brusa, M., Liu, T., Salvato, M., Buchner, J., Igo, Z., Waddell, S. G. H., Toba, Y., Arcodia, R., Comparat, J., Alexander, D. M., Shankar, F., Lapi, A., Ramos Almeida, C., Georgakakis, A., Merloni, A., Urrutia, T., Li, J., Terashima, Y., Shen, Y., Wu, Q., Dwelly, T., Nandra, K., and Wolf, J. (2023). A new discovery space opened by eROSITA: Ionised AGN outflows from X-ray selected samples. *arXiv e-prints*, page arXiv:2309.16528.

Nagao, T., Marconi, A., and Maiolino, R. (2006). The evolution of the broad-line region among SDSS quasars. A&A, 447(1):157–172.

Naiman, J. P., Pillepich, A., Springel, V., Ramirez-Ruiz, E., Torrey, P., Vogelsberger, M., Pakmor, R., Nelson, D., Marinacci, F., Hernquist, L., Weinberger, R., and Genel, S. (2018). First results from the IllustrisTNG simulations: a tale of two elements - chemical evolution of magnesium and europium. MNRAS, 477(1):1206–1224.

Nakajima, K. and Maiolino, R. (2022). Diagnostics for PopIII galaxies and direct collapse black holes in the early universe. MNRAS, 513(4):5134–5147.

Nakajima, K., Schaerer, D., Le Fèvre, O., Amorín, R., Talia, M., Lemaux, B. C., Tasca, L. A. M., Vanzella, E., Zamorani, G., Bardelli, S., Grazian, A., Guaita, L., Hathi, N. P., Pentericci, L., and Zucca, E. (2018). The VIMOS Ultra Deep Survey: Nature, ISM properties, and ionizing spectra of CIII]λ1909 emitters at z = 2-4. A&A, 612:A94.

Narayan, R. and Bartelmann, M. (1996). Lectures on Gravitational Lensing. *arXiv e-prints*, pages astro–ph/9606001.

Nardini, E., Lusso, E., and Bisogni, S. (2019). Towards an informed quest for accretion disc winds in quasars: the intriguing case of Ton 28. MNRAS, 482(1):L134–L138.

Nardini, E., Reeves, J. N., Gofford, J., Harrison, F. A., Risaliti, G., Braito, V., Costa, M. T., Matzeu, G. A., Walton, D. J., Behar, E., Boggs, S. E., Christensen, F. E., Craig, W. W., Hailey, C. J., Matt, G., Miller, J. M., O'Brien, P. T., Stern, D., Turner, T. J., and Ward, M. J. (2015). Black hole feedback in the luminous quasar PDS 456. *Science*, 347(6224):860–863.

Nardini, E., Risaliti, G., Watabe, Y., Salvati, M., and Sani, E. (2010). The role of nuclear activity as the power source of ultraluminous infrared galaxies. MNRAS, 405(4):2505–2520.

Nardini, E., Wang, J., Fabbiano, G., Elvis, M., Pellegrini, S., Risaliti, G., Karovska, M., and Zezas, A. (2013). The Exceptional Soft X-Ray Halo of the Galaxy Merger NGC 6240. ApJ, 765(2):141.

Nardini, E. and Zubovas, K. (2018). Multi-phase outflows as probes of AGN accretion history. MNRAS, 478(2):2274–2280.

Navarro, J. F., Frenk, C. S., and White, S. D. M. (1997). A Universal Density Profile from Hierarchical Clustering. ApJ, 490(2):493–508.

Nayakshin, S. and Zubovas, K. (2012). Quasar feedback: accelerated star formation and chaotic accretion. MNRAS, 427(1):372–378.

Negus, J., Comerford, J. M., Müller Sánchez, F., Barrera-Ballesteros, J. K., Drory, N., Rembold, S. B., and Riffel, R. A. (2021). The Physics of the Coronal-line Region for Galaxies in Mapping Galaxies at Apache Point Observatory. ApJ, 920(1):62.

Negus, J., Comerford, J. M., Sánchez, F. M., Revalski, M., Riffel, R. A., Bundy, K., Nevin, R., and Rembold, S. B. (2023). A Catalog of 71 Coronal Line Galaxies in MaNGA: [Ne V] Is an Effective AGN Tracer. ApJ, 945(2):127.

Nelson, D., Pillepich, A., Springel, V., Weinberger, R., Hernquist, L., Pakmor, R., Genel, S., Torrey, P., Vogelsberger, M., Kauffmann, G., Marinacci, F., and Naiman, J. (2018). First results from the IllustrisTNG simulations: the galaxy colour bimodality. MNRAS, 475(1):624–647.

Nenkova, M., Sirocky, M. M., Nikutta, R., Ivezić, Ž., and Elitzur, M. (2008). AGN Dusty Tori. II. Observational Implications of Clumpiness. ApJ, 685(1):160–180.

Nesvadba, N. P. H., De Breuck, C., Lehnert, M. D., Best, P. N., Binette, L., and Proga, D. (2011). The black holes of radio galaxies during the “Quasar Era”: masses, accretion rates, and evolutionary stage. A&A, 525:A43.

Nesvadba, N. P. H., Lehnert, M. D., De Breuck, C., Gilbert, A. M., and van Breugel, W. (2008). Evidence for powerful AGN winds at high redshift: dynamics of galactic outflows in radio galaxies during the “Quasar Era”. A&A, 491(2):407–424.

Netzer, H. (2015). Revisiting the Unified Model of Active Galactic Nuclei. ARA&A, 53:365–408.

Nierenberg, A. M., Gilman, D., Treu, T., Brammer, G., Birrer, S., Moustakas, L., Agnello, A., Anguita, T., Fassnacht, C. D., Motta, V., Peter, A. H. G., and Sluse, D. (2020). Double dark matter vision: twice the number of compact-source lenses with narrow-line lensing and the WFC3 grism. MNRAS, 492(4):5314–5335.

Nieto, J. L. and Tiennot, L. (1984). Surface photometry and distance of NGC 4156 from high-resolution optical observations. A&A, 131:291–302.

Nisbet, D. M. and Best, P. N. (2016). The mass fraction of AGN and the Fundamental Plane of black hole activity from a large X-ray-selected sample of LINERs. MNRAS, 455(3):2551–2566.

Noeske, K. G., Weiner, B. J., Faber, S. M., Papovich, C., Koo, D. C., Somerville, R. S., Bundy, K., Conselice, C. J., Newman, J. A., Schiminovich, D., Le Floc’h, E., Coil, A. L., Rieke, G. H., Lotz, J. M., Primack, J. R., Barmby, P., Cooper, M. C., Davis, M., Ellis, R. S., Fazio, G. G., Guhathakurta, P., Huang, J., Kassin, S. A., Martin, D. C., Phillips, A. C., Rich, R. M., Small, T. A., Willmer, C. N. A., and Wilson, G. (2007). Star Formation in AEGIS Field Galaxies since z=1.1: The Dominance of Gradually Declining Star Formation, and the Main Sequence of Star-forming Galaxies. ApJ, 660(1):L43–L46.

Noll, S., Burgarella, D., Giovannoli, E., Buat, V., Marcillac, D., and Muñoz-Mateos, J. C. (2009). Analysis of galaxy spectral energy distributions from far-UV to far-IR with CIGALE: studying a SINGS test sample. A&A, 507(3):1793–1813.

Norman, C. and Scoville, N. (1988). The Evolution of Starburst Galaxies to Active Galactic Nuclei. ApJ, 332:124.

Ofek, E. O. (2014). MAAT: MATLAB Astronomy and Astrophysics Toolbox. Astrophysics Source Code Library, record ascl:1407.005.

Ohyama, Y., Yoshida, M., and Takata, T. (2003). Superwind-driven Intense H_2 Emission in NGC 6240. II. Detailed Comparison of Kinematic and Morphological Structures of the Warm and Cold Molecular Gas. AJ, 126(5):2291–2298.

Oknyansky, V. (2022). Changing looks of the nucleus of the Seyfert galaxy NGC 1566 compared with other changing-look AGNs. *Astronomische Nachrichten*, 343(1-2):e210080.

Oknyansky, V. L., Winkler, H., Tsygankov, S. S., Lipunov, V. M., Gorbovskoy, E. S., van Wyk, F., Buckley, D. A. H., and Tyurina, N. V. (2019). New changing look case in NGC 1566. MNRAS, 483(1):558–564.

Osterbrock, D. E. (1981). Seyfert galaxies with weak broad H alpha emission lines. ApJ, 249:462–470.

Osterbrock, D. E. and Ferland, G. J. (2006). *Astrophysics of gaseous nebulae and active galactic nuclei.*

Oya, S., Terada, H., Hayano, Y., Watanabe, M., Hattori, M., and Minowa, Y. (2016). Simultaneous seeing measurement through the subaru telescope in the visible and near-infrared bands for the wavelength dependence evaluation. *Experimental Astronomy*, 42(1):85–98.

Pacifici, C., Iyer, K. G., Mobasher, B., da Cunha, E., Acquaviva, V., Burgarella, D., Calistro Rivera, G., Carnall, A. C., Chang, Y.-Y., Chartab, N., Cooke, K. C., Fairhurst, C., Kartaltepe, J., Leja, J., Małek, K., Salmon, B., Torelli, M., Vidal-García, A., Boquien, M., Brammer, G. G., Brown, M. J. I., Capak, P. L., Chevallard, J., Circosta, C., Croton, D., Davidzon, I., Dickinson, M., Duncan, K. J., Faber, S. M., Ferguson, H. C., Fontana, A., Guo, Y., Haeussler, B., Hemmati, S., Jafariyazani, M., Kassin, S. A., Larson, R. L., Lee, B., Mantha, K. B., Marchi, F., Nayyeri, H., Newman, J. A., Pandya, V., Pforr, J., Reddy, N., Sanders, R., Shah, E., Shahidi, A., Stevans, M. L., Triani, D. P., Tyler, K. D., Vanderhoof, B. N., de la Vega, A., Wang, W., and Weston, M. E. (2023). The Art of Measuring Physical Parameters in Galaxies: A Critical Assessment of Spectral Energy Distribution Fitting Techniques. ApJ, 944(2):141.

Padovani, P., Alexander, D. M., Assef, R. J., De Marco, B., Giommi, P., Hickox, R. C., Richards, G. T., Smolčić, V., Hatziminaoglou, E., Mainieri, V., and Salvato, M. (2017). Active galactic nuclei: what's in a name? A&A Rev., 25(1):2.

Paggi, A., Fabbiano, G., Nardini, E., Karovska, M., Elvis, M., and Wang, J. (2022). Dissecting the Extended X-Ray Emission in the Merging Pair NGC 6240: Photoionization and Winds. ApJ, 927(2):166.

Panessa, F., Baldi, R. D., Laor, A., Padovani, P., Behar, E., and McHardy, I. (2019). The origin of radio emission from radio-quiet active galactic nuclei. *Nature Astronomy*, 3:387–396.

Parker, M. L., Schartel, N., Grupe, D., Komossa, S., Harrison, F., Kollatschny, W., Mikula, R., Santos-Lleó, M., and Tomás, L. (2019). X-ray spectra reveal the reawakening of the repeat changing-look AGN NGC 1566. MNRAS, 483(1):L88–L92.

Pastoriza, M. and Gerola, H. (1970). Spectral Variation in the Seyfert Galaxy NGC 1566. Astrophys. Lett., 6:155.

Peng, C. Y., Impey, C. D., Rix, H.-W., Kochanek, C. S., Keeton, C. R., Falco, E. E., Lehár, J., and McLeod, B. A. (2006). Probing the Coevolution of Supermassive Black Holes and Galaxies Using Gravitationally Lensed Quasar Hosts. ApJ, 649(2):616–634.

Penston, M. V. and Perez, E. (1984). An evolutionary link between Seyfert I and II galaxies. MNRAS, 211:33P–39.

Pereira-Santaella, M., Colina, L., García-Burillo, S., Alonso-Herrero, A., Arribas, S., Cazzoli, S., Emonts, B., Piqueras López, J., Planesas, P., Storchi Bergmann, T., Usero, A., and Villar-Martín, M. (2016). High-velocity extended molecular outflow in the star-formation dominated luminous infrared galaxy ESO 320-G030. A&A, 594:A81.

Pereira-Santaella, M., Colina, L., García-Burillo, S., Combes, F., Emonts, B., Aalto, S., Alonso-Herrero, A., Arribas, S., Henkel, C., Labiano, A., Muller, S., Piqueras López, J., Rigopoulou, D., and van der Werf, P. (2018). Spatially resolved cold molecular outflows in ULIRGs. A&A, 616:A171.

Perna, M., Arribas, S., Catalán-Torrecilla, C., Colina, L., Bellocchi, E., Fluetsch, A., Maiolino, R., Cazzoli, S., Hernán Caballero, A., Pereira Santaella, M., Piqueras López, J., and Rodríguez del Pino, B. (2020). MUSE view of Arp220: Kpc-scale multi-phase outflow and evidence for positive feedback. A&A, 643:A139.

Perna, M., Arribas, S., Marshall, M., D'Eugenio, F., Übler, H., Bunker, A., Charlot, S., Carniani, S., Jakobsen, P., Maiolino, R., Rodríguez Del Pino, B., Willott, C. J., Böker, T., Circosta, C., Cresci, G., Curti, M., Husemann, B., Kumari, N., Lamperti, I., Pérez-González, P. G., and Scholtz, J. (2023). The ultra-dense, interacting environment of a dual AGN at z ~ 3.3 revealed by JWST/NIRSpec IFS. *arXiv e-prints*, page arXiv:2304.06756.

Perna, M., Arribas, S., Pereira Santaella, M., Colina, L., Bellocchi, E., Catalán-Torrecilla, C., Cazzoli, S., Crespo Gómez, A., Maiolino, R., Piqueras López, J., and Rodríguez del Pino, B. (2021). Physics of ULIRGs with MUSE and ALMA: The PUMA project. I. Properties of the survey and first MUSE data results. A&A, 646:A101.

Perna, M., Brusa, M., Cresci, G., Comastri, A., Lanzuisi, G., Lusso, E., Marconi, A., Salvato, M., Zamorani, G., Bongiorno, A., Mainieri, V., Maiolino, R., and Mignoli, M. (2015a). Galaxy-wide outflows in z ~1.5 luminous obscured quasars revealed through near-IR slit-resolved spectroscopy. A&A, 574:A82.

Perna, M., Brusa, M., Salvato, M., Cresci, G., Lanzuisi, G., Berta, S., Delvecchio, I., Fiore, F., Lutz, D., Le Floc'h, E., Mainieri, V., and Riguccini, L. (2015b). SINFONI spectra of heavily obscured AGNs in COSMOS: Evidence of outflows in a MIR/O target at z ~2.5. A&A, 583:A72.

Perna, M., Lanzuisi, G., Brusa, M., Cresci, G., and Mignoli, M. (2017a). An X-ray/SDSS sample. II. AGN-driven outflowing gas plasma properties. A&A, 606:A96.

Perna, M., Lanzuisi, G., Brusa, M., Mignoli, M., and Cresci, G. (2017b). An X-ray/SDSS sample. I. Multi-phase outflow incidence and dependence on AGN luminosity. A&A, 603:A99.

Perrotta, S., Hamann, F., Zakamska, N. L., Alexandroff, R. M., Rupke, D., and Wylezalek, D. (2019). ERQs are the BOSS of quasar samples: the highest velocity [O III] quasar outflows. MNRAS, 488(3):4126–4148.

Peterson, B. M., Ferrarese, L., Gilbert, K. M., Kaspi, S., Malkan, M. A., Maoz, D., Merritt, D., Netzer, H., Onken, C. A., Pogge, R. W., Vestergaard, M., and Wandel, A. (2004). Central Masses and Broad-Line Region Sizes of Active Galactic Nuclei. II. A Homogeneous Analysis of a Large Reverberation-Mapping Database. ApJ, 613(2):682–699.

Pillepich, A., Nelson, D., Hernquist, L., Springel, V., Pakmor, R., Torrey, P., Weinberger, R., Genel, S., Naiman, J. P., Marinacci, F., and Vogelsberger, M. (2018). First results from the IllustrisTNG simulations: the stellar mass content of groups and clusters of galaxies. MNRAS, 475(1):648–675.

Piotrowska, J. M., Bluck, A. F. L., Maiolino, R., and Peng, Y. (2022). On the quenching of star formation in observed and simulated central galaxies: evidence for the role of integrated AGN feedback. MNRAS, 512(1):1052–1090.

Piqueras López, J., Colina, L., Arribas, S., Alonso-Herrero, A., and Bedregal, A. G. (2012). VLT-SINFONI integral field spectroscopy of low-z luminous and ultraluminous infrared galaxies. I. Atlas of the 2D gas structure. A&A, 546:A64.

Polletta, M., Courvoisier, T. J. L., Hooper, E. J., and Wilkes, B. J. (2000). The far-infrared emission of radio loud and radio quiet quasars. A&A, 362:75–96.

Prochaska, J., Hennawi, J., Westfall, K., Cooke, R., Wang, F., Hsyu, T., Davies, F., Farina, E., and Pelliccia, D. (2020). PypeIt: The Python Spectroscopic Data Reduction Pipeline. *The Journal of Open Source Software*, 5(56):2308.

Prochaska, J. X., Hennawi, J., Cooke, R., Westfall, K., Wang, F., Pelliccia, D., EmAstro, Roberson, M., Pickering, T. E., Badpandabear, Tiffanyhsyu, Ellsworth Bowers, T., Wasserman, A., Tejos, N., ShaneBechtel, Sien Tie, S., Villaume, A., Holden, B., Simha, S., and Marijana777 (2022). pypeit/PypeIt: Version 1.8.1. Zenodo.

Puccetti, S., Fiore, F., Risaliti, G., Capalbi, M., Elvis, M., and Nicastro, F. (2007). Rapid N_H changes in NGC 4151. MNRAS, 377(2):607–616.

Rafanelli, P., Schulz, H., Barbieri, C., Komossa, S., Mebold, U., Baruffolo, A., and Radovich, M. (1997). Subarcsec structures in the double nucleus of NGC6240 disclosed with HST at 370, 430 and 500 NM. A&A, 327:901–908.

Raimundo, S. I., Vestergaard, M., Koay, J. Y., Lawther, D., Casasola, V., and Peterson, B. M. (2019). MUSE observations of a changing-look AGN - I. The reappearance of the broad emission lines. MNRAS, 486(1):123–140.

Rakshit, S. and Woo, J.-H. (2018). A Census of Ionized Gas Outflows in Type 1 AGNs: Gas Outflows in AGNs. V. ApJ, 865(1):5.

Ramos Almeida, C., Pérez García, A. M., and Acosta-Pulido, J. A. (2009). Near-Infrared Spectroscopy of Seyfert Galaxies. Nuclear Activity and Stellar Population. ApJ, 694(2):1379–1394.

Read, J. I. and Trentham, N. (2005). The baryonic mass function of galaxies. *Philosophical Transactions of the Royal Society of London Series A*, 363(1837):2693.

Reefe, M., Satyapal, S., Sexton, R. O., Doan, S. M., Secrest, N. J., and Cann, J. M. (2022). CLASS: Coronal Line Activity Spectroscopic Survey. ApJ, 936(2):140.

Reeves, J. N., O'Brien, P. T., Braito, V., Behar, E., Miller, L., Turner, T. J., Fabian, A. C., Kaspi, S., Mushotzky, R., and Ward, M. (2009). A Compton-thick Wind in the High-luminosity Quasar, PDS 456. ApJ, 701(1):493–507.

Reimers, D., Hagen, H. J., Baade, R., Lopez, S., and Tytler, D. (2002). Discovery of a new quadruply lensed QSO: HS 0810+2554 - A brighter twin to PG 1115+080. A&A, 382:L26–L28.

Revalski, M., Meena, B., Martinez, F., Polack, G. E., Crenshaw, D. M., Kraemer, S. B., Collins, N. R., Fischer, T. C., Schmitt, H. R., Schmidt, J., Maksym, W. P., and Rafelski, M. (2021). Quantifying Feedback from Narrow Line Region Outflows in Nearby Active Galaxies. III. Results for the Seyfert 2 Galaxies Markarian 3, Markarian 78, and NGC 1068. ApJ, 910(2):139.

Ricci, C., Kara, E., Loewenstein, M., Trakhtenbrot, B., Arcavi, I., Remillard, R., Fabian, A. C., Gendreau, K. C., Arzoumanian, Z., Li, R., Ho, L. C., MacLeod, C. L., Cackett, E., Altamirano, D., Gandhi, P., Kosec, P., Pasham, D., Steiner, J., and Chan, C. H. (2020). The Destruction and Recreation of the X-Ray Corona in a Changing-look Active Galactic Nucleus. ApJ, 898(1):L1.

Ricci, C. and Trakhtenbrot, B. (2022). Changing-look Active Galactic Nuclei. *arXiv e-prints*, page arXiv:2211.05132.

Riffel, R., Mallmann, N. D., Rembold, S. B., Ilha, G. S., Riffel, R. A., Storchi-Bergmann, T., Ruschel-Dutra, D., Vazdekis, A., Martín-Navarro, I., Schimoia, J. S., Ramos Almeida, C., da Costa, L. N., Vila-Verde, G. C., and Gatto, L. (2023). Mapping the stellar population and gas excitation of MaNGA galaxies with MEGACUBES. Results for AGN versus control sample. MNRAS, 524(4):5640–5657.

Riffel, R., Rodríguez-Ardila, A., Aleman, I., Brotherton, M. S., Pastoriza, M. G., Bonatto, C., and Dors, O. L. (2013). Molecular hydrogen and [Fe II] in active galactic nuclei - III. Low-ionization nuclear emission-line region and star-forming galaxies. MNRAS, 430(3):2002–2017.

Riffel, R. A., Bianchin, M., Riffel, R., Storchi-Bergmann, T., Schönell, A. J., Dahmer-Hahn, L. G., Dametto, N. Z., and Diniz, M. R. (2021a). Gemini NIFS survey of feeding and feedback in nearby active galaxies - IV. Excitation. MNRAS, 503(4):5161–5178.

Riffel, R. A., Storchi-Bergmann, T., and Riffel, R. (2015). Feeding versus feedback in active galactic nuclei from near-infrared integral field spectroscopy - X. NGC 5929. MNRAS, 451(4):3587–3605.

Riffel, R. A., Storchi-Bergmann, T., Riffel, R., Bianchin, M., Zakamska, N. L., Ruschel-Dutra, D., Schönell, A. J., Rosario, D. J., Rodriguez-Ardila, A., Fischer, T. C., Davies, R. I., Dametto, N. Z., Dahmer-Hahn, L. G., Crenshaw, D. M., Burtscher, L., and Bentz, M. C. (2021b). The AGNIFS survey: distribution and excitation of the hot molecular and ionized gas in the inner kpc of nearby AGN hosts. MNRAS, 504(3):3265–3283.

Riffel, R. A., Storchi-Bergmann, T., Zakamska, N. L., and Riffel, R. (2020). Ionized and hot molecular outflows in the inner 500 pc of NGC 1275. MNRAS, 496(4):4857–4873.

Risaliti, G., Elvis, M., Fabbiano, G., Baldi, A., and Zezas, A. (2005). Rapid Compton-thick/Compton-thin Transitions in the Seyfert 2 Galaxy NGC 1365. ApJ, 623(2):L93–L96.

Risaliti, G., Elvis, M., Fabbiano, G., Baldi, A., Zezas, A., and Salvati, M. (2007). Occultation Measurement of the Size of the X-Ray-emitting Region in the Active Galactic Nucleus of NGC 1365. ApJ, 659(2):L111–L114.

Risaliti, G., Elvis, M., and Nicastro, F. (2002). Ubiquitous Variability of X-Ray-absorbing Column Densities in Seyfert 2 Galaxies. ApJ, 571(1):234–246.

Risaliti, G., Maiolino, R., and Bassani, L. (2000). The hard X-ray properties of the Seyfert nucleus in NGC 1365. A&A, 356:33–40.

Risaliti, G., Salvati, M., Elvis, M., Fabbiano, G., Baldi, A., Bianchi, S., Braito, V., Guainazzi, M., Matt, G., Miniutti, G., Reeves, J., Soria, R., and Zezas, A. (2009). The XMM-Newton long look of NGC 1365: uncovering of the obscured X-ray source. MNRAS, 393(1):L1–L5.

Risaliti, G., Sani, E., Maiolino, R., Marconi, A., Berta, S., Braito, V., Della Ceca, R., Franceschini, A., and Salvati, M. (2006). The Double Active Galactic Nucleus in NGC 6240 Revealed through 3-5 μm Spectroscopy. ApJ, 637(1):L17–L20.

Rizzo, F., Vegetti, S., Fraternali, F., and Di Teodoro, E. (2018). A novel 3D technique to study the kinematics of lensed galaxies. MNRAS, 481(4):5606–5629.

Röck, B., Vazdekis, A., Ricciardelli, E., Peletier, R. F., Knapen, J. H., and Falcón-Barroso, J. (2016). MILES extended: Stellar population synthesis models from the optical to the infrared. A&A, 589:A73.

Rogers, N. S. J., Skillman, E. D., Pogge, R. W., Berg, D. A., Moustakas, J., Croxall, K. V., and Sun, J. (2021). CHAOS. VI. Direct Abundances in NGC 2403. ApJ, 915(1):21.

Rojas, A. F., Sani, E., Gavignaud, I., Ricci, C., Lamperti, I., Koss, M., Trakhtenbrot, B., Schawinski, K., Oh, K., Bauer, F. E., Bischetti, M., Boissay-Malaquin, R., Bongiorno, A., Harrison, F., Kakkad, D., Masetti, N., Ricci, F., Shimizu, T., Stalevski, M., Stern, D., and Vietri, G. (2020). BAT AGN Spectroscopic Survey - XIX. Type 1 versus type 2 AGN dichotomy from the point of view of ionized outflows. MNRAS, 491(4):5867–5880.

Ross, N. R., Assef, R. J., Kochanek, C. S., Falco, E., and Poindexter, S. D. (2009). The UV-Mid-IR Spectral Energy Distribution of a z = 1.7 Quasar Host Galaxy. ApJ, 702(1):472–479.

Rumbaugh, N., Shen, Y., Morganson, E., Liu, X., Banerji, M., McMahon, R. G., Abdalla, F. B., Benoit-Lévy, A., Bertin, E., Brooks, D., Buckley-Geer, E., Capozzi, D., Carnero Rosell, A., Carrasco Kind, M., Carretero, J., Cunha, C. E., D'Andrea, C. B., da Costa, L. N., DePoy, D. L., Desai, S., Doel, P., Frieman, J., García-Bellido, J., Gruen, D., Gruendl, R. A., Gschwend, J., Gutierrez, G., Honscheid, K., James, D. J., Kuehn, K., Kuhlmann, S., Kuropatkin, N., Lima, M., Maia, M. A. G., Marshall, J. L., Martini, P., Menanteau, F., Plazas, A. A., Reil, K., Roodman, A., Sanchez, E., Scarpine, V., Schindler, R., Schubnell, M., Sheldon, E., Smith, M., Soares-Santos, M., Sobreira, F., Suchyta, E., Swanson, M. E. C., Walker, A. R., Wester, W., and DES Collaboration (2018). Extreme Variability Quasars from the Sloan Digital Sky Survey and the Dark Energy Survey. ApJ, 854(2):160.

Runnoe, J. C., Brotherton, M. S., and Shang, Z. (2012). Updating quasar bolometric luminosity corrections. MNRAS, 422(1):478–493.

Rupke, D. S., Veilleux, S., and Sanders, D. B. (2005). Outflows in Infrared-Luminous Starbursts at z < 0.5. I. Sample, Na I D Spectra, and Profile Fitting. ApJS, 160(1):87–114.

Rupke, D. S. N. and Veilleux, S. (2011). Integral Field Spectroscopy of Massive, Kiloparsec-scale Outflows in the Infrared-luminous QSO Mrk 231. ApJ, 729(2):L27.

Rupke, D. S. N. and Veilleux, S. (2013). The Multiphase Structure and Power Sources of Galactic Winds in Major Mergers. ApJ, 768(1):75.

Rupke, D. S. N. and Veilleux, S. (2015). Spatially Extended Na I D Resonant Emission and Absorption in the Galactic Wind of the Nearby Infrared-Luminous Quasar F05189-2524. ApJ, 801(2):126.

Rusu, C. E., Oguri, M., Minowa, Y., Iye, M., Inada, N., Oya, S., Kayo, I., Hayano, Y., Hattori, M., Saito, Y., Ito, M., Pyo, T.-S., Terada, H., Takami, H., and Watanabe, M. (2016). Subaru Telescope adaptive optics observations of gravitationally lensed quasars in the Sloan Digital Sky Survey. MNRAS, 458(1):2–55.

Saito, T., Iono, D., Ueda, J., Espada, D., Sliwa, K., Nakanishi, K., Lu, N., Xu, C. K., Michiyama, T., Kaneko, H., Yamashita, T., Ando, M., Yun, M. S., Motohara, K., and Kawabe, R. (2018). Imaging the molecular outflows of the prototypical ULIRG NGC 6240 with ALMA. MNRAS, 475(1):L52–L56.

Sánchez, S. F., Pérez, E., Sánchez-Blázquez, P., García-Benito, R., Ibarra-Mede, H. J., González, J. J., Rosales-Ortega, F. F., Sánchez-Menguiano, L., Ascasibar, Y., Bitsakis, T., Law, D., Cano-Díaz, M., López-Cobá, C., Marino, R. A., Gil de Paz, A., López-Sánchez, A. R., Barrera-Ballesteros, J., Galbany, L., Mast, D., Abril-Melgarejo, V., and Roman-Lopes, A. (2016). Pipe3D, a pipeline to analyze Integral Field Spectroscopy Data: II. Analysis sequence and CALIFA dataproducts. Rev. Mexicana Astron. Astrofis., 52:171–220.

Sanders, D. B. and Mirabel, I. F. (1996). Luminous Infrared Galaxies. ARA&A, 34:749.

Sanders, R. L., Shapley, A. E., Kriek, M., Reddy, N. A., Freeman, W. R., Coil, A. L., Siana, B., Mobasher, B., Shivaei, I., Price, S. H., and de Groot, L. (2016). The MOSDEF Survey: Electron Density and Ionization Parameter at z $\sim$2.3. ApJ, 816(1):23.

Sani, E., Marconi, A., Hunt, L. K., and Risaliti, G. (2011). The Spitzer/IRAC view of black hole-bulge scaling relations. MNRAS, 413(2):1479–1494.

Sani, E., Risaliti, G., Salvati, M., Maiolino, R., Marconi, A., Berta, S., Braito, V., Della Ceca, R., and Franceschini, A. (2008). 3-5 μm Spectroscopy of Obscured AGNs in ULIRGs. ApJ, 675(1):96–105.

Sarzi, M., Kaviraj, S., Nedelchev, B., Tiffany, J., Shabala, S. S., Deller, A. T., and Middelberg, E. (2016). Cold-gas outflows in typical low-redshift galaxies are driven by star formation, not AGN. MNRAS, 456(1):L25–L29.

Scannapieco, C., Wadepuhl, M., Parry, O. H., Navarro, J. F., Jenkins, A., Springel, V., Teyssier, R., Carlson, E., Couchman, H. M. P., Crain, R. A., Dalla Vecchia, C., Frenk, C. S., Kobayashi, C., Monaco, P., Murante, G., Okamoto, T., Quinn, T., Schaye, J., Stinson, G. S., Theuns, T., Wadsley, J., White, S. D. M., and Woods, R. (2012). The Aquila comparison project: the effects of feedback and numerical methods on simulations of galaxy formation. MNRAS, 423(2):1726–1749.

Schaerer, D., Fragos, T., and Izotov, Y. I. (2019). X-ray binaries as the origin of nebular He II emission in low-metallicity star-forming galaxies. A&A, 622:L10.

Scharwächter, J., McGregor, P. J., Dopita, M. A., and Beck, T. L. (2013). Kinematics and excitation of the molecular hydrogen accretion disc in NGC 1275. MNRAS, 429(3):2315–2332.

Schawinski, K., Thomas, D., Sarzi, M., Maraston, C., Kaviraj, S., Joo, S.-J., Yi, S. K., and Silk, J. (2007). Observational evidence for AGN feedback in early-type galaxies. MNRAS, 382(4):1415–1431.

Schawinski, K., Urry, C. M., Simmons, B. D., Fortson, L., Kaviraj, S., Keel, W. C., Lintott, C. J., Masters, K. L., Nichol, R. C., Sarzi, M., Skibba, R., Treister, E., Willett, K. W., Wong, O. I., and Yi, S. K. (2014). The green valley is a red herring: Galaxy Zoo reveals two evolutionary pathways towards quenching of star formation in early- and late-type galaxies. MNRAS, 440(1):889–907.

Schawinski, K., Urry, C. M., Virani, S., Coppi, P., Bamford, S. P., Treister, E., Lintott, C. J., Sarzi, M., Keel, W. C., Kaviraj, S., Cardamone, C. N., Masters, K. L., Ross, N. P., Andreescu, D., Murray, P., Nichol, R. C., Raddick, M. J., Slosar, A., Szalay, A. S., Thomas, D., and Vandenberg, J. (2010). Galaxy Zoo: The Fundamentally Different Co-Evolution of Supermassive Black Holes and Their Early- and Late-Type Host Galaxies. ApJ, 711(1):284–302.

Schawinski, K., Virani, S., Simmons, B., Urry, C. M., Treister, E., Kaviraj, S., and Kushkuley, B. (2009). Do Moderate-Luminosity Active Galactic Nuclei Suppress Star Formation? ApJ, 692(1):L19–L23.

Schaye, J., Crain, R. A., Bower, R. G., Furlong, M., Schaller, M., Theuns, T., Dalla Vecchia, C., Frenk, C. S., McCarthy, I. G., Helly, J. C., Jenkins, A., Rosas-Guevara, Y. M., White, S. D. M., Baes, M., Booth, C. M., Camps, P., Navarro, J. F., Qu, Y., Rahmati, A., Sawala, T., Thomas, P. A., and Trayford, J. (2015). The EAGLE project: simulating the evolution and assembly of galaxies and their environments. MNRAS, 446(1):521–554.

Schechter, P. (1976). An analytic expression for the luminosity function for galaxies. ApJ, 203:297–306.

Schmidt, M. and Green, R. F. (1983). Quasar evolution derived from the Palomar bright quasar survey and other complete quasar surveys. ApJ, 269:352–374.

Scholtz, J., Harrison, C. M., Rosario, D. J., Alexander, D. M., Chen, C. C., Kakkad, D., Mainieri, V., Tiley, A. L., Turner, O., Cirasuolo, M., Sharples, R. M., and Stach, S. (2020). KASHz: No evidence for ionised outflows instantaneously suppressing star formation in moderate luminosity AGN at z ∼ 1.4-2.6. MNRAS, 492(3):3194–3216.

Schulz, R., Morganti, R., Nyland, K., Paragi, Z., Mahony, E. K., and Oosterloo, T. (2018). Mapping the neutral atomic hydrogen gas outflow in the restarted radio galaxy 3C 236. A&A, 617:A38.

Schutte, Z. and Reines, A. E. (2022). Black-hole-triggered star formation in the dwarf galaxy Henize 2-10. Nature, 601(7893):329–333.

Scoville, N., Sheth, K., Walter, F., Manohar, S., Zschaechner, L., Yun, M., Koda, J., Sanders, D., Murchikova, L., Thompson, T., Robertson, B., Genzel, R., Hernquist, L., Tacconi, L., Brown, R., Narayanan, D., Hayward, C. C., Barnes, J., Kartaltepe, J., Davies, R., van der Werf, P., and Fomalont, E. (2015). ALMA Imaging of HCN, CS, and Dust in Arp 220 and NGC 6240. ApJ, 800(1):70.

Scoville, N. Z., Evans, A. S., Thompson, R., Rieke, M., Hines, D. C., Low, F. J., Dinshaw, N., Surace, J. A., and Armus, L. (2000). NICMOS Imaging of Infrared-Luminous Galaxies. AJ, 119(3):991–1061.

Shakura, N. I. and Sunyaev, R. A. (1973). Black holes in binary systems. Observational appearance. A&A, 24:337–355.

Shankar, F., Weinberg, D. H., and Miralda-Escudé, J. (2009). Self-Consistent Models of the AGN and Black Hole Populations: Duty Cycles, Accretion Rates, and the Mean Radiative Efficiency. ApJ, 690(1):20–41.

Shankar, F., Weinberg, D. H., and Miralda-Escudé, J. (2013). Accretion-driven evolution of black holes: Eddington ratios, duty cycles and active galaxy fractions. MNRAS, 428(1):421–446.

Shapley, A. E., Steidel, C. C., Pettini, M., and Adelberger, K. L. (2003). Rest-Frame Ultraviolet Spectra of z˜3 Lyman Break Galaxies. ApJ, 588(1):65–89.

Shapovalova, A. I., Popović, L. Č., Burenkov, A. N., Chavushyan, V. H., Ilić, D., Kovačević, A., Bochkarev, N. G., and León-Tavares, J. (2010). Long-term variability of the optical spectra of NGC 4151. II. Evolution of the broad Hα and Hβ emission-line profiles. A&A, 509:A106.

Shappee, B. J., Prieto, J. L., Grupe, D., Kochanek, C. S., Stanek, K. Z., De Rosa, G., Mathur, S., Zu, Y., Peterson, B. M., Pogge, R. W., Komossa, S., Im, M., Jencson, J., Holoien, T. W. S., Basu, U., Beacom, J. F., Szczygieł, D. M., Brimacombe, J., Adams, S., Campillay, A., Choi, C., Contreras, C., Dietrich, M., Dubberley, M., Elphick, M., Foale, S., Giustini, M., Gonzalez, C., Hawkins, E., Howell, D. A., Hsiao, E. Y., Koss, M., Leighly, K. M., Morrell, N., Mudd, D., Mullins, D., Nugent, J. M., Parrent, J., Phillips, M. M., Pojmanski, G., Rosing, W., Ross, R., Sand, D., Terndrup, D. M., Valenti, S., Walker, Z., and Yoon, Y. (2014). The

Man behind the Curtain: X-Rays Drive the UV through NIR Variability in the 2013 Active Galactic Nucleus Outburst in NGC 2617. ApJ, 788(1):48.

Sharples, R., Bender, R., Agudo Berbel, A., Bezawada, N., Castillo, R., Cirasuolo, M., Davidson, G., Davies, R., Dubbeldam, M., Fairley, A., Finger, G., Förster Schreiber, N., Gonte, F., Hess, A., Jung, I., Lewis, I., Lizon, J. L., Muschielok, B., Pasquini, L., Pirard, J., Popovic, D., Ramsay, S., Rees, P., Richter, J., Riquelme, M., Rodrigues, M., Saviane, I., Schlichter, J., Schmidtobreick, L., Segovia, A., Smette, A., Szeifert, T., van Kesteren, A., Wegner, M., and Wiezorrek, E. (2013). First Light for the KMOS Multi-Object Integral-Field Spectrometer. *The Messenger*, 151:21–23.

Shen, Y. (2021). Extreme Variability and Episodic Lifetime of Quasars. ApJ, 921(1):70.

Shen, Y., Brandt, W. N., Richards, G. T., Denney, K. D., Greene, J. E., Grier, C. J., Ho, L. C., Peterson, B. M., Petitjean, P., Schneider, D. P., Tao, C., and Trump, J. R. (2016). The Sloan Digital Sky Survey Reverberation Mapping Project: Velocity Shifts of Quasar Emission Lines. ApJ, 831(1):7.

Sheng, Z., Wang, T., Jiang, N., Yang, C., Yan, L., Dou, L., and Peng, B. (2017). Mid-infrared Variability of Changing-look AGNs. ApJ, 846(1):L7.

Shin, J., Woo, J.-H., Chung, A., Baek, J., Cho, K., Kang, D., and Bae, H.-J. (2019). Positive and Negative Feedback of AGN Outflows in NGC 5728. ApJ, 881(2):147.

Shirazi, M. and Brinchmann, J. (2012). Strongly star forming galaxies in the local Universe with nebular He IIλ4686 emission. MNRAS, 421(2):1043–1063.

Sijacki, D., Vogelsberger, M., Genel, S., Springel, V., Torrey, P., Snyder, G. F., Nelson, D., and Hernquist, L. (2015). The Illustris simulation: the evolving population of black holes across cosmic time. MNRAS, 452(1):575–596.

Silk, J. (2013). Unleashing Positive Feedback: Linking the Rates of Star Formation, Supermassive Black Hole Accretion, and Outflows in Distant Galaxies. ApJ, 772(2):112.

Silk, J. and Norman, C. (2009). Global Star Formation Revisited. ApJ, 700(1):262–275.

Silk, J. and Rees, M. J. (1998). Quasars and galaxy formation. A&A, 331:L1–L4.

Smith, H. J. and Hoffleit, D. (1963a). Light Variability and Nature of 3C273. AJ, 68:292.

Smith, H. J. and Hoffleit, D. (1963b). Light Variations in the Superluminous Radio Galaxy 3C273. Nature, 198(4881):650–651.

Soltan, A. (1982). Masses of quasars. MNRAS, 200:115–122.

Spingola, C. and Barnacka, A. (2020). Constraining VLBI-optical offsets in high redshift galaxies using strong gravitational lensing. MNRAS, 494(2):2312–2326.

Spoon, H. W. W., Farrah, D., Lebouteiller, V., González-Alfonso, E., Bernard-Salas, J., Urrutia, T., Rigopoulou, D., Westmoquette, M. S., Smith, H. A., Afonso, J., Pearson, C., Cormier, D., Efstathiou, A., Borys, C., Verma, A., Etxaluze, M., and Clements, D. L. (2013). Diagnostics of AGN-Driven Molecular Outflows in ULIRGs from Herschel-PACS Observations of OH at 119 μm. ApJ, 775(2):127.

Springel, V., Di Matteo, T., and Hernquist, L. (2005). Modelling feedback from stars and black holes in galaxy mergers. MNRAS, 361(3):776–794.

Springel, V., Pakmor, R., Pillepich, A., Weinberger, R., Nelson, D., Hernquist, L., Vogelsberger, M., Genel, S., Torrey, P., Marinacci, F., and Naiman, J. (2018). First results from the IllustrisTNG simulations: matter and galaxy clustering. MNRAS, 475(1):676–698.

Stacey, H. R., McKean, J. P., Powell, D. M., Vegetti, S., Rizzo, F., Spingola, C., Auger, M. W., Ivison, R. J., and van der Werf, P. P. (2021). The rocky road to quiescence: compaction and quenching of quasar host galaxies at z ∼ 2. MNRAS, 500(3):3667–3688.

Steffen, A. T., Strateva, I., Brandt, W. N., Alexander, D. M., Koekemoer, A. M., Lehmer, B. D., Schneider, D. P., and Vignali, C. (2006). The X-Ray-to-Optical Properties of Optically Selected Active Galaxies over Wide Luminosity and Redshift Ranges. AJ, 131(6):2826–2842.

Steidel, C. C., Erb, D. K., Shapley, A. E., Pettini, M., Reddy, N., Bogosavljević, M., Rudie, G. C., and Rakic, O. (2010). The Structure and Kinematics of the Circumgalactic Medium from Far-ultraviolet Spectra of z $\underset{\sim}{=}$ 2-3 Galaxies. ApJ, 717(1):289–322.

Stern, D., Assef, R. J., Benford, D. J., Blain, A., Cutri, R., Dey, A., Eisenhardt, P., Griffith, R. L., Jarrett, T. H., Lake, S., Masci, F., Petty, S., Stanford, S. A., Tsai, C.-W., Wright, E. L., Yan, L., Harrison, F., and Madsen, K. (2012). Mid-infrared Selection of Active Galactic Nuclei with the Wide-Field Infrared Survey Explorer. I. Characterizing WISE-selected Active Galactic Nuclei in COSMOS. ApJ, 753(1):30.

Stern, D., Eisenhardt, P., Gorjian, V., Kochanek, C. S., Caldwell, N., Eisenstein, D., Brodwin, M., Brown, M. J. I., Cool, R., Dey, A., Green, P., Jannuzi, B. T., Murray, S. S., Pahre, M. A., and Willner, S. P. (2005). Mid-Infrared Selection of Active Galaxies. ApJ, 631(1):163–168.

Stern, D., Kirkpatrick, J. D., Allen, L. E., Bian, C., Blain, A., Brand, K., Brodwin, M., Brown, M. J. I., Cool, R., Desai, V., Dey, A., Eisenhardt, P., Gonzalez, A., Jannuzi, B. T., Menendez-Delmestre, K., Smith, H. A., Soifer, B. T., Tiede, G. P., and Wright, E. (2007). Mid-Infrared Selection of Brown Dwarfs and High-Redshift Quasars. ApJ, 663(1):677–685.

Stern, J. and Laor, A. (2012). Type 1 AGN at low z - II. The relative strength of narrow lines and the nature of intermediate type AGN. MNRAS, 426(4):2703–2718.

Sternberg, A. and Dalgarno, A. (1989). The Infrared Response of Molecular Hydrogen Gas to Ultraviolet Radiation: High-Density Regions. ApJ, 338:197.

Storchi-Bergmann, T., Baldwin, J. A., and Wilson, A. S. (1993). Double-peaked Broad Line Emission from the LINER Nucleus of NGC 1097. ApJ, 410:L11.

Storchi-Bergmann, T., Lopes, R. D. S., McGregor, P. J., Riffel, R. A., Beck, T., and Martini, P. (2010). Feeding versus feedback in NGC4151 probed with Gemini NIFS - II. Kinematics. MNRAS, 402(2):819–835.

Storchi-Bergmann, T. and Schnorr-Müller, A. (2019). Observational constraints on the feeding of supermassive black holes. *Nature Astronomy*, 3:48–61.

Strateva, I., Ivezić, Ž., Knapp, G. R., Narayanan, V. K., Strauss, M. A., Gunn, J. E., Lupton, R. H., Schlegel, D., Bahcall, N. A., Brinkmann, J., Brunner, R. J., Budavári, T., Csabai, I., Castander, F. J., Doi, M., Fukugita, M., Győry, Z., Hamabe, M., Hennessy, G., Ichikawa, T., Kunszt, P. Z., Lamb, D. Q., McKay, T. A., Okamura, S., Racusin, J., Sekiguchi, M., Schneider, D. P., Shimasaku, K., and York, D. (2001). Color Separation of Galaxy Types in the Sloan Digital Sky Survey Imaging Data. AJ, 122(4):1861–1874.

Sturm, E., González-Alfonso, E., Veilleux, S., Fischer, J., Graciá-Carpio, J., Hailey-Dunsheath, S., Contursi, A., Poglitsch, A., Sternberg, A., Davies, R., Genzel, R., Lutz, D., Tacconi, L., Verma, A., Maiolino, R., and de Jong, J. A. (2011). Massive Molecular Outflows and Negative Feedback in ULIRGs Observed by Herschel-PACS. ApJ, 733(1):L16.

Sugai, H., Malkan, M. A., Ward, M. J., Davies, R. I., and McLean, I. S. (1997). Excitation Mechanism of Molecular Hydrogen Emission in NGC 6240. ApJ, 481(1):186–192.

Sulentic, J. W., Zwitter, T., Marziani, P., and Dultzin-Hacyan, D. (2000). Eigenvector 1: An Optimal Correlation Space for Active Galactic Nuclei. ApJ, 536(1):L5–L9.

Tacconi, L. J., Genzel, R., Tecza, M., Gallimore, J. F., Downes, D., and Scoville, N. Z. (1999). Gasdynamics in the Luminous Merger NGC 6240. ApJ, 524(2):732–745.

Tadhunter, C. (2016). Radio AGN in the local universe: unification, triggering and evolution. A&A Rev., 24(1):10.

Talia, M., Mignoli, M., Cimatti, A., Kurk, J., Berta, S., Bolzonella, M., Cassata, P., Daddi, E., Dickinson, M., Franceschini, A., Halliday, C., Pozzetti, L., Renzini, A., Rodighiero, G., Rosati, P., and Zamorani, G. (2012). GMASS ultradeep spectroscopy of galaxies at z ~2. VI. Star formation, extinction, and gas outflows from UV spectra. A&A, 539:A61.

Tanaka, M., Hasegawa, T., and Gatley, I. (1991). Infrared Fluorescence of H 2 in NGC 6240: A Starburst Origin for the H 2 Luminosity. ApJ, 374:516.

Tanimoto, A., Ueda, Y., Odaka, H., Kawaguchi, T., Fukazawa, Y., and Kawamuro, T. (2019). XCLUMPY: X-Ray Spectral Model from Clumpy Torus and Its Application to the Circinus Galaxy. ApJ, 877(2):95.

Tecza, M., Genzel, R., Tacconi, L. J., Anders, S., Tacconi-Garman, L. E., and Thatte, N. (2000). Stellar Dynamics and the Implications on the Merger Evolution in NGC 6240. ApJ, 537(1):178–190.

Terrell, J. (1967). Luminosity Fluctuations and a Local Model of Quasi-Stellar Objects. ApJ, 147:827.

Thompson, T. A., Fabian, A. C., Quataert, E., and Murray, N. (2015). Dynamics of dusty radiation-pressure-driven shells and clouds: fast outflows from galaxies, star clusters, massive stars, and AGN. MNRAS, 449(1):147–161.

Thorne, K. S. (1974). Disk-Accretion onto a Black Hole. II. Evolution of the Hole. ApJ, 191:507–520.

Thuan, T. X. and Izotov, Y. I. (2005). High-Ionization Emission in Metal-deficient Blue Compact Dwarf Galaxies. ApJS, 161(2):240–270.

Tombesi, F., Cappi, M., Reeves, J. N., and Braito, V. (2012). Evidence for ultrafast outflows in radio-quiet AGNs - III. Location and energetics. MNRAS, 422(1):L1–L5.

Tombesi, F., Cappi, M., Reeves, J. N., Palumbo, G. G. C., Braito, V., and Dadina, M. (2011). Evidence for Ultra-fast Outflows in Radio-quiet Active Galactic Nuclei. II. Detailed Photoionization Modeling of Fe K-shell Absorption Lines. ApJ, 742(1):44.

Tombesi, F., Cappi, M., Reeves, J. N., Palumbo, G. G. C., Yaqoob, T., Braito, V., and Dadina, M. (2010). Evidence for ultra-fast outflows in radio-quiet AGNs. I. Detection and statistical incidence of Fe K-shell absorption lines. A&A, 521:A57.

Tombesi, F., Meléndez, M., Veilleux, S., Reeves, J. N., González-Alfonso, E., and Reynolds, C. S. (2015). Wind from the black-hole accretion disk driving a molecular outflow in an active galaxy. Nature, 519(7544):436–438.

Tozzi, G., Cresci, G., Marasco, A., Nardini, E., Marconi, A., Mannucci, F., Chartas, G., Rizzo, F., Amiri, A., Brusa, M., Comastri, A., Dadina, M., Lanzuisi, G., Mainieri, V., Mingozzi, M., Perna, M., Venturi, G., and Vignali, C. (2021). Connecting X-ray nuclear winds with galaxy-scale ionised outflows in two $z \sim 1.5$ lensed quasars. A&A, 648:A99.

Tozzi, G., Lusso, E., Casetti, L., Romoli, M., Andreuzzi, G., Montoya Arroyave, I., Nardini, E., Cresci, G., Middei, R., Bertolini, S., Calabretto, P., Cammelli, V., Cuadra, F., Dalla Ragione, M., Marconcini, C., Miceli, A., Mini, I., Palazzini, M., Rotellini, G., Saccardi, A., Samà, L., Sangalli, M., Serafini, L., and Spaccino, F. (2022). The optically elusive, changing-look active nucleus in NGC 4156. A&A, 667:L12.

Tozzi, G., Maiolino, R., Cresci, G., Piotrowska, J. M., Belfiore, F., Curti, M., Mannucci, F., and Marconi, A. (2023). Unveiling hidden active nuclei in MaNGA star-forming galaxies with He II λ4686 line emission. MNRAS, 521(1):1264–1276.

Trakhtenbrot, B., Arcavi, I., Ricci, C., Tacchella, S., Stern, D., Netzer, H., Jonker, P. G., Horesh, A., Mejía-Restrepo, J. E., Hosseinzadeh, G., Hallefors, V., Howell, D. A., McCully, C., Baloković, M., Heida, M., Kamraj, N., Lansbury, G. B., Wyrzykowski, Ł., Gromadzki, M., Hamanowicz, A., Cenko, S. B., Sand, D. J., Hsiao, E. Y., Phillips, M. M., Diamond, T. R., Kara, E., Gendreau, K. C., Arzoumanian, Z., and Remillard, R. (2019). A new class of flares from accreting supermassive black holes. *Nature Astronomy*, 3:242–250.

Tran, H. D., Osterbrock, D. E., and Martel, A. (1992). Extreme Spectral Variations of the Seyfert Galaxy Markarian 993. AJ, 104:2072.

Treister, E., Messias, H., Privon, G. C., Nagar, N., Medling, A. M., U, V., Bauer, F. E., Cicone, C., Muñoz, L. B., Evans, A. S., Muller-Sanchez, F., Comerford, J. M., Armus, L., Chang, C.-S., Koss, M., Venturi, G., Schawinski, K., Casey, C., Urry, C. M., Sanders, D. B., Scoville, N., and Sheth, K. (2020). The Molecular Gas in the NGC 6240 Merging Galaxy System at the Highest Spatial Resolution. ApJ, 890(2):149.

Tremaine, S., Gebhardt, K., Bender, R., Bower, G., Dressler, A., Faber, S. M., Filippenko, A. V., Green, R., Grillmair, C., Ho, L. C., Kormendy, J., Lauer, T. R., Magorrian, J., Pinkney, J., and Richstone, D. (2002). The Slope of the Black Hole Mass versus Velocity Dispersion Correlation. ApJ, 574(2):740–753.

Trussler, J., Maiolino, R., Maraston, C., Peng, Y., Thomas, D., Goddard, D., and Lian, J. (2020). Both starvation and outflows drive galaxy quenching. MNRAS, 491(4):5406–5434.

Übler, H., Maiolino, R., Curtis-Lake, E., Pérez-González, P. G., Curti, M., Perna, M., Arribas, S., Charlot, S., Marshall, M. A., D'Eugenio, F., Scholtz, J., Bunker, A., Carniani, S., Ferruit, P., Jakobsen, P., Rix, H.-W., Rodríguez Del Pino, B., Willott, C. J., Boeker, T., Cresci, G., Jones, G. C., Kumari, N., and Rawle, T. (2023). GA-NIFS: A massive black hole in a low-metallicity AGN at z ∼ 5.55 revealed by JWST/NIRSpec IFS. A&A, 677:A145.

Ueda, Y., Akiyama, M., Ohta, K., and Miyaji, T. (2003). Cosmological Evolution of the Hard X-Ray Active Galactic Nucleus Luminosity Function and the Origin of the Hard X-Ray Background. ApJ, 598(2):886–908.

Ulrich, M.-H., Maraschi, L., and Urry, C. M. (1997). Variability of Active Galactic Nuclei. ARA&A, 35:445–502.

Umeda, H., Ouchi, M., Nakajima, K., Isobe, Y., Aoyama, S., Harikane, Y., Ono, Y., and Matsumoto, A. (2022). EMPRESS. VII. Ionizing Spectrum Shapes of Extremely Metal-poor Galaxies: Uncovering the Origins of Strong He II and the Impact on Cosmic Reionization. ApJ, 930(1):37.

Urry, C. M. and Padovani, P. (1995). Unified Schemes for Radio-Loud Active Galactic Nuclei. PASP, 107:803.

Uttley, P., McHardy, I. M., and Vaughan, S. (2005). Non-linear X-ray variability in X-ray binaries and active galaxies. MNRAS, 359(1):345–362.

Vacca, W. D., Cushing, M. C., and Rayner, J. T. (2003). A Method of Correcting Near-Infrared Spectra for Telluric Absorption. PASP, 115(805):389–409.

van der Werf, P. P., Genzel, R., Krabbe, A., Blietz, M., Lutz, D., Drapatz, S., Ward, M. J., and Forbes, D. A. (1993). Near-Infrared Line Imaging of NGC 6240: Collision Shock and Nuclear Starburst. ApJ, 405:522.

Vanden Berk, D. E., Wilhite, B. C., Kron, R. G., Anderson, S. F., Brunner, R. J., Hall, P. B., Ivezić, Ž., Richards, G. T., Schneider, D. P., York, D. G., Brinkmann, J. V., Lamb, D. Q., Nichol, R. C., and Schlegel, D. J. (2004). The Ensemble Photometric Variability of ~25,000 Quasars in the Sloan Digital Sky Survey. ApJ, 601(2):692–714.

Vaona, L., Ciroi, S., Di Mille, F., Cracco, V., La Mura, G., and Rafanelli, P. (2012). Spectral properties of the narrow-line region in Seyfert galaxies selected from the SDSS-DR7. MNRAS, 427(2):1266–1283.

Vaughan, S., Reeves, J., Warwick, R., and Edelson, R. (1999). X-ray spectral complexity in narrow-line Seyfert 1 galaxies. MNRAS, 309(1):113–124.

Vayner, A., Wright, S. A., Murray, N., Armus, L., Boehle, A., Cosens, M., Larkin, J. E., Mieda, E., and Walth, G. (2021a). A Spatially Resolved Survey of Distant Quasar Host Galaxies. I. Dynamics of Galactic Outflows. ApJ, 919(2):122.

Vayner, A., Zakamska, N. L., Riffel, R. A., Alexandroff, R., Cosens, M., Hamann, F., Perrotta, S., Rupke, D. S. N., Bergmann, T. S., Veilleux, S., Walth, G., Wright, S., and Wylezalek, D. (2021b). Powerful winds in high-redshift obscured and red quasars. MNRAS, 504(3):4445–4459.

Vegetti, S. and Koopmans, L. V. E. (2009). Bayesian strong gravitational-lens modelling on adaptive grids: objective detection of mass substructure in Galaxies. MNRAS, 392(3):945–963.

Veilleux, S. (1991). A Study of the Structure and Kinematics of the Narrow-Line Region in Seyfert Galaxies. II. Analysis of the Line-Profile Parameters. ApJS, 75:383.

Veilleux, S., Kim, D. C., and Sanders, D. B. (2002). Optical and Near-Infrared Imaging of the IRAS 1 Jy Sample of Ultraluminous Infrared Galaxies. II. The Analysis. ApJS, 143(2):315–376.

Veilleux, S., Liu, W., Vayner, A., Wylezalek, D., Rupke, D. S. N., Zakamska, N. L., Ishikawa, Y., Bertemes, C., Barrera-Ballesteros, J. K., Chen, H.-W., Diachenko, N., Goulding, A. D., Greene, J. E., Hainline, K. N., Hamann, F., Heckman, T., Johnson, S. D., Grace Lim, H. X., Lutz, D., Lützgendorf, N., Mainieri, V., Maiolino, R., McCrory, R., Murphree, G., Nesvadba, N. P. H., Ogle, P., Sankar, S., Sturm, E., and Whitesell, L. (2023). First Results from the JWST Early Release Science Program Q3D: The Warm Ionized Gas Outflow in z 1.6 Quasar XID 2028 and Its Impact on the Host Galaxy. ApJ, 953(1):56.

Veilleux, S., Meléndez, M., Sturm, E., Gracia-Carpio, J., Fischer, J., González-Alfonso, E., Contursi, A., Lutz, D., Poglitsch, A., Davies, R., Genzel, R., Tacconi, L., de Jong, J. A., Sternberg, A., Netzer, H., Hailey-Dunsheath, S., Verma, A., Rupke, D. S. N., Maiolino, R., Teng, S. H., and Polisensky, E. (2013). Fast Molecular Outflows in Luminous Galaxy Mergers: Evidence for Quasar Feedback from Herschel. ApJ, 776(1):27.

Veilleux, S. and Osterbrock, D. E. (1987). Spectral Classification of Emission-Line Galaxies. ApJS, 63:295.

Venturi, G., Cresci, G., Marconi, A., Mingozzi, M., Nardini, E., Carniani, S., Mannucci, F., Marasco, A., Maiolino, R., Perna, M., Treister, E., Bland-Hawthorn, J., and Gallimore, J. (2021). MAGNUM survey: Compact jets causing large turmoil in galaxies. Enhanced line widths perpendicular to radio jets as tracers of jet-ISM interaction. A&A, 648:A17.

Venturi, G., Nardini, E., Marconi, A., Carniani, S., Mingozzi, M., Cresci, G., Mannucci, F., Risaliti, G., Maiolino, R., Balmaverde, B., Bongiorno, A., Brusa, M., Capetti, A., Cicone, C., Ciroi, S., Feruglio, C., Fiore, F., Gallazzi, A., La Franca, F., Mainieri, V., Matsuoka, K., Nagao, T., Perna, M., Piconcelli, E., Sani, E., Tozzi, P., and Zibetti, S. (2018). MAGNUM survey: A MUSE-Chandra resolved view on ionized outflows and photoionization in the Seyfert galaxy NGC1365. A&A, 619:A74.

Vignali, C., Iwasawa, K., Comastri, A., Gilli, R., Lanzuisi, G., Ranalli, P., Cappelluti, N., Mainieri, V., Georgantopoulos, I., Carrera, F. J., Fritz, J., Brusa, M., Brandt, W. N., Bauer, F. E., Fiore, F., and Tombesi, F. (2015). The XMM deep survey in the CDF-S. IX. An X-ray outflow in a luminous obscured quasar at $z \approx 1.6$. A&A, 583:A141.

Vika, M., Driver, S. P., Cameron, E., Kelvin, L., and Robotham, A. (2012). The near-IR M_{bh}-L and M_{bh}-n relations. MNRAS, 419(3):2264–2292.

Villar Martín, M., Emonts, B., Humphrey, A., Cabrera Lavers, A., and Binette, L. (2014). The triggering mechanism and properties of ionized outflows in the nearest obscured quasars. MNRAS, 440(4):3202–3219.

Vittoria Zanchettin, M., Feruglio, C., Massardi, M., Lapi, A., Bischetti, M., Cantalupo, S., Fiore, F., Bongiorno, A., Malizia, A., Marinucci, A., Molina, M., Piconcelli, E., Tombesi, F., Travascio, A., Tozzi, G., and Tripodi, R. (2023). NGC 2992: The interplay between the multiphase disk, wind and radio bubbles. *arXiv e-prints*, page arXiv:2308.04108.

Vogelsberger, M., Genel, S., Springel, V., Torrey, P., Sijacki, D., Xu, D., Snyder, G., Nelson, D., and Hernquist, L. (2014). Introducing the Illustris Project: simulating the coevolution of dark and visible matter in the Universe. MNRAS, 444(2):1518–1547.

Wadadekar, Y. (2004). Radio emission from AGN detected by the VLA FIRST survey. A&A, 416:35–40.

Wake, D. A., Bundy, K., Diamond-Stanic, A. M., Yan, R., Blanton, M. R., Bershady, M. A., Sánchez-Gallego, J. R., Drory, N., Jones, A., Kauffmann, G., Law, D. R., Li, C., MacDonald, N., Masters, K., Thomas, D., Tinker, J., Weijmans, A.-M., and Brownstein, J. R. (2017). The SDSS-IV MaNGA Sample: Design, Optimization, and Usage Considerations. AJ, 154(3):86.

Wang, J., Nardini, E., Fabbiano, G., Karovska, M., Elvis, M., Pellegrini, S., Max, C., Risaliti, G., U, V., and Zezas, A. (2014). Fast and Furious: Shock Heated Gas as the Origin of Spatially Resolved Hard X-Ray Emission in the Central 5 kpc of the Galaxy Merger NGC 6240. ApJ, 781(1):55.

Wang, J., Xu, D. W., and Wei, J. Y. (2018). Study of Outflows in Luminous Quasars at Redshift ~0.4-0.8. ApJ, 852(1):26.

Ward, S. R., Harrison, C. M., Costa, T., and Mainieri, V. (2022). Cosmological simulations predict that AGN preferentially live in gas-rich, star-forming galaxies despite effective feedback. MNRAS, 514(2):2936–2957.

Weedman, D. W. (1970). High-Velocity Gas Motions in Galactic Nuclei. ApJ, 159:405.

Weedman, D. W., Hao, L., Higdon, S. J. U., Devost, D., Wu, Y., Charmandaris, V., Brandl, B., Bass, E., and Houck, J. R. (2005). Mid-Infrared Spectra of Classical AGNs Observed with the Spitzer Space Telescope. ApJ, 633(2):706–716.

Weller, J., Ostriker, J. P., Bode, P., and Shaw, L. (2005). Fast identification of bound structures in large N-body simulations. MNRAS, 364(3):823–832.

Westfall, K. B., Cappellari, M., Bershady, M. A., Bundy, K., Belfiore, F., Ji, X., Law, D. R., Schaefer, A., Shetty, S., Tremonti, C. A., Yan, R., Andrews, B. H., Brownstein, J. R., Cherinka, B., Coccato, L., Drory, N., Maraston, C., Parikh, T., Sánchez-Gallego, J. R., Thomas, D., Weijmans, A.-M., Barrera-Ballesteros, J., Du, C., Goddard, D., Li, N., Masters, K., Ibarra Medel, H. J., Sánchez, S. F., Yang, M., Zheng, Z., and Zhou, S. (2019). The Data Analysis Pipeline for the SDSS-IV MaNGA IFU Galaxy Survey: Overview. AJ, 158(6):231.

Weymann, R. J., Morris, S. L., Foltz, C. B., and Hewett, P. C. (1991). Comparisons of the Emission-Line and Continuum Properties of Broad Absorption Line and Normal Quasi-stellar Objects. ApJ, 373:23.

Willott, C. J., Delorme, P., Reylé, C., Albert, L., Bergeron, J., Crampton, D., Delfosse, X., Forveille, T., Hutchings, J. B., McLure, R. J., Omont, A., and Schade, D. (2010). The Canada-France High-z Quasar Survey: Nine New Quasars and the Luminosity Function at Redshift 6. AJ, 139(3):906–918.

Woo, J.-H., Bae, H.-J., Son, D., and Karouzos, M. (2016). The Prevalence of Gas Outflows in Type 2 AGNs. ApJ, 817(2):108.

Woo, J.-H., Son, D., and Bae, H.-J. (2017). Delayed or No Feedback? Gas Outflows in Type 2 AGNs. III. ApJ, 839(2):120.

Wright, G. S., Joseph, R. D., and Meikle, W. P. S. (1984). The ultraluminous interacting galaxy NGC6240. Nature, 309(5967):430–431.

Wylezalek, D., Schnorr Müller, A., Zakamska, N. L., Storchi-Bergmann, T., Greene, J. E., Müller-Sánchez, F., Kelly, M., Liu, G., Law, D. R., Barrera-Ballesteros, J. K., Riffel, R. A., and Thomas, D. (2017). Zooming into local active galactic nuclei: the power of combining SDSS-IV MaNGA with higher resolution integral field unit observations. MNRAS, 467(3):2612–2624.

Yan, R., Bundy, K., Law, D. R., Bershady, M. A., Andrews, B., Cherinka, B., Diamond-Stanic, A. M., Drory, N., MacDonald, N., Sánchez-Gallego, J. R., Thomas, D., Wake, D. A., Weijmans, A.-M., Westfall, K. B., Zhang, K., Aragón-Salamanca, A., Belfiore, F., Bizyaev, D., Blanc, G. A., Blanton, M. R., Brownstein, J., Cappellari, M., D'Souza, R., Emsellem, E., Fu, H., Gaulme, P., Graham, M. T., Goddard, D., Gunn, J. E., Harding, P., Jones, A., Kinemuchi, K., Li, C., Li, H., Maiolino, R., Mao, S., Maraston, C., Masters, K., Merrifield, M. R., Oravetz, D., Pan, K., Parejko, J. K., Sanchez, S. F., Schlegel, D., Simmons, A., Thanjavur, K., Tinker, J., Tremonti, C., van den Bosch, R., and Zheng, Z. (2016). SDSS-IV MaNGA IFS Galaxy Survey—Survey Design, Execution, and Initial Data Quality. AJ, 152(6):197.

Yang, Q., Wu, X.-B., Fan, X., Jiang, L., McGreer, I., Shangguan, J., Yao, S., Wang, B., Joshi, R., Green, R., Wang, F., Feng, X., Fu, Y., Yang, J., and Liu, Y. (2018). Discovery of 21 New Changing-look AGNs in the Northern Sky. ApJ, 862(2):109.

Yaqoob, T., Warwick, R. S., and Pounds, K. A. (1989). Variable X-ray absorption in NGC 4151. MNRAS, 236:153–170.

York, D. G., Adelman, J., Anderson, John E., J., Anderson, S. F., Annis, J., Bahcall, N. A., Bakken, J. A., Barkhouser, R., Bastian, S., Berman, E., Boroski, W. N., Bracker, S., Briegel, C., Briggs, J. W., Brinkmann, J., Brunner, R., Burles, S., Carey, L., Carr, M. A., Castander, F. J., Chen, B., Colestock, P. L., Connolly, A. J., Crocker, J. H., Csabai, I., Czarapata, P. C., Davis, J. E., Doi, M., Dombeck, T., Eisenstein, D., Ellman, N., Elms, B. R., Evans, M. L., Fan, X., Federwitz, G. R., Fiscelli, L., Friedman, S., Frieman, J. A., Fukugita, M., Gillespie, B., Gunn, J. E., Gurbani, V. K., de Haas, E., Haldeman, M., Harris, F. H., Hayes, J., Heckman, T. M., Hennessy, G. S., Hindsley, R. B., Holm, S., Holmgren, D. J., Huang, C.-h., Hull, C., Husby, D., Ichikawa, S.-I., Ichikawa, T., Ivezić, Ž., Kent, S., Kim, R. S. J., Kinney, E., Klaene, M., Kleinman, A. N., Kleinman, S., Knapp, G. R., Korienek, J., Kron, R. G., Kunszt, P. Z., Lamb, D. Q., Lee, B., Leger, R. F., Limmongkol, S., Lindenmeyer, C., Long, D. C., Loomis, C., Loveday, J., Lucinio, R., Lupton, R. H., MacKinnon, B., Mannery, E. J., Mantsch, P. M., Margon, B., McGehee, P., McKay, T. A., Meiksin, A., Merelli, A., Monet, D. G., Munn, J. A., Narayanan, V. K., Nash, T., Neilsen, E., Neswold, R., Newberg, H. J., Nichol, R. C., Nicinski, T., Nonino, M., Okada, N., Okamura, S., Ostriker, J. P., Owen, R., Pauls, A. G., Peoples, J., Peterson, R. L., Petravick, D., Pier, J. R., Pope, A., Pordes, R., Prosapio, A., Rechenmacher, R., Quinn, T. R., Richards, G. T., Richmond, M. W., Rivetta, C. H., Rockosi, C. M., Ruthmansdorfer, K., Sandford, D., Schlegel, D. J., Schneider, D. P., Sekiguchi, M., Sergey, G., Shimasaku, K., Siegmund, W. A., Smee, S., Smith, J. A., Snedden, S., Stone, R., Stoughton, C., Strauss, M. A., Stubbs, C., SubbaRao, M., Szalay, A. S., Szapudi, I., Szokoly, G. P., Thakar, A. R., Tremonti, C., Tucker, D. L., Uomoto, A., Vanden Berk, D., Vogeley, M. S., Waddell, P., Wang, S.-i., Watanabe, M., Weinberg, D. H., Yanny, B., Yasuda, N., and SDSS Collaboration (2000). The Sloan Digital Sky Survey: Technical Summary. AJ, 120(3):1579–1587.

Yoshida, M., Yagi, M., Ohyama, Y., Komiyama, Y., Kashikawa, N., Tanaka, H., and Okamura, S. (2016). Giant Hα Nebula Surrounding the Starburst Merger NGC 6240. ApJ, 820(1):48.

Zakamska, N. L. and Greene, J. E. (2014). Quasar feedback and the origin of radio emission in radio-quiet quasars. MNRAS, 442(1):784–804.

Zakamska, N. L., Hamann, F., Pâris, I., Brandt, W. N., Greene, J. E., Strauss, M. A., Villforth, C., Wylezalek, D., Alexandroff, R. M., and Ross, N. P. (2016). Discovery of extreme [O III] λ5007 Å outflows in high-redshift red quasars. MNRAS, 459(3):3144–3160.

Zanchettin, M. V., Feruglio, C., Bischetti, M., Malizia, A., Molina, M., Bongiorno, A., Dadina, M., Gruppioni, C., Piconcelli, E., Tombesi, F., Travascio, A., and Fiore, F. (2021). The IBISCO survey. I. Multiphase discs and winds in the Seyfert galaxy Markarian 509. A&A, 655:A25.

Zhang, K., Dong, X.-B., Wang, T.-G., and Gaskell, C. M. (2011). The Blueshifting and Baldwin Effects for the [O III] λ5007 Emission Line in Type 1 Active Galactic Nuclei. ApJ, 737(2):71.

Zubovas, K. and Bourne, M. A. (2017). Do AGN outflows quench or enhance star formation? MNRAS, 468(4):4956–4967.

Zubovas, K. and King, A. (2012). Clearing Out a Galaxy. ApJ, 745(2):L34.

Zubovas, K. and King, A. R. (2014). Galaxy-wide outflows: cold gas and star formation at high speeds. MNRAS, 439(1):400–406.

Zubovas, K. and Nardini, E. (2020). Intermittent AGN episodes drive outflows with a large spread of observable loading factors. MNRAS, 498(3):3633–3647.

Zubovas, K., Nayakshin, S., King, A., and Wilkinson, M. (2013a). AGN outflows trigger starbursts in gas-rich galaxies. MNRAS, 433(4):3079–3090.

Zubovas, K., Nayakshin, S., Sazonov, S., and Sunyaev, R. (2013b). Outflows of stars due to quasar feedback. MNRAS, 431(1):793–798.